ProQuest Number: 10290255

ProQuest 10290255

STEREOSCOPIC LINE-SCAN IMAGING

USING ROTATIONAL MOTION

Richard Stephen Petty

A thesis submitted in partial fulfilment of the requirements of
The Nottingham Trent University for the degree of
Doctor of Philosophy

Department of Electrical and Electronic Engineering,
The Nottingham Trent University,
Burton Street,
Nottingham.

June 1997

Collaborating Establishment:

British Telecommunications Research Laboratories,
Martlesham Heath,
Ipswich.

97 PET Ref.

OR 1

Stereoscopic Line-scan Imaging Using Rotational Motion

R. S. Petty

ABSTRACT

This thesis describes work which has been carried out to investigate a rotating stereoscopic imaging system consisting of two line-scan cameras. Algorithms have been proposed and experimentally tested which allow three-dimensional co-ordinate information to be derived from a defined object space.

A rotating stereoscopic line-scan system would be particularly suited to applications in which information is required from the "all-round" observation of a scene. Such applications would include autonomous vehicle guidance, path-planning for complex manipulator manoeuvres or security surveillance scenarios. The ability to extract three-dimensional co-ordinate information from the stereoscopic field of view would allow a solid image model of the workspace to be constructed.

Initial work involved a theoretical appraisal of a line-scan camera used in a rotating two-dimensional mode. Such a system was constructed and experiments were undertaken to determine the suitability of the rotating sensor as the basis for the development of a rotating stereoscopic camera arrangement. The results from this section of the work verified that two-dimensional co-ordinate information can be obtained from a defined object space. Subsequently, a rotating stereoscopic line-scan system was constructed for which a theoretical mathematical model for measurement was developed. Application of the derived algorithms to the stereoscopic system enabled the position of targets in three-dimensional object space to be determined on completion of a calibration procedure.

Experimental work was conducted to quantify any measurement errors inherent in the stereoscopic configuration and to identify, if possible, the source of these errors. Further experiments were undertaken to determine the accuracy of measurement which could be achieved using the algorithms developed. The results indicate that the three-dimensional position of targets in object space can be determined, at best, to an accuracy of ±0.5mm in the X-axis (horizontal), ±0.6mm in the Y-axis (vertical) and ±1.2mm in the Z-axis (range) at a camera-to-object range of 1.5m.

ACKNOWLEDGEMENTS

I would like to extend my sincere thanks to the following people for their help during this work.

To my family and friends for their continued support throughout this research.

To Professor Max Robinson, Dr. Simon Godber and Dr. Paul Evans for their guidance and advice throughout this research project.

I would like to thank Dr. Simon Godber again for his advice regarding this thesis.

TABLE OF CONTENTS

    APPENDIX A

    Derivation of the Parallax Relationship for a Convergent Stereoscopic Camera System

    APPENDIX B

    Experimental Results from the Rotating Two-dimensional Line-scan System

    APPENDIX C

    Symbols used in the 'Analysis of a Rotating Stereoscopic Line-scan System'

    APPENDIX D

    Derivation of the '3-D Conformal Transformation' for use with the Rotating Stereoscopic Line-scan System

    APPENDIX E

    Research Papers Pertaining to the Research Presented in this Thesis

LIST OF FIGURES

LIST OF TABLES

LIST OF GRAPHS

1. INTRODUCTION

1.1 Background

Historically, the majority of research in the selection and design of visual feedback modality has concentrated on the standard television type sensor for machine vision applications in industrial inspection [1, 2, 3, 4, 5], robot vision [6, 7, 8, 9, 10, 11], control [12, 13, 14] and measurement [15, 16, 17, 18]. Although this device has proven to be effective in providing solutions to a broad range of different problems, there is evidence [19, 20, 21, 22, 23, 24, 25, 26, 27] to suggest the use of such sensors may not provide the optimum solution for a machine vision application.

The development and application of three-dimensional (i.e. binocular stereoscopic) systems has been undertaken at The Nottingham Trent University for a number of years [28, 29, 30, 31] and, more recently, has concentrated on the analysis of alternative sensor arrangements [32, 33, 34, 35]. Previous research has investigated the potential of one such device in a stereoscopic configuration [32]. This device is the line-scan sensor which has traditionally been used in industrial inspection [36, 37, 38, 39, 40] and measurement applications [41, 42, 43, 44].

The research presented in this thesis will investigate the characteristics associated with a rotating stereoscopic line-scan system. The main aim is to provide a system with the capability to extract co-ordinate information from a 'panoramic' view of the workspace surrounding the rotating camera platform. This will enable the relationship between objects in a scene of interest to be established, thus, allowing a theoretical model of the workspace to be constructed. Previous work [45, 46, 47, 48, 49, 50, 51] in this area has involved predominantly the use of the conventional television camera for the production of similar images. However, to obtain an 'all-round' field of view additional components have often been used in conjunction with the camera. These components have included a conic mirror, a fisheye lens and a vertical slit to facilitate the extraction of information from, for example, a 360° field of view.

A rotating line-scan camera arrangement will allow the field of view of the resultant images to be varied from any arc up to 360°. For an 'all-round' field of view the co-ordinate data derived from the images produced may be used to determine the relationship between objects of interest from an area of workspace completely surrounding the camera arrangement. This camera system

has many potential applications which include object surveillance and tracking [52, 53, 54], intruder detection [55] and image sequence analysis [56].

1.2 Objectives

The objectives of the research are summarised below in the context of the two phases in which the work was undertaken.

Phase (I) :

- The development of a rotating two-dimensional line-scan camera system and the subsequent determination of the operating parameters which govern image production.

The results from this part of the work were applied to the development of a stereoscopic arrangement of sensors.

Phase (II) :

- Theoretical evaluation of the three-dimensional co-ordinate measurement capability of the system based on conformal transformation design theory.
- Empirical evaluation of the three-dimensional co-ordinate measurement capability of the system.

After evaluation of the measurement capability the characteristics of the rotating line-scan system were assessed.

1.3 Structure of the Thesis

The arrangement of the thesis is summarised in the following paragraphs.

Chapter two provides background information for the research detailed in the chapters that follow. It introduces the three major enabling technologies of stereoscopic vision theory, photogrammetry and the principles of line-scan imaging.

Chapter three presents an analysis of rotating 2-D line-scan systems which is based on the principles of line-scan imaging in conjunction with the geometry of camera rotation. Following this, experimental results from a rotating system are presented to allow an assessment of this section of the research.

Chapter four presents the mathematical analysis of a stereoscopic arrangement of rotating line-scan sensors which includes the use of stereoscopic vision theory and aspects of photogrammetry.

Chapter five describes the stereoscopic experiments and outlines the results which enable an evaluation of the co-ordinate measurement capability to be made. Consequently, the characteristics of the rotating system are identified with respect to the image production parameters.

Chapter six is a summary of the results, conclusions and the direction of further work.

Following the main text and a list of the reference material, the appendices include results from the two-dimensional work, the derivation of the conformal transformation used with the rotating stereoscopic line-scan arrangement and published research papers related to this work.

2. THE ENABLING TECHNOLOGIES

2.1 Introduction

The research presented in this thesis investigates the characteristics associated with a rotating stereoscopic line-scan system. The main aim is to provide a system with the capability to extract information from a view of the workspace which surrounds the rotating camera platform. Essentially, this requires the ability to extract three-dimensional co-ordinate information using the stereoscopic arrangement under consideration.

The objective of this chapter is to provide background information on the enabling technologies used in this work. The discussion presented is divided into the following three broad areas :

- stereoscopy;
- photogrammetry;
- the line-scan device.

Stereoscopic design theory has been applied successfully by the 3-D Imaging Group of The Nottingham Trent University to the development of camera systems for use with teleoperated robotic manipulator arms [28, 29, 30, 31, 60, 61, 62, 63, 64, 65, 66, 67]. This design theory is based on research by Jones [57], which is an adaptation of earlier findings by Spottiswoode and Spottiswoode [58], and Valyus [59] regarding large screen stereoscopic systems. The design theory given by Jones has been successfully implemented by the, then, C.E.G.B. to develop stereoscopic video camera systems for the visual inspection of nuclear reactors by human operators. The important design parameters presented by Jones form the conceptual building blocks from which the development of a rotating stereoscopic line-scan system was approached.

An introduction to photogrammetry is given following the considerations on stereoscopic camera design. Horn [68] defines two main orientation methodologies which allow the transformation from image space co-ordinates to an object space co-ordinate system for a stereoscopic television camera arrangement. These orientation procedures are discussed as a background to the co-ordinate measurement algorithms which will be developed specifically for use with the rotating line-scan system.

Finally, the line-scan sensor is introduced and the method of generating images from this device is discussed.

2.2 Stereoscopy

The Manual of photogrammetry [69] defines stereoscopy as :

"......... the science and art that deals with the use of images to produce a three-dimensional visual model with characteristics analogous to those of actual features viewed using true binocular vision."

A basic knowledge of depth perception mechanisms utilised by a human observer is necessary to appreciate the principles behind stereoscopic vision systems. However, it is not within the scope of this thesis to provide a detailed study of human vision, although the basic principles will be discussed. A more thorough examination of these principles is given by Okoshi [70]. To summarise, an observer uses up to ten cues for depth perception. These can be split into two main groups and are listed below :

- Physiological cues :   binocular parallax;
                           monocular movement parallax;
                           accommodation;
                           convergence.

- Psychological cues :   occlusion;
                           shadows and shading;
                           linear perspective;
                           texture gradient;
                           retinal image size;
                           areal perspective.

The four physiological cues are generally accepted as being the most important group, of which binocular parallax is the more robust [71].

The use of stereoscopy in machine vision originates from the operating principle of the human visual system [72, 73]. Consider an object in the field of view of both eyes, each eye receives a slightly different view of the object. The amount of difference in each eye produced by an observed point is dependent on the distance between the eyes, the convergence angle and the distance of the object from the point of observation.

2.2.1 Stereoscopic Vision

Stereoscopic vision is a commonly used technique for obtaining three-dimensional co-ordinate information by viewing a scene from two different perspectives and locating corresponding points in both images. Two basic requirements must be realised to enable the use of stereoscopic imaging techniques with a camera system :

- Each object, or the point on each object, must be in the field of view of both cameras (*point A,* in Figure 2-1). The stereo-camera arrangement is usually adjusted to overlap in an area of space that covers the points of interest to achieve this requirement. This overlap (shaded region) is called the *stereoscopic region*. If an object, or a point on the object, cannot be seen by both cameras (*point B*) it is *occluded* and the depth information for that point cannot be determined.
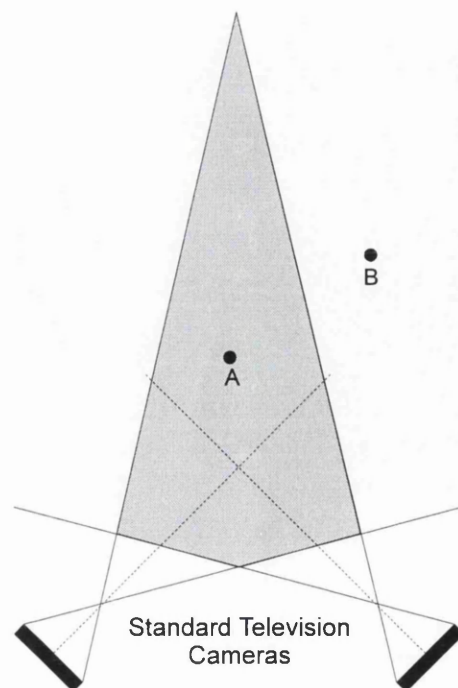
Figure 2-1 Stereoscopic Region

- Conjugate image points situated within the stereoscopic region must be located. This is referred to as the *correspondence problem* and is a fundamental obstacle to obtaining three-dimensional co-ordinate information from an object space using stereoscopy [68, 74]. Finding a solution to the correspondence problem is not within the scope of the research presented in this thesis. For this work a manual solution to the correspondence problem is adopted. There are solutions to this problem that have been developed by researchers over a period of years which include edge-detection and grey-level matching [68, 75], the use of the epi-polar line constraint, [76] the use of controlled illumination [77] and neural networks [78].

2.2.2 A Parallel Camera System

If the principle of stereoscopy is applied to a stereo-camera configuration [68] (Figure 2-2) depth information may be obtained from a scene of interest.
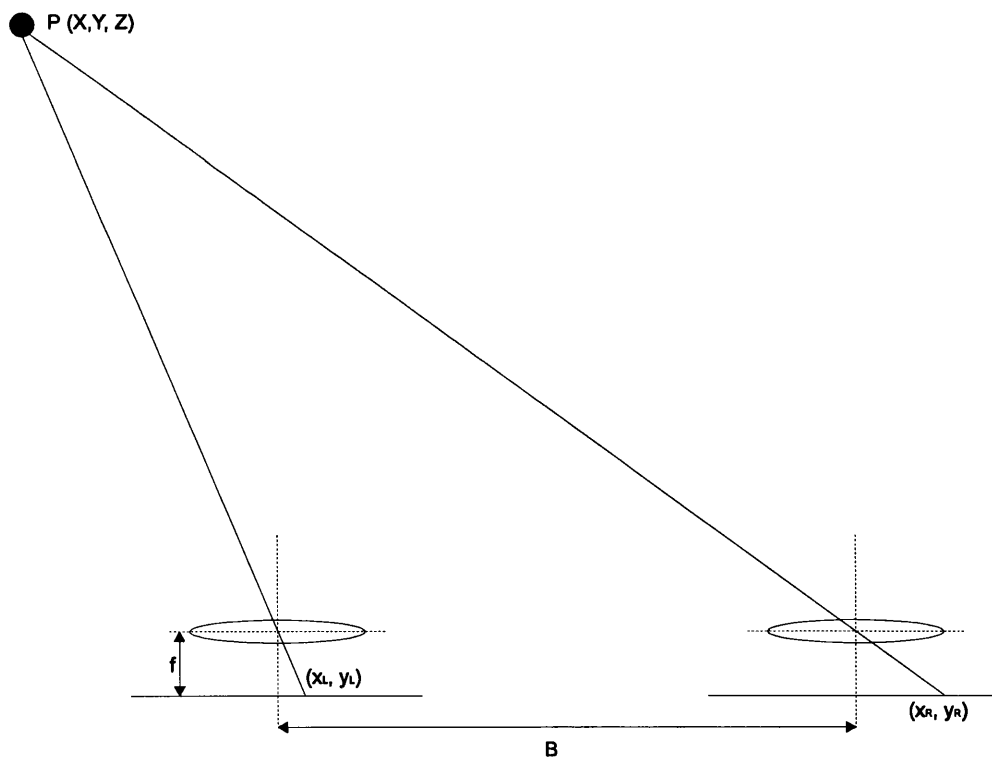
Figure 2-2 Disparity in a Simple Parallel System

Consider a point of interest, P, which lies within the field of view of a stereo-camera arrangement. Initially, a *disparity* value must be obtained for depth information to be resolved. The disparity is the difference in horizontal displacement, for the same point, observed in each of

the left and right images. For a parallel camera configuration, if the distance between the camera pair (B) and the focal length (f) of each camera remain constant then depth (z) is inversely proportional to the disparity (x_L - x_R). This relationship is determined by the following equation, known as the *parallax equation* :

$$z = \frac{Bf}{(x_L - x_R)}$$

Where,

x_L is the position of an object or point in the x-axis of image space, viewed by the left camera;

x_R is the position in the x-axis of the same object or point in the right camera view;

B is the separation of the two cameras and f is the focal length of the camera lenses.

The accuracy of this depth information is dependent on the size of each picture element, or pixel, and also on the parameters that govern the extent of the disparity, i.e., range, camera separation and focal length.

2.2.3   A Convergent Camera System

The derivation of the range formulae for a stereoscopic system was considered above for a simplistic arrangement of parallel cameras. Now if the cameras are arranged to converge (Figure 2-3), the formula resolving depth is more complicated. The derivation of this formulae is covered by the work of Jones [57].

The stereoscopic region is defined by the base length (B), the convergence angle (σ) and the focal length of the camera lens (f). The equation for the disparity, p, of a point in image space, at a range z from the stereoscopic camera base line is given by Jones as (see Appendix A for the derivation) :

$$p = 2f \tan\sigma - \frac{Bf}{z} \qquad\qquad \text{Equation 2-1}$$

f - focal length
B - camera base separation
σ - convergence angle
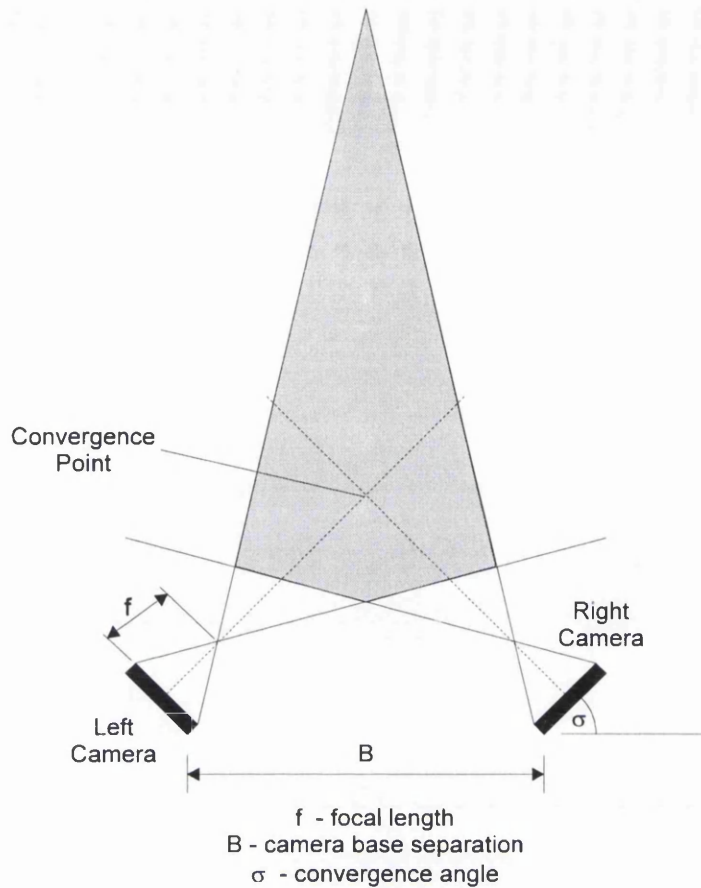
Figure 2-3 Stereoscopic Region for a Convergent Camera System

Depth resolution, or the minimum resolvable depth increment, in object space is an important consideration for a stereoscopic vision system. The equation which defines depth resolution 'δz' for a convergent camera system can be derived by differentiating Equation 2-1 :

$$\delta z = \frac{z^2}{Bf\delta p} \qquad\qquad\qquad \text{Equation 2-2}$$

Where,

δz is the smallest detectable increment in depth;

δp is the minimum detectable parallax.

Two fundamental points can be made about stereoscopic vision systems using television type cameras from consideration of Equation 2-2 :-

- the smallest detectable depth increment increases as the square of the object range;

- the depth resolution at a given range is dependent on the minimum detectable disparity.

These points can be appreciated from Figure 2-4. The potential stereoscopic region consists of many smaller segments which represent volume elements or *voxels* [76] in object space. A voxel is defined in the region of overlap formed by a left and a right pixel *sample* of object space. The whole of the stereoscopic region is made up of voxels.
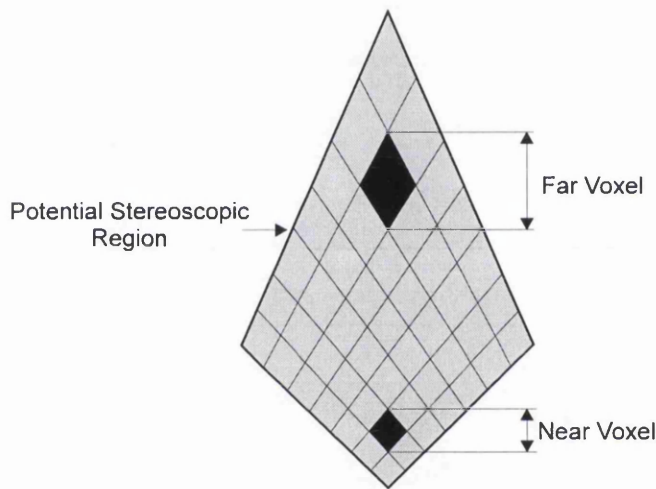
Figure 2-4 Increasing Voxel Size as a Function of Range

The divergent nature of the field of view for each camera results in the voxels being stretched as the range from the camera baseline increases. An example of a 'near' and a 'far' voxel is shown in the diagram above.

So far, the explanation of stereoscopy has made certain assumptions. For instance, it has been assumed the following parameters are known to a given degree of accuracy :

- the geometric alignment of the stereo-sensors in terms of the rotation about each co-ordinate axis;

- the focal length of the lenses;

- the separation between the two cameras.

In practice it is difficult to quantify these parameters to a known degree of accuracy. Therefore, some means of determining an approximate value for each must be introduced. The methods used to determine, or allow for errors in, these parameters and also provide a means to extract the resultant 3-D co-ordinate information are described in the following section.

2.3 Photogrammetry

Haggren [79] et al [80] describe photogrammetry as :

"The art, science and technology of obtaining reliable three-dimensional information about physical objects and the environment through processes of recording, measuring, and interpreting photographic images and patterns of electromagnetic radiant energy and other phenomena."

Historically, photogrammetric techniques have been used primarily for the extraction of co-ordinate information from photographs. However, photogrammetric machine vision replaces the photographic plate with a dynamic imaging sensor. In the majority of cases to date, this sensor has been the standard television camera. The success of the substitution of a photographic plate for a video camera suggests the type of imaging device is irrelevant to the principle of photogrammetry. This conclusion is confirmed in work by El-hakim [81] et al [82, 83, 84].

The main aim of photogrammetry is the faithful reproduction of three-dimensional co-ordinate information from an object of interest. This information is obtained from the scene as reflected light which is usually collected by a lens and focused onto a photosensitive device. The image obtained from such a device will contain points equivalent to those in the object space.

The simplest model of a camera is a perfect perspective projection from the world onto the image plane. This is governed by the *principle of collinearity* defined by Haggren [79] as :

 "the projection of a straight line through the optical centre of the lens from a point on an object in the real world to the same point on the image plane".

A simple inverse projection along this straight line does not define a unique point of interest as the point location along the line is unknown. Therefore, it is necessary to image the scene of interest from a minimum of two locations and the intersection of the projections for each conjugate image point will define a unique location for each equivalent point in object space.

2.3.1 The Requirement for Calibration

Photogrammetric calibration allows the three-dimensional co-ordinate analysis of a scene by compensating for systematic errors within the various modules of the imaging system, i.e., optics, physical arrangement of cameras, etc (Figure 2-5). These errors result in deviations from the straight line which links respective points in image space and object space. In machine vision applications it is usual to calibrate these modules collectively. This can involve placing a pre-calibrated object volume within the stereo-region of the camera system. The parameters governing the transformation from the image space co-ordinate system to the object space co-ordinate may then be determined. Previous work [32,33] at Nottingham used this calibration technique which involved placing a three-dimensional frame into a workspace within the stereoscopic region defined by the camera system. A discussion of the calibration frame used in this research is presented in Chapter 5.0.
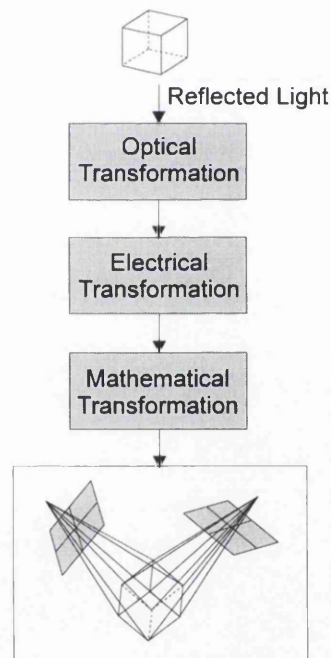
Figure 2-5 Object Space Definition from Reflected Light

The main reasons for calibration are :-

- it is not practical to measure precisely the base width and convergence angle for a given stereoscopic arrangement;

- the relative orientation of one camera to the other cannot be measured precisely;

- the true focal length of the camera-lens configuration is not known, and indeed is not necessarily the same for each camera;

- each of the left and right images are subject to distortion due to the behaviour of lenses varying from the ideal.

The following section introduces the concepts of orientation in photogrammetry, the theory of which is applied to the development of a calibration model specifically for use with a rotating stereoscopic line-scan system.

2.3.2 Concepts of Orientation

For this research a calibration model for use with a stereoscopic arrangement of rotating line-scan sensors is required which involves the development of 'unique' mathematical algorithms. Therefore, this section is confined to a discussion of conventional calibration methods, the basis of which allow the derivation of a mathematical model for the line-scan system (refer to Chapter 4.0).

To realise the inverse projection, and thus uniquely defining object space co-ordinates, a mathematical model of a stereo camera system must be considered. This model must provide for the fundamental transformation from the image space co-ordinate system to the object space co-ordinate system. On implementation of the transformation model the stereoscopic camera arrangement may be calibrated to allow 'corrected' co-ordinate information to be obtained from object space as a function of the equivalent image space quantities.

There has been a substantial amount of work undertaken by researchers in the field of television-type camera calibration methods over the years [85, 86, 87, 88, 89, 90, 91, 92]. Roberts [93] presents a generic algorithm approach to camera calibration in machine vision and Grattoni [94] critically reviews a series of camera calibration methods.

In the following sections the calibration methodologies of interior and exterior orientation, as defined by Horn [68], are addressed. These two orientation methodologies, of which exterior orientation can be sub-divided into relative and absolute orientation (Figure 2-6), are described

in a purposefully simplistic manner. Photogrammetry represents a research science in its' own right and accordingly it is not within the scope of this thesis to provide a more comprehensive description of this subject area. The reader is directed to "The Manual of Photogrammetry" [95] and "Elements of Photogrammetry" [96] for further information.

Concepts of
Orientation

Interior Orientation

Exterior Orientation

Relative Orientation

Absolute Orientation

Mathematical Alignment
of Camera and Object
Co-ordinate Systems
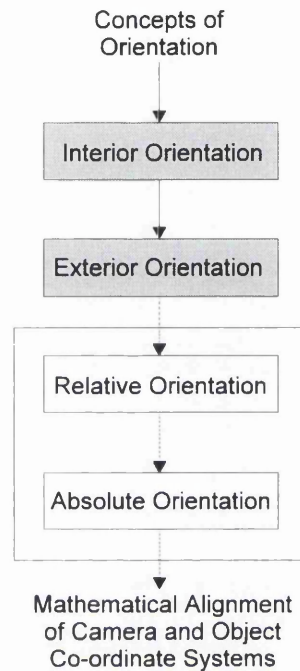
Figure 2-6 Concepts of Orientation

2.3.3 Interior Orientation

Interior orientation is the process of determining the effective focal length (the exact distance from the lens optical axis to the image plane) of the camera system, the exact place the optical axis pierces the image plane and the geometric distortion characteristics of the lens system. This section discusses lens distortion before presenting an analysis allowing the interior orientation for each camera of a stereoscopic arrangement to be determined.

All lenses have measurable distortions and other optical defects (aberrations). The aberrations [100] (for example, spherical and chromatic aberrations, coma, astigmatism and curvature of field) degrade the quality of an image and do not influence measurement directly, whereas, lens distortion causes a displacement of points in the image. Geometric lens distortion consists of the following two components :

- radial lens distortion, sometimes referred to as symmetric distortion;

- tangential lens distortion, sometimes referred to as asymmetric distortion.

Radial distortion causes points in the image to be displaced in a radial fashion and consists of a combination of pin-cushion and barrel distortion (Figure 2-7). Pin-cushion distortion causes the image to spread out in the outer portion of the image and the scale increases, (a), whilst barrel distortion causes the image to condense in the outer part of the image and the scale to decrease, (b).
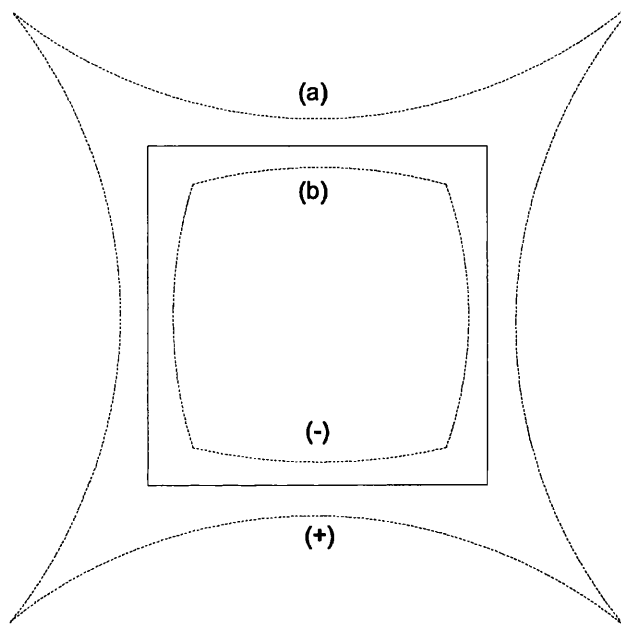
Figure 2-7 Pin-cushion Distortion (a) and Barrel Distortion (b)

Tangential distortion, sometimes referred to as decentering distortion, causes the displacement of points in an image perpendicular to the radial lines and results from imperfect fabrication of the lens. It is recognised [101] that this distortion can be tolerated to the degree that it does not affect the accuracy of measurements to any considerable extent.

An analysis allowing the interior orientation for each camera of a stereoscopic arrangement to be determined is presented in the following sections.

Figure 2-8 shows a three-dimensional image co-ordinate system which is commonly used [95] to define the location of image points with respect to the secondary principal point [97] of the camera-lens, O. In the image plane point O' is the central point of intersection in the x- and

y-axes of the image. The diagram shows the principal point [98] is coincident with point O' (given by image co-ordinates x_p, y_p), however, this ideal condition is difficult to achieve in practice. Therefore, assuming the principal point is not exactly in coincidence with point O', its position in the image may be defined by the co-ordinate location (x_p', y_p'). The position of an image point 'i' may be defined by the co-ordinates (x_i, y_i). The position of this image point with respect to the secondary principal point (O) is defined by the following three-dimensional co-ordinate location :

$$x'' = x_i - x_p'$$
$$y'' = y_i - y_p'$$
$$z'' = -f'$$
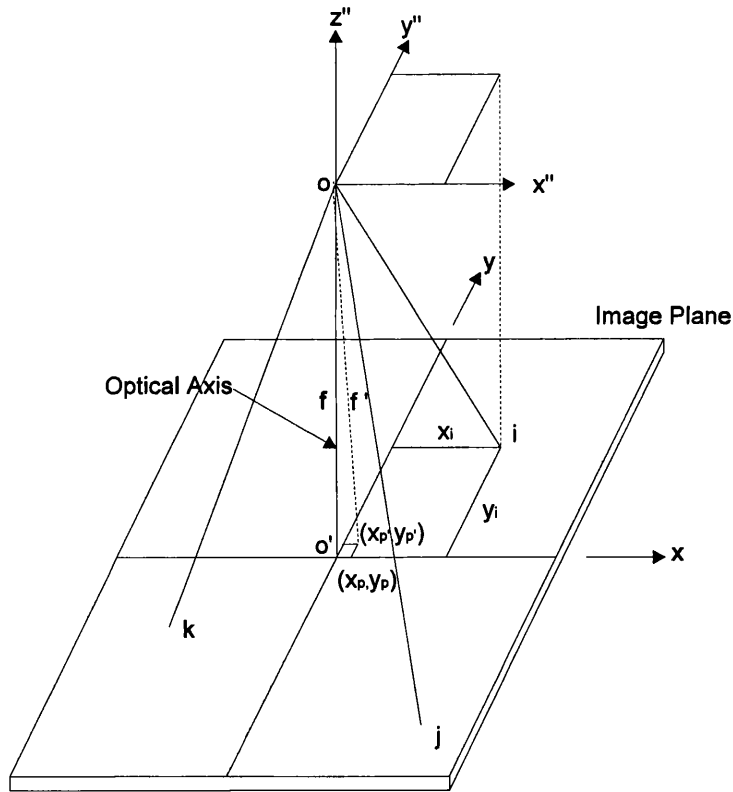
Figure 2-8 An Image Co-ordinate System

The interior orientation for each camera can be defined mathematically once the following parameters are known :-

- focal length, f ';
- co-ordinates of the principal point, x_p' and y_p';
- geometric distortion characteristics of the lens system.

Considering the parameter of lens distortion, one commonly used model for correcting lens distortion is that developed by Brown [102] :-

$$\Delta x_j = \bar{x}_j\left(l_1 r^2 + l_2 r^4 + l_3 r^6\right) + \left(p_1\left(r^2 + 2\bar{x}_j^2\right) + 2p_2\bar{x}_j\bar{y}_j\right)\left(1 + p_3 r^2\right)$$

$$\Delta y_j = \bar{y}_j\left(l_1 r^2 + l_2 r^4 + l_3 r^6\right) + \left(2p_1\bar{x}_j\bar{y}_j + p_2\left(r^2 + 2\bar{y}_j\right)^2\right)\left(1 + p_3 r^2\right)$$

Where,

Δx_j and Δy_j are corrections for geometric lens distortions present in the co-ordinates $\bar{x}_j$ and $\bar{y}_j$ of image point j; and r is given by :-

$$r = \sqrt{\bar{x}_j^2 + \bar{y}_j^2}$$

This model accounts for both symmetric radial distortion and asymmetric distortions caused by lens decentering. The terms which include the coefficients l_1, l_2 and l_3 represent symmetric radial distortion, and the terms which include p_1, p_2 and p_3 represent asymmetric distortion.

The image co-ordinates are corrected for lens distortion by the following expression :-

$$\bar{x}_j' = \bar{x}_j + \Delta x_j$$
$$\bar{y}_j' = \bar{y}_j + \Delta y_j$$

The following section now introduces the exterior orientation methodology.

2.3.4 Exterior Orientation

Exterior orientation can be sub-divided into *relative* and *absolute orientation* [98]. Once a relative transformation is undertaken the workspace is defined. However, for the camera system to interact with an object a relationship between the workspace and the object co-ordinate system must be established. This relationship may be determined using an absolute orientation methodology. This process is used when, for example, a camera system controls a robot arm and is commonly referred to as *hand-eye calibration* [99]. This section will discuss, in turn, relative and absolute orientation.

Relative Orientation :-

Relative orientation is the determination of the relative positions and angular orientation of the cameras in a stereoscopic pair when *only* projections of given points in each perspective image are known, i.e., the positions in object space are unknown. The main aim is to orient the two images so each corresponding pair of rays from the stereo-camera intersect in space. This condition can only be achieved if the camera lens is distortionless, the light rays travel in straight lines and no geometric distortion is introduced during the formation of an image.

To achieve relative orientation (Figure 2-9) one image, for example, the left image, is fixed in position, its orientation is also fixed and the scale of the model is initially set by assigning a base width equal to the camera separation under consideration. The right image is then adjusted by applying rotations and translations until all y parallax is cleared.
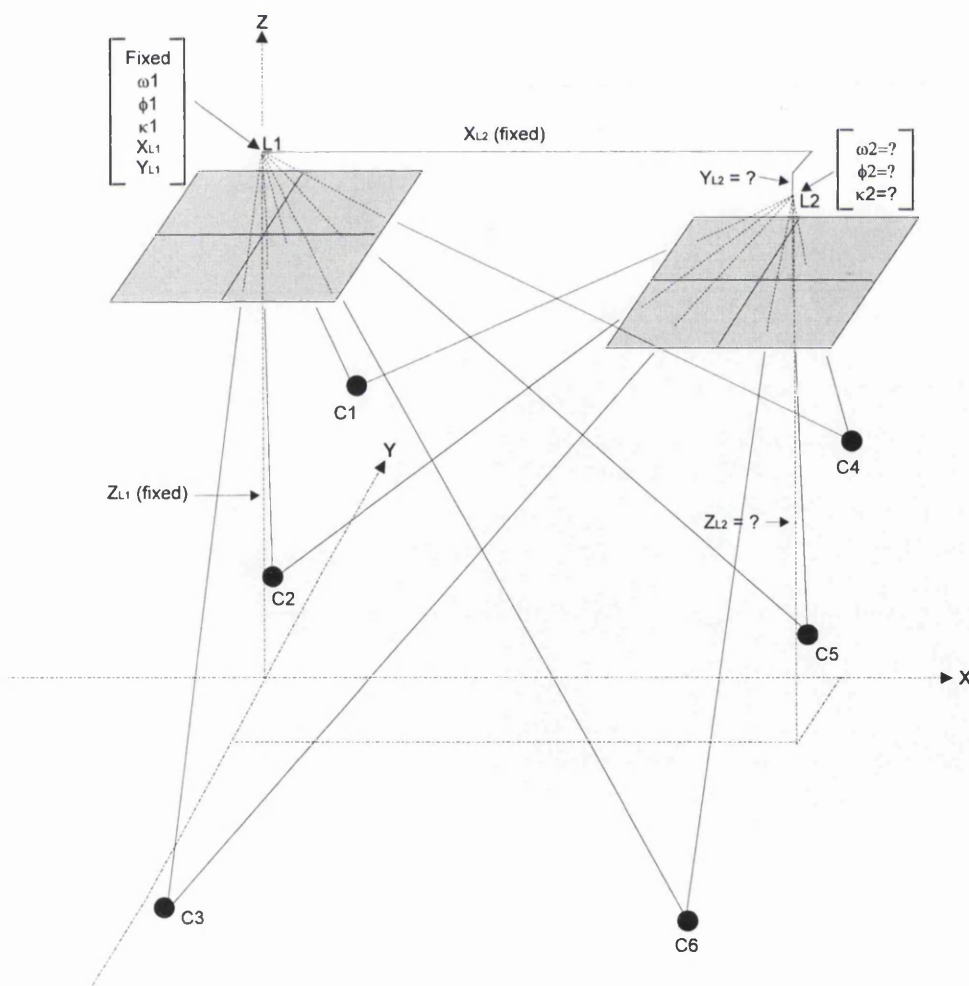
Figure 2-9 Relative Orientation Analysis

The left image is arbitrarily fixed in position and orientation by setting the three rotation angles, omega (ω_1), phi (ϕ_1) and kappa (κ_1), and X_{L1} and Y_{L1} equal to zero. Z_{L1} is also fixed at a value approximately equal to the camera-to-object range and X_{L2} is fixed at a value approximately equal to the actual camera base width. This fixes the initial scale of the mathematical stereo-model approximately equal to true scale.

Relative orientation is achieved by enforcing the condition that corresponding rays intersect at a point (points C1-C6, Figure 2-9). The enforcement of collinearity for intersecting corresponding rays is achieved by writing collinearity equations for both images for a minimum of five object points. Intersection of corresponding rays is automatically enforced as the equations from both images for a given object point contain the same object space co-ordinates. The resultant collinearity equations contain the five unknown elements of relative orientation for the right image (ω_2, ϕ_2, κ_2, Y_{L2} and Z_{L2}) and three unknown object space co-ordinates (X, Y and Z) for each point used in the analysis.

For each point in object space used in relative orientation, four collinearity equations can be written : an x and y equation of the following form for each of the perspective images:-

$$x = -f\left[\frac{m_{11}(X - X_L) + m_{12}(Y - Y_L) + m_{13}(Z - Z_L)}{m_{31}(X - X_L) + m_{32}(Y - Y_L) + m_{33}(Z - Z_L)}\right]$$

$$y = -f\left[\frac{m_{21}(X - X_L) + m_{22}(Y - Y_L) + m_{23}(Z - Z_L)}{m_{31}(X - X_L) + m_{32}(Y - Y_L) + m_{33}(Z - Z_L)}\right]$$

Where,

x and y are image co-ordinates of the point of interest in object space;

X, Y and Z are co-ordinates of the object points;

X_L, Y_L and Z_L are co-ordinates of the camera arrangement;

f is the camera-lens focal length and the m's are functions of the rotation angles.

Using a minimum of 5 object points, 20 equations can be written and a unique solution results as the number of unknowns is also 20, i.e., 5 unknown parameters for the right image and 15 unknown object space point co-ordinates. More than 5 points may be used in the relative orientation analysis with each additional point adding four equations and only three new unknowns. Therefore, each additional point adds one redundant equation. If redundancy exists

in the system of equations least squares techniques [103] may be used to obtain most probable values for the unknown transformation parameters.

Absolute Orientation :-

If the co-ordinates of given points in both of the images and their three-dimensional positions in object space are known a relationship between the camera and object co-ordinate systems may be established. Wolf [96] describes a *3-D conformal co-ordinate transformation* which converts from one three-dimensional system to another whilst maintaining true shape.
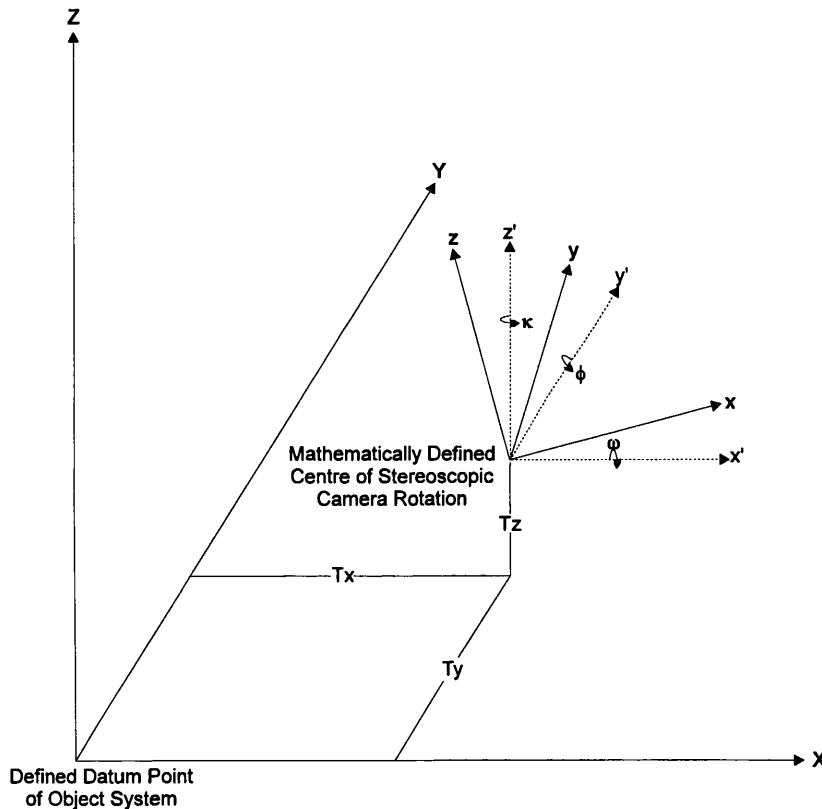
Figure 2-10 XYZ and xyz Three-dimensional Co-ordinate Systems

To achieve absolute orientation it is required to transform co-ordinates of points from an xyz system to an XYZ system. As observed in Figure 2-10, the camera and object co-ordinate systems are not mutually aligned. The necessary transformation equations can be expressed in terms of seven independent transformation factors : three rotation angles, omega (ω), phi (ϕ) and kappa (κ); three translation factors T_x, T_y and T_z; and a scale factor s. During a calibration phase the transformation model solves for these seven transformation factors simultaneously. This requires a minimum of three point co-ordinate locations to be known in both the XYZ and the xyz system.

For each known object space point location transformation equations of the following type result

$$X = s(m_{11}.x + m_{21}.y + m_{31}.z) + T_x$$
$$Y = s(m_{12}.x + m_{22}.y + m_{32}.z) + T_y \qquad \text{Equation 2-3}$$
$$Z = s(m_{13}.x + m_{23}.y + m_{33}.z) + T_z$$

Where,

m_{ab} are individual elements of the rotation matrix relating to the two co-ordinate systems.

The complete mathematical transformation can be expressed in the following matrix form :-

$$A.X = L + V \qquad \text{Equation 2-4}$$

Where,

A is a matrix of partial derivative coefficients;

X is a matrix of corrections to the successive approximations for the transformation factors;

L is a matrix of co-ordinate data for the known point locations evaluated at the successive approximations for the transformation factors;

V is a matrix of residuals to make the redundant equations consistent.

Equation 2-4 may be solved using a least squares technique. The solution is iterated, using Taylor's series [104], until negligibly small values are obtained for the corrections to successive approximations of the transformation parameters. Once the transformation parameters are known XYZ system co-ordinates with reference to the xyz system may be found by applying the relationships shown in Equation 2-3.

So far, the discussion of stereoscopic and photogrammetric theory has been associated with the standard television camera. To apply these principles to a stereoscopic configuration of line-scan sensors the method of obtaining two-dimensional images from these devices is discussed.

2.4 The Line-scan Sensor

The line-scan device benefits from all the advantages of the CCD technology apparent in modern television type sensors [105, 106, 107, 108, 109]. Furthermore, it is not locked to any given standard for information presentation and, therefore, can have a greater number of picture elements than the standard television camera. It consists of a line of contiguous photosites that can be oriented in a horizontal line or a vertical column relative to a scene of interest. Typically, the number of photosensitive elements can range from 256 to over 6000 in number, dependent on the application. Figure 2-11 illustrates the differences between the imaging areas of the line-scan and television type sensors.
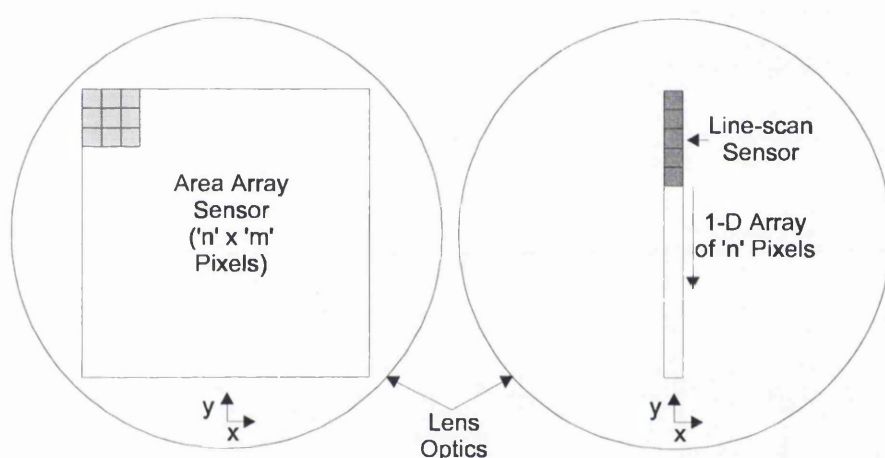
Figure 2-11 Imaging Areas of the Area Array and Linear Array Sensors

The lens distortions apparent in both the x- and y-axes of the area array sensor are only apparent in one axis of the line-scan device as it is, by design, one dimensional.

2.4.1 Two-dimensional Image Production

For the research presented, two-dimensional images from the line-scan device are required as the picture information returned is used by a human operator. To produce two-dimensional images, in the conventional sense, relative motion must be inherent between the camera and object system.

To illustrate this point, Figure 2-12 shows the field of view (FOV) from an area array camera. To obtain a similar FOV from a line-scan sensor relative motion must be inherent between the camera and object of interest. Figure 2-13 shows the effective field of view obtained from a

line-scan sensor after relative lateral [32] motion has taken place between camera and object. For the area array the FOV is restricted by the photosensitive area of the device, whereas for the line-scan device the FOV is restricted only by the capacity of the storage medium used.

Field Of View

Photosensitive
Area
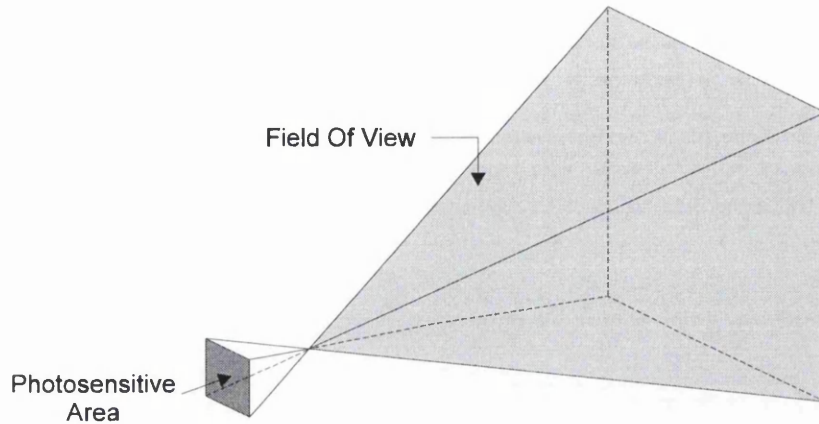
Figure 2-12 Area Array FOV

Effective
Field Of View
(after movement)

Effective
Photosensitive
Area
(after movement)
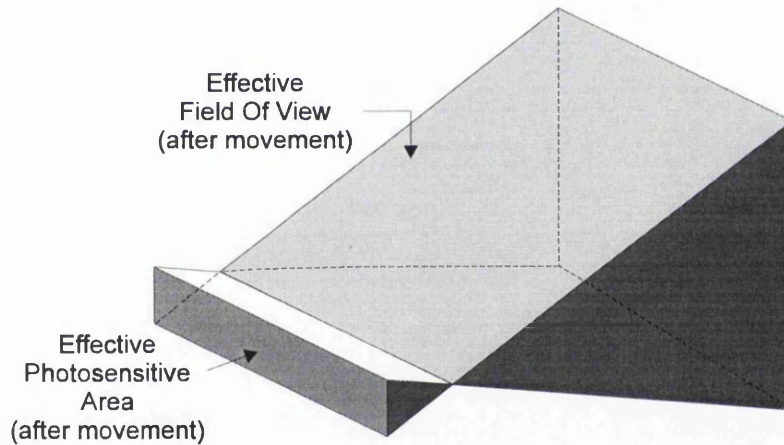
Figure 2-13 Line-scan FOV

2.4.2 Operation of the Line-scan Device

A block diagram of the internal structure of a typical line-scan sensor is shown in Figure 2-14.

With reference to this diagram, the line-scan sensor operates in the following way. Light reflected from an object is focused by the camera optics and is incident on the photosites of the line-scan device. The number of photons accumulated in the photosite is a linear function of the incident illumination intensity and the *integration period*. This period is defined as the time allowed for the photosites to collect charge and is analogous to the shutter speed in photographic cameras. The minimum integration period is determined by a combination of the transport clock rate, or *scan rate*, and the number of photosites on the sensing chip.
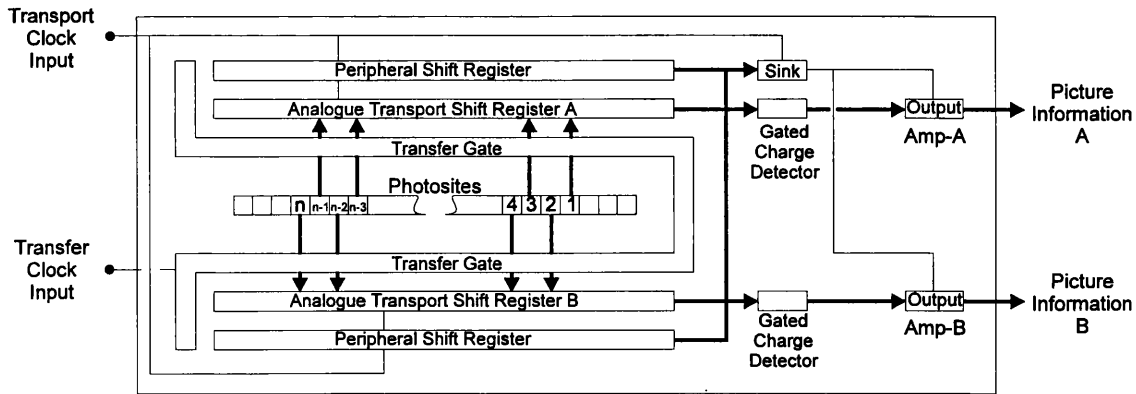
Figure 2-14 Line-scan Internal Block Diagram

The line-scan camera provides an analogue voltage output which is proportional to the photon count at a particular photosite, the quantity of photons depending on the integration period. The relationship between the number of pixels and the integration period is seen in Figure 2-15. In practical terms, increasing the transport clock speed leads to a smaller integration period and results in less photons being collected by each photo-sensitive element. Subsequently, the output voltage from each photosite will be smaller and the image will appear darker.
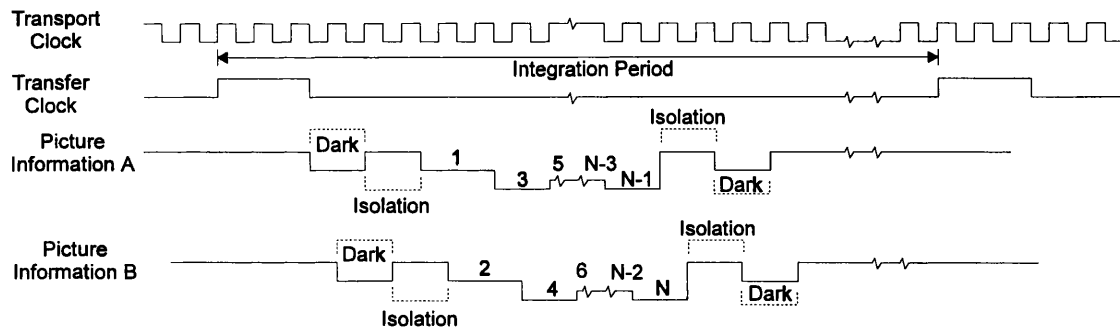
Figure 2-15 Line-scan Timing Diagram

Throughout relative motion between the sensor and object picture information is provided as a continuous stream of analogue voltage levels, each level representing the number of photons collected from a photosite. The relationship of each voltage level to a particular photosite is locked to the transport clock with which it is driven. Each photon dependent voltage in a line of picture information must be stored before further information can be obtained from the sensor. The image data can be stored so when displayed on a video monitor, the relationship of adjacent pixel columns generates a two-dimensional image of the object space under observation.

Ideally, no relative movement will occur between the device and object during the integration period, as any movement will result in image blur. A similar condition would exist in a photographic camera if the shutter was left open and the object moved in the FOV. After a line of picture information is stored, the camera can be moved in relation to the object and the storage process repeated. This acquisition and storage process is continued until the image storage area is full and a two-dimensional image can be displayed.

In practice, the relative movement between the camera and object is continuous, as is the transfer of picture information from the sensor to the storage device. The relationship of the object motion and the integration period is adjusted so that any distortions in the images generated are minimised. If this requirement is not met, the returned picture data may introduce blurring in the image.

Usually, a storage medium or framestore is connected to the line-scan camera, where the photon dependent voltages are converted to a digital format before storage. The timing of the picture information is determined by control signals from the framestore. These are critical for the correct interconnection of the framestore and camera, without which it would be impossible to store, and consequently display, picture information correctly.

Once the picture information from the line-scan device is stored within a framestore, the two-dimensional images generated may be manipulated and processed in a similar fashion to those produced from a standard television camera.

2.5 Research Decisions

The primary aim of this research is to investigate the characteristics associated with a rotating stereoscopic line-scan system. To achieve this the measurement capability of the system is assessed as a function of the parameters that allow image production, for example, camera base width, camera-to-base convergence angle etc. It is not the purpose of this work to demonstrate the highest possible accuracy of the returned co-ordinate information. Therefore, it has been decided to implement an absolute orientation methodology to allow three-dimensional co-ordinate information to be obtained from a calibration volume in object space. Specifically, a three-dimensional conformal transformation procedure is adopted which aligns the camera and object systems used.

The interior orientation and relative orientation of the stereo-camera is assumed and, therefore, will not be incorporated in the measurement algorithms.

The interior orientation of each camera is assumed for the following reasons :

- The lens distortions apparent in both the x- and y-axes of the area array sensor are only apparent in one axis of the line-scan device as it is, by design, one dimensional.

- It is considered the distortion introduced by the relative motion will be more significant than the error introduced by not including interior orientation. Therefore, the focal length of the lens and the pierce pixel value will be assumed and lens distortion will be ignored.

- Shih [110] has investigated the effect of neglecting lens distortion and results are presented which show the measurement error relates to less than 0.5 pixel when considering objects situated away from the corners of the image. For this research sub-pixel techniques are not used and, therefore, ignoring lens distortion is considered not to have a significant influence on the level of accuracy expected from the co-ordinate measurement information.

The relative orientation of the stereo-camera pair is assumed for the following reasons :

- For this research the relative alignment of the stereoscopic camera arrangement is configured manually.

- The Manual of Photogrammetry [111] states that there are six possible errors resulting from a misalignment of the stereo-camera. Only two of these errors, x-tilt error and y-tilt error, have a significant effect.

From the points above it is concluded that relative orientation can be assumed, provided the relative alignment of the stereoscopic camera base width and convergence angle can be configured manually to a known degree of accuracy.

2.6 Summary

This chapter has discussed the enabling technologies utilised in this research. The principle of stereoscopic vision will be applied to a 3-D arrangement of rotating line-scan sensors to obtain two-dimensional perspective images in the conventional sense. The object system used in this research will be a three-dimensional calibrated frame containing a distribution of target points known to a defined degree of accuracy. The calibration frame will be discussed in Chapter 5.0.

A three-dimensional conformal transformation will be applied to the stereo-camera arrangement. This will mathematically align the camera and object co-ordinate systems allowing the extraction of 3-D co-ordinate information from the object system after completion of a calibration phase.

Before considering a stereoscopic arrangement of line-scan sensors a rotating two-dimensional camera arrangement is investigated. The following chapter discusses the principles of two-dimensional line-scan image generation using rotation as the relative movement parameter. The theoretical algorithms associated with a two-dimensional line-scan system are presented which are discussed with respect to preliminary experimental work.

3. A ROTATING TWO-DIMENSIONAL LINE-SCAN SYSTEM

3.1 Introduction

This chapter presents an analysis of a rotating two-dimensional line-scan camera system. The operating characteristics are discussed followed by a theoretical analysis which allows the extraction of two-dimensional co-ordinate data from a defined area of object space. Subsequently, the applicability of the 2-D measurement algorithms to the line-scan system are assessed by a series of experimental procedures. The results from this work are used to assess the suitability of the sensor for use in a rotating stereoscopic configuration.

3.2 Rotating Line-scan Characteristics

To produce two-dimensional images from a line-scan sensor relative motion must be inherent between the camera and object of interest. In this work the sensor rotates with respect to a static scene to produce images from which co-ordinate information may be extracted. This section describes the characteristics of the 2-D line-scan system which are fundamental to the analysis subsequently undertaken. This discussion will be divided into the following areas :-

- the orientation of the line-scan device;
- the production of 2-D Images;
- the field of view of the line-scan camera;
- the mode of camera rotation and datum point of the camera-lens.

Once the orientation of the line-scan device is defined with respect to object space the method of 2-D image production is discussed. Following this, the parameters which govern image production, i.e., the FOV in each axis of the sensor arrangement, will be reviewed. Finally, the modes of rotation and the reference point of the camera-lens used in this work will be outlined.

3.2.1 Orientation of the Line-scan Device

The orientation of the line-scan device relative to an object or scene of interest is dependent on the application and the type of relative motion required. A requirement of this investigation is to produce two-dimensional images using a rotating camera from which co-ordinate analysis can be attempted. Therefore, the line-scan device is oriented in a vertical format and the rotation

takes place perpendicular to this, i.e., in the horizontal axis. The movement axis of the sensor is defined as the x-axis with the y-axis being perpendicular to this, and thus, along the line of the device. The 2-D axes relating the camera and an object system are defined in Figure 3-1, where the co-ordinate locations *(x,y)* and *(X,Y)* refer to image and object space distances, respectively.
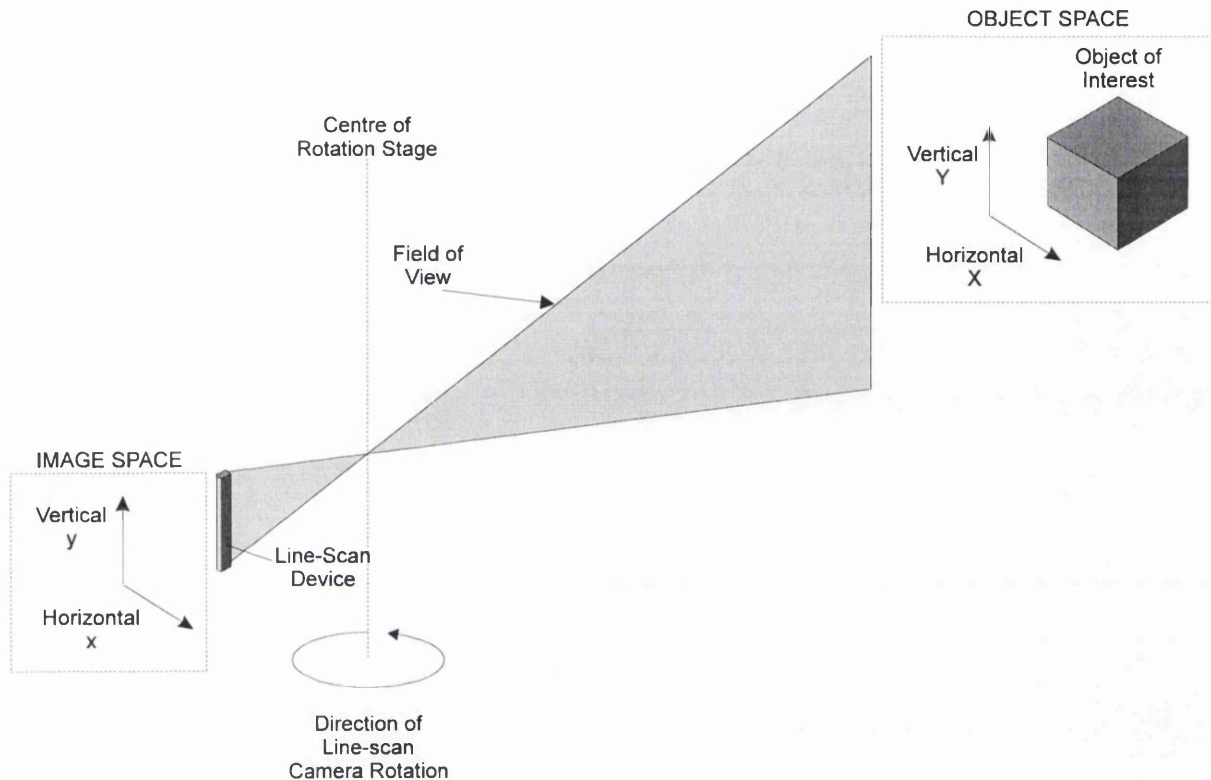
Figure 3-1 Definition of the X- and Y-axes

The next section will discuss the method used to produce two-dimensional images from a rotating line-scan arrangement.

3.2.2 The Production of 2-D Images

To produce images suitable for co-ordinate analysis it is required that a correlation exists between the technique used to obtain the image information and the method of displaying it. If the rotation of the line-scan camera is constant in both speed and direction, and is perpendicular to the principal axis of the sensor, the sequential columns of image data obtained will form a two-dimensional image. To view this image the sequential data is stored to allow presentation on a standard video monitor. The storage device used to achieve this is a *framestore* and it consists of input, storage and output modules. The input section must allow the column information from the line-scan device to enter the storage area and provide the timing and control necessary for

this data transfer to be accomplished. The information in the framestore memory is then passed to the output section and converted to a format which can be viewed on a standard monitor (Figure 3-2). The framestore used in this work is discussed in Chapter 5.0.
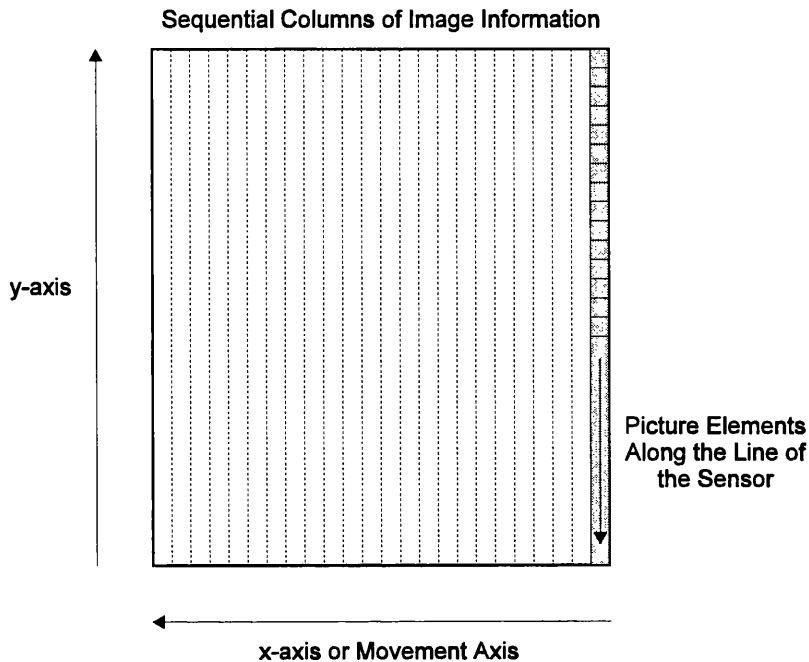
Figure 3-2 Two-dimensional Image Displayed on a Video Monitor

A two-dimensional image produced from a line-scan device may be in a similar format to that returned from a standard television type sensor, e.g., 512 pixels by 512 lines, however, this does not have to be the case. A line-scan image could be a single column in width or cover an area as large as the maximum number of photosite elements along the line of the device multiplied by the storage capacity available in the x-axis, e.g., 6000 pixels by 6000 lines.

3.2.3 Field of View (FOV) from a Line-scan Sensor

For a rotating line-scan sensor the following points apply :

- the FOV in the movement axis, or x-axis, is determined by the interaction of the integration period and the rotation speed of the camera;

- the field of view along the line of the sensor, or y-axis, is dependent on the sensor-to-object range and the focal length of the lens.

The FOV from a line-scan sensor in the y-axis is similar to that produced from an area array device and is discussed in Section 3.3.6. The parameters which allow the production of 2-D images in the x-axis are unique to the line-scan system. These parameters are now considered.

Field of View in the Movement Axis :-

The integration period determines the amount of time each photosensitive element accumulates photons reflected from a scene of interest. Variation of this time period alters the number of photons and, therefore, the resultant electrical charge at each photosite. This results in a change in brightness of each pixel in the image observed.

The integration period has a further affect on the x-axis of the images produced. Each column of pixels are subject to the same integration period and varying this parameter results in a change in the time taken to obtain a set number of columns to form an image. Increasing the integration period results in an increase in the time taken to capture an image, for a constant rotation speed. As the total number of pixel columns in the final image remains constant a larger FOV of x-axis object space will result as the camera has more time to rotate. This change in the field of view alters the appearance of objects in the image produced. Consider the object in Figure 3-3 with a circle and square printed on one face. As the FOV increases the object appears *squashed* in the x-axis (Figure 3-4). By decreasing the integration period a smaller FOV in object space is observed resulting in an image where the object appears *stretched* (Figure 3-5).
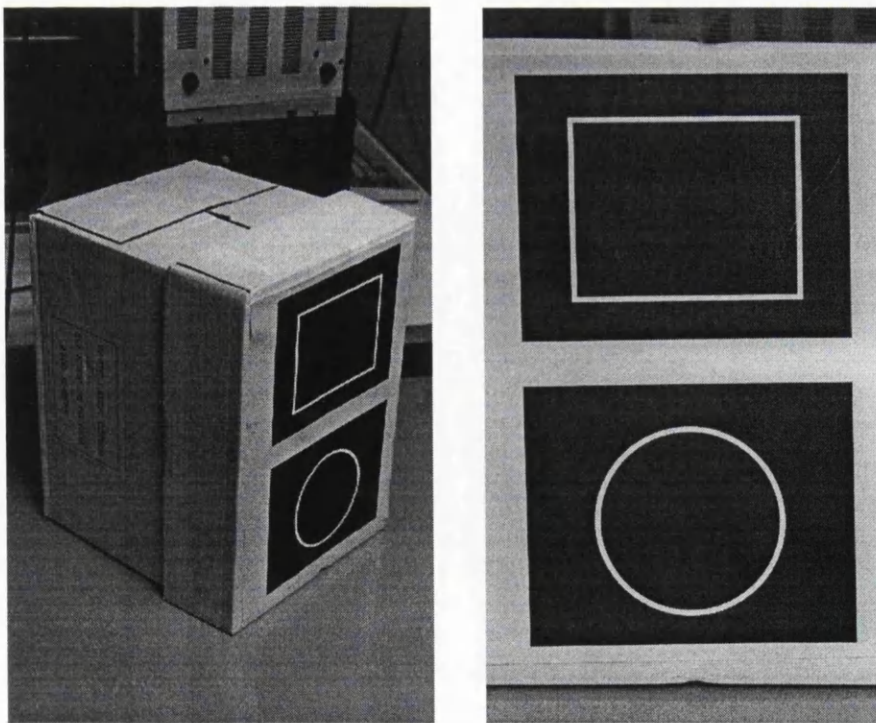
Figure 3-3 Photograph of a Box with a Square and Circle with a 'Normal' Aspect Ratio
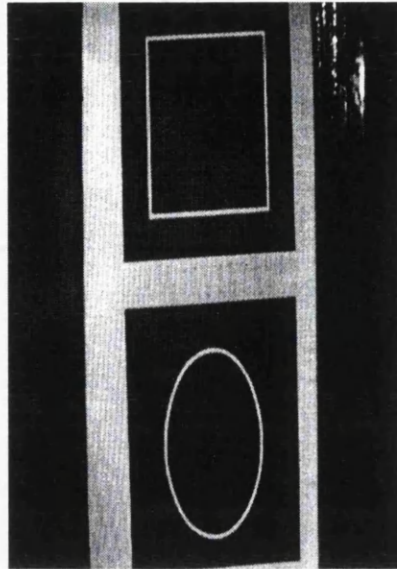
Figure 3-4 Line-scan Image with a 'Squashed' x-axis
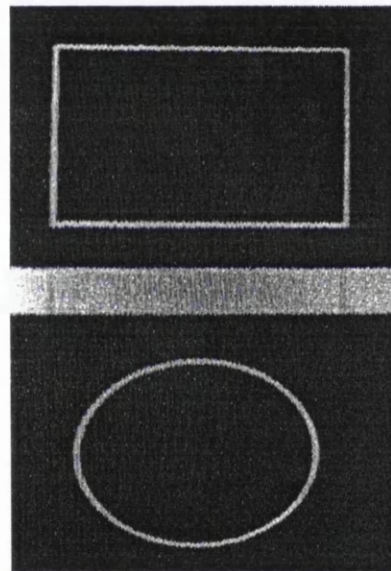
Figure 3-5 Line-scan Image with a 'Stretched' x-axis

The rotation speed determines the distance travelled by the camera in a specific time interval or integration period. If the time period remains constant and the rotation speed is increased or decreased the x-axis of the returned image will display a different field of view. A higher rotation speed allows the sensor to rotate a greater angle and results in an increased FOV in the image produced, for a constant integration period. Thus, the apparent size of objects in the x-axis of image space decreases in a similar way to that illustrated in Figure 3-4. Accordingly, a decrease in rotation speed produces a smaller field of view and results in an increase in the apparent size of objects in the image. This is analogous to decreasing the integration period (Figure 3-5).

Varying the integration period and / or the rotation speed results in a change in the field of view observed from the x-axis of object space. Thus, for a rotating line-scan system it can be stated :

- The FOV of an image can be varied from any arc up to 360° (Figure 3-6). If the camera rotates 360° in the x-axis the images produced will contain information from the object space completely surrounding the 2-D line-scan arrangement.

- If the field of view is less than 360°, the area of object space under consideration depends on the start point of image capture (Figure 3-7).

Considering these two points, the images produced by a rotating line-scan system may display information at a given resolution from a selected part of the surrounding object space.
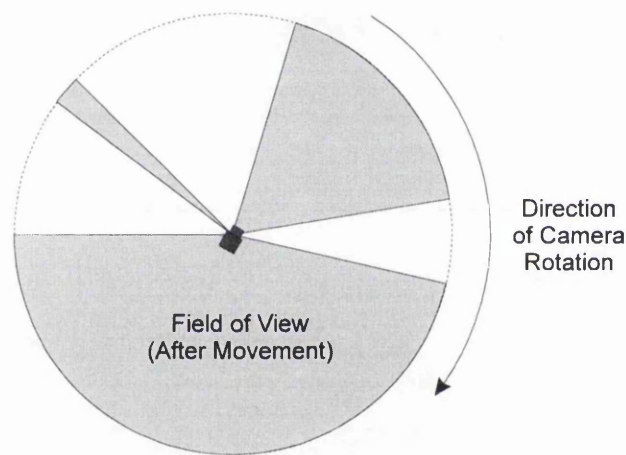
Figure 3-6 Variable Camera Rotation Angle
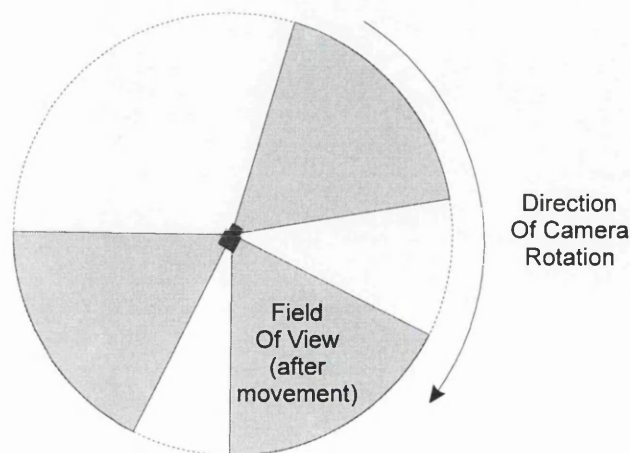
Figure 3-7 Variable Start of Image Capture

To observe the effect of varying the rotation angle and start of image capture consider the following. Figure 3-8 is an image produced from the rotating line-scan system. The image contains information from a 360° FOV of the laboratory produced by the interaction of the integration period and rotation speed. Near the left and right hand edges of the image the same 'white' object is observed (a datasheet) which demonstrates the 'all-round' capability of the system. Figure 3-9 shows two images where the field of view in object space is successively decreased thus allowing recognition of this object. The images are produced by maintaining a constant integration period and reducing the rotation speed of the camera. A similar effect would be observed by maintaining a constant rotation speed and reducing the integration period.
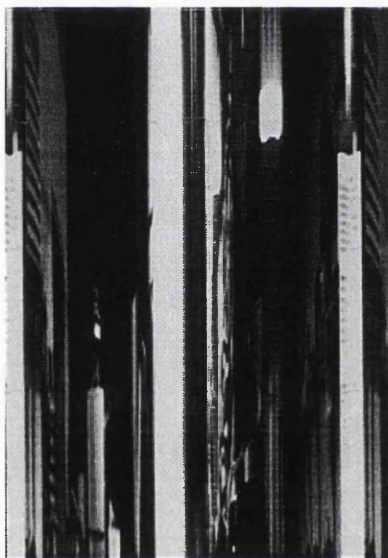
Figure 3-8 A 360° FOV of the Laboratory
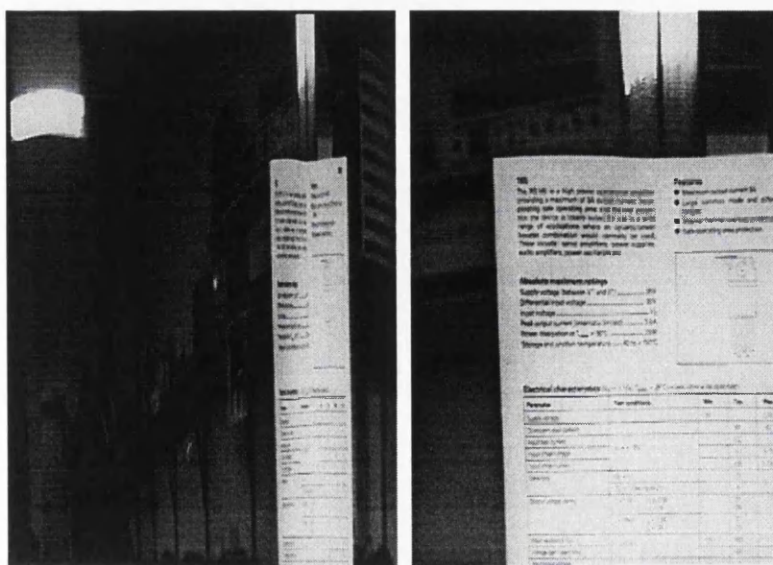
Figure 3-9 Decreasing FOV Due to a Reduction in Rotation Speed

The start point for each image (Figure 3-8 and Figure 3-9) was controlled manually by the operator to allow the field of view of the line-scan sensor to cover the same object in the workspace.

The field of view in the x-axis resulting from the interaction of integration period and rotation speed has been discussed. The following sections define the datum point of the camera-lens and its position with respect to the centre of the rotation stage before presentation of the two-dimensional mathematical analysis.

3.2.4 Datum Point for the Camera-lens Arrangement

A datum point from which camera-to-object distances are referenced is defined for the 2-D analysis presented in Section 3.3 and Section 3.4. The selected datum is referred to as the *secondary principal point* [97] of the camera-lens which is defined as the distance from the image sensor equal to the focal length of the camera-lens arrangement (Figure 3-10).
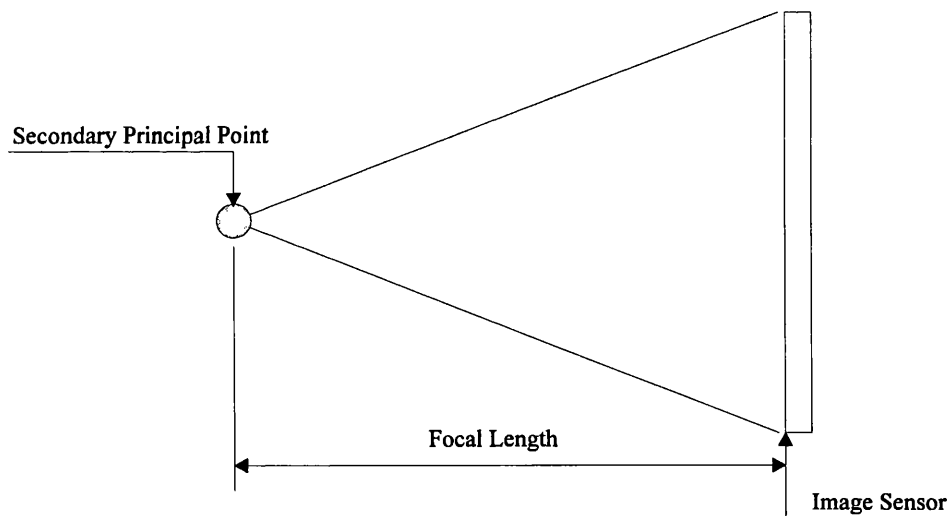
Figure 3-10 Datum for Camera-lens Configuration

3.2.5 Mode of Camera Rotation

The line-scan camera may be positioned in one of three distinct locations with reference to the centre of the rotation stage. The possible locations of the camera are classified in accordance with the following (Figure 3-11) :-

- The camera may be located at the *centre* of the rotation stage, shown by *(a)*;

- *along* the central axis of the rotation stage, given by position *(b)*;
- away *from* the central axis of the rotation stage, illustrated by *(c)*.

Circular Path of Camera Rotation

Secondary Principal Point of Camera-Lens Configuration

Central Axis of Rotation

Field of View in the Movement Axis After Camera Rotation

(b)   (c)   (a)

(a) Centre of Rotation
(b) Along the Central Axis of Rotation
(c) Deviation From the Central Axis of Rotation
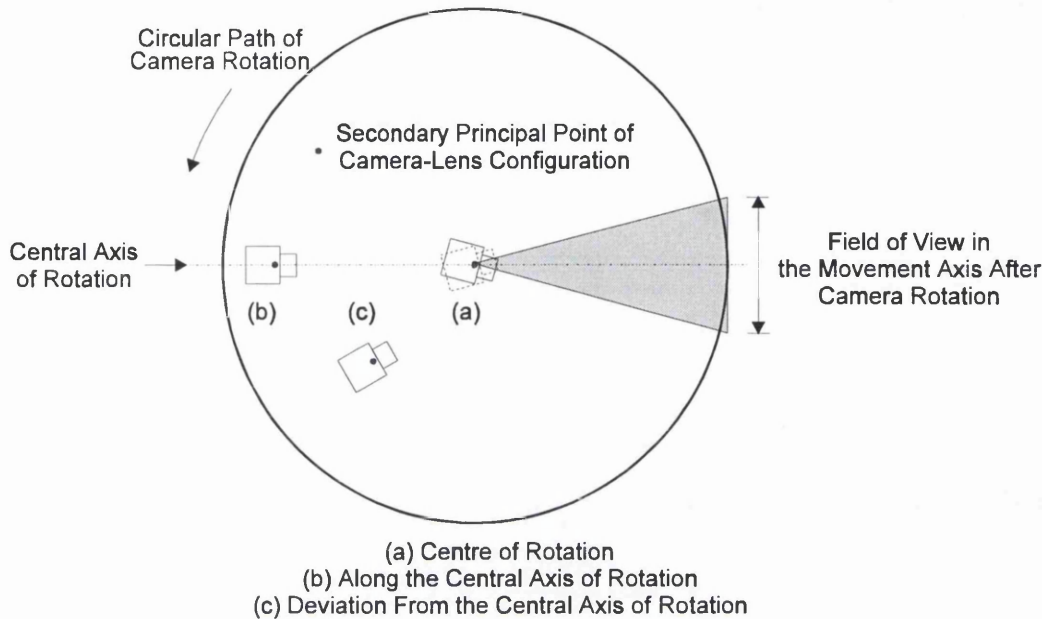
Figure 3-11 2-D Camera Position

It is required to confirm that 2-D co-ordinate measurements can be obtained from object space using the line-scan camera system before investigating a stereoscopic arrangement of sensors. The theoretical and experimental analysis which follows considers the camera locations as depicted in Figure 3-11 to achieve this.

3.3   Theoretical Analysis for Centre of Rotation Operation

The analysis presented allows the calculation of theoretical 2-D image space co-ordinate values, in pixels, which are equivalent to known co-ordinate information in object space, in mm. Subsequently, theoretical pixel values will be compared to equivalent image space information obtained from the experimental work presented onwards from Section 3.6.2. From this the theoretical and experimental characteristics of the rotating 2-D line-scan system will be identified for variations in the parameters affecting image production. Following this, in Section 3.7, the measurement capability is assessed by transforming the difference between theoretical and experimental pixel values into equivalent object space errors.

Consider the secondary principal point of the camera-lens to be aligned with the centre of the rotation stage (Figure 3-12). For distances in the X-axis the object space surrounding the

camera system consists of a series of imaginary concentric circles. The range from the secondary principal point increases with the radius of the concentric circle in object space.
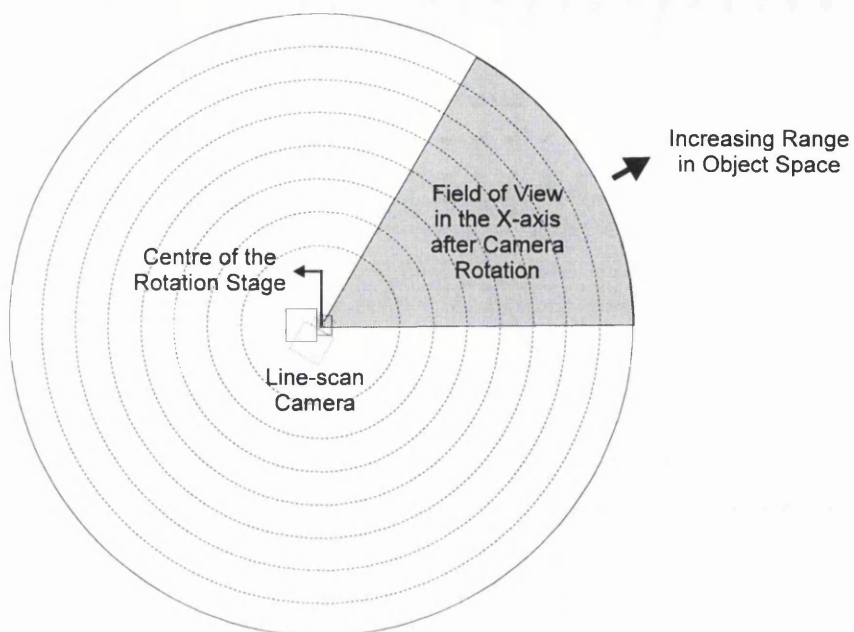
Figure 3-12 X-axis Range Map (Plan View)

For this work a metre-rule is placed in a defined area of workspace (Figure 3-13) to allow comparison of calculated and observed image space values obtained from this object. Thus, the object space arrangement is considered in this theoretical analysis to allow the derivation of appropriate 2-D algorithms. The suitability of this analysis to the line-scan system will be determined by comparing the theoretical and experimental results obtained from this work.
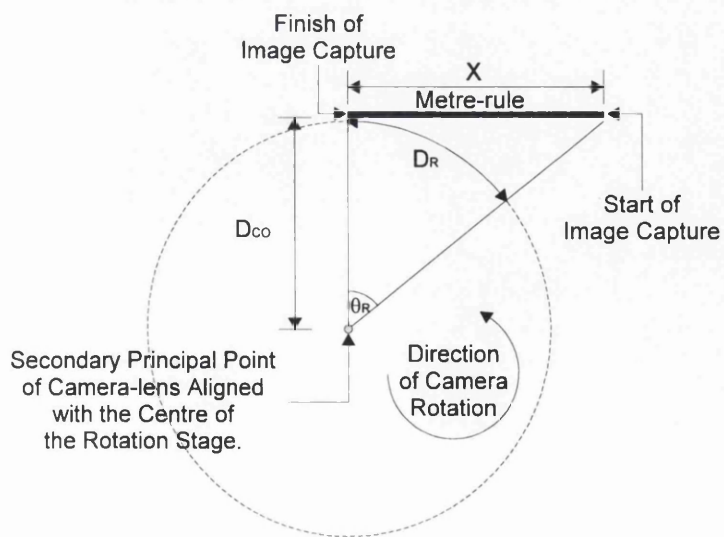
Figure 3-13 Relative Alignment of Metre-rule and 2-D Camera

A metre-rule is selected for use in this investigation as the simplicity of the shape allows the analysis to be minimised whilst allowing a relationship between image and object space distances to be formed. The location of the metre-rule with reference to the rotating 2-D camera system is illustrated in Figure 3-13.

The derivation of the X-axis algorithm which relates distances in image space to equivalent distances in object space is now considered.

3.3.1 Camera Rotation Angle

The camera rotation angle (θ_R) is the angle the camera must rotate to capture an image of the metre-rule (Figure 3-13). Accordingly, the camera rotation angle is given by :

$$\theta_R = \tan^{-1}\left(\frac{X}{D_{co}}\right) \qquad\qquad \text{Equation 3-1}$$

Where,

θ_R $\equiv$ camera rotation angle, in degrees;

X $\equiv$ length of metre-rule in the X-axis of object space, in mm;

D_{co} $\equiv$ camera-to-object distance at finish of image capture, in mm.

3.3.2 Camera Rotation Distance

The camera rotation distance (D_R) is the circumference of the range circle through which the camera rotates to capture an image of the object of interest. Referring to Figure 3-13, the following expression for D_R results :

$$D_R = \left(\frac{\theta_R}{360}\right)(360\ D_{co}) = (\theta_R\ D_{co}) \qquad\qquad \text{Equation 3-2}$$

Where,

D_R $\equiv$ camera rotation distance, in mm.

3.3.3 Camera Time-of-flight

The camera time-of-flight (T_c) is the time taken to rotate θ_R. This is dependent on the rotation speed (S_R) of the camera arrangement, controlled by the rotating stage stepper motor. The camera time-of-flight is inferred from the following fundamental relationship :

$$\text{Time} = \left(\frac{\text{Distance}}{\text{Speed}} \right) \qquad\qquad \text{Equation 3-3}$$

To establish a relationship for the time-of-flight the distance covered by the camera is expressed with reference to one revolution and divided by the speed. The distance is as follows, in mm :

$$\text{Distance} = \frac{\text{Distance of Camera Rotation}}{\text{Distance of One Rotation}} = \frac{D_R}{360 D_{CO}}$$

The rotation speed is expressed as, in seconds :

$$\text{Speed} = \frac{S_R}{60}$$

Therefore, the camera time-of-flight is :

$$T_c = \left(\frac{D_R}{6\, S_R D_{CO}} \right) \qquad\qquad \text{Equation 3-4}$$

Where,

T_c $\equiv$ camera time-of-flight, in seconds;

S_R $\equiv$ rotation displacement speed, in revolutions per minute.

Substituting the expression for D_R from Equation 3-2 into Equation 3-4 results in the following expression for the camera time of flight, T_c :

$$T_c = \left(\frac{\theta_R}{6 S_R} \right) \qquad\qquad \text{Equation 3-5}$$

3.3.4 Camera Integration Period

To form a relationship between equivalent object and image space distances the integration period, i.e. the time to obtain a column of pixel information, is now considered. The integration period (T_i) is dependent on the camera scan rate and the number of picture elements along the y-axis of the one-dimensional element. Thus, the integration period is defined as follows :

$$T_i = \left(\frac{n}{F_{SR}} \right)$$

Equation 3-6

Where,

F_{SR} $\equiv$ scan rate of the line-scan camera, in Hz;

n $\equiv$ number of pixels along the line of the sensor.

In the following text the parameters which interact to produce the two-dimensional images are referred to as the camera scan rate (F_{SR}) and the rotational speed (S_R). The integration period, related to the camera scan rate by Equation 3-6, will not be referred to directly as the scan rate is the parameter which is varied in all of the experimental work considered.

3.3.5 X-axis Algorithm

Substituting T_i (Equation 3-6) for the expression given by T_c (Equation 3-5) allows the formation of a relationship between the camera scan rate and rotation angle. Thus, for one pixel column in x-axis image space the equivalent camera rotation angle in object space is :

$$\theta_R = \frac{6\, n\, S_R}{F_{SR}}$$

Equation 3-7

For a number of pixels, x, in the x-axis the equivalent camera rotation angle is given by :

$$\theta_R = \frac{6\, n\, S_R\, x}{F_{SR}}$$

Equation 3-8

Where,

x $\equiv$ number of pixels in the x-axis of image space necessary to view a point of interest, with reference to the start of image capture.

From Equation 3-1 and Equation 3-8 an expression for the theoretical number of x pixels in image space which relates to an image of the object space depicted in Figure 3-13 can be obtained :

$$x = \left(\frac{F_{SR}\, \theta_R}{6\, n\, S_R} \right) = \left(\frac{F_{SR}\, \tan^{-1}\!\left(\dfrac{X}{D_{CO}} \right)}{6\, n\, S_R} \right)$$

Equation 3-9

3.3.6 Y-axis Algorithm

To compare co-ordinate information derived from image space with equivalent observed image space data the metre-rule arrangement as depicted by Figure 3-13 is utilised.
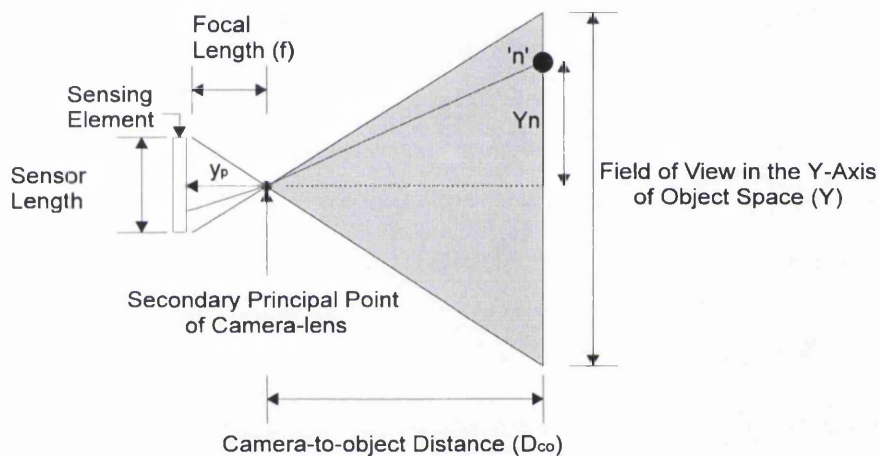
Figure 3-14 Y-axis Field of View (Side Elevation)

For the purpose of the Y-axis experimentation the metre-rule is oriented in the vertical axis of object space, i.e., perpendicular to the original position. The derivation of the Y-axis algorithm for use with the rotating 2-D camera system is now considered.

The axis of the line-scan image along the line of the sensor, otherwise referred to as the Y-axis, can be modelled on the principle of the pin-hole camera [112] (Figure 3-14). Therefore, the derivation for Y is based on the following equation :

$$Y = \frac{D_{CO}\,(y_p - y)\, SL}{f}$$

Equation 3-10

Where; Y $\equiv$ Y co-ordinate of a point 'n' in object space (Figure 3-14), in mm;

       D_{co} $\equiv$ camera-to-object distance at the instant of image capture, in mm;

       y $\equiv$ y co-ordinate of a point 'n' in image space, in pixels;

       SL $\equiv$ sensing element length, in mm;

       f $\equiv$ camera-lens focal length, in mm;

       y_p $\equiv$ the pixel through which the optical axis of the lens pierces the sensor.

Equation 3-10 can be re-arranged to give an expression for the number of pixels in the y-axis of image space relating to a point in the Y-axis object space :

$$y = y_p - \left(\frac{f\,Y}{SL\ D_{co}} \right) \qquad\qquad \text{Equation 3-11}$$

For two points, a and b, in object space. From Equation 3-11 the distance between them is :

$$y|_{a-b} = \left| \left(y_p - \left(\frac{f\,Y_a}{SL\ D_{CO_a}} \right) \right) - \left(y_p - \left(\frac{f\,Y_b}{SL\ D_{CO_b}} \right) \right) \right|$$

Simplifying the expression above gives :

$$y|_{a-b} = \left| \frac{f}{SL} \left(\frac{Y_b}{D_{CO_b}} - \frac{Y_a}{D_{CO_a}} \right) \right| \qquad\qquad \text{Equation 3-12}$$

Therefore, for a fixed distance in the Y-axis of object space, i.e., a known distance between two points, if the camera-to-object distance is the same to both points Equation 3-12 becomes :

$$y = \left(\frac{fY}{SL\ D_{co}} \right) \qquad\qquad \text{Equation 3-13}$$

The analysis has been for a camera placed at the centre of rotation. A 2-D analysis for camera positions *along* and away *from* the central axis of rotation is presented in the next section.

3.4 Theoretical Analysis for Other Modes of Camera Rotation

If a line-scan camera is located *along* or away *from* the central axis of rotation (Figure 3-11) the algorithms relating equivalent distances in image space and object space are governed by the parameters already considered for centre of rotation operation.

3.4.1 X-axis Consideration

The X-axis algorithm (Equation 3-9) is a function of the camera rotation angle necessary to view an object of interest, i.e., if the rotation angle is known theoretical distances in the x-axis of image space may be obtained, regardless of camera position with respect to the rotation centre. Consider Equation 3-9, if the scan rate and rotation speed are maintained at a constant value then, where k_x is a constant for a given camera arrangement :

$$x = k_x \, \theta_R$$

Thus exhibiting the camera rotation angle as the main factor governing the extraction of distances in the X-axis, irrespective of the camera position with respect to the centre of rotation.

Deviation Along *the Central Axis of Rotation :*
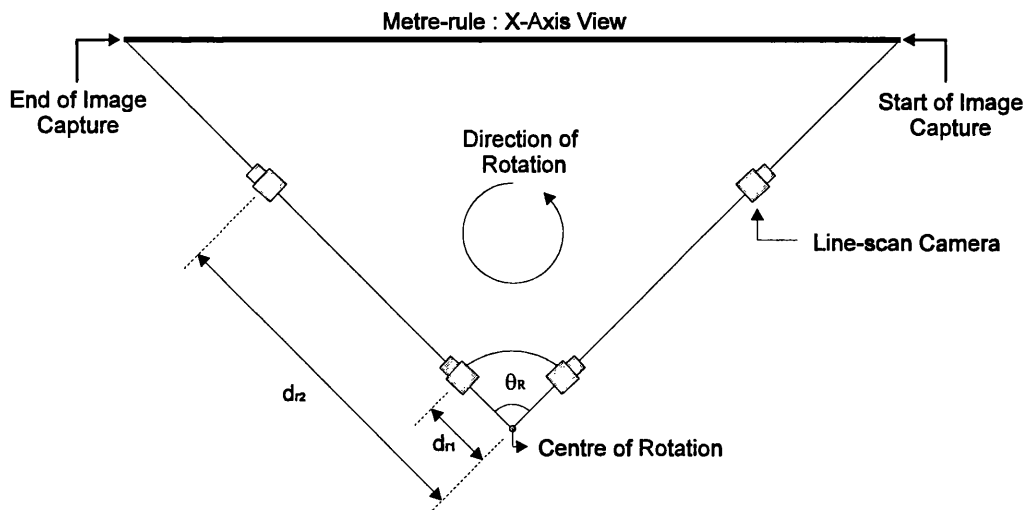
Figure 3-15 Camera Position Deviation Along the Central Axis of Rotation

For camera deviation along the central axis of rotation, from d_{r1} to d_{r2} (Figure 3-15), the rotation angle is constant and equivalent to the angle produced if the camera is placed at the rotation centre. Thus, the X-axis algorithm is applicable to a camera position along the central axis if the camera-to-object distance, D_{CO}, is replaced by the rotation centre to object distance, D_{RO}.

Deviation From *the Central Axis of Rotation :*

This is not the case for camera positions away from the central axis of rotation. Consider the camera to be positioned at, for example, 90° to the central axis (Figure 3-16). The rotation angle necessary to view the same area of object space is not simply that given by Equation 3-1. From Figure 3-17, as the distance from the central axis of rotation increases from d_{S1} to d_{S2} the camera rotation angle increases from θ_{R1} to θ_{R2}. Therefore, a new value for θ_R needs to be derived for substitution into the X-axis algorithm (Equation 3-9).
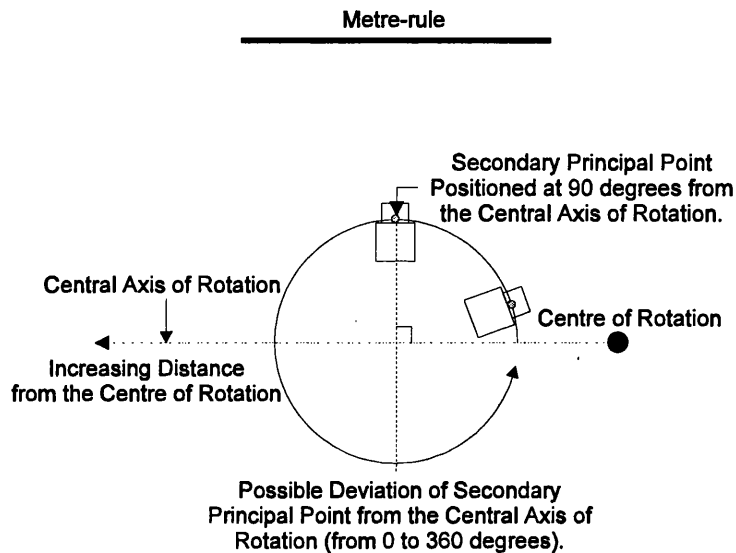
Figure 3-16 Principal Point Deviation From the Central Axis of Rotation
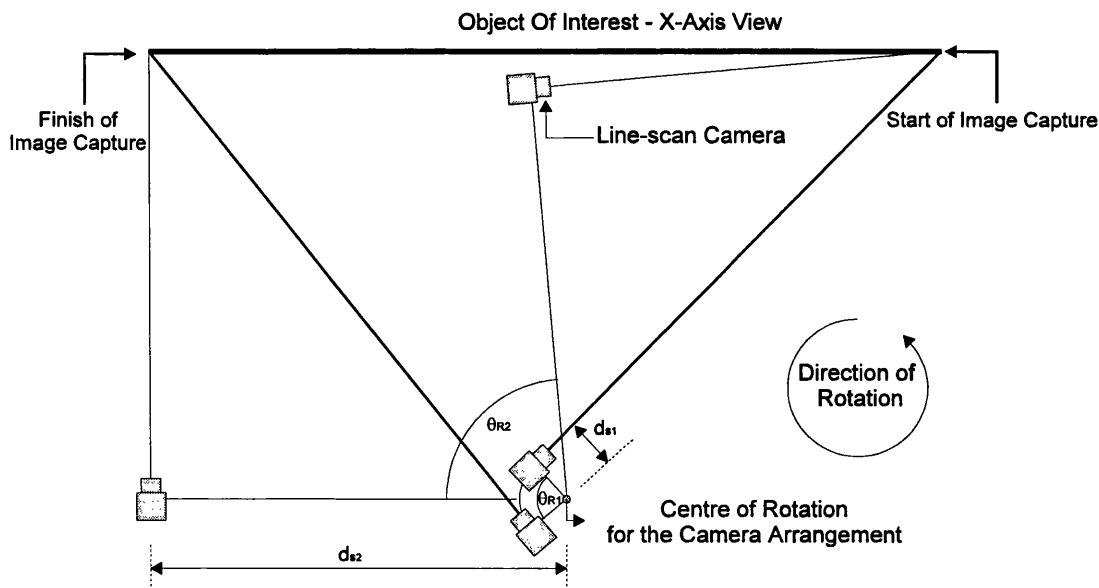
Figure 3-17 Camera Position Deviation from the Central Axis of Rotation

For a camera deviation of 90° from the central axis of rotation, with reference to Figure 3-18, the following expression gives the camera rotation angle :

$$\theta_R = \cos^{-1}\left[\frac{d_s}{\sqrt{D_{RO}^2 + X^2}}\right] - \cos^{-1}\left[\frac{d_s}{D_{RO}}\right] + \cos^{-1}\left[\frac{D_{RO}}{\sqrt{D_{RO}^2 + X^2}}\right] \qquad \text{Equation 3-14}$$

Substituting θ_R from Equation 3-14 into the X-axis algorithm (Equation 3-9) allows the calculation of theoretical x pixel values from the defined object space (Figure 3-13).
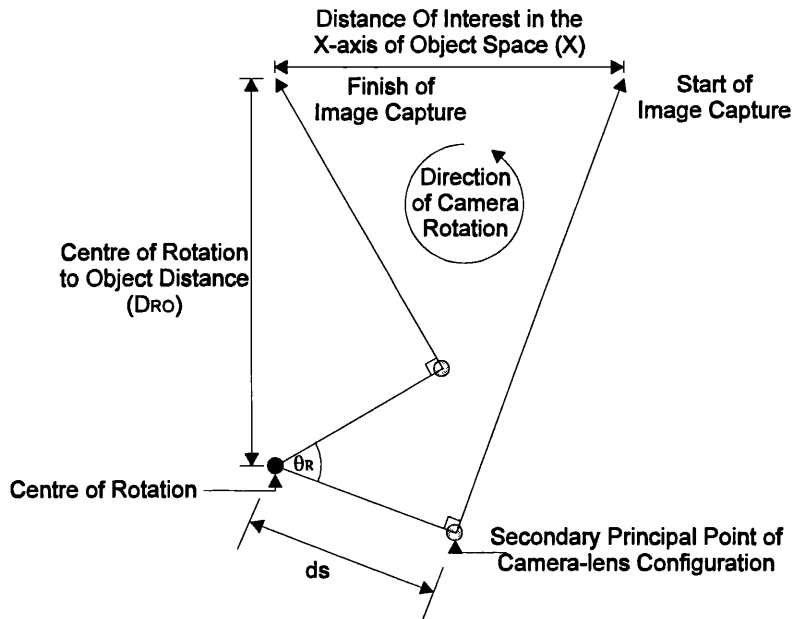
Figure 3-18 Derivation of the Camera Rotation Angle

3.4.2 Y-axis Consideration

Consider the Y-axis algorithm which relates distances in image space to equivalent distances in object space (Equation 3-13). For a given arrangement the focal length of the camera and the sensing element length may be considered as a constant value, k_y. Thus, it can be stated:

$$\left(\frac{y}{Y}\right) = \left(\frac{k_y}{D_{CO}}\right)$$

From the above, it is observed that the Y-axis image space to object space distance ratio is governed by the camera-to-object distance (D_{CO}). For each camera position (Figure 3-11) the camera-to-object distance at the instant of image capture is required.

For a camera located at the *centre* of the rotation stage the camera-to-object distance is illustrated in Figure 3-19. In this case, the algorithm relating image space and object space distances is given by Equation 3-13.
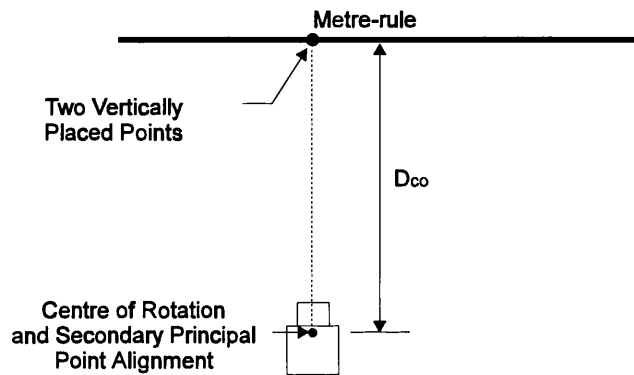
Figure 3-19 D_{CO} for Centre of Rotation Operation

Deviation Along the Central Axis of Rotation :-

For camera positions *along* the central axis of the rotation the camera-to-object distance at the instant of image capture is realised by inference from Figure 3-20 :

$$D_{CO} = (D_{RO} - d_r) \qquad\qquad\qquad \text{Equation 3-15}$$

Where,

D_{RO} $\equiv$ rotation centre to object distance, in mm;

d_r $\equiv$ the distance from the secondary principal point of the camera to the centre of rotation along the central axis of rotation, in mm.
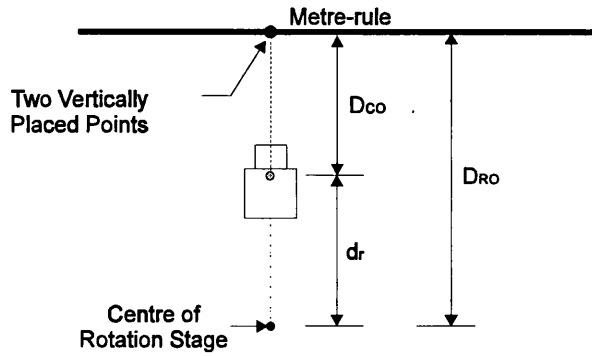
Figure 3-20 D_{CO} for Deviation Along the Central Axis of Rotation

Substituting the expression for D_{CO} from Equation 3-15 into Equation 3-13 results in the following Y-axis algorithm for camera operation *along* the central axis of rotation :

$$y = \frac{fY}{SL\left(D_{RO} - d_r\right)}$$

Equation 3-16

Deviation from the Central Axis of Rotation :-

For a camera located away *from* the central axis of rotation the expression for the camera-to-object distance (Figure 3-21) is :

$$D_{CO} = \sqrt{D_{RO}^2 - d_s^2}$$

Equation 3-17

Where,

d_s $\equiv$ the distance of the camera-lens secondary principal point from the centre of rotation away from the central axis of rotation, in mm.
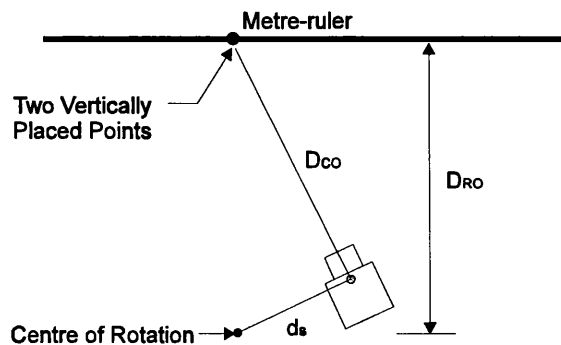
Figure 3-21 D_{CO} for Deviation from the Central Axis of Rotation

Substituting the expression for D_{CO} from Equation 3-17 into Equation 3-13 results in the following Y-axis algorithm for camera operation away from the central axis of rotation :

$$y = \frac{fY}{SL\sqrt{\left(D_{RO}^2 - d_s^2\right)}}$$

Equation 3-18

Now the 2-D co-ordinate algorithms have been derived the following sections will detail the development of a two-dimensional rotating line-scan system. The experimentation will then be described, the results from which will be compared to the equivalent theoretical work to establish if the algorithms can be applied successfully to the rotating system.

3.5 The Development of A Rotating 2-D Line-scan System

A *Fairchild Weston CCD1300R 1024 element line-scan camera* [113] is used for the two-dimensional investigation, part of the existing equipment within the 3-D Imaging Group. The sensing element consists of a column of 13 x 13 micron square photosites on a 13 micron pitch. Thus, the pixels are contiguous along the length of the sensor, giving a total imaging length of 13.31mm.

Additional equipment is required to produce two-dimensional images with this sensor and enable the picture information obtained to be presented in a suitable fashion for human interpretation. This is necessary as a manual method of identifying point positions is adopted for this research (see Section 2.2.1). The 2-D system was constructed from equipment available within the research group at The Nottingham Trent University. The equipment included :

- an image storage area, or framestore [114], that allows image manipulation.
- interfacing hardware between the framestore and camera.
- a rotational stage driven by a microprocessor controlled stepper motor;
- a metre-rule allowing image space measurements to be made with reference to known distances in object space.

The 'C' software programming language [115] was used to control image capture and effect manipulation.

A block diagram of the 2-D rotating camera system is presented in Figure 3-22.
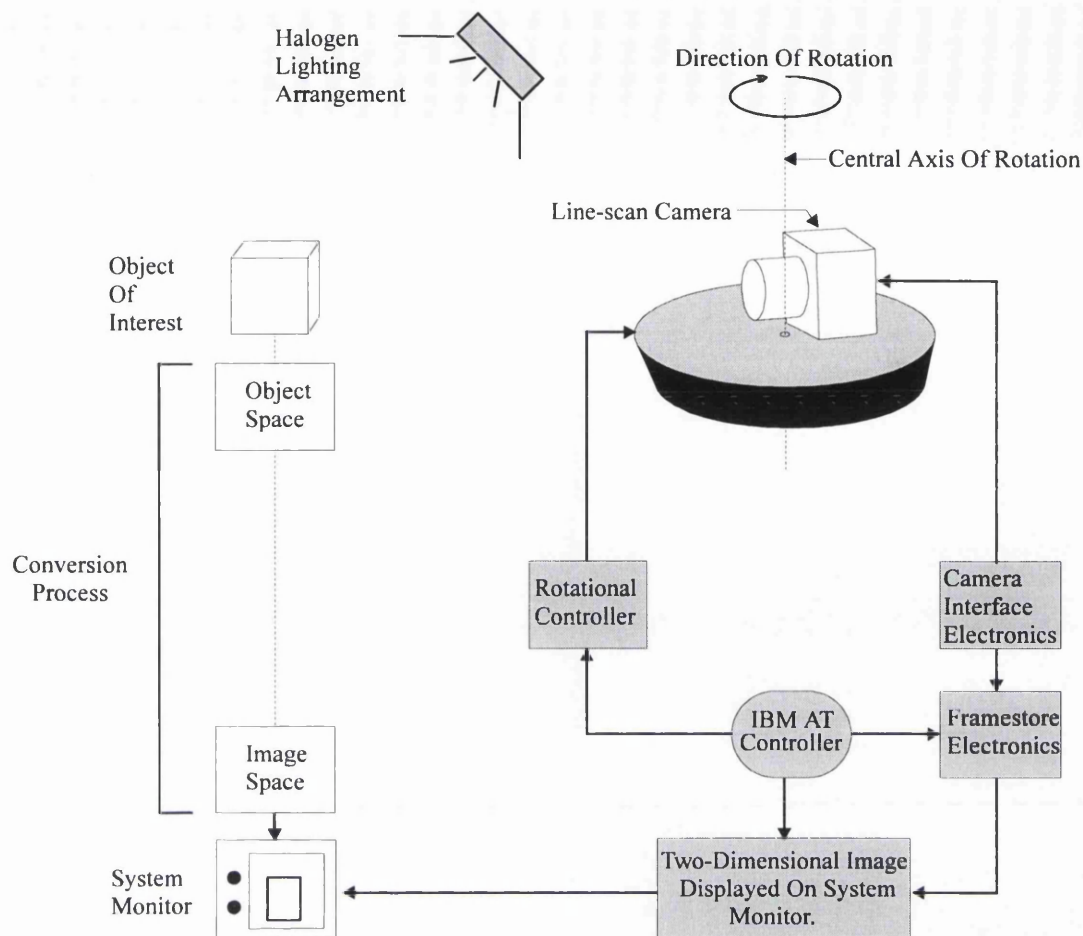
Figure 3-22 2-D Rotating Line-scan Camera System

Rotating Stage :

To provide relative motion between the camera and object of interest a rotation stage is used. The rotating stage is driven by a stepper motor arrangement providing a resolution of 0.01° per step rotation. The camera is fixed to this rotational stage thus allowing it to rotate with respect to an object of interest.

A Parker Digiplan IF1 micro-processor controller [116] is used to drive the stepper motor. However, this controller only provides an interface through which the motor parameters can be altered, therefore it is necessary to provide instructions on which the controller can act. This can be done in one of two ways, either by using a simple programming terminal or by some form of micro-computer. An IBM "AT" Clone computer [117] is used as it allows a list of complex commands to be stored, manipulated and repeated without laborious interaction between operator and terminal.

Metre-rule :

To allow 2-D image space measurements to be compared with a known distances in object space a metre-rule is used in this analysis (Section 3.3). The metre-rule is manufactured from polystyrene which has a linear coefficient of thermal expansion [118] of 7.00×10^{-5} K^{-1} at room temperature. Thus, for each degree rise in temperature the length of the metre-rule will increase by 0.07 mm. This validates the use of the metre-rule as any possible variation in its length is several orders of magnitude lower than the level of accuracy anticipated from this investigation.

3.5.1 System Operation

The operation of the experimental system is now described (refer to Figure 3-22). Prior to image capture, the framestore and interface module are reset and the capture software within the store started. The stage controller is instructed, via the host computer, to bring the rotating stage to a point from where the camera motion is required to start. The rotation speed is set and the instruction given for the movement to begin.

At a point in the camera rotation, determined by a 'line-of-sight' technique, the operator initiates the capture of picture information from the sensor. The point at which image generation is started depends on the camera rotation speed and scan rate and also the field of view required from object space. Due to the manual nature of the image start point it is a matter of 'trial and error' to obtain the desired field of view in the movement axis as a result of variations in the scan rate and / or rotation speed settings. As the sequential columns of image data are transferred to the framestore, the speed of the stage is maintained. The stage is halted after an entire image is captured. At this point in time, a two-dimensional picture is resident in the framestore and can then be manipulated by the operator.

3.5.2 Manual Location of Point Position

For this work a manual method of point location is adopted. Therefore, consideration of the possible image space error is necessary.

For a point in the x-axis of image space, when manually locating the position it is possible one pixel to the left or right of the central pixel could be a valid location (Figure 3-23). This, therefore, may give rise to an error of ±1 pixel, i.e., a total error of ±2 pixels when measuring distances between two points of interest in image space. Similar consideration may also be applied to image space measurements in the Y-axis, when measuring the distance between two points.

Point Of Interest

Picture Elements (Pixels)

X-axis Of Image Space
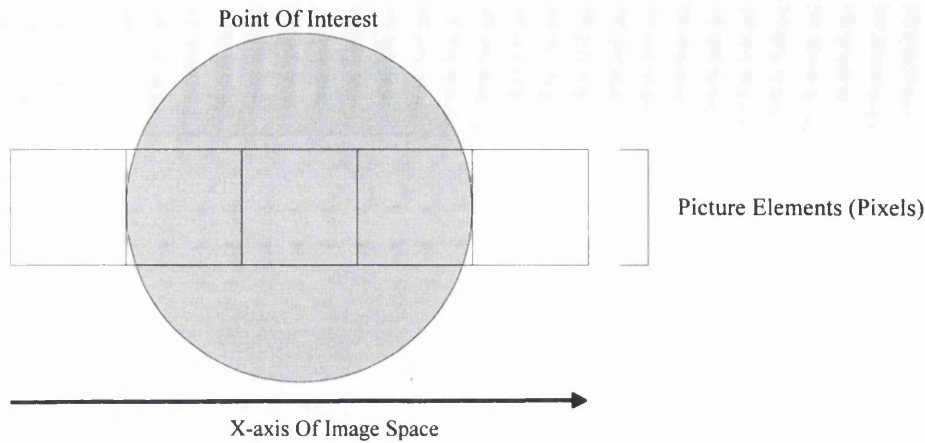
Figure 3-23 Possible Pixel Measurement Error

To assess the effect of the manual location of point position in image space an experiment is discussed in Section 3.6.1 to determine the repeatability of the image space information.

3.6 Experimental Work with Two-dimensional Line-scan Systems

The main aim of the experimental work is to investigate the application of the two-dimensional algorithms, derived in Section 3.3, to a rotating line-scan system. These algorithms allow theoretical image space values to be calculated from a defined object space for a given camera arrangement. The experimentation will allow image space values to be observed for a variation of the parameters considered in the two-dimensional analysis. Therefore, on completion of this work observed x and y pixel values can be compared with their equivalent theoretical values.

The experimental work allows two things to be achieved :

- the relationship between observed pixel values and the parameters that affect image production can be observed thus allowing an assessment of the rotating 2-D line-scan characteristics;

- the suitability of the algorithms can be assessed by comparing the theoretical pixel values with the equivalent observed pixel values. Therefore, the measurement capability of the system can be assessed as the error values, in pixels, can be transformed to object space information to give an error, in mm.

Specifically, for the modes of camera rotation considered (Figure 3-11) the x and y-axis algorithms, given by Equation 3-9 and Equation 3-13 respectively, will be tested by comparing theoretical pixel data with observed pixel readings for variations in the following parameters :-

- camera-to-object distance (D_{CO}): a range of 0.5m to 1.4m is used;
- camera rotation speed (S_R): a range of 1.67rpm to 8.33rpm is used;
- camera scan rate : a range of 30kHz to 90kHz is used.

A metre-rule is used as the object from which image space measurements in the x-axis and y-axis are made. A sample of the images containing the metre-rule used in the 2-D experimental work are shown. The image in Figure 3-24 contains a 3 x 360° field of view of object space in which the metre-rule is positioned, thus demonstrating the "all-round" vision capability of the rotating line-scan system. Figure 3-25 contains two images of the metre-rule in which the rotation speed has been reduced successively to allow the metre-rule to occupy a greater area in image space. For each parameter variation considered in this analysis image space measurements are made between two selected points on the metre-rule in each axis of object space.
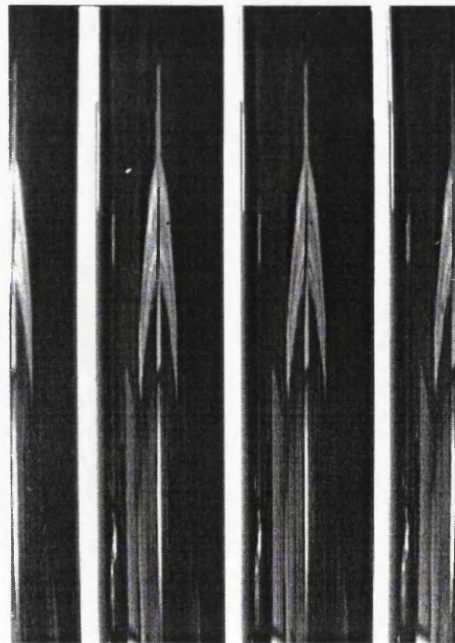
Figure 3-24 Field of View of the Metre-Rule Produced from the Interaction of Camera Scan Rate and Rotation Speed
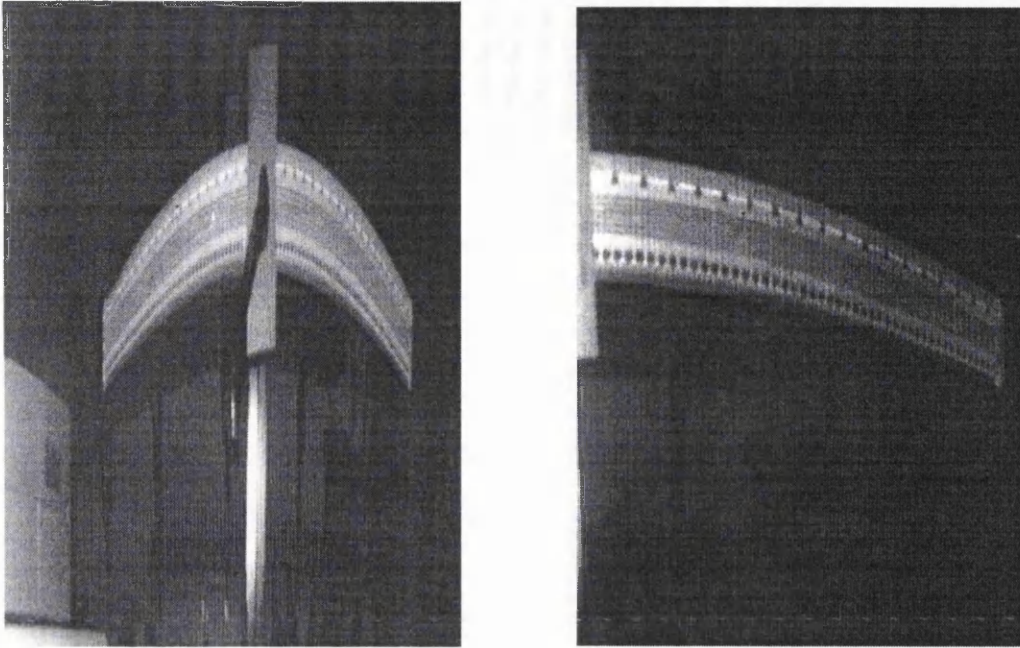
Figure 3-25 A Decreasing Field of View in Object Space Resulting in an Increasing Size of the Metre-rule in the Image Produced

In the X-axis of object space a fixed distance of 610mm was selected from the metre-rule and the fixed distance used for Y-axis measurements was 200mm. The alignment of the camera system with respect to the object is shown in Figure 3-13 for image space measurements from the X-axis of object space. For measurements from the Y-axis of object space the metre-rule was oriented vertically, where the points of interest on the object were aligned with the finish of image capture shown in Figure 3-13. For the experimental work the following object space information was required before calculation of the theoretical 2-D co-ordinate information:-

- for measurements in the X-axis of Object Space :
    - the camera-to-object distance at the end of image capture. This is measured manually with a tape measure;
    - the camera rotation angle. This is calculated using the fixed distance on the ruler and the camera-to-object distance.

- For measurements in the Y-axis of Object Space :
    - the camera-to-object distance at the end of image capture. This is measured manually with a tape measure.

For the object space measurements a retractable steel tape was used. The measurement accuracy of this instrument is governed by human skill but, with care, the measurement inaccuracy achieved can be as low as ±0.01 per cent [119]. For this analysis the level of inaccuracy is considered to be sufficiently low to enable the measurement error to be ignored.

For all the experimentation undertaken a set focal length of 25mm was used. This was considered sufficient to assess the characteristics and determine the measurement capability of the 2-D rotating line-scan system. The parameter variations of camera-to-object distance, scan rate and rotation speed, in conjunction with the focal length setting, were selected to allow the metre-rule to occupy the observed field of view throughout all experimental procedures.

The following section presents the results from the two-dimensional investigation. However, before this the repeatability of image data is assessed.

3.6.1 Repeatability of Image Space Data

To assess the repeatability of the image data a metre-rule was imaged ten times. The rule was oriented vertically, then horizontally, to obtain image measurements between two points selected in each of the X- and Y-axes of object space, respectively. The parameter settings for this experiment were as follows :-

Rotation Speed (rpm)	1.67
Scan Rate (kHz)	50
Focal Length (mm)	25
Camera-to-object Distance (mm)	1500

The results from this preliminary experiment are provided as follows :

x Image Distance (pixels)	y Image Distance (pixels)
286	494
286	494
286	494
287	493
287	494
287	494
286	494
287	494
286	494
286	494

Table 3-1 The Repeatability of x and y Image Space Pixel Values

From Table 3-1, the number of pixels between two points on the ruler changed by a maximum of ± 1 pixel in each of the x- and y-axes for ten consecutive experimental runs. Thus, for the experimental arrangement the repeatability of the image space data is considered sufficient, considering the manual method of point location used (Section 3.5.2), to allow an investigation of the 2-D line-scan system.

Once the repeatability of the image space measurements was established further experiments were completed. The following sections present the results obtained from both the theoretical and experimental aspects of this two-dimensional investigation. For each mode of camera rotation results are presented graphically for equivalent calculated and observed x and y image space values for a variation in the system parameters already described. These results are discussed in Section 3.8.

3.6.2 Centre of Rotation - X-axis Results

The aim of this work is to investigate the relationship between x-axis image space quantities and variations in camera-to-object distance, rotation speed and scan rate for a camera placed at the centre of the rotation stage (Figure 3-11). After obtaining image space measurements the X-axis algorithm (Equation 3-9) is used to calculate the pixel values associated with the experimental x-axis data. Tables of results from the 2-D analysis are presented in Appendix B.

Experimental Hypothesis A :

"To demonstrate the effect of varying the camera-to-object distance on observed and calculated x image space values for the line-scan camera positioned at the centre of the rotation stage"

Experimental Arrangement :

Rotation Speed (rpm)	1.67
Scan Rate (kHz)	80
Focal Length (mm)	25
Camera-to-object Distance (mm)	500 - 1400

Experimental Results :

The observed and theoretical x pixel values for a variation in the camera-to-object distance are presented in Table B.1 and are illustrated in Graph 3-1.
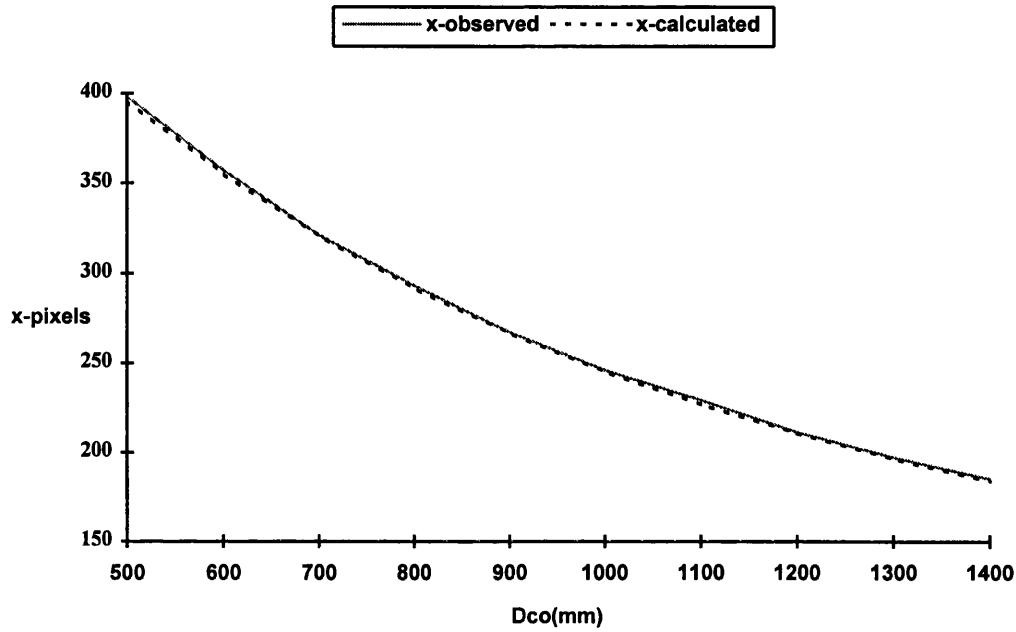
Graph 3-1 x pixel Values for a Variation in Camera-to-object Distance

Experimental Hypothesis B :

"To demonstrate the effect of a varying the camera rotation speed on observed and calculated x image space values for the line-scan camera positioned at the centre of the rotation stage"

Experimental Arrangement :

Rotation Speed (rpm)	1.67 - 8.33
Scan Rate (kHz)	80
Focal Length (mm)	25
Camera-to-object Distance (mm)	500

Experimental Results :

The observed and theoretical x pixel values for a variation in the camera rotation speed are presented in Table B.2 and are illustrated in Graph 3-2.
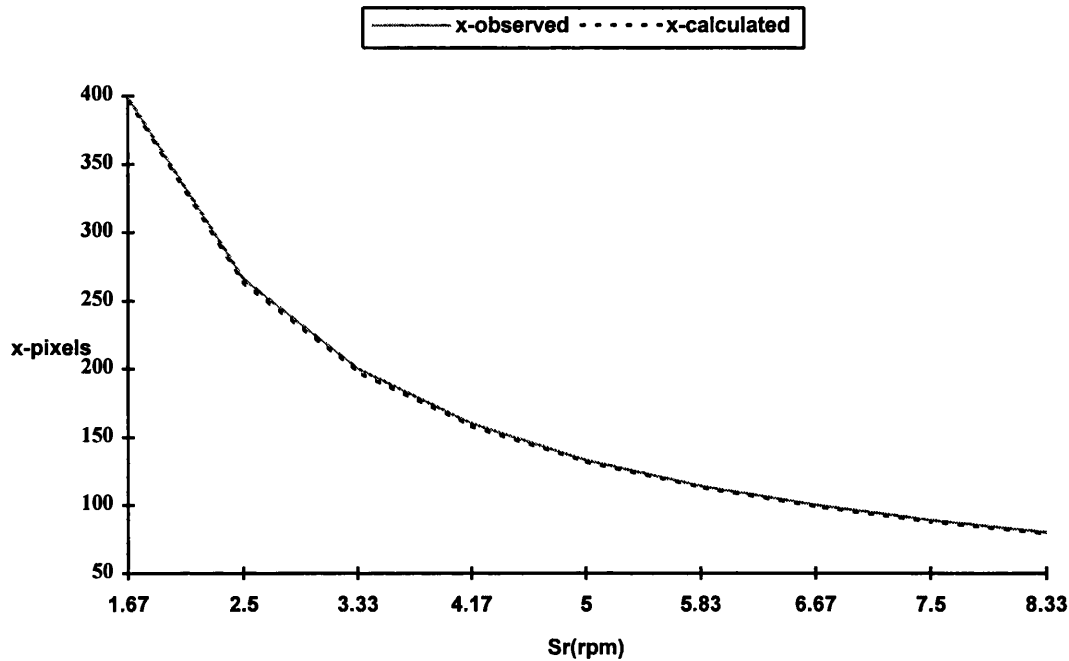
Graph 3-2 x pixel Values for a Variation in Camera Rotation Speed

Experimental Hypothesis C :

"To demonstrate the effect of a variation in the camera scan rate on the observed and calculated x image space values for the line-scan camera positioned at the centre of the rotation stage"

Experimental Arrangement :

Rotation Speed (rpm)	1.67
Scan Rate (kHz)	30 - 90
Focal Length (mm)	25
Camera-to-object Distance (mm)	500

Experimental Results :

The observed and theoretical x pixel values for a variation in the camera rotation speed are presented in Table B.3 and are illustrated in Graph 3-3.
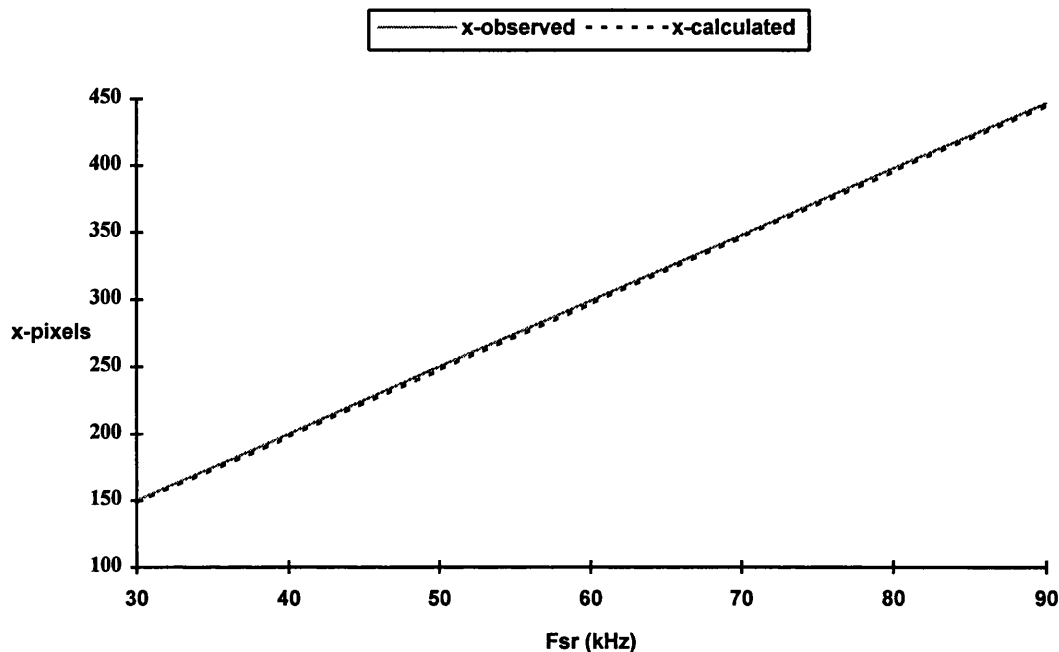
Graph 3-3 x pixel Values for a Variation in Camera Scan Rate

3.6.3 Centre of Rotation - Y-axis Results

The aim of the work in this section is to investigate the relationship between y-axis image space quantities and variations in the parameters of camera-to-object distance, rotation speed and scan rate for a camera positioned at the centre of the rotation stage (Figure 3-11). After obtaining image space measurements the Y-axis algorithm (Equation 3-13) is used to obtain the theoretical y pixel values associated with the experimental y-axis data.

Experimental Hypothesis D :

"To demonstrate the effect of varying the camera-to-object distance on observed and calculated y image space values for the line-scan camera positioned at the centre of the rotation stage"

Experimental Arrangement :

Rotation Speed (rpm)	1.67
Scan Rate (kHz)	80
Focal Length (mm)	25
Camera-to-object Distance (mm)	500 - 1400

Experimental Results :

The observed and theoretical y pixel values for a variation in the camera-to-object distance are presented in Table B.4 and are illustrated in Graph 3-4.
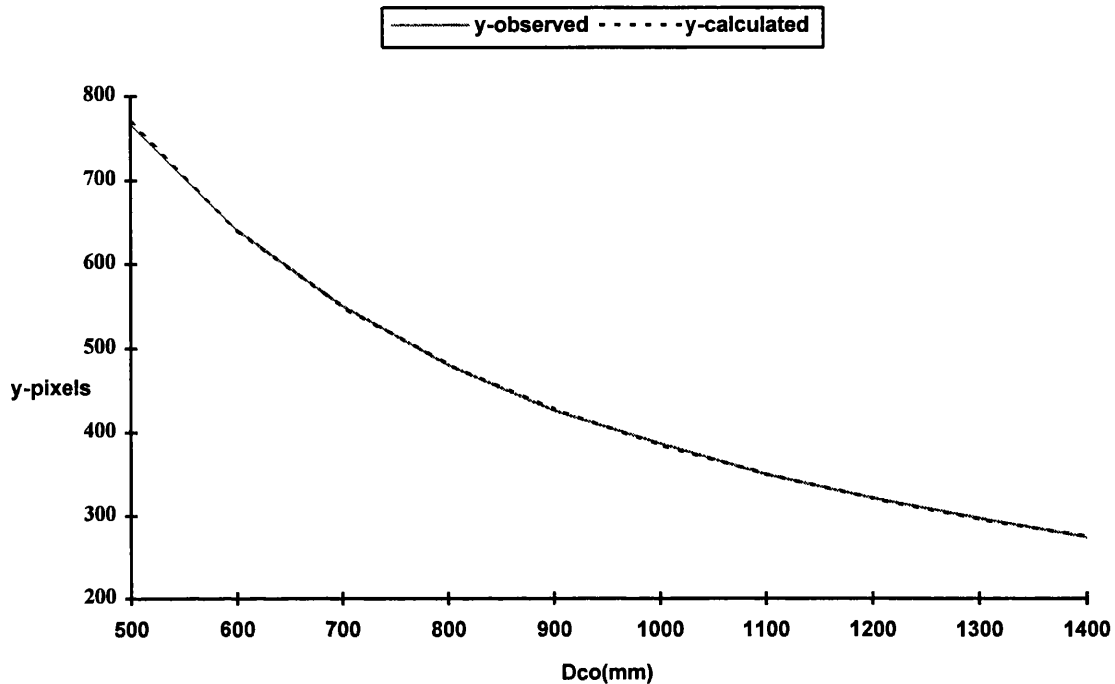
Graph 3-4 y pixel Values for a Variation in Camera-to-object Distance

Experimental Hypothesis E :

"To demonstrate the effect of a variation in the rotation speed on the observed and calculated y image space values for the line-scan camera positioned at the centre of the rotation stage"

Experimental Arrangement :

Rotation Speed (rpm)	1.67 - 8.33
Scan Rate (kHz)	80
Focal Length (mm)	25
Camera-to-object Distance (mm)	500

Experimental Results :

The observed and theoretical y pixel values for a variation in the camera rotation speed are presented in Table B.5 and are illustrated in Graph 3-5.
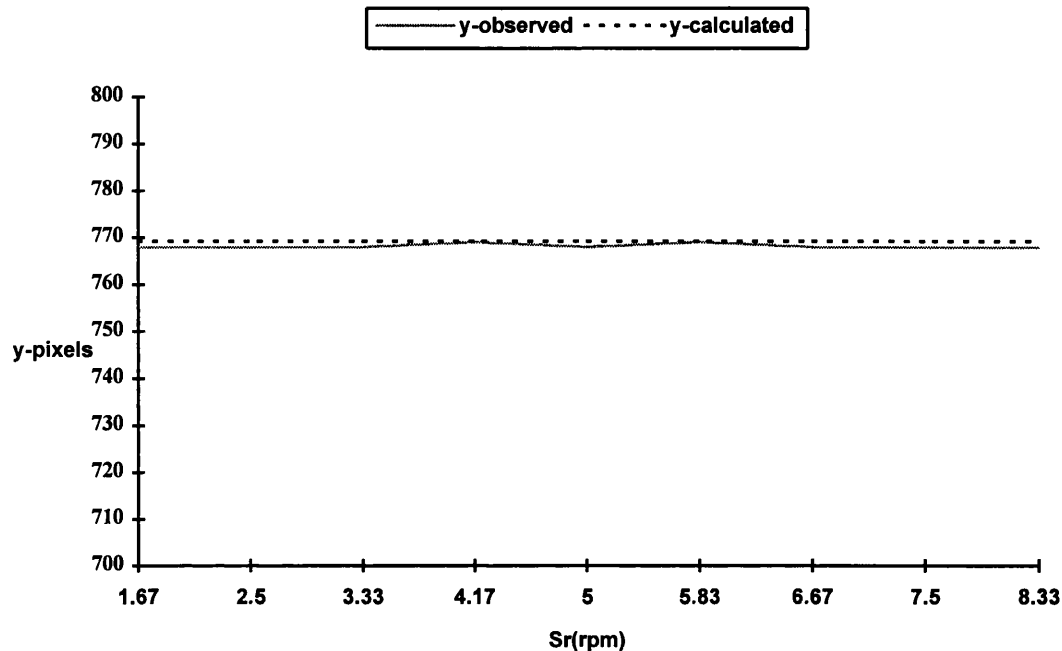
Graph 3-5 y pixel Values for a Variation in Camera Rotation Speed

Experimental Hypothesis F :

"To demonstrate the effect of a variation in the camera scan rate on the observed and calculated y image space values for the line-scan camera positioned at the centre of the rotation stage"

Experimental Arrangement :

Rotation Speed (rpm)	1.67
Scan Rate (kHz)	30 -90
Focal Length (mm)	25
Camera-to-object Distance (mm)	500

Experimental Results :

The observed and theoretical y pixel values for a variation in the camera scan rate are presented in Table B.6 and are illustrated in Graph 3-6.
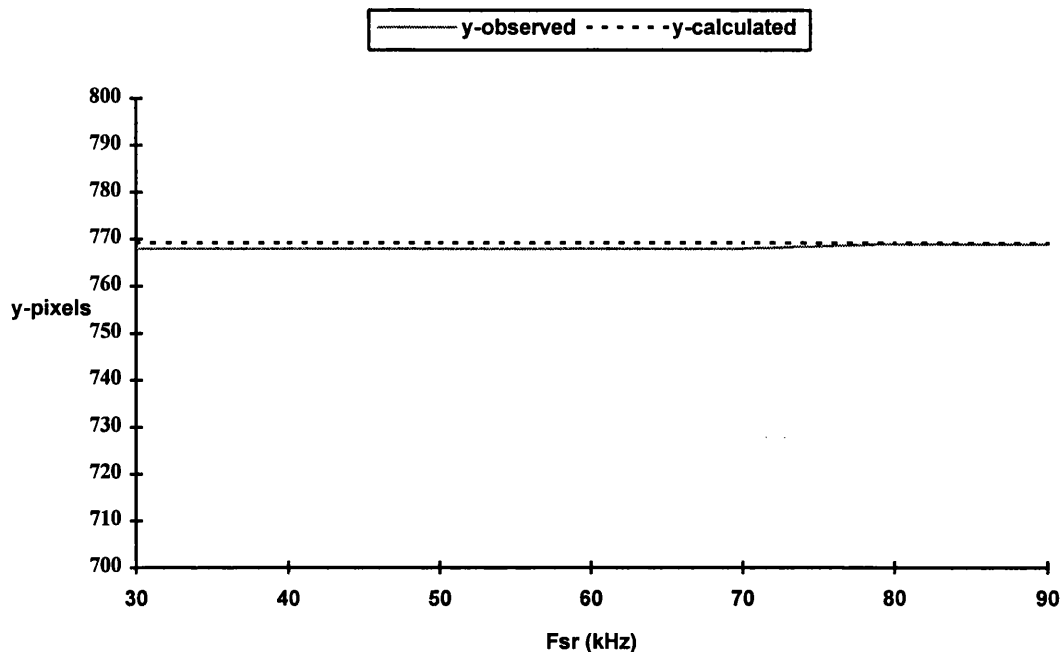
Graph 3-6 y pixel Values for a Variation in Camera Scan Rate

3.6.4 Deviation Along the Central Axis of Rotation - X-axis Results

The aim of the work in this section is to investigate the relationship between x-axis image space quantities and variations in the rotation centre to object distance, rotation speed and scan rate for camera positions along the central axis of rotation (Figure 3-11). After obtaining the measurements the X-axis algorithm (Equation 3-9) is used, as described in Section 3.4.1, to obtain theoretical x pixel values associated with the experimentally observed data.

Experimental Hypothesis G :

"To demonstrate the effect of varying the camera position along the central axis of rotation on the observed and calculated x image space values"

Experimental Arrangement :

Distance Along Central Axis (mm)	50 - 500
Rotation Speed (rpm)	1.67
Scan Rate (kHz)	80
Focal Length (mm)	25
Rotation Centre to Object Distance (mm)	700

Experimental Results :

The observed and theoretical x pixel values for a varying distance of camera position along the central axis of rotation are presented in Table B.7 and are illustrated in Graph 3-7.
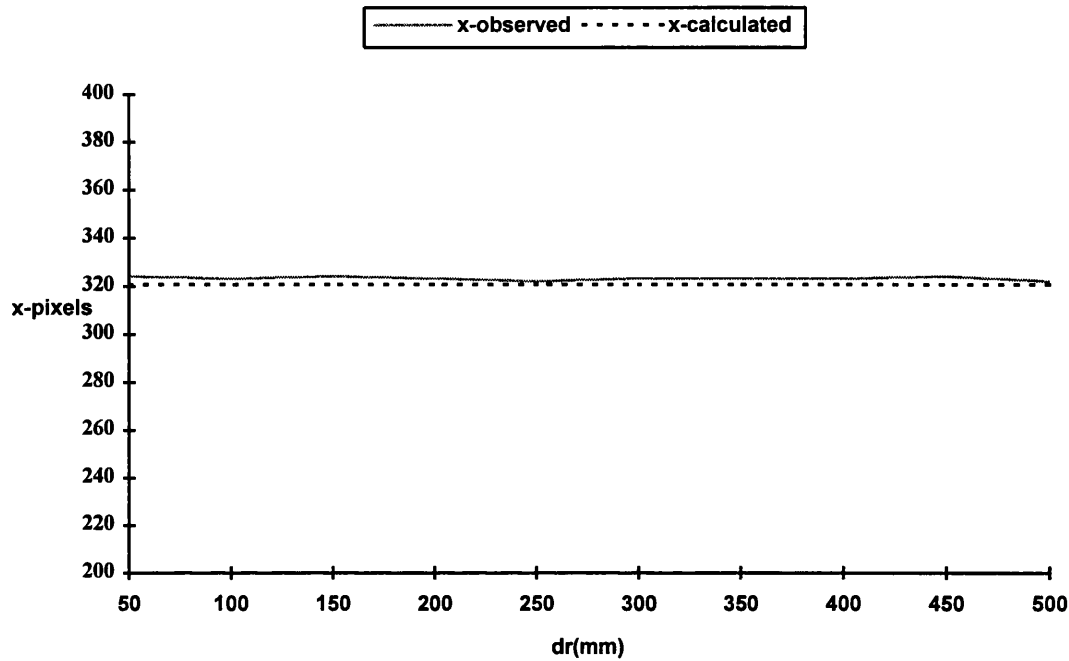
Graph 3-7 x pixel Values for Variation of Camera Distance Along the Central Axis of Rotation

Experimental Hypothesis H :

"To demonstrate the effect of varying the rotation centre to object distance on observed and calculated x pixel values for the camera positioned away from the central axis of the rotation"

Experimental Arrangement :

Distance Along Central Axis (mm)	250
Rotation Speed (rpm)	1.67
Scan Rate (kHz)	80
Focal Length (mm)	25
Rotation Centre to Object Distance (mm)	600 - 1500

Experimental Results :

The observed and theoretical x pixel values for a variation in the centre of rotation to object distance are presented in Table B.8 and are illustrated in Graph 3-8.
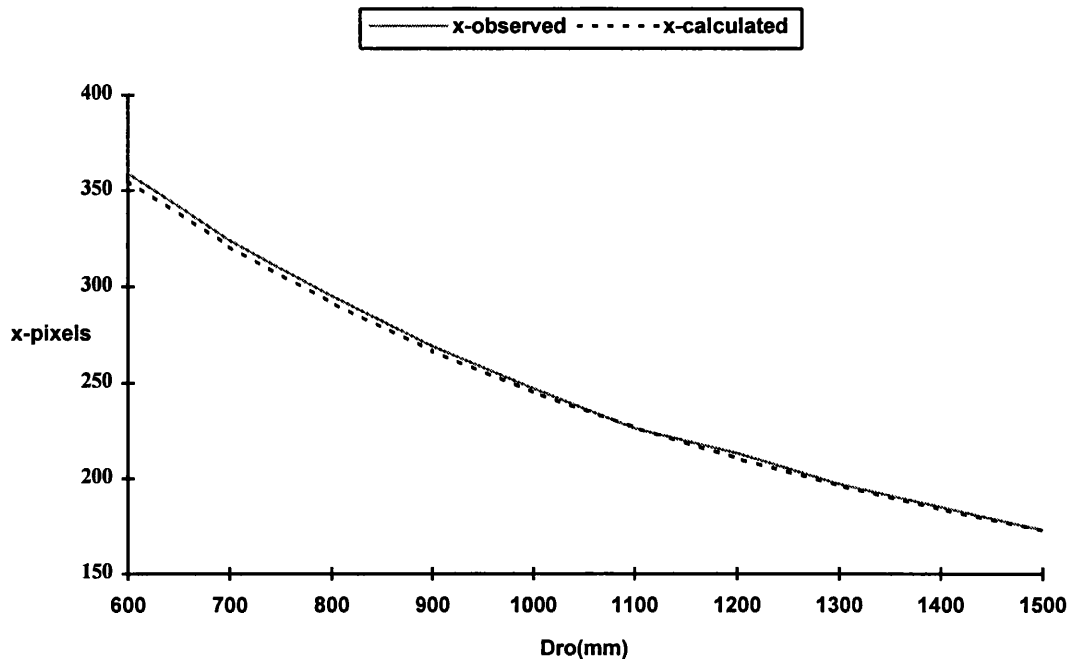
Graph 3-8 x pixel Values for a Variation in Rotation Centre to Object Distance

Experimental Hypothesis I :

"To demonstrate the effect of a variation in rotation speed on the observed and calculated x image space values for the camera positioned along the central axis of the rotation stage"

Experimental Arrangement :

Distance Along Central Axis (mm)	250
Rotation Speed (rpm)	1.67 - 8.33
Scan Rate (kHz)	80
Focal Length (mm)	25
Rotation Centre to Object Distance (mm)	700

Experimental Results :

The observed and theoretical x pixel values for a variation in the camera rotation speed are presented in Table B.9 and are illustrated in Graph 3-9.
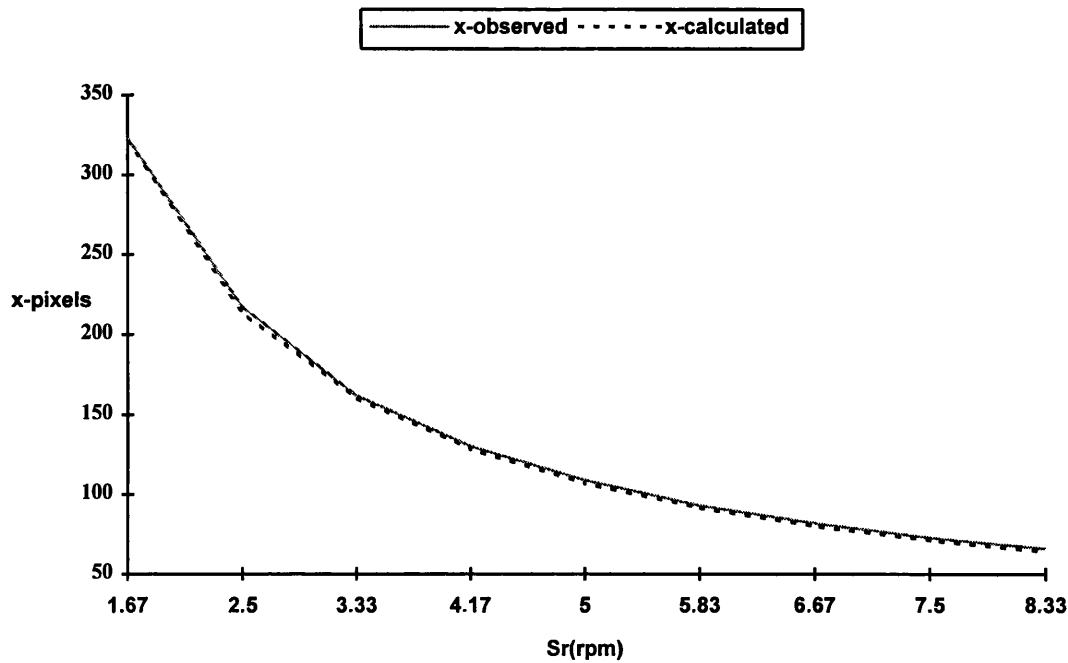
Graph 3-9 x pixel Values for a Variation in Rotation Speed

Experimental Hypothesis J :

"To demonstrate the effect of a variation in the camera scan rate on the observed and calculated x image space values for the line-scan camera positioned along the central axis of the rotation stage"

Experimental Arrangement :

Distance Along Central Axis (mm)	250
Rotation Speed (rpm)	1.67
Scan Rate (kHz)	30 - 90
Focal Length (mm)	25
Rotation Centre to Object Distance (mm)	700

Experimental Results :

The observed and theoretical x pixel values for a variation in the camera scan rate are presented in Table B.10 and are illustrated in Graph 3-10.

—— x-observed · · · · · ·x-calculated

x-pixels

(y-axis: 100, 150, 200, 250, 300, 350, 400)

(x-axis: Fsr (kHz) — 30, 40, 50, 60, 70, 80, 90)
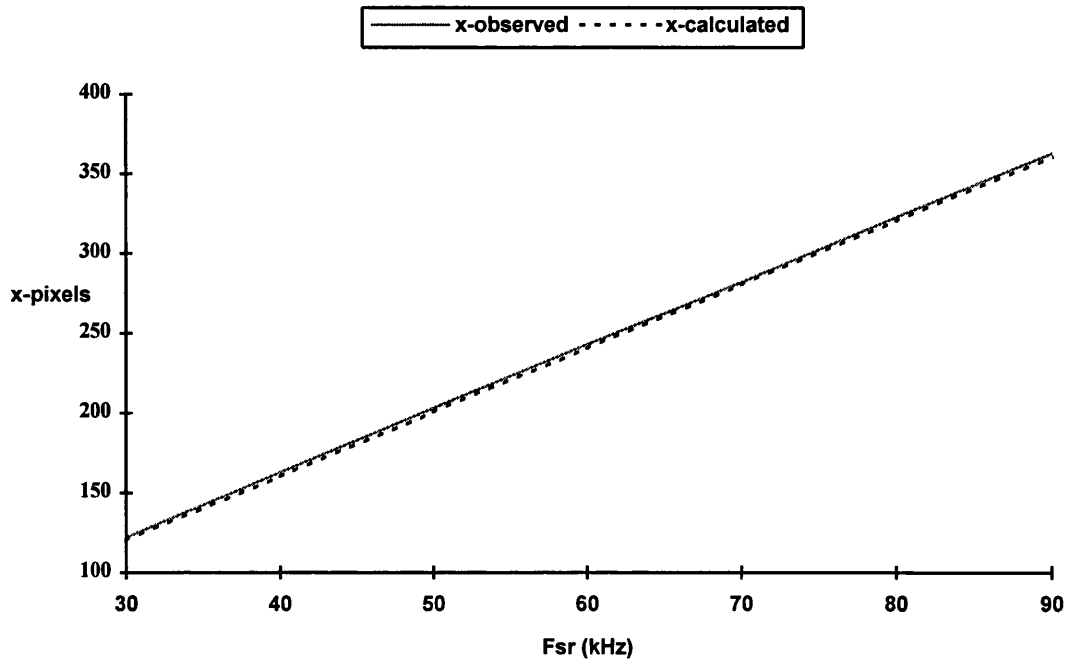
Graph 3-10 x- pixel Values for a Variation in Camera Scan Rate

3.6.5 Deviation Along the Central Axis of Rotation - Y-axis Results

The aim of this work is to investigate the relationship between y-axis image space quantities and variations in camera position along the central axis of rotation (Figure 3-11) and centre of rotation to object distance. After obtaining the experimental observations the Y-axis algorithm (Equation 3-16) is used, as described in Section 3.4.2, to calculate the y pixel values associated with the experimental data.

Experimental Hypothesis K :

"To demonstrate the effect of varying the camera position along the central axis of rotation on the observed and calculated y image space values"

Experimental Arrangement :

Distance Along Central Axis (mm)	50 - 300
Rotation Speed (rpm)	1.67
Scan Rate (kHz)	80
Focal Length (mm)	25
Rotation Centre to Object Distance (mm)	700

Experimental Results :

The observed and theoretical y pixel values for a varying distance of camera position along the central axis of rotation are presented in Table B.11 and are illustrated in Graph 3-11.
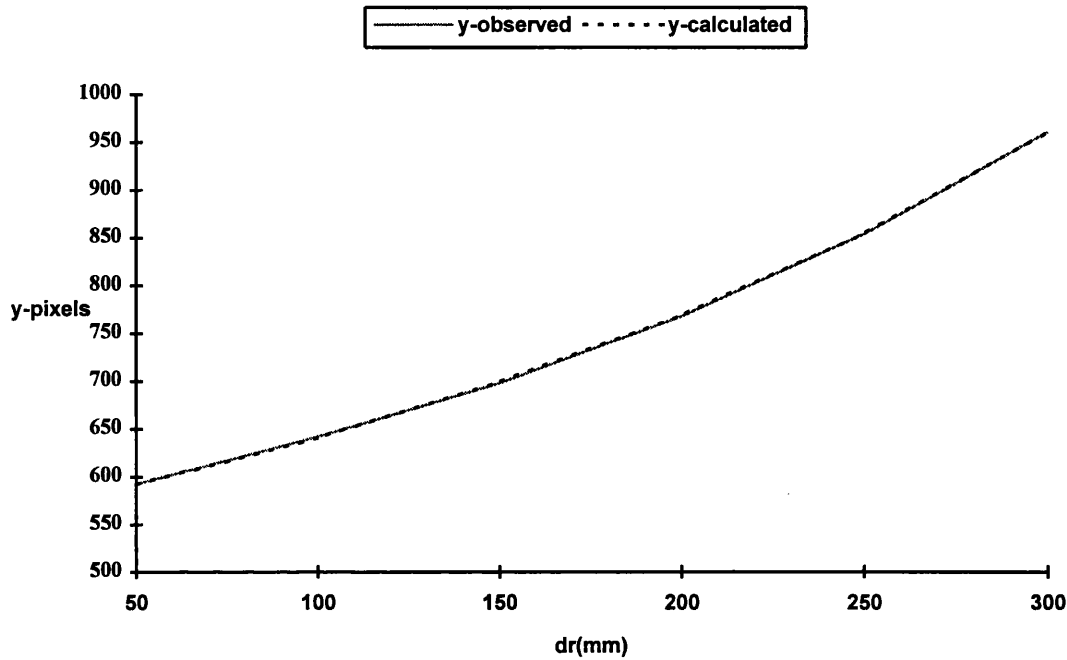
Graph 3-11 y pixel Values for Distance Variation Along Central Axis of Rotation

Experimental Hypothesis L :

"To demonstrate the effect of varying the rotation centre to object distance on observed and calculated y pixel values for the camera positioned along the central axis of the rotation stage"

Experimental Arrangement :

Distance Along Central Axis (mm)	250
Rotation Speed (rpm)	1.67
Scan Rate (kHz)	80
Focal Length (mm)	25
Rotation Centre to Object Distance (mm)	700 - 1400

Experimental Results :

The observed and theoretical y pixel values for a variation in the centre of rotation to object distance are presented in Table B.12 and are illustrated in Graph 3-12.
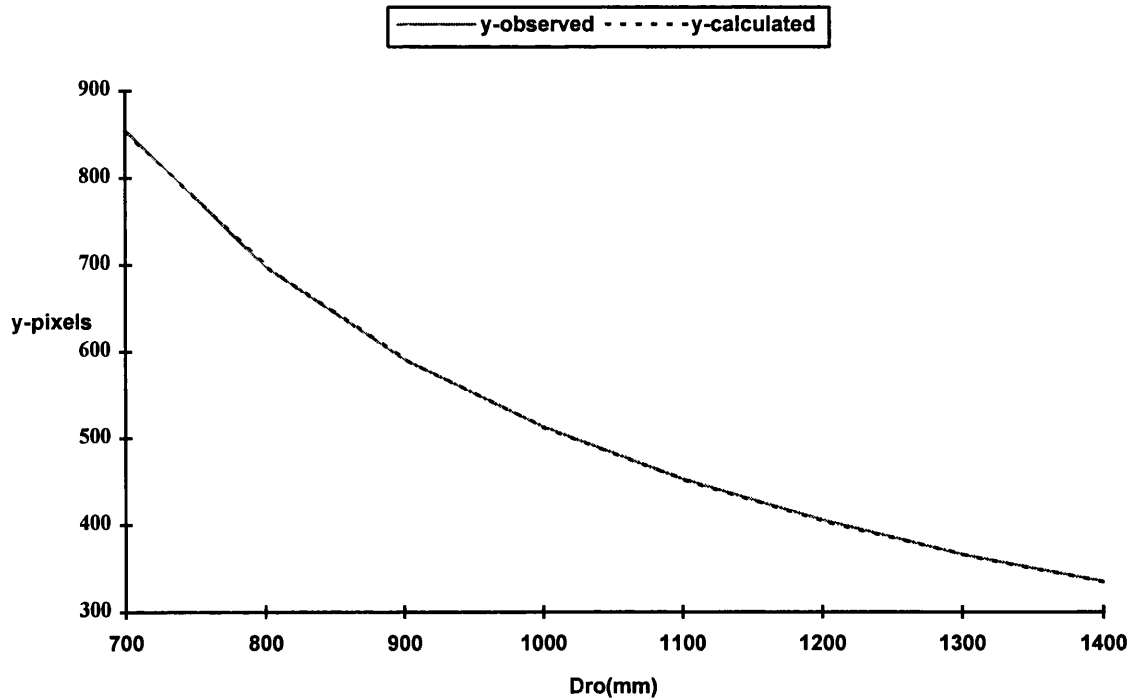
Graph 3-12 y pixel Values for Variation in Rotation Centre to Object Distance

3.6.6 Deviation From the Central Axis of Rotation - X-axis Results

The aim of the work in this section is to investigate the relationship between x-axis image space quantities and variations in the rotation centre to object distance, rotation speed and scan rate for camera positions away from the central axis of rotation (Figure 3-11). After obtaining the measurements the X-axis algorithm (Equation 3-9) is used, as described in Section 3.4.1, to calculate x pixel values associated with the experimentally observed data.

Experimental Hypothesis M :

"To demonstrate the effect of a variation of the camera position from the central axis of rotation on the observed and calculated x image space values"

Experimental Arrangement :

Distance From Central Axis (mm)	50 - 500
Rotation Speed (rpm)	1.67
Scan Rate (kHz)	80
Focal Length (mm)	25
Rotation Centre to Object Distance (mm)	700

Experimental Results :

The observed and theoretical x pixel values for a variation in camera position from the central axis of rotation are presented in Table B.13 and are illustrated in Graph 3-13.
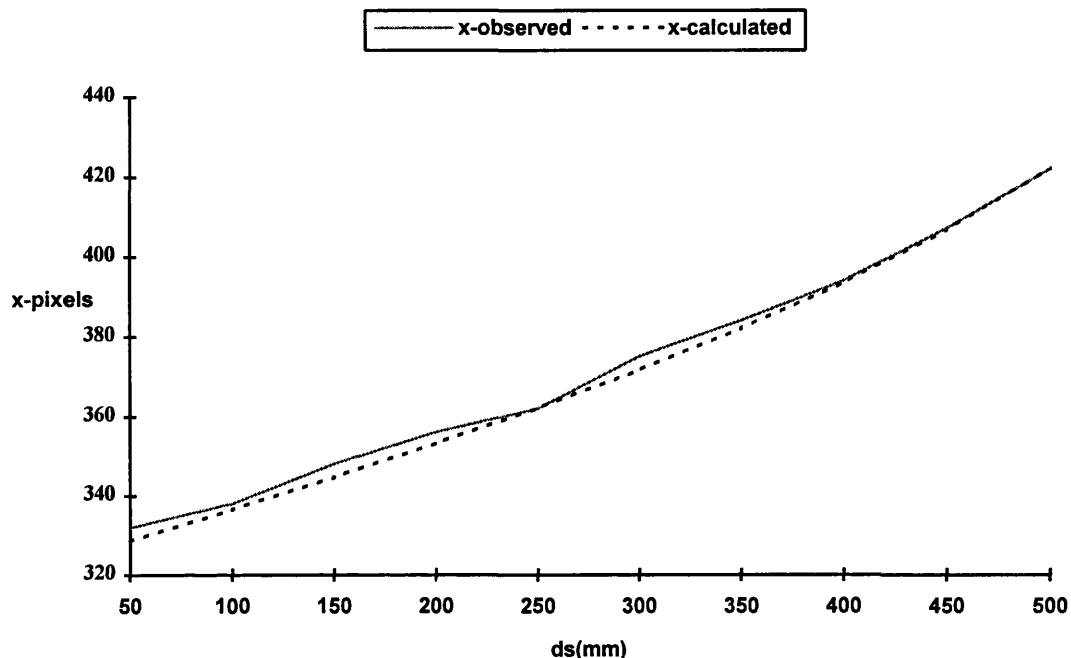
Graph 3-13 x pixel Values for Distance Variation From Central Axis of Rotation

Experimental Hypothesis N :

"To demonstrate the effect of a variation of the rotation centre to object distance on the observed and calculated x image space values for a camera position from the central axis of rotation"

Experimental Arrangement :

Distance From Central Axis (mm)	250
Rotation Speed (rpm)	1.67
Scan Rate (kHz)	80
Focal Length (mm)	25
Rotation Centre to Object Distance (mm)	600 - 1500

Experimental Results :

The observed and theoretical x pixel values for a variation the rotation centre to object distance are presented in Table B.14 and are illustrated in Graph 3-14.
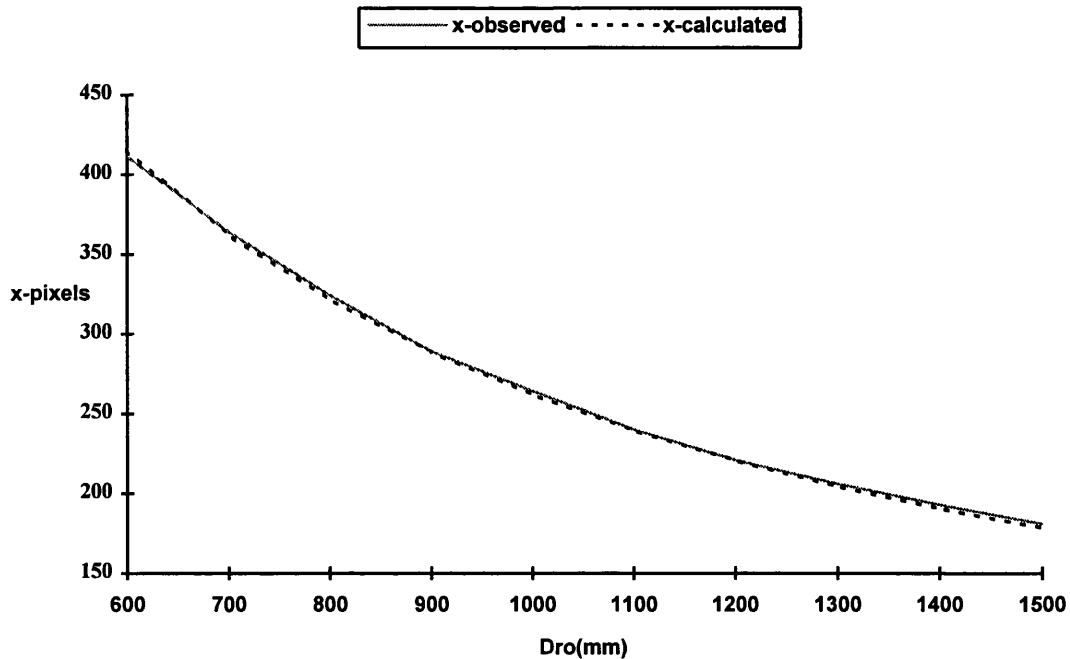
Graph 3-14 x pixel Values for a Variation in Rotation Centre to Object Distance

Experimental Hypothesis O :

"To demonstrate the effect of a variation in camera rotation speed on the observed and calculated x image space values for a camera position from the central axis of rotation"

Experimental Arrangement :

Distance From Central Axis (mm)	250
Rotation Speed (rpm)	0.83 - 8.33
Scan Rate (kHz)	80
Focal Length (mm)	25
Rotation Centre to Object Distance (mm)	700

Experimental Results :

The observed and theoretical x pixel values for a variation in camera rotation speed are presented in Table B.15 and are illustrated in Graph 3-15.
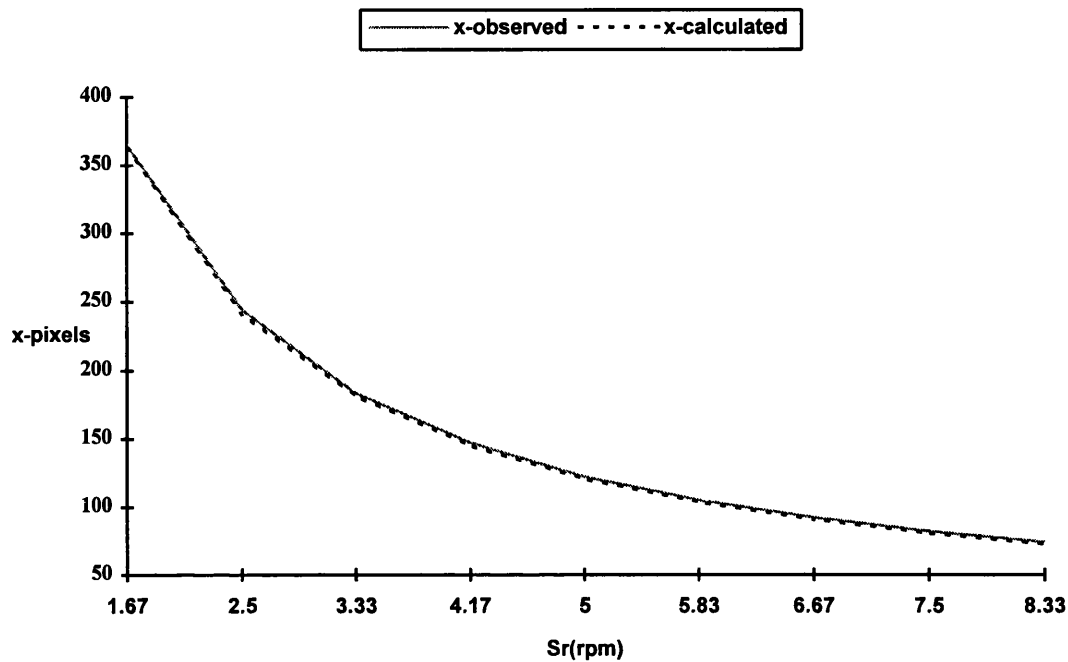
Graph 3-15 x pixel Values for a Variation in Rotation Speed

Experimental Hypothesis P :

"To demonstrate the effect of a variation in camera scan rate on the observed and calculated x image space values for a camera position from the central axis of rotation"

Experimental Arrangement :

Distance From Central Axis (mm)	250
Rotation Speed (rpm)	1.67
Scan Rate (kHz)	30 - 90
Focal Length (mm)	25
Rotation Centre to Object Distance (mm)	700

Experimental Results :

The observed and theoretical x pixel values for a variation in camera scan rate are presented in Table B.16 and are illustrated in Graph 3-16.
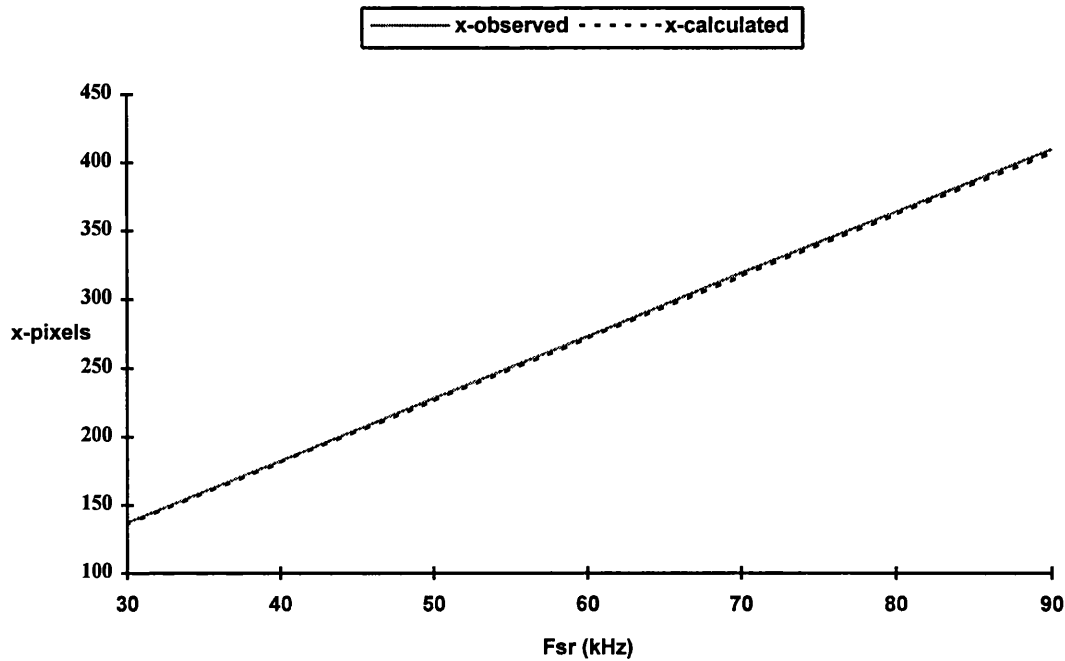
Graph 3-16 x pixel Values for a Variation in Scan Rate

3.6.7 Deviation From the Central Axis of Rotation - Y-axis Results

The aim of this work is to investigate the relationship between y-axis image space quantities and variations in camera position away from the central axis of rotation (Figure 3-11) and centre of rotation to object distance. After obtaining the experimental observations the Y-axis algorithm (Equation 3-18) is used, as described in Section 3.4.2, to obtain theoretical y pixel values associated with the experimental data.

Experimental Hypothesis Q :

"To demonstrate the effect of a variation of the camera position from the central axis of rotation on the observed and calculated y image space values"

Experimental Arrangement :

Distance From Central Axis (mm)	50 - 500
Rotation Speed (rpm)	1.67
Scan Rate (kHz)	80
Focal Length (mm)	25
Rotation Centre to Object Distance (mm)	700

Experimental Results :

The observed and theoretical y pixel values for a variation in camera position from the central axis of rotation are presented in Table B.17 and are illustrated in Graph 3-17.
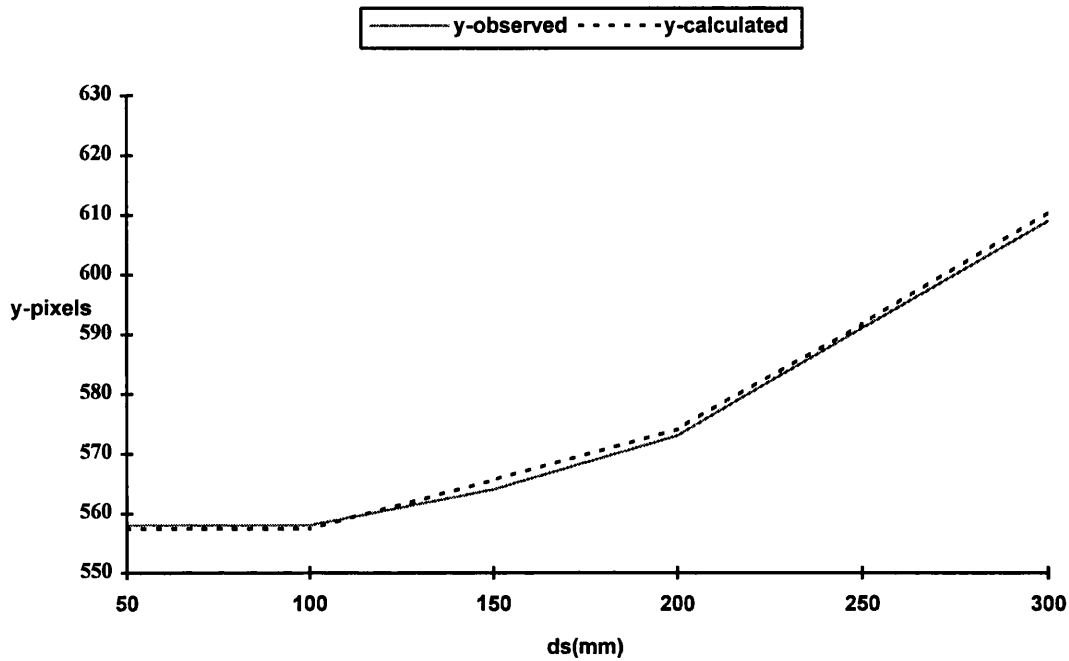
Graph 3-17 y pixel Values for Distance Variation from Central Axis of Rotation

Experimental Hypothesis R :

"To demonstrate the effect of a variation of the rotation centre to object distance on the observed and calculated y image space values for a camera position from the central axis of rotation"

Experimental Arrangement :

Distance From Central Axis (mm)	250
Rotation Speed (rpm)	1.67
Scan Rate (kHz)	80
Focal Length (mm)	25
Rotation Centre to Object Distance (mm)	600 - 1500

Experimental Results :

The observed and theoretical x pixel values for a variation the rotation centre to object distance are presented in Table B.18 and are illustrated in Graph 3-18.
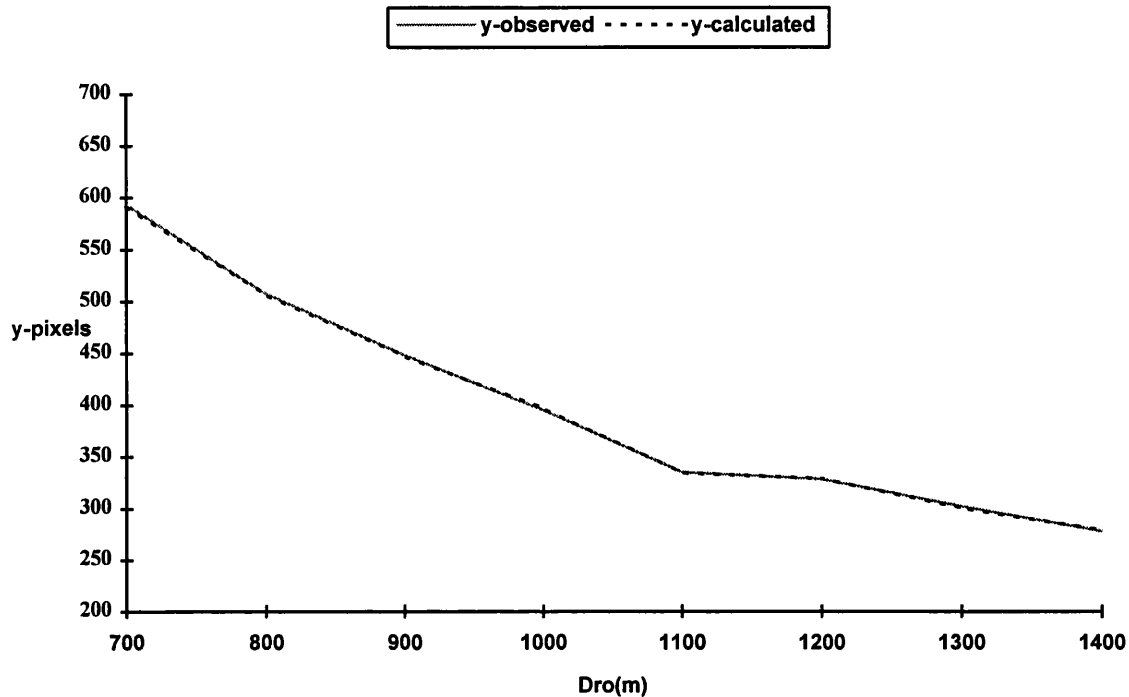
Graph 3-18 y pixel Values for a Rotation Centre to Object Distance Variation

3.7 The 2-D Measurement Analysis

This section will present results obtained from the rotating two-dimensional line-scan investigation, presented in Section 3.6. Results are obtained allowing the measurement characteristics of the 2-D arrangement to be identified from this analysis. The two-dimensional measurement capability of the rotating line-scan system is discussed in Section 3.8.

3.7.1 Centre of Rotation

This section evaluates the measurement capability for a rotating 2-D system with the camera placed at the centre of the rotation stage. To achieve this the two-dimensional algorithms are re-arranged to allow the pixel errors obtained from each experiment to be represented in mm of object space. For this investigation a fixed distance in each co-ordinate axis was selected from a metre-rule, therefore, the resulting object space errors are the difference between the known distance and the theoretical distance calculated using the 2-D algorithms.

X-axis Results :-

The objectives of this part of the investigation are given by the experimental hypotheses A, B and C (Section 3.6.2) and the results are illustrated in Graph 3-1, Graph 3-2 and Graph 3-3 respectively.

Each x-axis pixel error is transformed to an equivalent error in mm of object space by re-arranging Equation 3-9 :-

$$e_x = \left[D_{CO}\left(\tan\left(\frac{6nS_R\left(x_{obs} - x_{cal}\right)}{F_{SR}} \right) \right) \right] \qquad \text{Equation 3-19}$$

Where,

e_x is object space error in the X-axis, in mm;

x_{obs} is the number of pixels observed in the x-axis;

x_{cal} is the theoretically obtained number of pixels in the x-axis.

Table 3-2, Table 3-3 and Table 3-4 present object space errors determined from Equation 3-19 for each variation in the parameters considered in the X-axis experimental analysis. The resulting rms errors for variations in camera-to-object-range, rotation speed and scan rate are 2.9mm, 4.4mm and 3.7mm respectively.

D_{CO} (mm)	e_x (mm)
500	2.7
600	2.5
700	0.5
800	2.7
900	1.0
1000	2.0
1100	6.1
1200	1.6
1300	2.0
1400	3.8
rms error (mm)	2.9

Table 3-2 X-axis Object Space Error Due to a Variation in Camera-to-Object Range

S_R (rpm)	e_x (mm)
1.67	3.8
2.50	3.7
3.33	4.9
4.17	4.7
5.00	3.7
5.83	3.9
6.67	4.5
7.50	5.0
8.33	5.0
rms error (mm)	4.4

Table 3-3 X-axis Object Space Error Due to a Variation in Rotation Speed

F_{SR} (kHz)	e_x (mm)
30	4.8
40	4.9
50	4.8
60	3.4
70	2.3
80	2.7
90	1.9
rms error (mm)	3.7

Table 3-4 X-axis Object Space Error Due to a Variation in Scan Rate

Y-axis Results :-

The aims of this work are given by experimental hypotheses D, E and F (Section 3.6.3) and the results are illustrated in Graph 3-4, Graph 3-5 and Graph 3-6 respectively.

To evaluate the measurement capability in the y-axis for the line-scan system the difference between observed and theoretical pixel values is calculated to give an error, in pixels. Each error is transformed to an equivalent error in mm of object space by re-arranging Equation 3.11 :

$$e_y = \left[\frac{D_{CO}.SL.\left(|y_{obs} - y_{cal}| \right)}{f} \right]$$

Equation 3-20

Where,

e_y is object space error in the Y-axis, in mm;

y_{obs} is the number of pixels observed in the y-axis;

y_{cal} is the theoretically obtained number of pixels in the y-axis.

Table 3-5, Table 3-6 and Table 3-7 present object space errors determined from Equation 3-20 for each variation in the parameters considered in the Y-axis experimental analysis. The resulting rms errors for variations in camera-to-object-range, rotation speed and scan rate are 0.5mm, 0.3mm and 0.3mm respectively.

D_{CO} (mm)	e_y (mm)
500	0.6
600	0.3
700	0.2
800	0.3
900	0.7
1000	0.7
1100	0.4
1200	0.3
1300	0.8
1400	0.6
rms error (mm)	0.5

Table 3-5 Y-axis Object Space Error Due to a Variation in Camera-to-Object Range

S_R (rpm)	e_y (mm)
1.67	0.3
2.50	0.3
3.33	0.3
4.17	0.1
5.00	0.3
5.83	0.1
6.67	0.3
7.50	0.3
8.33	0.3
rms error (mm)	0.3

Table 3-6 Y-axis Object Space Error Due to a Variation in Rotation Speed

F_{SR} (kHz)	e_y (mm)
30	0.3
40	0.3
50	0.3
60	0.3
70	0.3
80	0.1
90	0.1
rms error (mm)	0.3

Table 3-7 Y-axis Object Space Error Due to a Variation in Scan Rate

3.7.2 Deviation Along the Central Axis of Rotation

This section evaluates the measurement capability for a rotating 2-D system with the camera placed along the central axis of rotation. To achieve this Equation 3-19 is used to obtain the X-axis measurement errors and Equation 3-16 is re-arranged, as follows, to allow calculation of the measurement error in the y-axis of object space :

$$e_y = \left[\frac{SL(|y_{obs} - y_{cal}|)(D_{RO} - d_r)}{f} \right]$$

For this investigation a fixed distance in each co-ordinate axis was selected from a metre-rule, therefore, the resulting object space errors are the difference between the known distance and the theoretical distance calculated using the 2-D algorithms.

X-axis Results :-

The objectives of this work are given by experimental hypotheses G, H, I and J (Section 3.6.4) and the results are illustrated in Graph 3-7, Graph 3-8, Graph 3-9 and Graph 3-10 respectively.

Table 3-8, Table 3-9, Table 3-10 and Table 3-11 present object space errors determined from Equation 3-19 for the parameters considered in the experimental analysis. The resulting rms errors for a variation in distances along the central axis of rotation, the rotation centre to object range, rotation speed and scan rate are 2.8mm, 4.7mm, 9.4mm and 5.5mm respectively.

d_r (mm)	e_x (mm)
50	4.8
100	3.1
150	4.1
200	2.6
250	1.3
300	2.1
350	1.8
400	1.5
450	1.8
500	0.6
rms error (mm)	2.8

Table 3-8 X-axis Object Space Error Due to a Variation in Camera Distance Along the Central Axis of Rotation

D_{RO} (mm)	e_x (mm)
600	5.2
700	5.2
800	6.3
900	5.0
1000	4.5
1100	1.2
1200	7.0
1300	2.0
1400	3.8
1500	4.0
rms error (mm)	4.7

Table 3-9 X-axis Object Space Error Due to a Variation in Rotation Centre to Object Range

S_R (rpm)	e_x (mm)
1.67	3.6
2.50	7.5
3.33	5.0
4.17	6.6
5.00	9.9
5.83	7.7
6.67	11.3
7.50	12.0
8.33	14.9
rms error (mm)	9.4

Table 3-10 X-axis Object Space Error Due to a Variation in Rotation Speed

F_{SR} (kHz)	e_x (mm)
30	7.1
40	8.1
50	6.5
60	5.2
70	2.5
80	3.6
90	3.1
rms error (mm)	5.5

Table 3-11 X-axis Object Space Error Associated With a Variation in Scan Rate

Y-axis Results :-

The aims of this part of the investigation are given by the experimental hypotheses K and L (Section 3.6.5) and the results are illustrated in Graph 3-11 and Graph 3-12.

Table 3-12 and Table 3-13 present errors determined by Equation 3-20 for variation of the parameters considered in the experimental work. The errors for variations in camera distance along the central axis and rotation centre to object distance are 0.3mm and 0.7mm respectively.

d_r (mm)	e_y (mm)
50	0.4
100	0.3
150	0.4
200	0.3
250	0.2
300	0.3
rms error (mm)	0.3

Table 3-12 Y-axis Object Space Error Due to a Variation in Camera Distance Along the Central

Axis of Rotation

D_{RO} (mm)	e_y (mm)
700	0.5
800	0.5
900	0.3
1000	0.6
1100	0.3
1200	0.7
1300	0.9
1400	1.2
rms error (mm)	0.7

Table 3-13 Y-axis Object Space Error Due to a Variation in Rotation Centre to Object Distance

3.7.3 Deviation From the Central Axis of Rotation

This section will evaluate the measurement capability for the 2-D system with the camera placed away from the central axis of rotation. To achieve this θ_R (Equation 3-14) is substituted into the X-axis algorithm (Equation 3-9) and re-arranged to allow calculation of the object space error :

$$e_x = \sqrt{\left(\frac{d_s + D_{RO}}{\dfrac{d_s}{D_{RO}} + \cos\left(\dfrac{6nS_R(x_{obs} - x_{cal})}{F_{SR}} \right)} \right)^2 - D_{RO}^2}$$

To allow calculation of the Y-axis object space error Equation 3-18 is re-arranged as follows :

$$e_y = \left[\frac{SL(|y_{obs} - y_{cal}|)\sqrt{(D_{RO}^2 - d_s^2)}}{f} \right]$$

X-axis Results :-

The objectives of this work are given by the hypotheses M, N, O and P (Section 3.6.6) and the results are illustrated in Graph 3-13, Graph 3-14, Graph 3-15 and Graph 3-16 respectively.

Table 3-14, Table 3-15, Table 3-16 and Table 3-17 present object space errors determined by Equation 3-19 for each variation in the parameters considered in the X-axis experimental work. The resulting rms errors for variations in the distance from the central axis, the rotation centre to object range, rotation speed and scan rate are 2.8mm, 4.4mm, 7.2mm and 3.2mm respectively.

d_s (mm)	e_x (mm)
50	3.1
100	2.0
150	4.7
200	3.9
250	0.1
300	4.3
350	2.6
400	0.6
450	0.4
500	0.2
rms error (mm)	2.8

Table 3-14 X-axis Object Space Error Due to a Variation in Camera Distance From the Central

Axis of Rotation

D_{RO} (mm)	e_x (mm)
600	4.2
700	2.6
800	4.2
900	0.7
1000	4.2
1100	0.9
1200	0.7
1300	3.7
1400	6.9
1500	8.4
rms error (mm)	4.4

Table 3-15 X-axis Object Space Error Due to a Variation in Rotation Centre to Object Range

S_R (rpm)	e_x (mm)
1.67	3.9
2.50	5.2
3.33	5.1
4.17	7.4
5.00	5.2
5.83	7.0
6.67	8.1
7.50	9.1
8.33	10.7
rms error (mm)	7.2

Table 3-16 X-axis Object Space Error Due to a Variation in Rotation Speed

F_{SR} (kHz)	e_x (mm)
30	4.3
40	2.4
50	3.7
60	2.5
70	3.2
80	2.6
90	3.1
rms error (mm)	3.2

Table 3-17 X-axis Object Space Error Associated With a Variation in Scan Rate

Y-axis Results :-

The aims of this part of the investigation are given by the experimental hypotheses Q and R (Section 3.6.7) and the results are illustrated in Graph 3-17 and Graph 3-18. Table 3-18 and Table 3-19 show object space errors determined by Equation 3-20 for a variation in the parameters considered in this work. The rms errors for variations in camera distance along the central axis and rotation centre to object distance are 0.4mm and 0.6mm respectively.

d_s (mm)	e_y (mm)
50	0.2
100	0.2
150	0.6
200	0.4
250	0.2
300	0.5
rms error (mm)	0.4

Table 3-18 Y-axis Object Space Error Due to a Variation in Camera Distance From the Central Axis of Rotation

D_{RO} (mm)	e_y (mm)
700	0.4
800	0.4
900	0.4
1000	0.8
1100	0.3
1200	0.4
1300	1.0
1400	0.5
rms error (mm)	0.6

Table 3-19 Y-axis Object Space Error Due to a Variation in Rotation Centre to Object Distance

The following section will now summarise the work presented in this chapter.

3.8 Summary

A summary of the rotating two-dimensional line-scan investigation is now presented. The discussion is divided into the following areas :

- the characteristics of rotating 2-D line-scan systems which govern image production in each axis of the considered arrangements;
- the measurement capability associated with the 2-D line-scan arrangements considered in this investigation;
- the applicability of a rotating line-scan sensor to the development of a stereoscopic arrangement of these devices.

3.8.1 Rotating 2-D Line-scan System Characteristics

For this rotating two-dimensional line-scan investigation three modes of camera operation were identified. From Figure 3-11, these are as follows :

- the camera may be located at the *centre* of the rotation stage;
- the camera may be located at a position *along* the central axis of rotation;
- the camera may be located at a position away *from* the central axis of rotation.

For each mode of camera rotation the parameters which govern image production were altered in a series of defined steps to enable the experimental characteristics to be identified. The following presents a discussion of the characteristics obtained from each mode considered.

Centre of Rotation Operation :

The following summarises the X-axis characteristics of a rotating 2-D line-scan system with the camera placed at the centre of the rotation stage :-

- the extent of the FOV in the X-axis is dependent on the camera-to-object range, the camera rotation speed and the camera scan rate;
- the extent of the FOV in the X-axis is proportional to the camera-to-object range and the camera rotation speed as observed from Graph 3-1 and Graph 3-2 respectively;
- the extent of the FOV in the X-axis is inversely proportional to the camera scan rate (Graph 3-3).

The following summarises the Y-axis characteristics of a rotating 2-D line-scan system with the camera placed at the centre of the rotation stage :-

- the extent of the FOV in the Y-axis is dependent on the camera-to-object range (Graph 3-4);
- the extent of the FOV in the Y-axis is independent of the camera rotation speed and scan rate as observed from Graph 3-5 and Graph 3-6 respectively;

Deviation Along the Central Axis of Rotation Operation :

The characteristics for centre of rotation operation are applicable to this mode of camera operation. However, it is noted from this configuration that the angle of camera rotation necessary to view an object of interest is the same as the rotation angle viewed by an equivalent centre of rotation arrangement (Figure 3-15). Therefore, although the field of view in the X-axis is independent of the distance along the central axis of rotation (Graph 3-7) it is controlled by the actual rotation centre to object distance (Graph 3-8). Whereas, the field of view in the Y-axis is governed by the actual camera-to-object distance (refer to Graph 3-11 and Graph 3-12) and not directly by the rotation centre to object distance.

Deviation From the Central Axis of Rotation Operation :

The characteristics for centre of rotation operation are equally applicable to this mode of camera operation. However, for camera positions from the central axis of rotation the angle of rotation

necessary to view an object of interest is different than that observed from equivalent camera arrangements described previously (Figure 3-17). Also, the FOV in the X-axis is dependent on the distance of the camera from the central axis of rotation (Graph 3-13) due to the difference in the geometry of the system from centre of rotation and deviation along the central axis configurations. As in the previous cases, the field of view in the Y-axis is governed by the actual camera-to-object distance (Graph 3-17 and Graph 3-18).

3.8.2 The 2-D Measurement Capability

The 2-D measurement capability of the line-scan system, as discussed in Section 3.7, is now summarised for the modes of system operation and parameter variations considered.

Centre of Rotation Operation :

For a fixed distance in object space the X-axis rms measurement errors for variations in camera-to-object distance, rotation speed and scan rate are ±2.9mm, ±4.4mm and ±3.7mm respectively (Table 3-21). To identify the measurement capability these values are expressed in terms of the image space error, i.e., the number of pixels of error these values represent. The image space pixel errors due to variation in the camera-to-object distance, rotation speed and scan rate are ±1.5 (Table B.1), ±1.8 (Table B.2) and ±2.2 (Table B.3) x pixels respectively. This demonstrates that the image space errors in each case are of similar magnitudes and the differences in the equivalent object space errors are due to variations in the available resolution in object space due to the changes in the parameters considered.

To demonstrate the varying resolution available from X-axis object space consider the following. For incremental changes in camera-to-object distance, rotation speed and scan rate the object space errors are given in Table 3-2, Table 3-3 and Table 3-4 respectively. If the error obtained from image space was a constant of, say, ± 1 pixels in each case then from Table B.1, Table B.2 and Table B.3 the resultant object space errors from this assumption are provided in Table 3-20. This demonstrates a decrease in the resolution for increasing camera-to-object distances and rotation speeds and an increase in resolution for increasing scan rates.

e_x for increasing D_{CO} (mm)	e_x for increasing S_R (mm)	e_x for increasing F_{SR} (mm)
1.9	1.1	3.0
1.3	1.7	2.2
1.7	2.2	1.8
1.8	2.8	1.5
2.0	3.4	1.3
2.2	3.9	1.1
2.4	4.1	1.0
2.7	4.5	
2.9	5.6	
3.2		

Table 3-20 Object Space Error for an Assumed Image Space Error

For a fixed distance in object space the Y-axis measurement errors for variations in camera-to-object distance, rotation speed and scan rate are ±0.5mm, ±0.3mm and ±0.3mm respectively (Table 3-21). The image space pixel errors due to variation in the camera-to-object distance, rotation speed and scan rate are ±1.2 (Table B.4), ±1.0 (Table B.5) and ±1.0 (Table B.6) y pixels respectively. This confirms that the error due to incremental changes in rotation speed and scan rate are constant, illustrated in Table 3-6 and Table 3-7 respectively, and of the same order of magnitude as the error produced for the repeatability of image space measurements (Section 3.6.1). Therefore, Y-axis measurement accuracy is considered to be independent of rotation speed and scan rate.

Object Space Error	D_{CO}	S_R	F_{SR}
X-axis (mm)	2.9	4.4	3.7
Y-axis (mm)	0.5	0.3	0.3

Table 3-21 Object Space rms Errors For Centre of Rotation Operation.

Deviation Along the Central Axis of Rotation :

For a fixed distance in object space the X-axis measurement errors for variations in camera position along the central axis of rotation, rotation centre to object distance, rotation speed and scan rate are ±2.8mm, ±4.7mm, ±9.4mm and ±5.5mm, respectively (Table 3-22). The associated image space pixel errors are ±2.5 (Table B.7), ±2.4 (Table B.8), ±2.0 (Table B.9) and ±1.2 (Table B.10) x pixels respectively.

For a fixed distance in object space the Y-axis measurement errors for variations in camera position along the central axis of rotation and rotation centre to object distance are ±0.3mm and ±0.7mm, respectively (Table 3-23). The associated image space errors are ±1.2 (Table B.11) and ±1.2 (Table B.12) y pixels respectively.

Object Space Error	d_r	D_{RO}	S_R	F_{SR}
X-axis (mm)	2.8	4.7	9.4	5.5

Table 3-22 X-axis Object Space rms Errors For Camera Positions Along the Central Axis of Rotation

Object Space Error	d_r	D_{CO}
Y-axis (mm)	0.3	0.7

Table 3-23 Y-axis Object Space rms Errors For Camera Positions Along the Central Axis of Rotation

Deviation From the Central Axis of Rotation :

For a fixed distance in object space the X-axis measurement errors for variations in camera position from the central axis of rotation, rotation centre to object distance, rotation speed and scan rate are ±2.8mm, ±4.4mm, ±7.2mm and ±3.2mm respectively (Table 3-24). The associated image space pixel errors are ±2.2 (Table B.13), ±2.1 (Table B.14), ±2.0 (Table B.15) and ±1.8 (Table B.16) x pixels respectively.

For a fixed distance in object space the Y-axis measurement errors for variations in camera position from the central axis of rotation and rotation centre to object distance are ±0.3mm and ±0.6mm, respectively (Table 3-25). The associated image pixel errors are ±1.0 (Table B.11) and ±1.0 (Table B.12) y pixels respectively.

Object Space Error	d_s	D_{RO}	S_R	F_{SR}
X-axis (mm)	2.8	4.4	7.2	3.2

Table 3-24 X-axis Object Space rms Errors for Camera Positions From the Central Axis of Rotation

Object Space Error	d_s	D_{CO}
Y-axis (mm)	0.4	0.6

Table 3-25 Y-axis Object Space rms Errors for Camera Positions From the Central Axis of Rotation

In Section 3.6.1 the repeatability of the image data was established as ± 1 pixel for x and y pixel measurements between two points. The maximum pixel deviation in the results presented is ±2.5 pixels which represents an error of ±1.5 pixels greater than precision established for the system. The level of accuracy obtained from this analysis is considered to validate the use of the 2-D co-ordinate algorithms for use with the rotating line-scan system for the following reasons :

- a manual method of identifying image points is adopted in this research and therefore measurements are subject to error due to human interpretation;
- sub-pixel methods are not utilised in this research, therefore, a maximum resolution of 1 pixel is available for image space measurements;
- no calibration procedure is adopted in the two-dimensional investigation.

3.8.3 Analysis of a Stereoscopic Arrangement of Rotating Line-scan Sensors

From this investigation of a two-dimensional arrangement of rotating line-scan sensors the following is concluded :

- the characteristics of a 2-D rotating line-scan system have been identified;
- co-ordinate analysis from two-dimensional line-scan images has been successfully undertaken.

Therefore, from an analysis of a stereoscopic arrangement of rotating line-scan sensors the extraction of three-dimensional co-ordinate information from an object space surrounding the camera arrangement may be successfully achieved. The following chapter provides the theoretical analysis necessary to allow the characteristics of a stereoscopic system to be established and demonstrate the potential for extraction of 3-D co-ordinate information from such an arrangement.

4. ANALYSIS OF A ROTATING STEREOSCOPIC LINE-SCAN SYSTEM

4.1 Introduction

The primary aim of this research is to characterise rotating stereoscopic line-scan systems. A method selected for identification of the attributes associated with a rotating line-scan system is to investigate the measurement capability of such an arrangement.

This chapter presents a theoretical analysis of a rotating three-dimensional (3-D) line-scan camera arrangement. Algorithms which govern co-ordinate measurement will be derived allowing conversion from camera image space, in pixels, to object space co-ordinate information, represented in mm of object space.

4.2 The Potential Stereoscopic Region

The principle of stereoscopy may be applied to the development of algorithms for the extraction of co-ordinate information from the 3-D line-scan arrangement. A brief discussion of the fundamental aspects concerned with stereoscopic imaging was given in Section 2.2. This chapter will detail the application of stereoscopic vision techniques to the development of a mathematical model for a rotating line-scan system.

Initially, a stereoscopic volume must be produced to allow for the potential extraction of 3-D co-ordinate information from object space (Figure 4-1). The two overlapping fields of view (FOV) of a line-scan camera system define the stereoscopic region in object space. The stereoscopic region results *only* after rotation of the 3-D camera arrangement with respect to a static scene or object of interest has taken place.

Consider a point of interest in object space located within the stereoscopic field of view of the camera arrangement. To obtain range information for this point a *disparity* value must be identified from image space. For any point of interest located within the stereoscopic region a disparity value can be resolved. It is the fundamental relationship between disparity and range that allows co-ordinate measurement algorithms to be derived for use with the rotating line-scan system.

S - Start point of image capture
F - Finish point of image capture
l - Left line-scan sensor
r - Right line-scan sensor
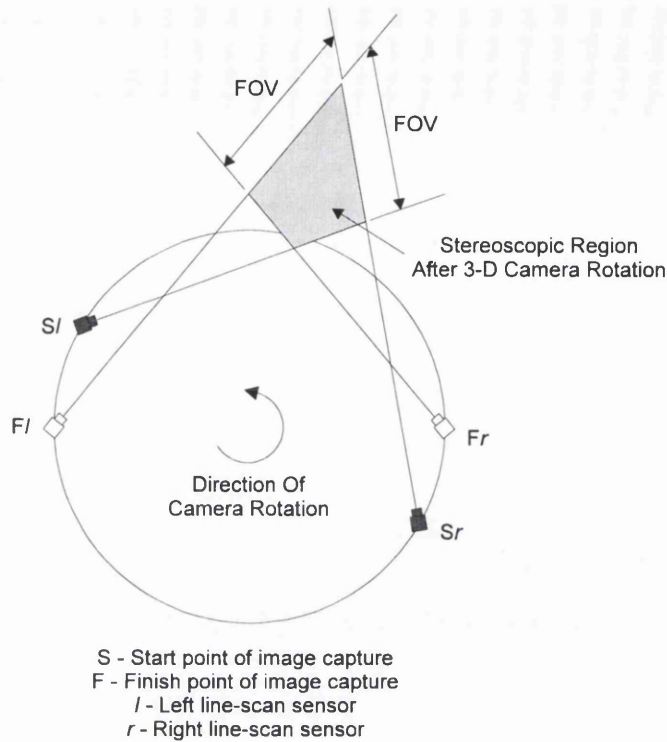
Figure 4-1 Stereoscopic Region Produced *after* Line-scan Camera Rotation

4.3 Image Production Parameters

The derivation of the algorithms which allow the extraction of co-ordinate data from object space incorporate the parameters which control the nature of image production for the stereoscopic line-scan arrangement. These parameters are as follows :

- camera-to-camera base width (B);

- camera-to-base width convergence angle (θc);

- camera scan rate (F_{SR});

- rotational displacement speed of the rotating platform (S_R);

- camera-lens focal length (f).

The following section outlines the procedure for converting from image space pixels to object space co-ordinates for the rotating line-scan system. A definition of the symbols used in the derivation of the 3-D algorithms is given in Appendix C.

4.4 Image Space to Object Space Conversion

A calibration frame is positioned within the defined stereoscopic region to allow comparison of co-ordinate information derived from image space with equivalent object space data. The calibration frame used in this research contains a distribution of targets for which the relative X, Y and Z co-ordinate locations are known to a defined degree of accuracy. The calibration frame used for this work is discussed in Chapter 5.0.

The calibration frame is defined by a cartesian co-ordinate reference system, otherwise known as a rectangular co-ordinate system [120], thus, information resolved from image space is formatted in the same way to allow comparison of calculated and known object space co-ordinate values. This is achieved by using the image space data in conjunction with the system geometry to produce a cylindrical model representation. The cartesian convention is obtained from this by applying cylindrical-to-cartesian co-ordinate transformation equations [121].
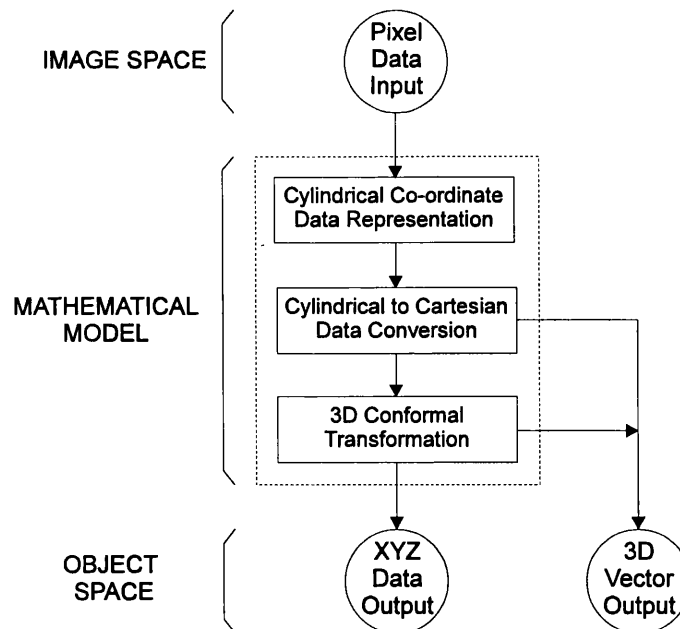
Figure 4-2 The Mathematical Model

The flowchart shown in Figure 4-2 summarises the conversion from camera image space to equivalent object space co-ordinate information. In the following sections the derivation of the algorithms relating to the mathematical model are presented.

4.5 Cylindrical Co-ordinate Data Representation

To format the image space information in cartesian form the stereoscopic arrangement and surrounding object space is initially modelled on a cylindrical co-ordinate reference system.

4.5.1 Cylindrical Representation in the X-Z Plane

Consider the area surrounding the centre of the stereoscopic camera rotation (Figure 4-3). The object space consists of a series of imaginary concentric circles in the X-Z plane.
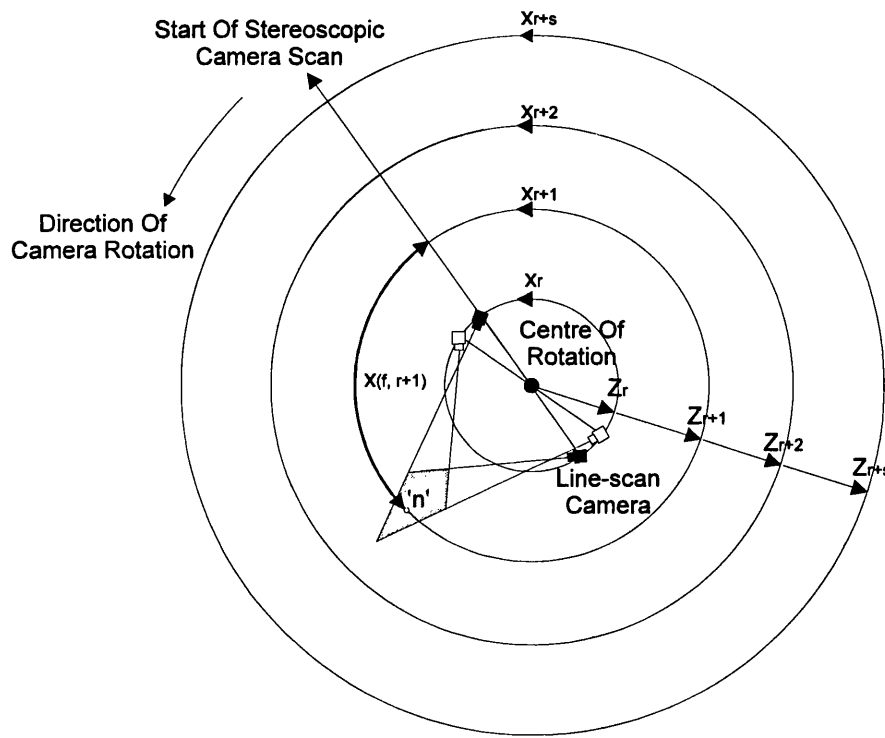
Figure 4-3 Cylindrical Co-ordinate Representation in the X-Z Plane

The X-axis is defined as being coincident with the circumference of each concentric circle and the Z-axis is positioned along adjacent ring elements. Therefore, for a point of interest 'n' situated in the stereoscopic region the general co-ordinate location may be defined as $(X_{(f,r+1)}, Z_{(r+1)})$ in the X-Z plane. Where, $X_{(f, r+1)}$ is the point location on the circumference of the $(r+1)$ circle as a function of the start of the camera rotation and $Z_{(r+1)}$ is the radial distance from the centre of rotation to the $(r+1)$ concentric ring element.

4.5.2 Three-Dimensional Cylindrical Representation

Consideration of the Y-axis in conjunction with the X-Z plane results in a 3-D cylindrical representation of the stereoscopic camera system and surrounding object space (Figure 4-4). The Y-axis consists of a series of concentric circles which can be grouped into cylinders. For each increment of radial distance from the centre of rotation the Y-axis is represented by a unique range cylinder. From Figure 4-4, it can be stated that :

- δX is an element of the circumference for the concentric ring of interest which is dependent on the object space resolution in the movement axis;

- δY is the distance between adjacent concentric rings for each range cylinder which is dependent on the resolution of the linear array sensor in the Y-axis,

- δZ is the distance between concentric range cylinders which is dependent on the object space resolution in the movement axis.
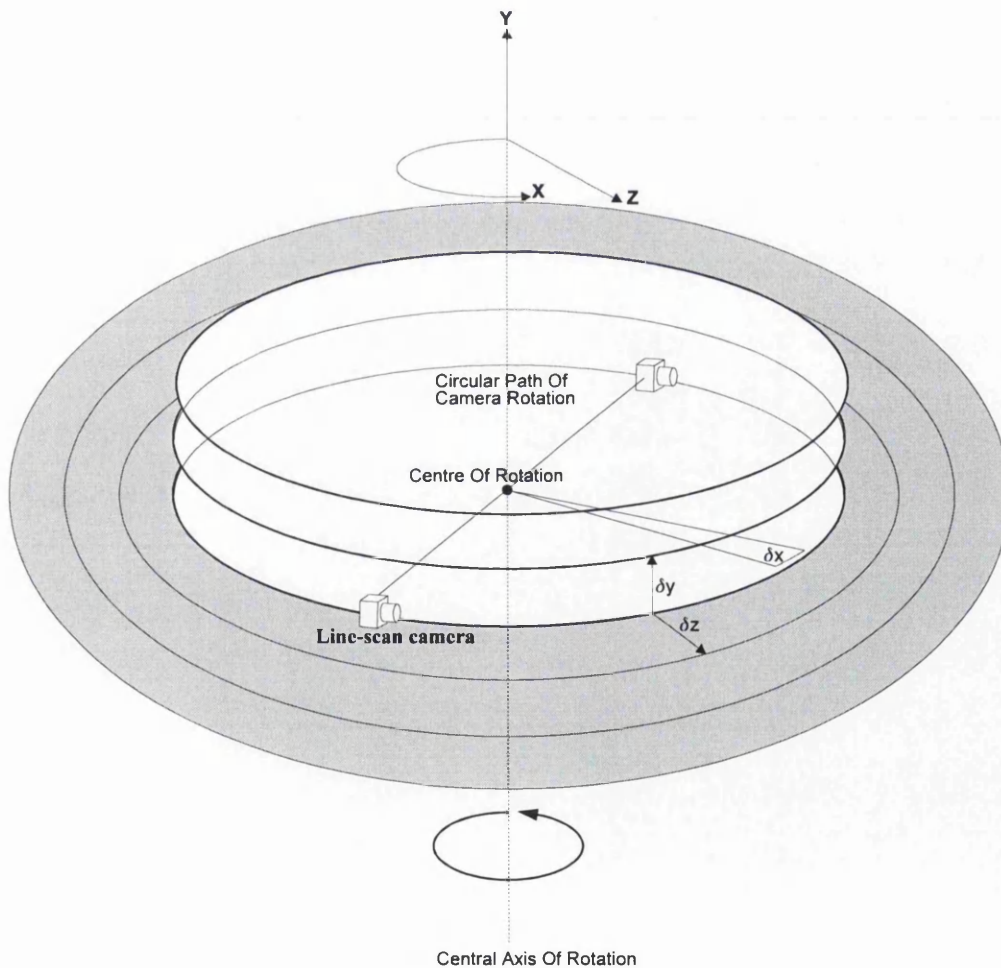
Figure 4-4 3-D Cylindrical Co-ordinate Representation

The mathematical analysis of the cylindrical model is now presented.

4.5.3 Analysis of the Cylindrical Model

A general cylindrical co-ordinate model is shown in Figure 4-5 where the model origin is equivalent to the centre of the stereoscopic rotation. A point in the stereoscopic region of object space, 'n', may be represented in cartesian form by X, Y and Z. The equivalent cylindrical parameters inferred from the stereoscopic camera arrangement are Z_n, Y_n and Θ_n.

Where,

Z_n $\equiv$ 'line-of-sight' distance from the centre of the rotational stage to a point, 'n', of interest in cylindrical object space, in mm;

Y_n $\equiv$ Y co-ordinate of a point 'n' in cylindrical object space, in mm;

Θ_n $\equiv$ rotation angle from a fixed reference point (the start point of camera scan) to a point, 'n', of interest in cylindrical object space, in degrees.

The camera system parameters with relation to this cylindrical model are derived in Section 4.6.
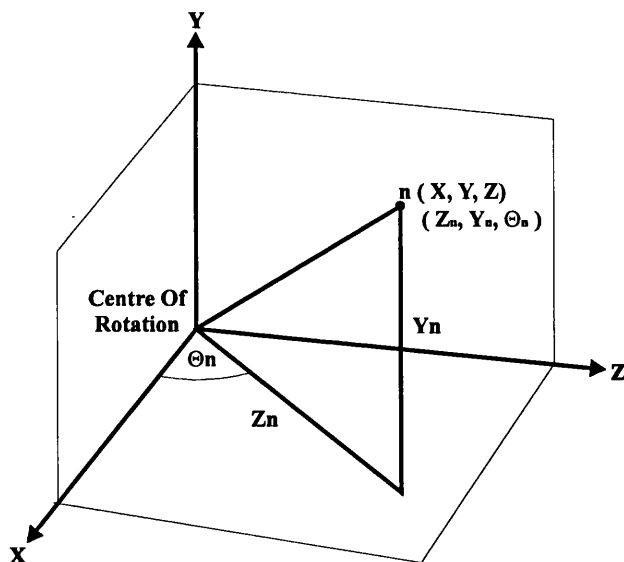
Figure 4-5 General Cylindrical Co-ordinate Model

From Figure 4-5 the cylindrical-to-cartesian co-ordinate transformation equations are:-

$$X = Z_n \cos \Theta_n \hspace{4cm} \text{Equation 4-1}$$

$$Y = Y_n \hspace{4.8cm} \text{Equation 4-2}$$

$$Z = Z_n \sin \Theta_n \hspace{4cm} \text{Equation 4-3}$$

Where,

X	≡	X co-ordinate of a point 'n' in cartesian object space, in mm;
Y	≡	Y co-ordinate of a point 'n' in cartesian object space, in mm;
Z	≡	Z co-ordinate of a point 'n' in cartesian object space, in mm.

For a point of interest, 'n', once the cylindrical parameters for the stereoscopic camera arrangement are derived the cartesian equivalent can be calculated.

4.6 Cylindrical Parameters

This section presents the derivation of the camera system parameters Z_n, Y_n and Θ_n.
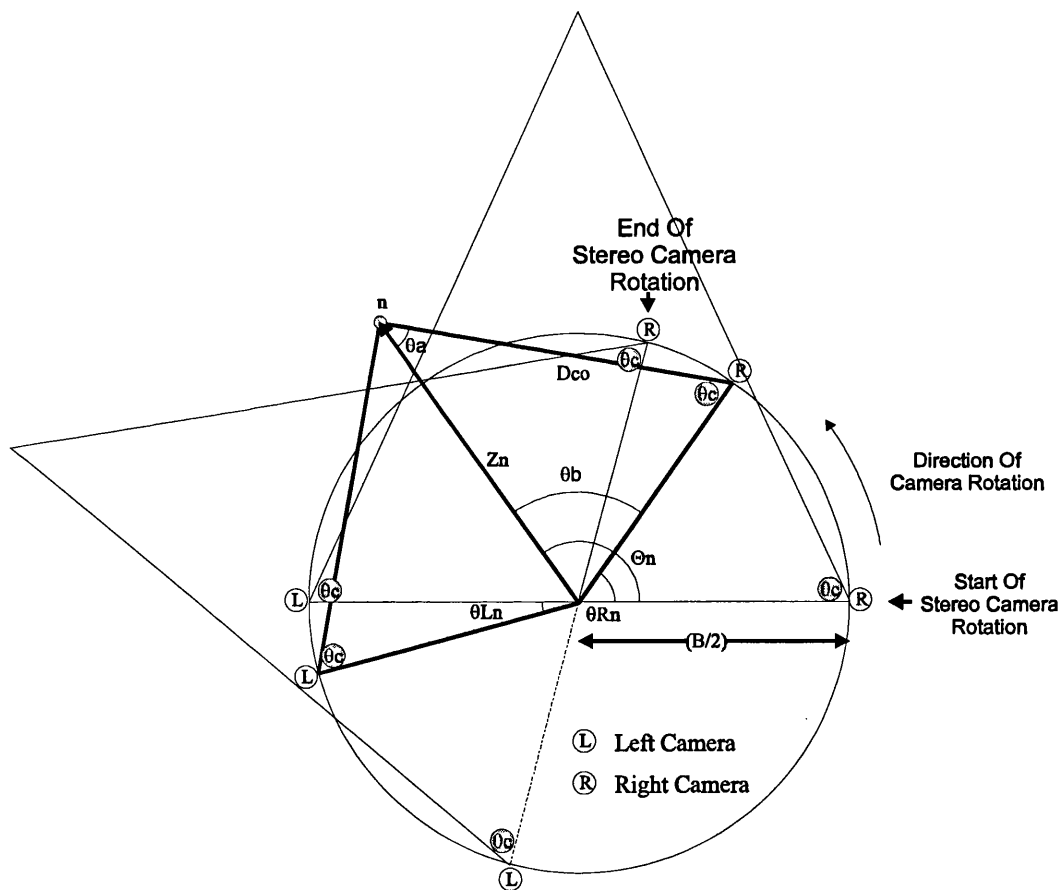
Figure 4-6 Derivation of Camera Model Parameters

From Figure 4-6, θ_{Ln} and θ_{Rn} depict the respective rotation angles of the left and right cameras necessary to view a point of interest, 'n', in object space. These rotation angles are derived from the left and right image space x-pixel distances and k_x is the pixel-to-angle conversion factor. Refer to Section 3.3.5 for the derivation of the pixel-to-angle conversion factor.

4.6.1 Z_n Derivation

From Figure 4-6, using the sine rule, Z_n can be expressed as follows :-

$$Z_n = \frac{B \sin\theta_c}{2 \sin\theta_a}$$

Equation 4-4

Where,

Z_n ≡ 'line-of-sight' distance from the centre of the rotational stage to a point, 'n', of interest in cylindrical object space, in mm;

θ_c ≡ camera to base width convergence angle, in degrees;

B ≡ camera to camera base width distance, in mm.

θ_a is given by the following :-

$$2\theta_a = 360 - 2\theta_c - (180 - \theta_{Rn} + \theta_{Ln})$$

$$\therefore \theta_a = 90 - \theta_c - \left(\frac{\theta_{Ln} - \theta_{Rn}}{2}\right)$$

Equation 4-5

Where,

θ_{Ln} ≡ rotation angle necessary to view a point of interest 'n' for the left camera, with respect to the image start point, in degrees,

θ_{Rn} ≡ rotation angle necessary to view a point of interest 'n' for the right camera, with respect to the image start point, in degrees.

Substituting θ_a from Equation 4-5 into Equation 4-4 gives :-

$$Z_n = \frac{B \sin\theta_c}{2 \cos\left(\theta_c + \left(\frac{\theta_{Ln} - \theta_{Rn}}{2}\right)\right)}$$

Equation 4-6

Where the term $(\theta_{Ln} - \theta_{Rn})$ is the angular disparity for a point of interest 'n' in object space. To produce an expression for Zn in terms of the left and right x-pixel distances obtained from image space the angles of left and right camera rotation are substituted for as follows :-

$$\theta_{Ln} = k_x x_{Ln}$$

Equation 4-7

$$\theta_{Rn} = k_x x_{Rn}$$

Equation 4-8

Where,

x_{Ln} ≡ x-axis pixel distance to the point of interest 'n' obtained from left image space, with respect to the start of image capture;

x_{Rn} ≡ x-axis pixel distance to the point of interest 'n' obtained from right image space, with respect to the start of image capture;

k_x ≡ the x-pixel distance-to-rotation angle conversion factor.

Substituting for θ_{Ln} and θ_{Rn} from Equation 4-7 and Equation 4-8 respectively into Equation 4-6 results in Z_n, expressed as a function of x-pixel distances obtained from image space :-

$$Z_n = \frac{B \sin\theta_c}{2 \cos\left(\theta_c + \left(k_x\left(\frac{x_{Ln} - x_{Rn}}{2}\right)\right)\right)}$$

Equation 4-9

Where the term (x_{Ln}-x_{Rn}) is the disparity value for a point of interest 'n' in object space expressed as a x-pixel value obtained from the perspective images.

4.6.2 Y_n Derivation

The axis of the line-scan image along the line of the sensor, otherwise referred to as the Y-axis, can be modelled on the principle of the pin-hole camera, as shown in Figure 4-7. As such the derivation for Y_n is based on the following equation :-

$$Y_n = \frac{SL D_{co}(y_p - y_n)}{f}$$

Equation 4-10

Where,

Y_n ≡ Y co-ordinate of a point 'n' in cylindrical object space, in mm;

D_{co} ≡ camera-to-object distance at the instant of image capture, in mm;

y_n ≡ Y co-ordinate of a point 'n' derived from image space, in pixels,

SL ≡ sensing *element length*, in mm;

f ≡ camera lens focal length, in mm;

y_p ≡ the pixel through which the optical axis of the lens pierces the sensor.
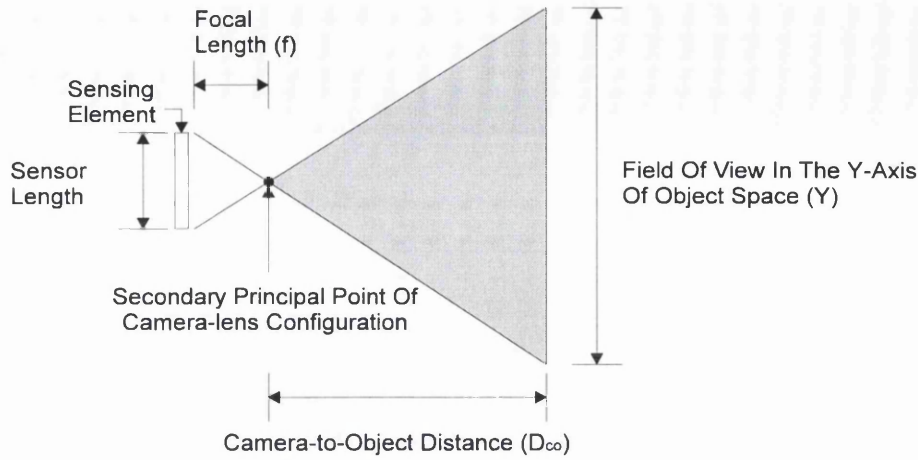
Figure 4-7 Y-axis field of view (side elevation)

To obtain Y_n for the stereoscopic line-scan arrangement the camera-to-object distance at the instant of image capture must be derived. Referring to Figure 4-6 and using the sine rule :

$$D_{co} = \frac{Z_n \sin \theta_b}{\sin \theta_c}$$

Equation 4-11

From Figure 4-6, θ_b is given by the expression :-

$$\theta_b = 180 - \theta_a - \theta_c$$

Equation 4-12

Substituting θ_a from Equation 4-5 into Equation 4-12 results in the expression for θ_b :-

$$\theta_b = 90 + \left(\frac{\theta_{Ln} - \theta_{Rn}}{2} \right)$$

Equation 4-13

Substituting θ_b (Equation 4-13) into Equation 4-11 results in the expression for D_{CO} :-

$$D_{co} = \frac{Z_n \sin \left(90 + \left(\frac{\theta_{Ln} - \theta_{Rn}}{2} \right) \right)}{\sin \theta_c}$$

Equation 4-14

Expanding Equation 4-14 to include Z_n (from Equation 4-6) gives :-

$$D_{co} = \frac{B\cos\left(-\left(\frac{\theta_{Ln} - \theta_{Rn}}{2}\right)\right)}{2\cos\left(\theta_c + \left(\frac{\theta_{Ln} - \theta_{Rn}}{2}\right)\right)}$$

Equation 4-15

Substituting the camera rotation angles (Equation 4-15) for the expressions in Equation 4-7 and Equation 4-8, the camera-to-object distance in terms of left and right x image distances is :

$$D_{co} = \frac{B\cos\left(-k_x\left(\frac{x_{Ln} - x_{Rn}}{2}\right)\right)}{2\cos\left(\theta_c + \left(k_x\left(\frac{x_{Ln} - x_{Rn}}{2}\right)\right)\right)}$$

Equation 4-16

Substituting the expression for D_{co} from Equation 4-16 into Equation 4-10 results in the expression for Y_n :-

$$Y_n = \frac{B(y_p - y_n)SL}{2f} \cdot \frac{\cos\left(-k_x\left(\frac{x_{Ln} - x_{Rn}}{2}\right)\right)}{\cos\left(\theta_c + \left(k_x\left(\frac{x_{Ln} - x_{Rn}}{2}\right)\right)\right)}$$

Equation 4-17

4.6.3 Θ_n Derivation

From Figure 4-6 the reference angle for a point of interest, Θn, can be expressed as :-

$$\Theta_n = \theta_{Rn} + \theta_b$$

Equation 4-18

Substituting θ_b from Equation 4-13 and for the rotation angles given by Equation 4-7 and Equation 4-8 into Equation 4-18 results in the expression for the reference angle :-

$$\Theta_n = 90 + \frac{k_x x_{Rn}}{2} + \frac{k_x x_{Ln}}{2}$$

Equation 4-19

4.7 Cylindrical to Cartesian Co-ordinate Data Conversion

Substituting the expressions for Z_n, Y_n and Θ_n derived in Section 4.6 into the cylindrical-to-cartesian transformation equations given in Section 4.5.3 results in algorithms which relate image space to cartesian object space.

4.7.1 The X-axis Cartesian Algorithm

The algorithm which relates image space and cartesian object space distances in the X-axis is :

$$X = \frac{B\sin\theta_c \sin\left(k_x\left(\frac{-X_{Rn}-X_{Ln}}{2}\right)\right)}{2\cos\left(\theta_c + \left(k_x\left(\frac{X_{Ln}-X_{Rn}}{2}\right)\right)\right)}$$

Equation 4-20

4.7.2 The Y-axis Cartesian Algorithm

The algorithm which relates image space and cartesian object space distances in the Y-axis is:

$$Y = \frac{B(y_p - y_n)SL}{2f} \cdot \frac{\cos\left(-k_x\left(\frac{X_{Ln}-X_{Rn}}{2}\right)\right)}{\cos\left(\theta_c + \left(k_x\left(\frac{X_{Ln}-X_{Rn}}{2}\right)\right)\right)}$$

Equation 4-21

4.7.3 The Z-axis Cartesian Algorithm

The algorithm which relates image space and cartesian object space distances in the Z-axis is:

$$Z = \frac{B\sin\theta_c \cos\left(k_x\left(\frac{-X_{Rn}-X_{Ln}}{2}\right)\right)}{2\cos\left(\theta_c + \left(k_x\left(\frac{X_{Ln}-X_{Rn}}{2}\right)\right)\right)}$$

Equation 4-22

The following section details the application of a three-dimensional conformal transformation to the rotating line-scan system which aligns the camera system with the calibration frame and allows individual X, Y and Z co-ordinate components to be obtained from object space.

4.8 Application of A Three-dimensional Conformal Transformation

The 3-D conformal co-ordinate transformation, discussed in Section 2.3.4, is now applied to allow the extraction of individual X, Y and Z co-ordinate information. The 3-D transformation aligns the centre of the stereoscopic camera rotation to the calibration volume (Figure 4-8) thus allowing co-ordinate data to be obtained from object space on completion of a calibration phase.

S - Start point of image capture
F - Finish point of image capture
I - Left line-scan sensor
r - Right line-scan sensor
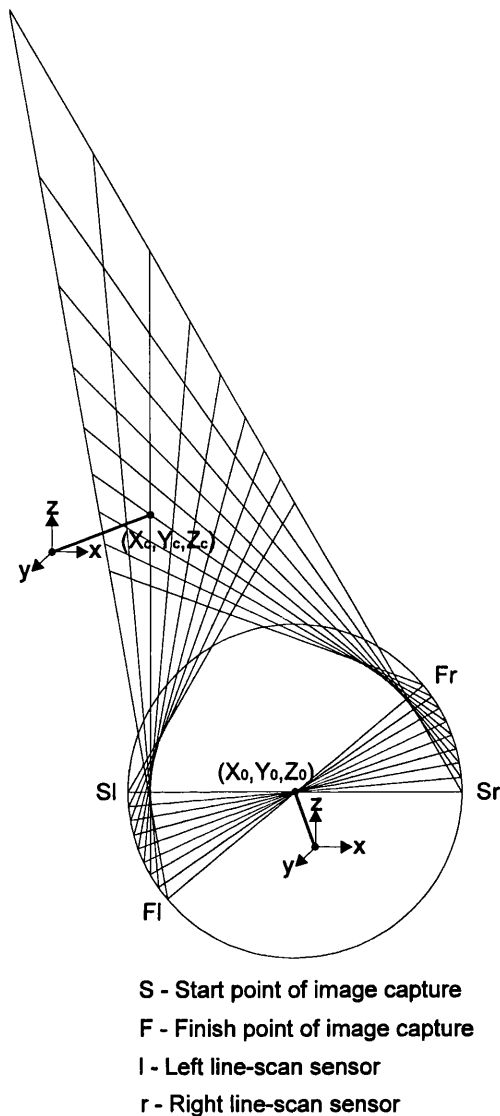
Figure 4-8 Camera to Calibration Volume Mathematical Alignment

The three-dimensional conformal co-ordinate transformation equations are developed in general by Wolf [96]. Applying the algorithms derived from Section 4.7 to these transformation equations results in a 3-D conformal transformation specifically for use with the stereoscopic line-scan system. Refer to Appendix D for the derivation of this transformation model.

The following sections present the analyses which allow an assessment of the stereoscopic volume structure to be made. In Section 4.9 algorithms are derived which allow the boundary of the stereoscopic volume in each co-ordinate axis to be calculated for a given camera arrangement. Following this, in Section 4.10, algorithms are derived which allow the size of individual voxels within the stereoscopic volume to be determined.

4.9 Calculating the Boundary of the Stereoscopic Volume

This section describes the mathematical analysis which enables the calculation of the stereoscopic volume boundary for the line-scan system. This allows the coverage of the stereoscopic volume in the X-, Y- and Z-axes to be calculated with reference to the centre of rotation and the start base line (illustrated as *Sl-Sr* in Figure 4-9) of the 3-D camera scan.

Zmax (Z₂,X₄)

Stereoscopic Region
In The X-Z Plane
After Camera Rotation

Xmin (X₁,Z₃)

Xmax (X₂,Z₄)

Zmin (Z₁,X₃)

Z₂   Z₄   Z₁   Z₃(X₁=0)

Fr

Direction
Of Camera
Rotation

X₄   X₂   X₃   Sr

Sl   Centre Of
Rotation
(Xo,Zo)

Fl

S - Start point of image capture
F - Finish point of image capture
l - Left line-scan sensor
r - Right line-scan sensor
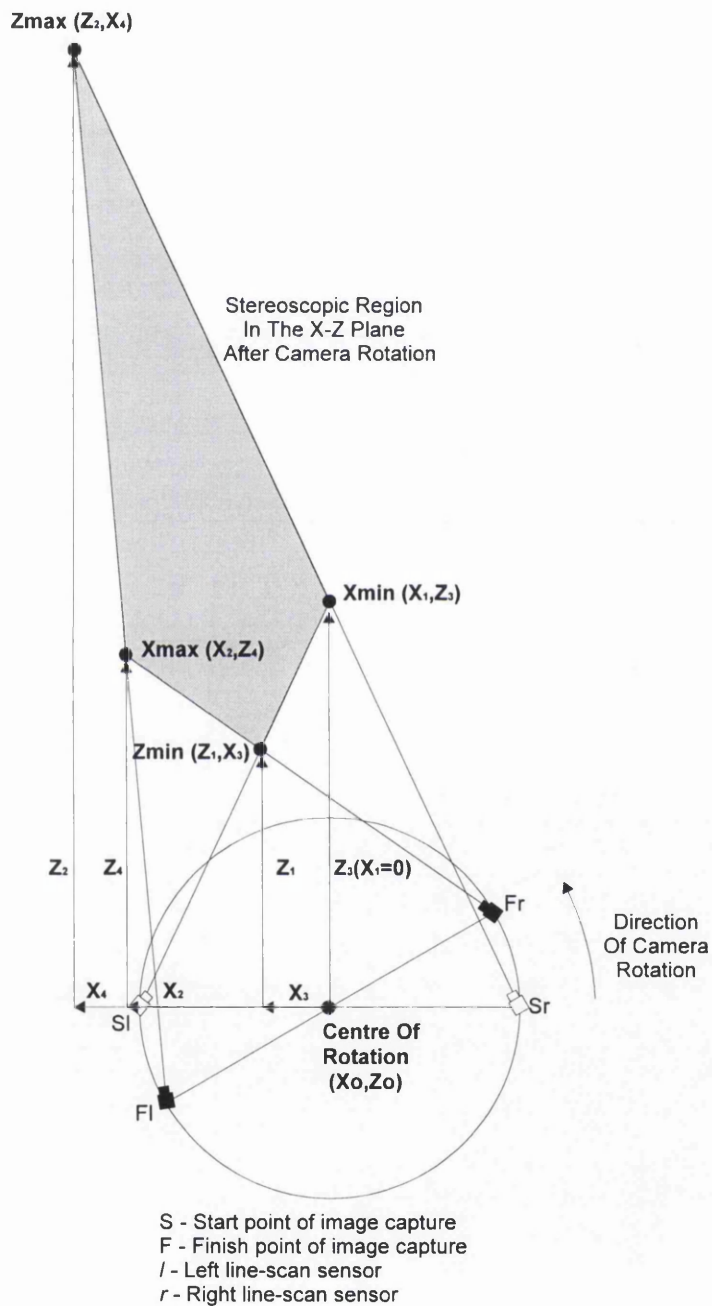
Figure 4-9 Stereoscopic Perimeter in the X-Z plane

4.9.1 Stereoscopic Perimeter in the X-Z Plane

Consider Figure 4-9, the stereoscopic perimeter in the *X-Z* plane may be circumscribed by the four co-ordinate point locations defined as X_{min}, X_{max}, Z_{min} and Z_{max}. The point locations are calculated with reference to the centre of the camera rotation (X_o, Z_o).

Calculation of X_{min} :

X_{min} has the co-ordinates (X_1, Z_3) and exists when the camera rotation angles are equal to zero. As the rotation angles are equal to zero the associated left and right x-pixel distances are also equal to zero. Therefore from Equation 4-20, X_1 is :-

$$X_1 = 0 \qquad\qquad \text{Equation 4-23}$$

From Equation 4-22 Z_3 is given by :-

$$Z_3 = \frac{B\sin\theta c}{2\cos\theta c} \qquad\qquad \text{Equation 4-24}$$

Calculation of X_{max} :

X_{max} has the co-ordinates (X_2, Z_4) and exists when the camera rotation angles are at a maximum for a given stereoscopic arrangement. The rotation angle maximum occurs when the left and right pixel values are at a maximum. For the framestore used in this research programme the maximum value for the left and right image space x-pixel distances is 1023. Therefore, from Equation 4-20, X_2 can be expressed by:-

$$X_2 = \frac{B\sin\theta c \sin(-1023 k_x)}{2\cos\theta c} \qquad\qquad \text{Equation 4-25}$$

From Equation 4-22 Z_4 is given by :-

$$Z_4 = \frac{B\sin\theta c \cos(-1023 k_x)}{2\cos\theta c} \qquad\qquad \text{Equation 4-26}$$

Calculation of Z_{min} :

Z_{min} has the co-ordinates (Z_1, X_3) as shown in Figure 4-9 and exists when the left camera rotation angle is zero and the right camera rotation angle is at a maximum. This results in a left x-pixel value of zero and a right x-pixel value of 1023. Therefore, from Equation 4-20 the expression for X_3 is :-

$$X_3 = \frac{B \sin \theta c \sin(-511.5k_x)}{2 \cos(\theta c - 511.5k_x)}$$

Equation 4-27

From Equation 4-22 the equation for Z_1 is :-

$$Z_1 = \frac{B \sin \theta c \cos(-511.5k_x)}{2 \cos(\theta c - 511.5k_x)}$$

Equation 4-28

Calculation of Z_{max} :

Z_{max} has the co-ordinates (Z_2, X_4) and exists when the left camera rotation angle is at a maximum and the right camera rotation angle is zero. Thus, the left x-pixel value is 1023 and the right x-pixel value is zero which results in an expression for X_4 as derived from Equation 4-20 :-

$$X_4 = \frac{B \sin \theta c \sin(-511.5k_x)}{2 \cos(\theta c + 511.5k_x)}$$

Equation 4-29

From Equation 4-22, Z_2 is expressed as :-

$$Z_2 = \frac{B \sin \theta c \cos(-511.5k_x)}{2 \cos(\theta c + 511.5k_x)}$$

Equation 4-30

4.9.2 Field of View in the Y-axis

The size of the field of view in the Y-axis varies as a function of the camera-to-object distance at the instant of image capture. Therefore, from Figure 4-10, the field of view in the Y-axis

increases as a function of the range from the secondary principal point of the camera lens. For the purpose of this analysis the field of view in the Y-axis is considered at X_{min}, X_{max}, Z_{min} and Z_{max} as calculated previously in Section 4.9.1.
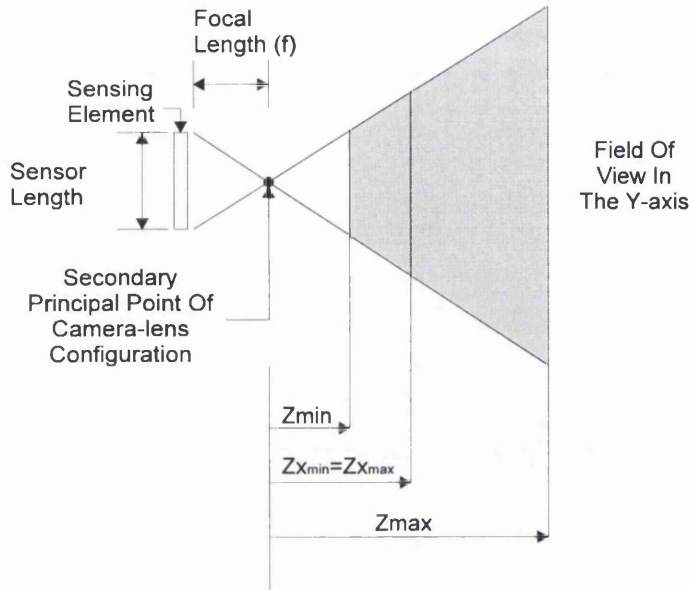
Figure 4-10 Field of View in the Y-axis

The following derives the algorithms relating to the Y-axis field of view at X_{min} (and, therefore, X_{max}), Z_{min} and Z_{max} (Figure 4-10). When calculating the extent of the field of view in the Y-axis this is dependent on the sensor resolution. For the purpose of this research the linear array sensor consists of 1024 pixel elements in the Y-axis which is represented by 0 - 1023 pixels in image space. Therefore 1023 is substituted into Equation 4-21 for $(y_p - y_n)$ to calculate the object space FOV at the defined camera-to-object distances.

Calculation of Y_{xmin} :

X_{min} has the co-ordinates (X_1, Z_3) and exists when the camera rotation angles are equal to zero. Therefore, from Equation 4-21 the FOV in the Y-axis of object space at X_{min} is given by :-

$$Y_{x\,min} = \frac{511.5\ B\ SL}{f\ \cos\theta c}$$ Equation 4-31

Calculation of Y_{xmax} :

X_{max} has the co-ordinates (X_2, Z_4) and exists when the camera rotation angles are at a maximum for the stereoscopic arrangement. Therefore, from Equation 4-21 the following results for Y_{xmax}:-

$$Y_{x\,max} = \frac{511.5\ B\ SL}{f\cos\theta c}$$

Equation 4-32

When calculating the (X,Z) co-ordinates for both X_{min} and X_{max} in Section 4.9.1 the Z co-ordinate components are different. This arises as the Z co-ordinate is referenced from the baseline of the start of camera scan. When calculating the field of view in the Y-axis the range components for X_{min} and X_{max} are equal as they are dependent on the secondary principal point to object distance.

Calculation of Y_{zmin} :

Z_{min} has the co-ordinates (Z_1, X_3) and exists when the left camera rotation angle is zero and the right camera rotation angle is at a maximum. Therefore, from Equation 4-21 the following expression results :-

$$Y_{z\,min} = \frac{511.5\ B\ SL}{f}\cdot\frac{\cos(511.5k_x)}{\cos(\theta c - (511.5k_x))}$$

Equation 4-33

Calculation of Y_{zmax} :

Z_{max} has the co-ordinates (Z_2, X_4) and exists when the left camera rotation angle is at a maximum and the right camera rotation angle is zero. Therefore, the left x-pixel value is 1023 pixels and the right x-pixel value is zero giving the following from Equation 4-21 :-

$$Y_{z\,max} = \frac{511.5\ B\ SL}{f}\cdot\frac{\cos(-511.5k_x)}{\cos(\theta c + (511.5k_x))}$$

Equation 4-34

4.9.3 Determination of Znear, Zfar and the Convergence Radius

In Section 4.9.1 the boundary of the stereoscopic volume in the X-Z plane is calculated in terms of four co-ordinate point locations. For a given experimental arrangement Z_{near}, Z_{far} and Z_{con} may also be evaluated, as illustrated in Figure 4-11.

Zfar

Stereoscopic Region
In The X-Z Plane
After Camera Rotation

Zcon

Znear

Fr

Direction
Of Camera
Rotation

Sl

Centre Of
Rotation

Sr

Fl

S - Start point of image capture
F - Finish point of image capture
l - Left line-scan sensor
r - Right line-scan sensor
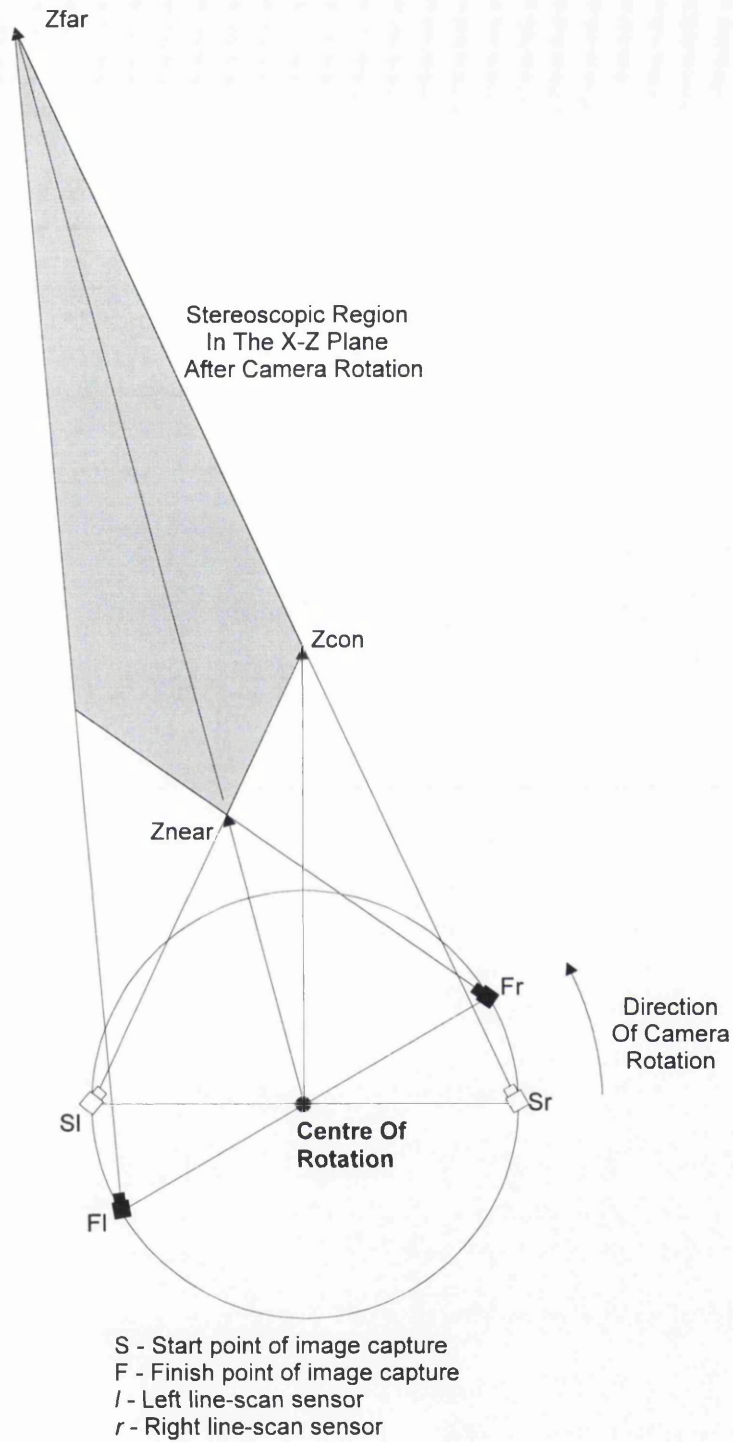
Figure 4-11 The Extent of the Stereoscopic Region

Where,

Z_{near} ≡ 'line-of-sight' distance from the centre of the rotational stage to the near

point of the stereoscopic region, in cylindrical object space, in mm;

Z_{far} ≡ 'line-of-sight' distance from the centre of the rotational stage to the far

point of the stereoscopic region, in cylindrical object space, in mm;

Z_{con} ≡ 'line-of-sight' distance from the centre of the rotational stage to the convergence circumference, in cylindrical object space, in mm.

For any position in the arc of the camera rotation Z_{near}, Z_{far} and Z_{con} will remain constant for a fixed experimental arrangement.

From Figure 4-11 Z_{con} is given by the equation :-

$$Z_{con} = \frac{B\tan\theta_c}{2}$$
  Equation 4-35

Consider Figure 4-11, Z_{near} exists when the left camera rotation angle is zero and the right camera rotation angle is at a maximum. This corresponds to a left pixel value of zero and a right image space pixel value of 1023. Therefore, from Equation 4-9 the expression results :

$$Z_{near} = \frac{B\sin\theta_c}{2\cos(\theta_c - 511.5k_x)}$$
  Equation 4-36

From Figure 4-11 it is observed that Z_{far} exists when the left camera rotation angle is at a maximum and the right camera rotation angle is zero. This corresponds to a left pixel value of 1023 and a right image space pixel value of zero. Therefore, from Equation 4-9 the expression results :-

$$Z_{far} = \frac{B\sin\theta_c}{2\cos(\theta_c + 511.5k_x)}$$
  Equation 4-37

4.10 Theoretical Voxel Size Within the Stereoscopic Volume

This section presents the mathematical analysis which enables the resolution at any point location within the stereoscopic volume to be identified. This allows the size of a voxel in three-dimensional space to be assessed. Therefore, the measurement capability associated with a rotating stereoscopic line-scan system may be expressed as a function of the available

resolution in object space. Ultimately, this analysis will allow the suitability of the 3-D algorithms to an experimental system (refer to Chapter 5.0) to be determined.

The theoretical voxel size for a point location is expressed in terms of mm / pixel in all three co-ordinate axes.

S - Start point of image capture
F - Finish point of image capture
l - Left line-scan sensor
r - Right line-scan sensor
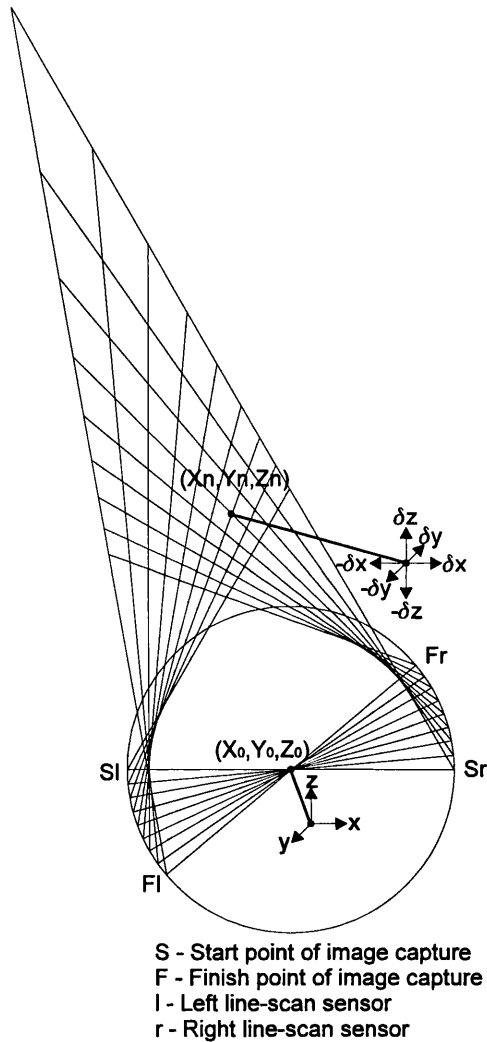
Figure 4-12 Calculation of Object Space Point Resolution / Voxel Size

From Figure 4-12, consider a point of interest 'n' at a co-ordinate location (X_n, Y_n, Z_n). For this point X, Y and Z are calculated using Equation 4-20, Equation 4-21 and Equation 4-22 respectively. To calculate the voxel size in object space surrounding this point it is necessary to theoretically translate the point in object space and then calculate the theoretical change in pixels. This then allows the size of the voxel surrounding the point of interest to be determined in mm / pixel.

For a point location 'n' the following outlines the steps undertaken to calculate the surrounding voxel size :

- for a known 'real' pixel location in image space, corresponding to a point in object space, the X, Y and Z co-ordinate positions are calculated;

- the point location in object space is translated theoretically by known distance increments in each co-ordinate axis. For this analysis each point location is theoretically translated about its original position in the X-axis by δx and $-\delta x$, in the Y-axis by δy and $-\delta y$ and in the Z-axis by δz and $-\delta z$;

- for each theoretical distance increment theoretical, or 'new', pixel locations are calculated;

- the theoretical object space translation is divided by the difference between the 'real' and calculated image space distances to obtain the voxel size, in mm / pixel, surrounding the point of interest.

The following sections present the mathematical analysis which enables the voxel size surrounding selected point locations within a defined stereoscopic region to be identified.

4.10.1 Calculation of Cartesian Voxel Dimensions in the X-axis

Consider a point 'n' located in the stereoscopic region for which the cartesian X co-ordinate location is known. From Figure 4-13 applying theoretical incremental changes of δx and $-\delta x$ results in the reference angles $\Theta_{\delta x}$ and $\Theta_{-\delta x}$ respectively. This section will present the analysis allowing the new pixel values to be calculated for theoretical point translations in the X-axis.
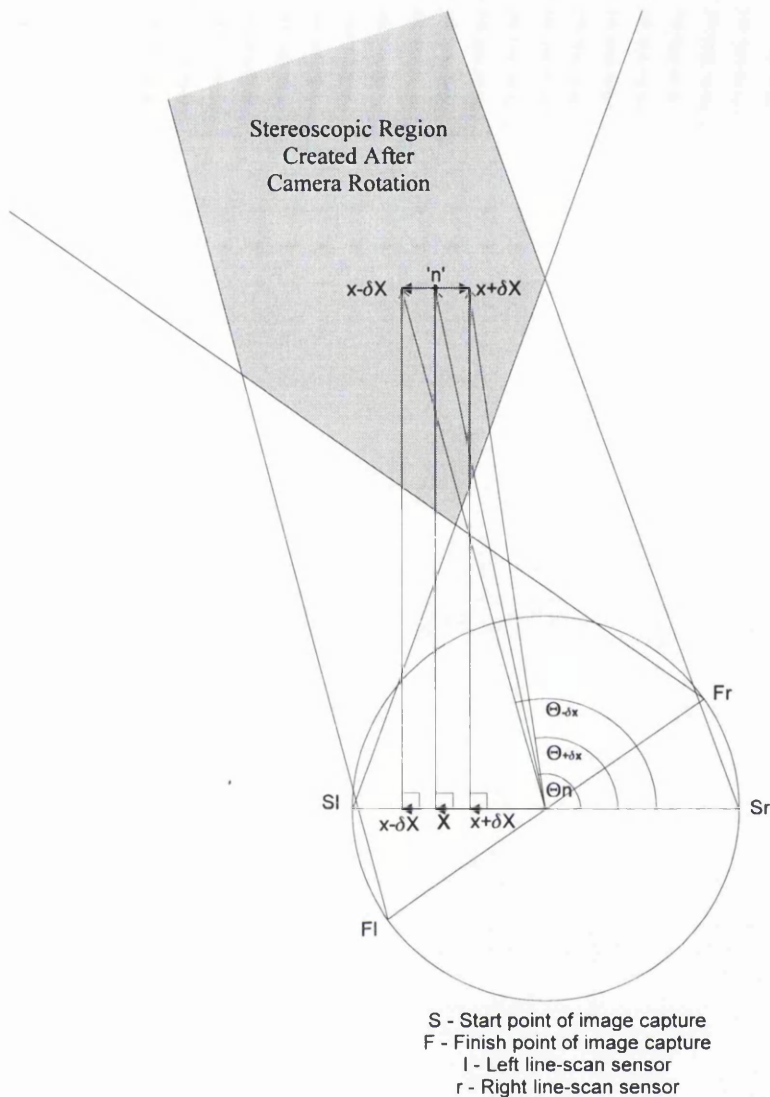
Figure 4-13 Incremental Change in X-axis Point Location

Calculation of theoretical pixel values for a point after a positive translation in the X-axis :

Consider the incremental change *(X+δx)*. Referring to Figure 4-14(a) and using the theorem of Pythagorus :

$$\tan(180 - \Theta_{\delta x}) = \left(\frac{|Z|}{|X + \delta x|} \right)$$

Therefore, the reference angle associated with the incremental change *(X+δx)* is :

$$\Theta_{\delta x} = 180 - \tan^{-1}\left(\frac{|Z|}{|X + \delta x|} \right) \qquad\qquad \text{Equation 4-38}$$
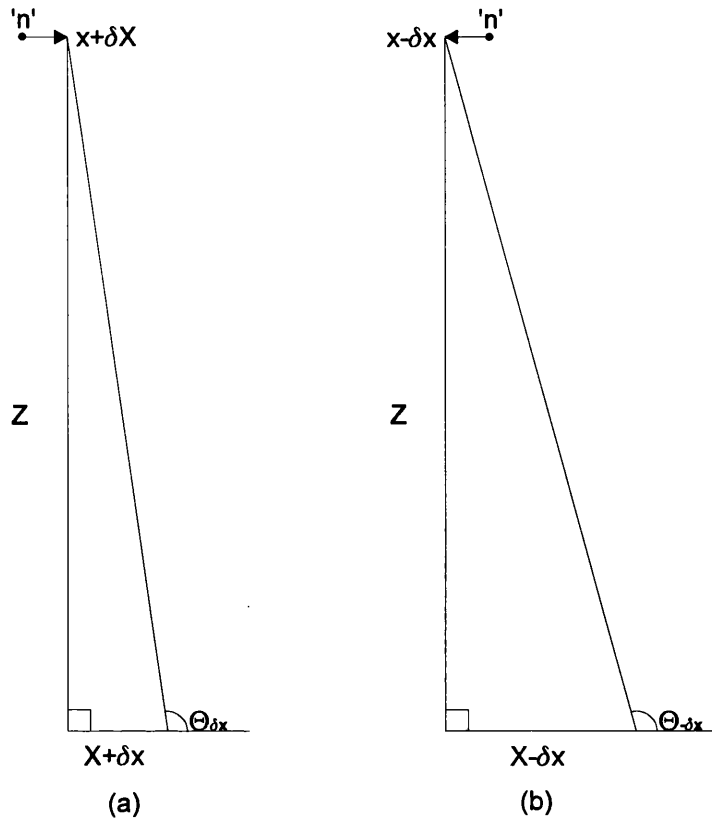
Figure 4-14 Calculation of Voxel Size in the X-axis of Object Space

The general expression for the reference angle, expressed in terms of left and right x-pixel image space distances given by Equation 4-19, is :

$$\Theta_n = 90 + \frac{k_x . x_{Rn}}{2} + \frac{k_x . x_{Ln}}{2}$$

The reference angle $\Theta_{\delta x}$ given by Equation 4-38 can now be equated to this general equation which is expressed in terms of the theoretical x-pixel distances obtained *after* the theoretical object space translation is applied to the original pixel location :

$$\Theta_{\delta x} = 180 - \tan^{-1}\left(\frac{|Z|}{|X + \delta x|}\right) = 90 + \frac{k_x\{x_R + x_L\}_{\delta x}}{2} \qquad \text{Equation 4-39}$$

The theoretical x-pixel image space distances for the incremental change *(x+δx)* is therefore :

$$\{x_R + x_L\}_{\delta x} = \frac{2}{k_x}\left(90 - \tan^{-1}\left(\frac{|Z|}{|X+\delta x|}\right)\right)$$

Rearranging the expression above gives :

$$\{-x_R - x_L\}_{\delta x} = -\frac{2}{k_x}\left(90 - \tan^{-1}\left(\frac{|Z|}{|X+\delta x|}\right)\right)$$

<div align="right">Equation 4-40</div>

Now consider the X-axis algorithm, from Equation 4-20 :

$$X = \frac{B\sin\theta c \sin\left(k_x\left(\frac{-x_{Rn} - x_{Ln}}{2}\right)\right)}{2\cos\left(\theta c + \left(k_x\left(\frac{x_{Ln} - x_{Rn}}{2}\right)\right)\right)}$$

Substituting Equation 4-40 into Equation 4-20 results in the following expression for the incremental translation *(X+δx)* :

$$X + \delta x = \frac{B\sin\theta c \sin\left(\tan^{-1}\left(\frac{|Z|}{|X+\delta x|}\right) - 90\right)}{2\cos\left(\theta c + \left(k_x\left(\frac{\{x_L - x_R\}_{\delta x}}{2}\right)\right)\right)}$$

<div align="right">Equation 4-41</div>

Where;

X ≡ the X-axis object space co-ordinate associated with the 'real' point in image space;

Z ≡ the Z-axis object space co-ordinate associated with the 'real' point in image space;

δx ≡ the theoretical translation in the positive direction of object space applied to the original object space co-ordinate;

$\{x_L\text{-}x_R\}$ ≡ the theoretical disparity value associated with the point of interest after the translation in the X-axis is applied.

Equation 4-41 can be re-arranged to give an expression in terms of the theoretical disparity value $\{x_L - x_R\}$:

$$\{x_L - x_R\}_{\delta x} = \frac{2}{k_x}\left(\cos^{-1}\left(\frac{B\sin\theta c\sin\left(\tan^{-1}\left(\frac{|Z|}{|X+\delta x|}\right)-90\right)}{2.(X+\delta x)}\right)-\theta c\right)$$ Equation 4-42

To establish the individual pixel values, $\{x_L\}_{\delta x}$ and $\{x_R\}_{\delta x}$ Equation 4-40 and Equation 4-42 are used to form a pair of simultaneous equations. The left x-pixel value for the theoretical translation $(X+\delta x)$ is :

$$\{x_L\}_{\delta x} = \frac{1}{k_x}\left(\left(\cos^{-1}\left(\frac{B\sin\theta c\sin\left(\tan^{-1}\left(\frac{|Z|}{|X+\delta x|}\right)-90\right)}{2(X+\delta x)}\right)-\theta c\right)+\left(90-\tan^{-1}\left(\frac{|Z|}{|X+\delta x|}\right)\right)\right)$$

Equation 4-43

Once $\{x_L\}_{\delta x}$ is obtained $\{x_R\}_{\delta x}$ can be calculated by substituting Equation 4-43 into Equation 4-40 to give :

$$\{x_R\}_{\delta x} = \frac{1}{k_x}\left(-\left(\cos^{-1}\left(\frac{B\sin\theta c\sin\left(\tan^{-1}\left(\frac{|Z|}{|X+\delta x|}\right)-90\right)}{2(X+\delta x)}\right)-\theta c\right)+\left(90-\tan^{-1}\left(\frac{|Z|}{|X+\delta x|}\right)\right)\right)$$

Equation 4-44

Calculation of theoretical pixel values for a point after a negative translation in the X-axis :

Referring to Figure 4-13 and Figure 4-14(b), for a known translation $(X-\delta x)$ the algorithms relating to the calculation of the theoretical pixel values for $\{x_L\}_{-\delta x}$ and $\{x_R\}_{-\delta x}$ can be derived in a similar fashion, resulting in :-

$$\{x_L\}_{-\delta x} = \frac{1}{k_x}\left(\left(\left(\cos^{-1}\left(\frac{B\sin\theta c\sin\left(\tan^{-1}\left(\frac{|Z|}{|X-\delta x|}\right)-90\right)}{2(X-\delta x)}\right)\right)-\theta c\right)+\left(90-\tan^{-1}\left(\frac{|Z|}{|X-\delta x|}\right)\right)\right)$$

<div align="right">Equation 4-45</div>

$$\{x_R\}_{-\delta x} = \frac{1}{k_x}\left(\left(-\left(\cos^{-1}\left(\frac{B\sin\theta c\sin\left(\tan^{-1}\left(\frac{|Z|}{|X-\delta x|}\right)-90\right)}{2(X-\delta x)}\right)\right)-\theta c\right)+\left(90-\tan^{-1}\left(\frac{|Z|}{|X-\delta x|}\right)\right)\right)$$

<div align="right">Equation 4-46</div>

Calculation of the theoretical voxel size surrounding a point of interest in the X-axis :

For a point 'n' which is theoretically translated by $-\delta x$ and $+\delta x$ the new image space distances in the x-axis have been calculated. The theoretical number of x pixels associated with $-\delta x$ and $+\delta x$ can be calculated for *left* image space values (Equation 4-45 and Equation 4-43) and for *right* image space values (Equation 4-46 and Equation 4-44).

To obtain the theoretical voxel size in mm / pixel in object space the overall theoretical displacement $2\delta x$, represented in mm, is divided by the sum of the differences between the original pixel values x_{Ln} and x_{Rn} and the theoretical pixel values resulting from the displacements of $+\delta x$ and $-\delta x$.

The following equation gives the resolution surrounding a point 'n' in the X-axis of object space in terms of left image space values as calculated from Equation 4-43 and Equation 4-45 :-

$$XL_{vox} = \frac{2.\delta x}{\left|x_{Ln}-\{x_L\}_{-\delta x}\right|+\left|x_{Ln}-\{x_L\}_{\delta x}\right|}$$

<div align="right">Equation 4-47</div>

Where,

XL_{vox} $\equiv$ theoretical resolution surrounding a point 'n' in the X-axis of cartesian object space as inferred from left image space values, in mm / pixel.

The resolution in the X-axis of object space in terms of right image space values as calculated from Equation 4-44 and Equation 4-46 is :-

$$XR_{vox} = \frac{2.\delta x}{\left| x_{Rn} - \{x_R\}_{-\delta x} \right| + \left| x_{Rn} - \{x_R\}_{\delta x} \right|}$$

<div align="right">Equation 4-48</div>

Where,

     XR_{vox} ≡   theoretical resolution surrounding a point 'n' in the X-axis of cartesian object space as inferred from right image space values, in mm / pixel.

4.10.2 Calculation of Cartesian Voxel Dimensions in the Z-axis

Consider point 'n' located in the stereoscopic region for which the cartesian Z co-ordinate location is known. As shown in Figure 4-15 applying an incremental change of δz and $-\delta z$ results in the new reference angles $\Theta_{\delta z}$ and $\Theta_{-\delta z}$ respectively.
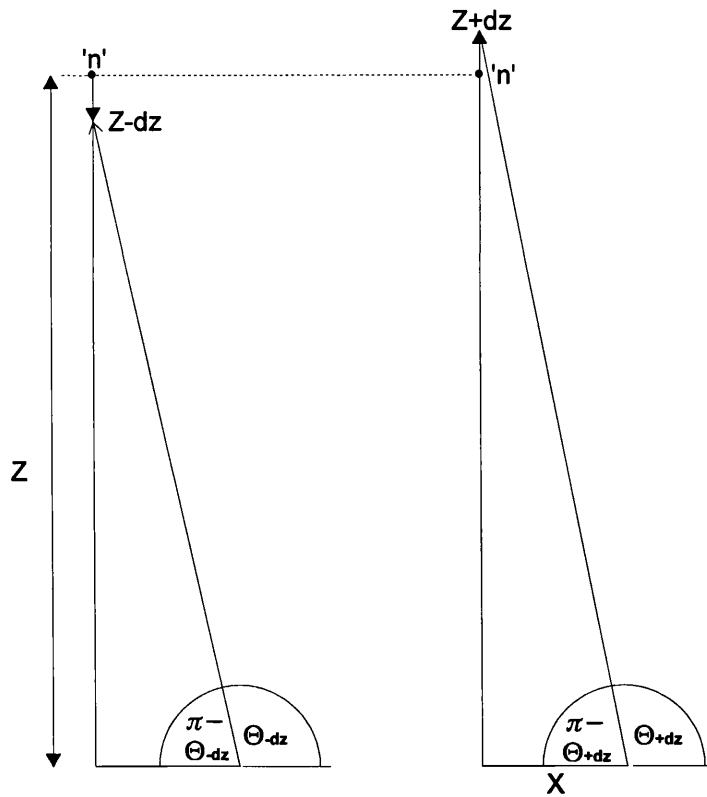
Figure 4-15 Calculation Of Voxel Size in the Z-axis

Referring to Figure 4-12 and Figure 4-15, for known theoretical translations of *(Z-δz)* and *(Z+δz)*, the algorithms enabling the calculation of the theoretical pixel values for {x_L} and {x_R} can be derived using a similar methodology to that used in the derivation of the X-axis resolution algorithms in Section 4.10.1.

The left x-pixel value for the theoretical translation *(Z+δz)* is :

$$\{x_L\}_{\delta z} = \frac{1}{k_x}\left(\left(\left(\cos^{-1}\left(\frac{B\sin\theta c\cos\left(\tan^{-1}\left(\frac{|Z+\delta z|}{|X|}\right)-90\right)}{2(Z+\delta z)}\right)-\theta c\right)+\left(90-\tan^{-1}\left(\frac{|Z+\delta z|}{|X|}\right)\right)\right)\right)$$

<div align="right">Equation 4-49</div>

The right x-pixel value for the translation *(Z+δz)* can then be expressed as :

$$\{x_R\}_{\delta z} = \frac{1}{k_x}\left(\left(-\left(\cos^{-1}\left(\frac{B\sin\theta c\cos\left(\tan^{-1}\left(\frac{|Z+\delta z|}{|X|}\right)-90\right)}{2(Z+\delta z)}\right)-\theta c\right)+\left(90-\tan^{-1}\left(\frac{|Z+\delta z|}{|X|}\right)\right)\right)\right)$$

<div align="right">Equation 4-50</div>

The left x-pixel value for the theoretical translation *(Z-δz)* can be calculated by :

$$\{x_L\}_{-\delta z} = \frac{1}{k_x}\left(\left(\left(\cos^{-1}\left(\frac{B\sin\theta c\cos\left(\tan^{-1}\left(\frac{|Z-\delta z|}{|X|}\right)-90\right)}{2(Z-\delta z)}\right)-\theta c\right)+\left(90-\tan^{-1}\left(\frac{|Z-\delta z|}{|X|}\right)\right)\right)\right)$$

<div align="right">Equation 4-51</div>

The right x-pixel value for the theoretical translation *(Z+δz)* can then be calculated as :

$$\{x_R\}_{-\delta z} = \frac{1}{k_x}\left(\left(\left(-\cos^{-1}\left(\frac{B\sin\theta c\cos\left(\tan^{-1}\left(\frac{|Z-\delta z|}{|X|}\right)-90\right)}{2(Z-\delta z)}\right)\right)-\theta c\right)+\left(90-\tan^{-1}\left(\frac{|Z-\delta z|}{|X|}\right)\right)\right)$$

<div align="right">Equation 4-52</div>

To obtain the theoretical resolution in terms of mm / pixel in left image space the overall theoretical displacement $2\delta z$, nominally represented in mm, is divided by the difference in the disparity information at $(Z+\delta z)$, obtained from Equation 4-49 and Equation 4-50, and at $(Z-\delta z)$, obtained from Equation 4-51 and Equation 4-52. The following equation, therefore, defines the theoretical resolution surrounding a point 'n' in the Z-axis in object space, in mm / pixel :-

$$Z_{vox} = \frac{2.\delta z}{\left|\left|\{x_L\}_{\delta z}-\{x_R\}_{\delta z}\right|-\left|\{x_L\}_{-\delta z}-\{x_R\}_{-\delta z}\right|\right|}$$

<div align="right">Equation 4-53</div>

Where,

Z_{vox} $\equiv$ theoretical resolution surrounding a point 'n' in the Z-axis of cartesian object space as inferred from right image space values, in mm / pixel.

4.10.3 Calculation of Voxel Dimensions in the Y-axis

To calculate the theoretical resolution in the Y-axis of object space surrounding a point of interest the Y-axis algorithm as defined by Equation 4-21 is used as follows :-

$$Y = \frac{B(y_p-y_n)SL}{2f} \cdot \frac{\cos\left(-k_x\left(\frac{x_{ln}-x_m}{2}\right)\right)}{\cos\left(\theta c+\left(k_x\left(\frac{x_{ln}-x_m}{2}\right)\right)\right)}$$
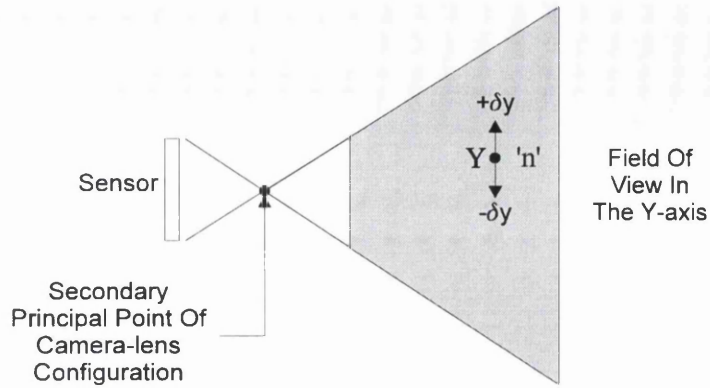
Figure 4-16 Calculation of Voxel Size in the Y-axis

Consider Figure 4-16, for known incremental changes of $(Y+\delta y)$ and $(Y-\delta y)$ the new y-pixel value is calculated. For a theoretical incremental change in the Y-axis of $+\delta y$, from Equation 4-21, the following algorithm defines the change in the y-pixel value :

$$y_{\delta y} = y_p - \left(\frac{(Y + \delta y)2f \cos\left(\theta c + \left(k_x\left(\frac{x_{\ln} - x_m}{2} \right) \right) \right)}{B\,SL \cos\left(-k_x\left(\frac{x_{\ln} - x_m}{2} \right) \right)} \right) \qquad \text{Equation 4-54}$$

For a theoretical incremental change in the Y-axis of $-\delta y$, from Equation 4-21, the following algorithm defines the change in the y-pixel value :

$$y_{-\delta y} = y_p - \left(\frac{(Y - \delta y)2f \cos\left(\theta c + \left(k_x\left(\frac{x_{\ln} - x_m}{2} \right) \right) \right)}{B\,SL \cos\left(-k_x\left(\frac{x_{\ln} - x_m}{2} \right) \right)} \right) \qquad \text{Equation 4-55}$$

From Equation 4-54 and Equation 4-55 the voxel size surrounding a point of interest 'n' is :

$$Y_{vox} = \frac{2.\delta y}{\left| y_n - \{ y\delta y \} \right| + \left| y_n - \{ y_{-\delta y} \} \right|} \qquad \text{Equation 4-56}$$

Where,

$Y_{vox} \quad \equiv \quad$ theoretical resolution surrounding a point 'n' in the Y-axis of cartesian object space as inferred from Y image space values, in mm / pixel.

4.11 Summary

The work presented in this chapter is summarised as follows :

- the stereoscopic region for the rotating stereoscopic line-scan system has been defined;

- the image production parameters for the stereoscopic system have been identified;

- the line-scan arrangement and surrounding object space has been modelled using a cylindrical co-ordinate system;

- algorithms relating stereoscopic image space to cartesian object space have been derived for all three co-ordinate axes;

- a three-dimensional conformal transformation model has been derived for use with the camera arrangement to allow individual X, Y and Z-axis co-ordinate information to be obtained from a defined object space;

- algorithms allowing the boundary of the stereoscopic volume to be identified have been presented;

- algorithms, which enable the size of individual voxels in each axis of object space to be determined, have been derived to allow an assessment of the available resolution in object space for a given stereoscopic arrangement.

In the following chapter, experiments are discussed and results presented to evaluate the applicability of the 3-D mathematical analysis to a rotating arrangement of stereoscopic sensors.

5. EXPERIMENTS WITH THE ROTATING STEREOSCOPIC LINE-SCAN SYSTEM

5.1 Introduction

Results from the investigation of the rotating two-dimensional system (refer to Chapter 3.0) in conjunction with the three-dimensional analysis (Chapter 4.0) provide the basis from which a rotating stereoscopic line-scan system can be developed.

This chapter describes the constituent elements of the rotating stereoscopic line-scan system and the experiments conducted to validate the theoretical analysis. Specifically, experiments were undertaken to investigate the following :

- the use of the algorithms, presented in Section 4.10, to calculate the size of voxels within the stereoscopic volume, therefore, allowing the available resolution to be determined for the experimental arrangements considered in this part of the analysis;

- the suitability of the 3-D conformal transformation model, derived specifically for the line-scan system, (Section 4.8) in extracting X, Y and Z co-ordinate information from a calibration frame in object workspace.

Once the algorithms governing the resolution and the 3-D transformation are investigated the measurement capability of the line-scan system is quantified for variations in the stereoscopic parameters. Ultimately, the results from this work will allow the characteristics of the rotating stereoscopic line-scan system to be identified.

The ability to obtain 2-D (x, y) co-ordinates of targets in object space from left and right perspective images is a fundamental prerequisite of this research. The apparatus used to achieve this is described in the following section.

5.2 The Rotating Stereoscopic Line-scan System

The rotating line-scan system (Figure 5-1) is constructed from equipment available within the 3-D imaging research group. The experimental arrangement consists of the following elements :

- two 1024 element CCD line-scan cameras;

- a framestore to allow storage of 2-D images from each camera;

- two standard video monitors to display the perspective images obtained;

- a rotation stage and controller;

- a function generator to control the camera scan rate;

- a halogen lighting arrangement to control scene illumination;

- an overall system controller.
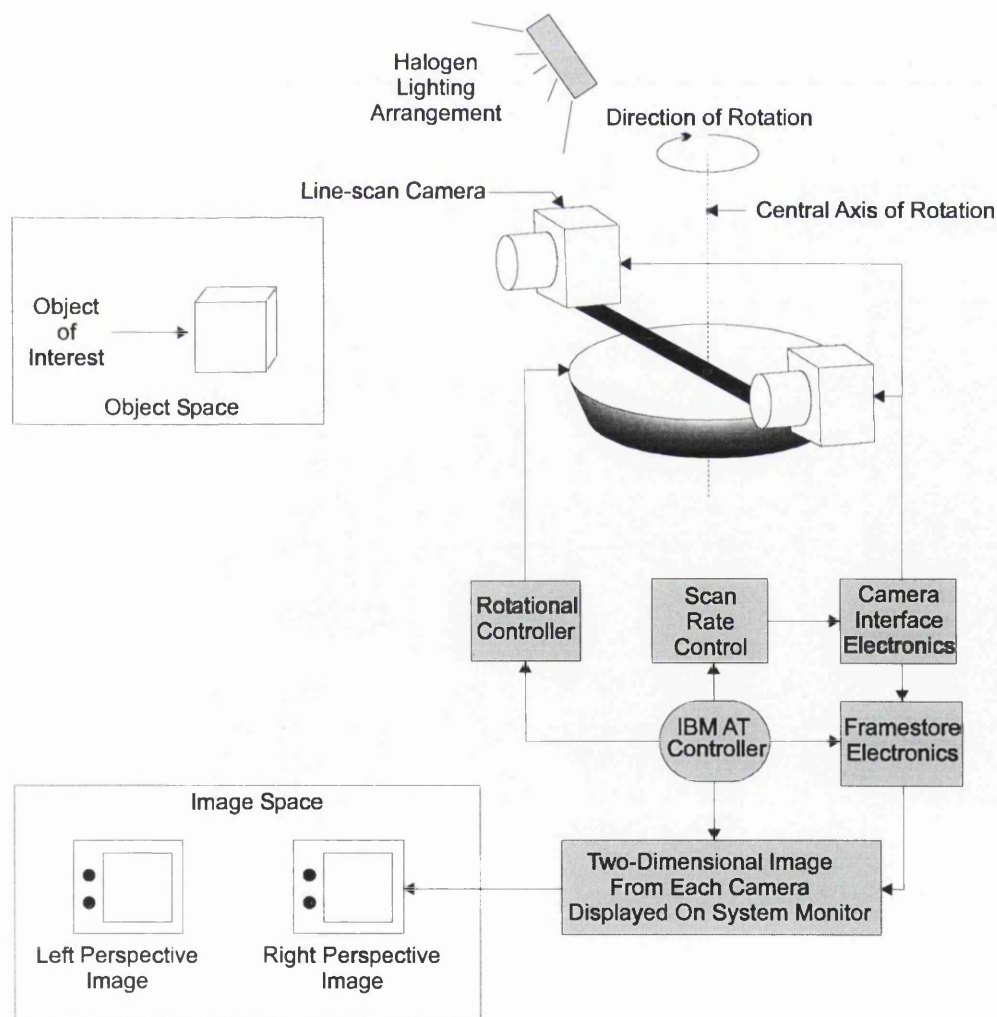
Figure 5-1 Block Diagram of the Stereoscopic Line-scan System

In addition, a calibration frame was built and calibrated specifically for use with the rotating system (Figure 5-2 and Figure 5-3). Software allowing implementation of the mathematical model was written and software allowing control of image capture and manipulation, used previously at Nottingham [32], was utilised in this work.
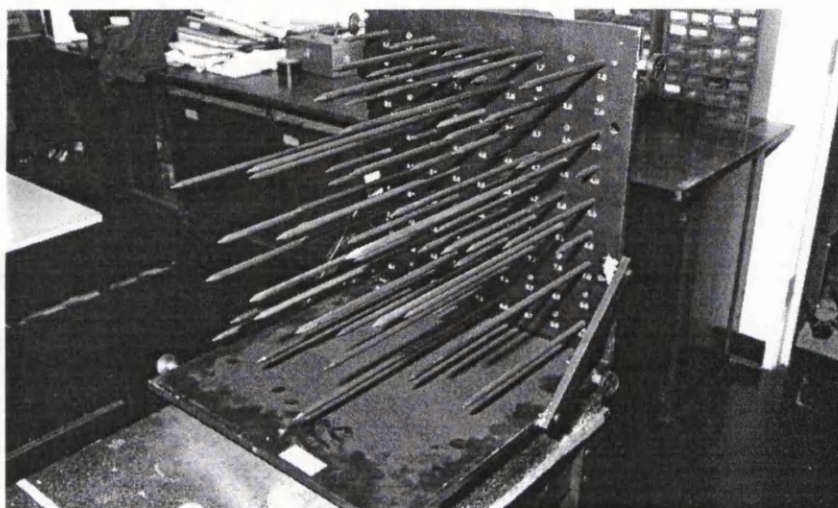
Figure 5-2 A Photograph of the Calibration Frame : Perspective View
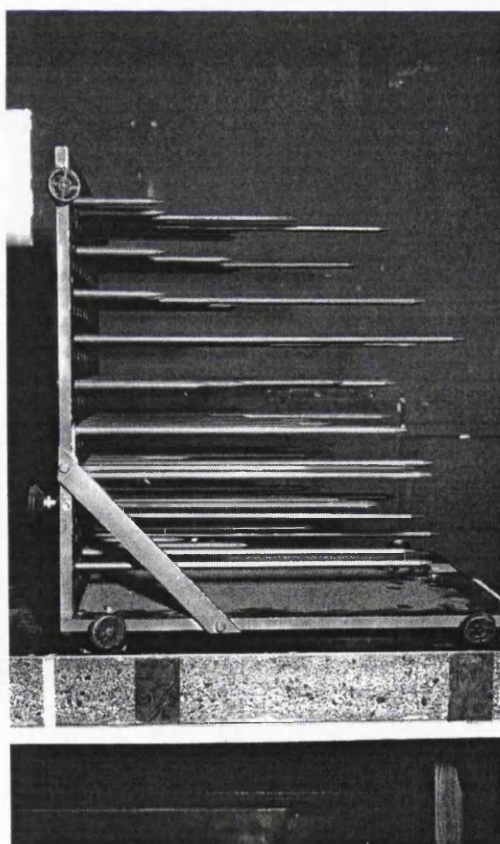
Figure 5-3 A Photograph of the Calibration Frame : Side Elevation

The sections following discuss the elements of the experimental system in more detail.

5.2.1 Line-scan Cameras

Two *Fairchild Weston CCD1300R 1024 element line-scan cameras* [113] are used in this work. The sensing element of the camera consists of a column of 13 micron square photosites on a 13 micron pitch. Thus, the photosites are contiguous along the length of the sensor, giving a total imaging length of 13.31mm.

There are several standards associated with the coupling between the camera body and television lenses. These standards are not discussed here but a detailed description is given by Kruegle [122]. This investigation uses the C-mount coupling to maintain continuity with work undertaken previously at Nottingham which used this standard. The Cosmicar [97] C-mount lenses used in this investigation were as follows :

- 25mm f1.4;
- 50mm f1.8;
- 75mm f1.4.

5.2.2 Rotating Stereoscopic Camera Arrangement

The stereoscopic arrangement consists of two line-scan cameras (Figure 5-4) which, after rotation, generate perspective images from which disparity information can be inferred, as described in Section 4.2.
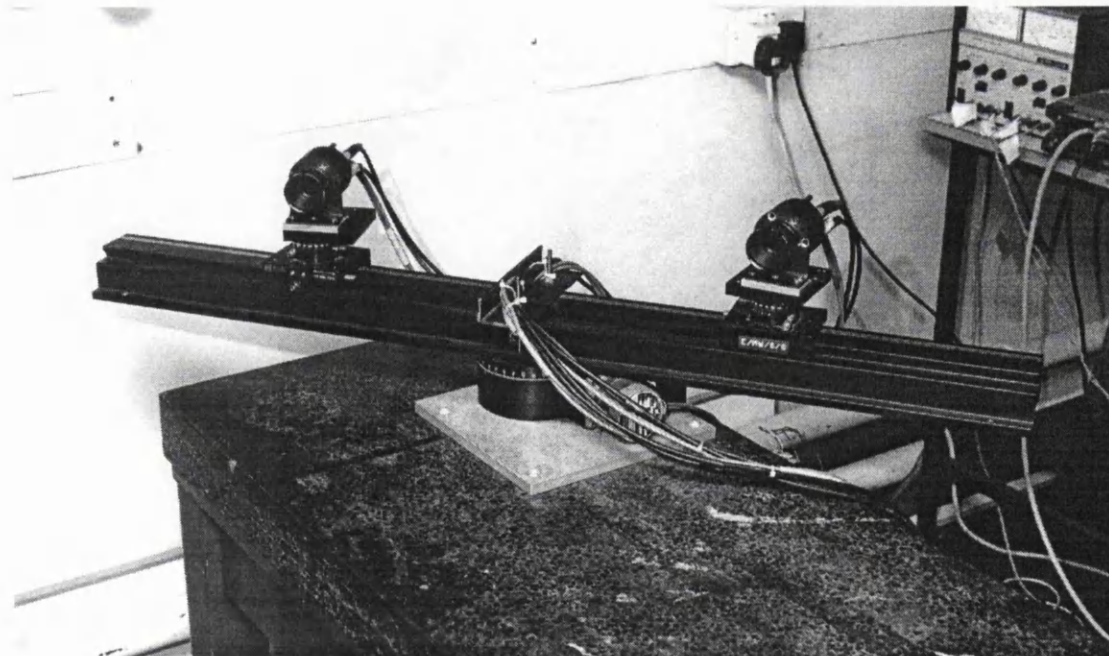
Figure 5-4 The Rotating Stereoscopic Line-scan Camera Configuration

The stereo-camera base width and camera-to-base convergence angle are configured manually in the experimental work described in this chapter. The cameras are mounted on an optical rail which is fixed to the rotation stage. Each camera is individually mounted on a 360° rotary table enabling 'full' rotation about the vertical axis, thus, allowing variation of the convergence angle between the two cameras. The two rotary tables are fixed to an optical carrier which allows each camera to be placed at a selected position along the optical rail and, thus, allows variation of the base width.

The camera arrangement is fixed to a rotation stage driven by a stepper motor controller [116]. The controller is connected by an RS 232 link to a computer interface which allows control of the rotation stage by an operator. For this work, a movement of one step by the motor results in a 0.01° alteration in the angular position of the rotation stage.

The scan rate for each camera is controlled by a Hewlett-Packard 8116A function generator.

The distance between the stereo-camera and the calibration frame is verified manually using a steel tape measure. To establish a standard for all camera-to-object range measurements the reference of the camera arrangement is defined as the rotation centre and the calibration frame reference is designated as the target point with X, Y, Z cartesian co-ordinates of (0,0,0).

5.2.3 Framestore

Picture information from each line-scan sensor is stored on a column by column basis so the combined data can be viewed as a complete two-dimensional image. All the work completed as part of this investigation involves the production of two-dimensional images in this way to enable human viewing. This allows the operator to see the picture information and, thus, identify points of interest within the field of view.

For this work a DIS3000 framestore [114] is used to store the sequential columns of picture information. The DIS3000 is a modular 8-bit framestore similar in operating principle to most 'off-the-shelf' framestores currently available.

Essentially, the DIS3000 consists of two thirds of a colour framestore. The memory in each third can be configured to store an image of 2047 pixels by 2047 lines, consisting of 512 x 512 blocks

(Figure 5-5). For this work an image area of 1024 x 1024 is used to store information from each camera, so only a quarter of the total memory capability is used. Although the numbering system is retained and used for commands with the framestore software each monitor is rotated clockwise through 90° to obtain the image in the correct orientation. Thus, every command interfacing with the image displayed has its image space axes reversed, i.e., moving the cursor in the x-axis of the image is controlled by the y-axis register in memory.
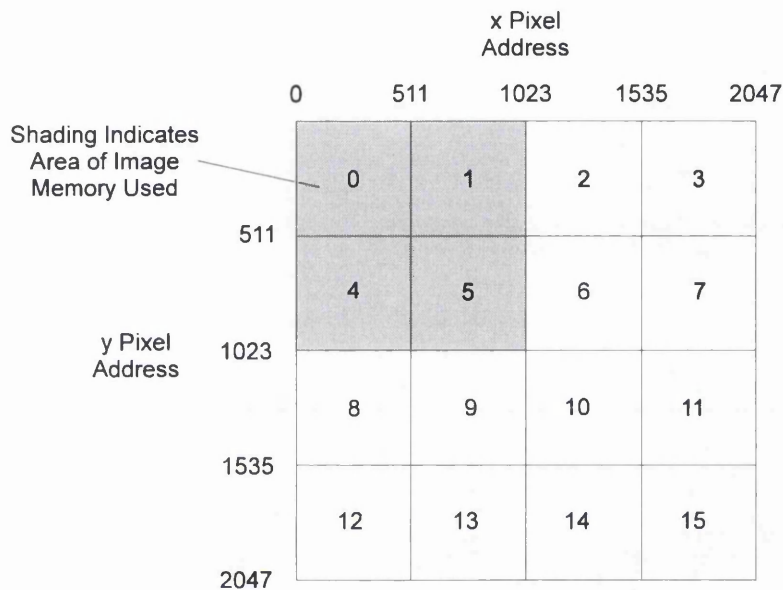
Figure 5-5 Internal Memory Arrangement for the DIS3000 Framestore

A control processor is used to access the image areas within the framestore. This allows control of image capture and the application of image processing and manipulation algorithms supplied with the store. The control processor is connected to an overall host computer, via a dedicated interface unit, allowing framestore image functions to be executed from the host environment.

The stereoscopic pair of images are displayed on two standard television monitors to allow information within the framestore to be interpreted by the system operator. An important feature of the framestore is the ability to introduce a measuring mark, in the shape of a crosshair, into each image area. The crosshair is injected directly into the image storage area and, therefore, is unaffected by distortions in the display. The cursor is moved in the image by software commands and pixel locations recorded as required.

5.2.4 Illumination Arrangement

Variation of the camera scan rate alters the brightness of the resultant images as the magnitude of the photon generated voltage is proportional to the integration period, which is a function of the scan rate (refer to Section 3.3.4). If the integration period is reduced there is a decrease in the number of photons collected and, inversely, the number of photons will rise with an increase in this time period. The amplitude of the picture information at the camera output is determined by the photosite electron charge and the fixed gain of the camera itself. Thus, if the scan rate is increased the overall brightness of the image falls and, accordingly, decreasing the scan rate increases the image brightness. Possible solutions to counteract the effects of this variation are:

- control the amount of light incident on the sensing element;
- control the amplification at the output amplifiers of the sensors;
- vary the sensitivity of the analogue to digital conversion at the framestore input;
- enhance the image via software supplied with the framestore.

The simplest, and most practical, solution is to control the amount of light incident on the sensor as the amplification of the sensor is fixed, the sensitivity of the framestore input is complex to control and enhancement of the image is computationally intensive. The light incident on the sensor can be controlled by either adjusting the iris of the lens or by controlling the scene illumination. The available iris adjustment limits the scan rates that can be considered for this investigation. Therefore, to allow a greater range of scan rates a method for scene illumination control is used.
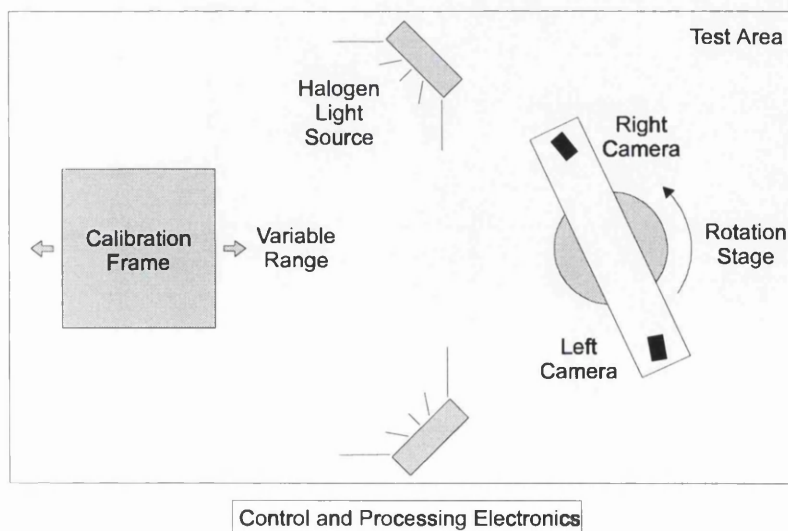
Figure 5-6 Light Source Arrangement Around the Test Area

To provide illumination in the workspace surrounding the camera arrangement two 500 watt a.c. halogen flood lamps [123], manufactured by Tota Light, are used. Each lamp is placed at a selected position in the test area and can be moved closer to, or further away from, the camera base line, dependent on the camera-to-object range setting (Figure 5-6). Each lamp is controlled manually over a wide illumination range by rheostats connected to a 240V mains supply. Thus, any variation in camera scan rate, and the subsequent affect on image brightness, can be counteracted by adjusting the brightness levels of the light sources.

A photograph of the test area is provided in Figure 5-7.
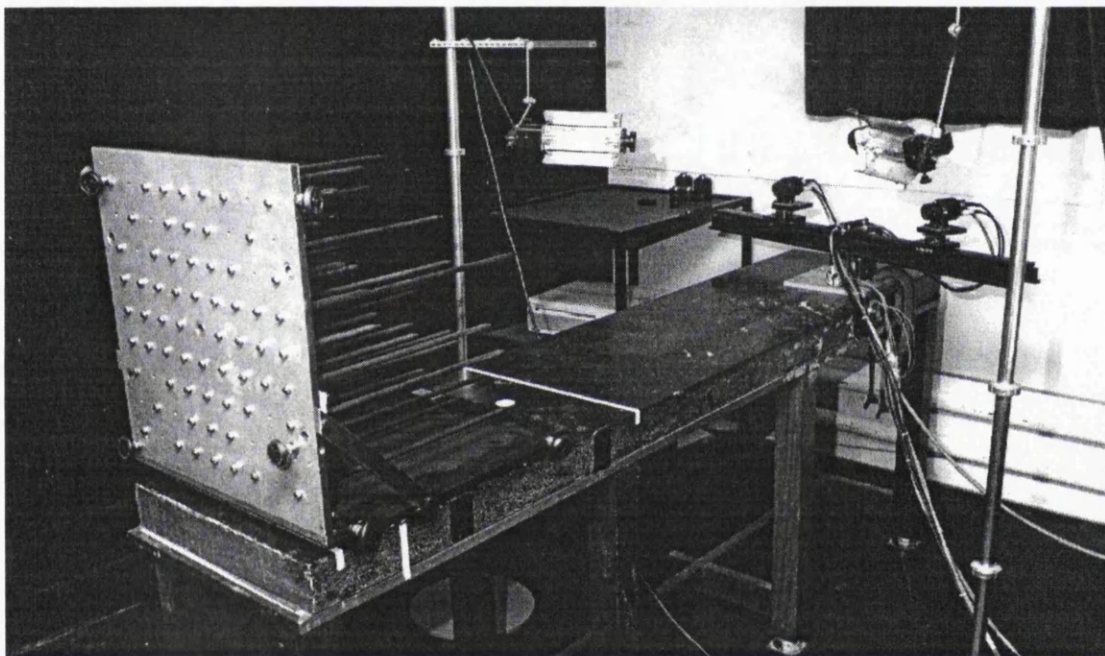
Figure 5-7 A Photograph of the Test Area

5.2.5 Host Controller

The rotation speed, scan rate and framestore are controlled by a host computer (Figure 5-8) which is a Tandy 4000LX 20MHz IBM 'AT' Clone [117]. This allows :

- control of the system components from a remote point;
- implementation of the measurement algorithms via a computer program.

To control the rotating stage a communication channel is linked to the host processor. The speed of this communication link is not critical, therefore, a serial protocol is used to allow control from the host. This consists of an RS 232 link which connects the microprocessor controller of the rotating stage to the 'AT' computer. The speed of serial communications is set at 9600 baud and incorporates an 'echo-back' form of error checking.

To control the camera scan rate an IEEE 488 bus interface card [124] is used to provide remote communications between the HP function generator and the host processor. The transfer of information can proceed as fast as the function generator can respond, i.e., up to 1Mbs, although this is not critical for the experimental set-up.

The framestore is controlled, via the host, by a dedicated interface unit.
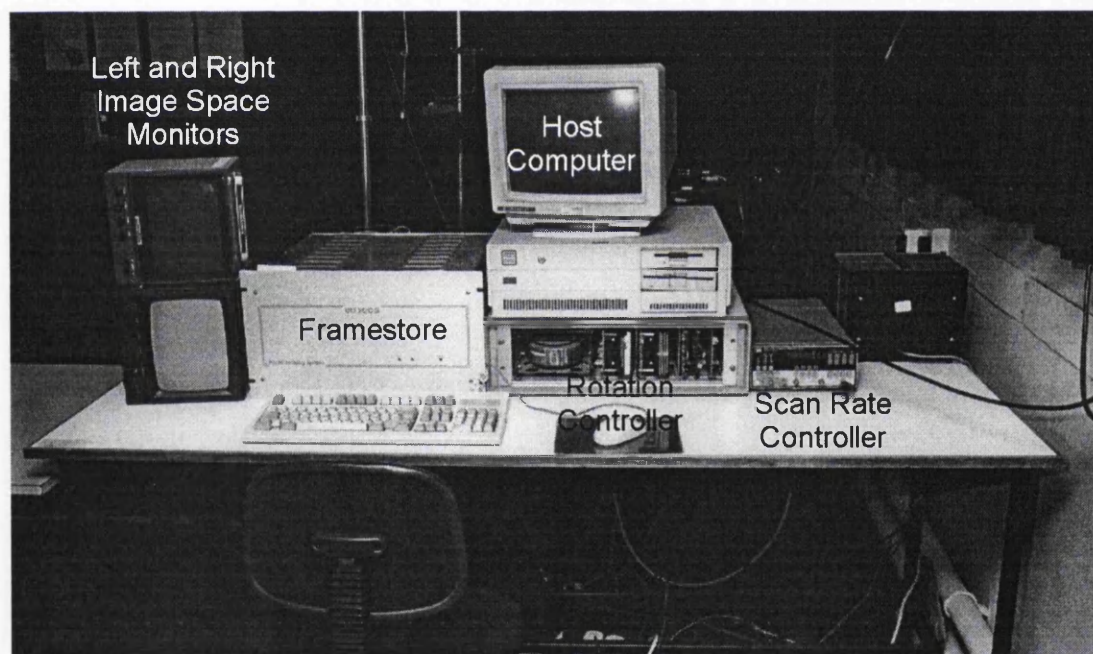
Figure 5-8 System Components Controlled by the Host Computer

5.2.6 The Image Space Co-ordinate System

The images obtained after camera rotation are retained in the framestore. The co-ordinate system used to locate points of interest in each image is shown in Figure 5-9. The co-ordinate system origin is located in the top right hand corner of each image, as viewed on each monitor.
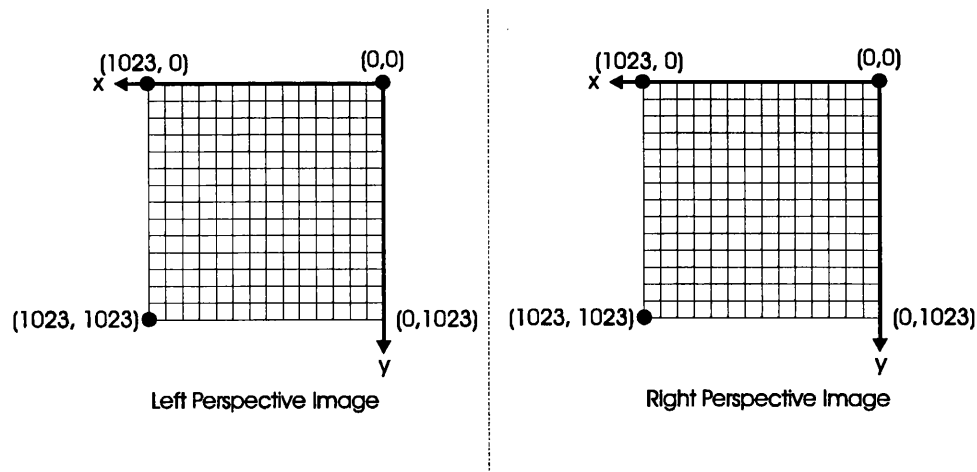
Figure 5-9 The Image Space Co-ordinate System

Image manipulation software enables a crosshair to be placed manually over each point of interest and its location recorded in the x, y co-ordinate system for both perspective images. Also, a function supplied with the framestore allows the operator to identify grey level values associated with the position of the crosshair in image space. This aids the identification of selected object space targets in image space.

5.2.7 The Calibrated Object Space Co-ordinate System

The requirements for a calibrated object volume are discussed in Section 2.3.1. A calibrated frame, used previously at Nottingham [30, 31, 32], was used in initial experimental work with the line-scan arrangement. However, due to the number of system parameters considered in this work, the varying field of views produced from the rotating configuration provide insufficient target points for the mathematical model derived in Chapter 4.0. The parameters include :

- camera-to-object distance;
- rotation speed and scan rate;
- convergence angle and base width;
- focal length of the camera-lens.

A minimum of four control targets are required from each considered stereoscopic FOV for the initial camera calibration and a number of different object space targets, say 10 or more, are required to provide a reliable indication of the measurement capability. Therefore, a new calibration frame manufactured from aluminium was constructed for this work. This consists of a

series of rods distributed about a defined three-dimensional volume. Each rod is black anodised with a polished 'white' tip as the calibrated target (Figure 5-10) allowing a high contrast in the images produced from the line-scan system. The dimension of the frame is 500mm in each of the co-ordinate axes, as illustrated in Figure 5-11, with a total of 64 targets distributed in the volume. Each target within the volume is defined by a cartesian point location (X, Y, Z). From this configuration the number of possible targets is sufficient to allow an evaluation of the measurement characteristics associated with the stereoscopic line-scan system.

Polished Tip Used as the Calibrated → Target Point

Black Anodised Aluminium Rod
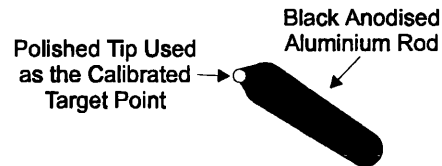
Figure 5-10 A Calibrated Target Located within the Frame Volume

Y

500mm

500mm

X

500mm

Z
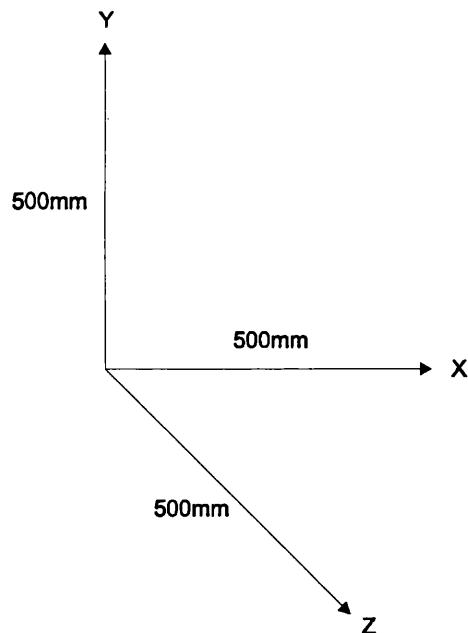
Figure 5-11 Dimensions of the Calibration Frame Cartesian Co-ordinate System

The position of each target was arranged to minimise the number of occluded points in the images produced. The targets were calibrated using an LK co-ordinate measurement machine [125, 126] situated in the Department of Mechanical Engineering at The Nottingham Trent University. The calibration procedure involved placing a probe, with a 0.995mm radius, on the tip of each aluminium rod. The 3-D co-ordinates of each target centre were then calculated, with respect to a reference target, by the co-ordinate measurement machine.

The accuracy of the calibration technique is to ± 0.01mm which is at least one order of magnitude better than the accuracy anticipated from the stereoscopic line-scan system. Thus, the calibration data for the frame is considered to provide the definitive co-ordinates of the target positions, i.e., the calibration error is considered insignificant for the purposes of this work.

The calibration frame is constructed from aluminium which has a linear expansion coefficient [118] of 2.50×10^{-5} K^{-1}. Therefore, for each degree rise above room temperature a metre length of aluminium will expand by 0.025mm. As the volume of the calibration frame is 500mm^3 the maximum change in the dimensions of each axis is 0.0125mm per degree change in temperature. Thus, assuming a worst case temperature variation of ±5.0°, the maximum change in the dimensions of the calibration frame is ±0.0625mm. This maximum possible error is of the same magnitude as that of the calibration technique applied to the object volume and, therefore, the error due to thermal expansion is considered to be negligible for this work.

5.2.8 Operating Software

Software was written to allow the determination of three-dimensional co-ordinate information in object space. The software code was written in the 'C' programming language [115] and allows implementation of the following procedures :

- the calibration of the camera / calibration frame system in the first instance using the 3-D conformal transformation procedure;
- calculation of 3-D co-ordinate information for targets of interest in object space using the transformation parameters returned from the calibration routine;
- calculating the object space errors between 3-D co-ordinates resolved by the camera system and known co-ordinate information from the calibration frame.
- determination of voxel dimensions in the X, Y and Z-axes of object space.

5.3 System Operation

This section outlines the general experimental procedure and the method of manually locating target positions in each of the two perspective images.

5.3.1 General Experimental Procedure

Prior to camera rotation and image capture the following parameters are set for each experiment carried out :

- focal length;

- stereo camera separation;

- camera-to-base convergence angle;

- camera scan rate and rotation speed;

- distance from the camera arrangement to the calibration frame.

After setting these parameters both the framestore and speed controller are initialised and the relevant software executed to allow simultaneous stereoscopic image capture of the calibration frame as the camera system rotates in object space. Image capture is initiated by the operator at a desired point in the rotation. When a full two-dimensional image from each sensor is generated the rotation is stopped and the stereo-camera returned to the original position. This initial run allows certain parameters, within the confines of the system, to be monitored and adjusted accordingly. These include :

- the focus for each camera;

- the image capture start point;

- the level of object illumination necessary.

The optimum setting for each parameter is achieved by considering the images taken on consecutive passes of the calibration frame. An individual parameter is altered on each pass until its optimum setting is obtained. This set-up procedure continues until fully optimised images of the workspace are produced.

After this 'initialisation' process the stereo-camera is rotated again and perspective images of the calibration frame are produced. The images are then analysed to determine the relative positions of targets on the calibration frame. From this image information, targets are selected and the associated pixel data is passed to the 3-D conformal calibration routine to allow determination of the appropriate transformation parameters. Following the calibration phase, different targets are selected from the perspective images of the calibration volume and their 3-D co-ordinates are calculated. This calculated target information is compared to the known calibration frame data to evaluate the measurement capability of the rotating system for each experimental set-up.

5.3.2 Manual Location of Target Positions

The two-dimensional size of a target in an image is dependent on the parameters which influence resolution in each axis. The scan rate, rotation speed and camera-to-object range determine the X-axis resolution and the Y-axis resolution is dependent on camera-to-object range and the focal length of the lens. Hence, due to the interaction of these parameters, the centroid of a target in object space may occupy more than one pixel in image space. Furthermore, if spread over two or more pixels, the target centre may not occur on a pixel site. Thus, to determine a target position manually, weighting factors are required to decide the pixel location of a target centre. The following considerations are given to the location of each target position in image space :

- if a target is spread over several pixels the pixel closest to the operator's interpretation of its centroid is assigned as its location;
- if the target centroid is at an intersection between pixels the target design aids the position assignment. The targets are 'white' and the remaining frame is black, thus, a framestore function determines which pixel has the highest grey level value, i.e., values of 255 and 0 represent white and black, respectively.

The experimental work, which aims to corroborate the algorithms derived in Chapter 4.0 for use with the rotating line-scan system, is now described.

5.4 The Experimental Strategy

The experimental work is defined, in sequence, by four main categories (Figure 5-12) :

- preliminary tests and experiments;
- determination of voxel size in object space;
- co-ordinate measurement capability;
- rotating stereoscopic line-scan characteristics.

The experimental work is now outlined in more detail, after which will follow the results from this part of the research.

What limits the measurement
capability of the system ?

Preliminary Tests
and Experiments

Can the available resolution
of the system be determined ?

Determination
of Voxel Size in
Object Space

Can the mathematical model
be applied to the system ?

Co-ordinate
Measurement
Capability

How does a variation in the
system parameters influence
the measurement capability ?

Rotating
Stereoscopic
Line-scan
Characteristics

Figure 5-12 The Strategy Applied to Experimentation with the Stereoscopic Line-scan System

Preliminary Tests and Experiments :

Preliminary tests are undertaken to evaluate the distortion inherent in each axis of the line-scan arrangement. Specifically, the following possible sources of error are quantified :

- the distortion in the x-axis of image space due to the camera scan rate and rotation speed settings;
- the distortion in the y-axis of image space due to lens deformations.

Preliminary experimental work is then undertaken to investigate the application of the Direct Linear Transformation (DLT) to the rotating stereoscopic arrangement in determining 3-D co-ordinate information from object space.

Determination of Voxel Size in Object Space :

Following the preliminary work, experimentation is undertaken to determine whether voxel dimensions in object space can be resolved using the algorithms presented in Section 4.10. This allows the available resolution of the considered stereoscopic arrangements to be evaluated. This section of the work is divided into :

- the procedure for the experimental determination of voxel dimensions;
- a summary of the method for the theoretical determination of voxel dimensions;
- evaluation of the theoretical analysis in the determination of voxel dimensions.

The Co-ordinate Measurement Capability :

After the algorithms allowing the extraction of voxel dimensions are evaluated the applicability of the 3-D conformal transformation to the stereoscopic system is investigated. Specifically, the experimentation will examine the following :

- the selection of control targets for use in the calibration procedure;
- the effect of varying the start of image capture on the measurement capability;
- the accuracy and precision of 3-D co-ordinate measurements;
- the effect of changing the camera / object system relationship on the measurement capability;
- the ability to resolve 3-D vectors from object space.

Rotating Stereoscopic Line-scan Characteristics :

Once the ability to resolve 3-D object space co-ordinates is known the characteristics of the stereoscopic system can be identified. This involves an assessment of the measurement capability for variations in the parameters which govern stereoscopic image production, i.e., camera base width, convergence angle, range, scan rate etc.

5.5 Preliminary Tests and Experiments

This section quantifies the effects of the movement and lens distortions on the expected accuracy of the camera system and evaluates the application of DLT to the stereoscopic arrangement of rotating sensors.

5.5.1 Error Due to Movement Distortion

The x-axis of the line-scan image is produced from the rotational movement of the camera with respect to a static object. Thus, two possible sources of error in x-axis dimensions exist :

- variation in the camera scan rate;
- variation in the speed of camera rotation during image capture.

Error Due to a Variation in Scan Rate :

The scan rate clock is produced by a Hewlett-Packard 8116A function generator. The manufacturers specification states the repeatability of the frequency output is ±1.25% of the desired setting. The worst case error produced in the image x-axis due to this variation is when the slowest frequency is used with the fastest rotation speed, 100kHz and 2.0rpm respectively.

For one pixel column in the x-axis, which represents the resolution available in image space, the equivalent camera rotation angle in object space is (refer to Section 3.3.5) :

$$\theta_{res} = \left(\frac{6144.S_R}{F_{SR}} \right) = 0.12°$$

Where,

θ_{res} ≡ the angular resolution in object space, in degrees.

Therefore, 1 pixel in the x-axis represents a 0.12° rotation angle in object space. Assuming there is no error in the rotation speed the error due to the scan frequency represents ±0.0015° for each pixel. Thus, the variation in the x-axis due to the error in frequency is two orders of magnitude less than the angular resolution. Accordingly, the possible error produced by the function generator is considered insignificant for this work.

Error Due to a Variation in Rotation Speed :

To assess the characteristics of the rotation stage for variations in speed a two channel optical encoder [127] was attached to the gear shaft of the motor. For the rotation speeds considered in the stereoscopic experiments the encoder was used to obtain the time period at intervals in the rotation. The time period of each pulse generated by the encoder was measured via a Tektronix TDS350 two channel 200mhz / 1 Gs/s Oscilloscope. At each speed setting the time period was measured 10 times during the rotation to allow the consistency of the speed to be examined.

The rotation speeds considered in this investigation are 0.67, 1.00, 1.34, 1.67 and 2.00 rpm. For each speed setting the time period is evaluated whilst the stereoscopic camera arrangement is fixed to the rotation stage. This allows the error due to camera rotation, and not just the error in the rotation stage, to be evaluated.

Rotation Speed (rpm)	0.67	1.00	1.34	1.67	2.00
Time Interval	Time Period (ms)				
1	2.7	1.6	1.3	1.0	0.8
2	2.7	1.8	1.2	0.9	0.8
3	2.3	1.8	1.3	1.0	0.8
4	2.7	1.8	1.2	1.0	0.8
5	2.3	1.7	1.3	1.0	0.8
6	2.5	1.6	1.2	0.9	0.8
7	2.3	1.7	1.2	1.0	0.8
8	2.3	1.6	1.3	0.9	0.8
9	2.5	1.7	1.2	1.0	0.8
10	2.7	1.7	1.2	1.0	0.8
Standard Deviation (ms)	0.19	0.08	0.05	0.05	0.00

Table 5-1 Consistency of Time Period for Rotation Speeds Considered in the Analysis

Table 5-1 reveals the error in the rotation speed decreases as the speed increases. To transform these results into values which allow the consistency of the rotation speed to be assessed consider the following discussion.

The gear shaft of the stepper motor undergoes 1 revolution per 200 steps of the rotation. It is known one revolution of the rotating stage is equivalent to 36,000 steps, therefore, 1 revolution of the gear shaft corresponds to 2° of camera rotation. Thus, a 1° change in rotation occurs every 100 steps. From this the rotation speed of the platform is defined by :

$$\text{rotation speed} = \frac{\text{angular distance}}{\text{time period}} = \frac{1}{100T}(°/s) \qquad \text{Equation 5-1}$$

To obtain the speed in revolutions per minute Equation 5-1 is multiplied by 60 (to convert from seconds to minutes) and divided by 360 (to convert from degrees to a revolution) to give :

$$\text{rotation speed} = \frac{1}{600T}(rpm) \qquad \text{Equation 5-2}$$

Using Equation 5-2, the results from Table 5-1 are converted to equivalent rotation speeds and are presented in Table 5-2.

Rotation Speed (rpm)	0.67	1.00	1.34	1.67	2.00
Time Interval	Calculated Rotation Speed (rpm)				
1	0.62	1.04	1.28	1.67	2.08
2	0.62	0.93	1.39	1.85	2.08
3	0.72	0.93	1.28	1.67	2.08
4	0.62	0.93	1.39	1.67	2.08
5	0.72	0.98	1.28	1.67	2.08
6	0.67	1.04	1.39	1.85	2.08
7	0.72	0.98	1.39	1.67	2.08
8	0.72	1.04	1.28	1.85	2.08
9	0.67	0.98	1.39	1.67	2.08
10	0.62	0.98	1.39	1.67	2.08
Mean Speed (rpm)	0.67	0.98	1.35	1.72	2.08

Table 5-2 Calculated Rotation Speeds

From Table 5-2 the following can be stated :

- for a setting of 0.67rpm the maximum deviation of 0.05 represents a possible worst case error of 7% in the actual rotation speed;

- for a setting of 1.00rpm the maximum deviation of 0.07 represents a possible worst case error of 7% in the actual rotation speed;

- for a setting of 1.34rpm the maximum deviation of 0.06 represents a possible worst case error of 4% in the actual rotation speed;

- for a setting of 1.67rpm the maximum deviation of 0.18 represents a possible worst case error of 11% in the actual rotation speed;

- for a setting of 2.00rpm the maximum deviation of 0.08 represents a possible worst case error 4% in the actual rotation speed.

From the mean values of the rotation speeds (Table 5-2), the overall errors are considered to be insignificant for the purposes of this investigation. These results are now discussed with respect to the angular resolution in the movement axis. As stated previously, the angular resolution in the x-axis of object space is given by :

$$\theta_{res} = \left(\frac{6144.S_R}{F_{SR}} \right)$$

Thus, for a speed setting of 0.67rpm and a scan rate of 100kHz one vertical column of picture information represents a camera rotation angle of 0.04°. The error associated with this speed setting is 7% and, thus, the error in terms of the angular resolution is a maximum of 0.003°. The maximum error in angular resolution for each rotation speed is presented in Table 5-3.

Speed Setting (rpm)	Angular Resolution (°)	Resolution Error (°)
0.67	0.04	0.003
1.00	0.06	0.004
1.34	0.09	0.004
1.67	0.11	0.01
2.00	0.13	0.005

Table 5-3 Angular Resolution Errors for the Experimental Rotation Speeds

From Table 5-3, the worst case error in angular resolution represents 0.09 of a pixel generated in the x-axis of image space. As stated in Section 3.6.1, the repeatability of the image data is ±1 pixel in the x-axis, thus, the error due to inconsistencies in rotation speed is a factor of 10 times less than that due to the manual location of object targets in image space. Thus, the error in rotation speed is considered to be insignificant for this work.

5.5.2 Error Due to Lens Distortion

A theoretical analysis of lens distortion is presented in Section 2.3.3. To summarise, the deformities are divided into two sections, aberrations and distortions - aberrations cause blurring in an image and distortions cause a shift in point position according to the passage of refracted light through the lens. Both aberrations and distortions become worse as the aperture of the lens is increased. Of the deformities, distortions [100] have a greater influence on system accuracy.

In previous work by the 3-D imaging group [32] distortions in the 25mm and 50mm lenses used in this research were investigated. It is considered unnecessary to evaluate the distortion effects again, thus, the results from the analysis are discussed with respect to this work. The experiment, previously undertaken, was conducted with the lens iris set at the largest aperture diameter, and as deformities increase as a function of the aperture opening, the percentage error across the lens presented is considered to be the worst case distortions.

From this analysis it was deduced that barrel distortion is apparent in the 25mm lens. This results in a displacement of points in an image of 0.8% from the centre to the top of the image

and 1% from the centre to the bottom. The sensor used in this investigation contains 1024 photosite elements in the Y-axis, thus, an image point is subject to a maximum shift of 5 pixels from the centre of the image. However, if the camera-to-object range is increased, the amount of the image occupied by the same distance in object space reduces due to the increase in the FOV in the y-axis of the image. In other words, as range increases, the object size in the image reduces and is not influenced by lens distortions to such an extent. Indeed, if the range for the 25mm lens test was doubled, the number of pixels from the centre of the image would be halved. This test was completed at a range of 0.65m. If this was doubled the distortion would represent an error of 2 - 3 pixels in a point location from the centre of the screen. As the error due to the manual location of point positions in an image is ±1 pixel (Section 3.6.1), i.e. a maximum of 2 pixels, by minimising the aperture diameter and increasing camera-to-object range this error, although present, will not significantly alter the capability of the camera system to resolve co-ordinate data to the expected level of accuracy. Furthermore, as the distortion error in the 25mm lens is recognised the level of accuracy obtained from the 3-D co-ordinate measurements can be quantified with respect to this.

From analysis of the 50mm lens it was determined that distortion is apparent, however, the amount of displacement is reduced compared to that with the 25mm lens. The small displacement value presents a problem when attempting to identify the distortion type (either pincushion or barrel). However, from the manufacturers data, the lens deformity is expected to be barrel distortion. This results in a displacement of points in both perspective images of 0.3% from the centre of the image to the top, and 0.1% from the centre to the bottom. The worst case error will result in a shift of between 1 and 2 pixels for a point of interest in an image. As this is the worst case by minimising the aperture diameter the error due to distortion in this lens will not be greater than the error inherent in the method of manually locating image points.

For this work a 75mm lens is also used. It is considered the error in this lens will be, at worst, the same as that in the 50mm lens [101]. Therefore, for the reason stated above the distortion error is considered insignificant when compared with the error in identifying points in image space.

From the results of this analysis the lens aperture diameter is reduced to a minimum for each experiment and the points of interest are limited to an area as close to the image centre as possible. Therefore, the lens distortions will be reduced to a level that is insignificant compared

to the expected accuracy of the line-scan system. This procedure is adopted for the experiments described in this chapter. Nevertheless, under certain conditions, i.e., small camera-to-object range, large base width etc., it may not be possible to apply this procedure and lens distortions may contribute significantly to the errors.

5.5.3 Application of the Direct Linear Transformation (DLT)

Relating the position of a target in two perspective images to its 3-D location in workspace has been investigated extensively, leading to the development of many photogrammetric models [128]. Thus, an approach to resolving co-ordinate information from a stereo line-scan camera is to apply an existing technique. To achieve this a software version of the DLT algorithm [85], used previously at Nottingham [30, 31, 32], was adapted to assess whether it could be applied to the rotating line-scan system to resolve 3-D co-ordinates from object space.

Experimental Hypothesis :

"To determine if DLT can be applied to a rotating stereoscopic line-scan system"

Experimental Conditions :

Image data is obtained for targets from the calibration frame for each arrangement considered. The DLT algorithm requires image co-ordinates for six control targets to calculate the transformation model between the camera and object systems. Initially, to assess the use of DLT with the camera system the control data is passed to the algorithm again after the calibration.

A series of four experiments are outlined to determine the suitability of DLT to the stereoscopic system in extracting three-dimensional co-ordinate information from object space.

The parameter settings for each experiment are shown in Table 5-4. For experiments A and B the aspect ratio, x pixels : y pixels in image space, is set at 9 : 28 and 18 : 28 respectively. To provide a further test the parameters for experiments C and D are configured to produce a 1 : 1 aspect ratio in image space. This is done in an attempt to provide the DLT algorithm with image data from a 'simulated' square array camera, i.e., the aspect ratio in image space is similar to that of an image produced from a type of television camera used in machine vision.

Parameter	A	B	C	D
θ_c (°)	75	75	65	75
B (mm)	500	500	500	500
S_R (rpm)	0.83	0.83	1.67	0.83
D_{CO} (mm)	800	800	1000	800
F_{SR} (kHz)	50	100	230	160
Aspect Ratio (x:y)	9 : 28	18 : 28	1 : 1	1 : 1

Table 5-4 System Parameter Settings for DLT Experiments A, B, C and D

Experimental Results :

For each experiment, once the calibration was completed, the control target data was passed to the calculation procedure. In theory, for the DLT algorithm to be applicable to the stereoscopic system, the error in the three-dimensional co-ordinate data resulting from the calculation procedure should have approached zero for the control targets used in the analysis.

Control Target	X error (mm)	Y error (mm)	Z error (mm)
1	4.4	381.9	0.1
2	341.6	382.6	2.3
3	361.5	189.3	0.8
4	170.3	358.8	72.9
5	169.8	194.3	72.5
6	60.8	381.5	329.5

Table 5-5 Co-ordinate Errors for Control Targets after DLT Calculation for Experiment A

Control Point	X error (mm)	Y error (mm)	Z error (mm)
1	4.4	382.0	0.1
2	341.5	382.8	2.5
3	361.5	189.4	1.6
4	170.4	358.3	72.5
5	169.8	194.3	72.2
6	60.8	381.6	329.5

Table 5-6 Co-ordinate Errors for Control Targets after DLT Calculation for Experiment B

Control Point	X error (mm)	Y error (mm)	Z error (mm)
1	4.4	381.7	0.1
2	341.6	382.7	2.0
3	361.5	189.4	1.1
4	170.3	359.1	73.0
5	169.8	194.3	72.4
6	320.3	340.0	142.3

Table 5-7 Co-ordinate Errors for Control Targets after DLT Calculation for Experiment C

Control Point	X error (mm)	Y error (mm)	Z error (mm)
1	4.5	382.0	0.9
2	361.2	189.6	0.5
3	169.9	194.1	71.6
4	319.8	340.2	140.7
5	312.1	252.6	211.2
6	60.8	381.6	328.6

Table 5-8 Co-ordinate Errors for Control Targets after DLT Calculation for Experiment D

From Table 5-5, Table 5-6, Table 5-7 and Table 5-8 the 3-D co-ordinate errors in control target position confirm the DLT algorithm cannot be applied to a rotating arrangement of line-scan sensors. The prediction of the control target positions fails as the basis on which DLT was developed is different to the line-scan configuration. Thus, if traditional photogrammetric algorithms cannot be used the specific algorithms, developed in Chapter 4.0, are now tested.

5.6 Determination of Voxel Dimensions in Object Space

For the rotating stereoscopic line-scan system the resolution available is determined directly by the X, Y and Z dimensions of each volume element in object space. The objective of the work in this section is to evaluate the algorithms, derived in Section 4.10, in the determination of object space voxel dimensions from the line-scan system.

5.6.1 Problem Definition

The voxel structure generated by the camera system conforms to a cylindrical co-ordinate system and the algorithms used to resolve 3-D object space measurements are based on the application of a cartesian co-ordinate system. This section defines the limitations associated with determining cylindrical voxel dimensions from cartesian co-ordinate information.

The Requirement for the Determination of Voxel Dimensions:

Consider a target in object space, within the stereoscopic volume (Figure 5-13), with its three-dimensional co-ordinates resolved by the line-scan system.

For a target of interest, once the 3-D co-ordinates resolved by the camera system are compared to the equivalent co-ordinates from the calibration frame data (Figure 5-14) three-dimensional measurement errors, in mm of object space, are identified. To further evaluate these errors they may be compared to the dimensions of the volume elements surrounding the target considered.

This allows each 3-D measurement error to be related to the minimum resolvable distance in each axis of object space, thus, inaccuracies in the experimental procedure may be identified.
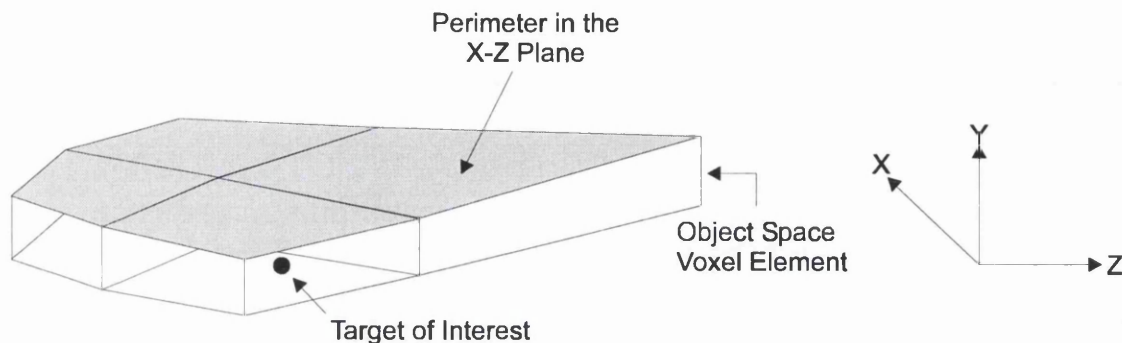
Figure 5-13 Representation of the Interlocking Structure of Volume Elements
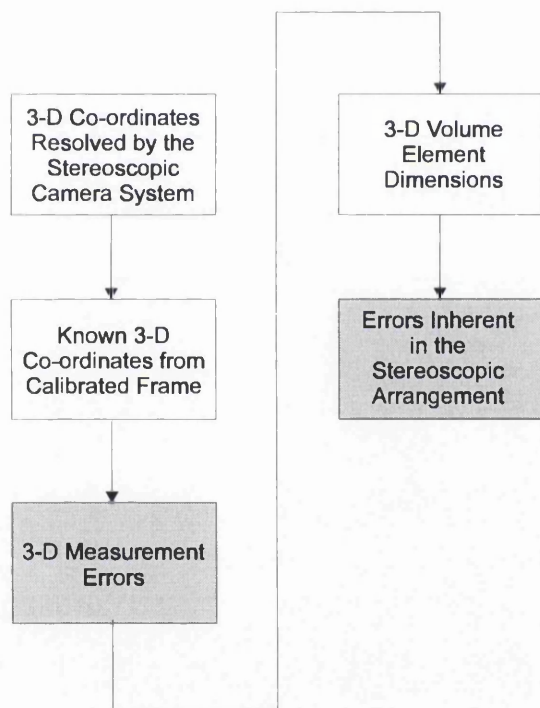
Figure 5-14 The Requirement for the Determination of Voxel Dimensions

Problems with the Imposition of a Cartesian Co-ordinate System on Voxel Structures:

The algorithms governing the extraction of 3-D co-ordinates are modelled initially on a cylindrical system (refer to Section 4.5.2). They are transformed into a cartesian format (Section 4.7) to allow comparison of co-ordinates resolved by the camera system with co-ordinates from a calibrated frame which is defined by a cartesian reference system. This allows an assessment of the measurement errors associated with the stereoscopic camera system.

These measurement inaccuracies may then be compared to the resolution available in object space. Resolving voxel dimensions using cartesian measurements is not ideal in defining the resolution of the line-scan system. However, to determine errors inherent in the arrangement some form of comparison must be used. Comparing co-ordinates resolved by the camera system with the equivalent known co-ordinate data provides a measure of accuracy with reference to the calibration frame, but, does not assess the inaccuracies inherent in the stereoscopic camera arrangement.

Ideally, to allow a direct comparison of measurement errors and voxel dimensions the co-ordinate information resolved by the camera system should be in a cylindrical format. This would require a calibrated frame defined by cylindrical co-ordinates instead of the cartesian volume used in this work.

The method of determining voxel dimensions from cartesian information resolved by the line-scan system is now described. Only the X-Z plane is considered as Y-axis measurements in cylindrical and cartesian systems are obtained in the same way. Whilst recognised as not being an ideal solution, results presented in Sections 5.6.6 and 5.6.7 demonstrate the validity of this approach.

5.6.2 The Cartesian Measurement of Voxel Dimensions

Consider the voxel structure in the X-Z plane for a given camera arrangement (Figure 5-15). This is a simplistic representation of the stereoscopic plane resulting from a range of x pixel values of 0 - 5 in left and right image space, where a 1 pixel increment governs the resolution available in object space. If a cartesian X-Z co-ordinate system is imposed on this plane, by translating along each axis, the X-Z plane intersects adjacent voxel boundaries.

Thus, from Figure 5-15, by transposing a cartesian plane on the cylindrical structure the dimensions of individual voxels may be identified from cartesian measurements. However, the mathematical model derived in Chapter 4.0 actually aligns the X-Z cartesian plane in object space with the camera base line at the start of rotation (Figure 5-16). Therefore, the X and Z information relating to voxel dimensions will be different from both Figure 5-15 and Figure 5-16 due to rotation of the X-Z plane from the 'ideal' position to the start of rotation base line.
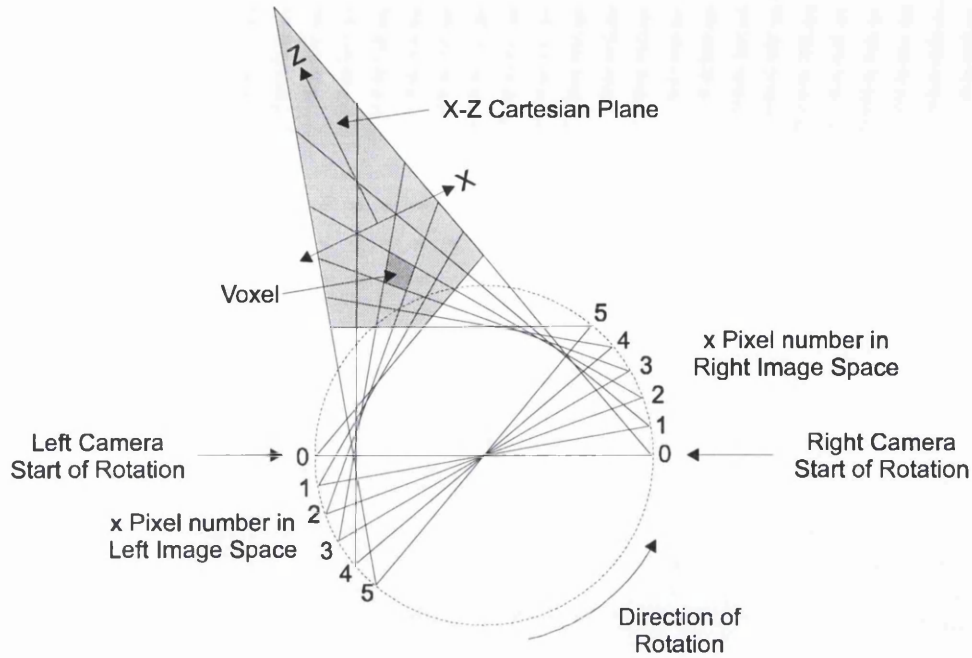
Figure 5-15 Ideal Cartesian X-Z Reference Plane for Measurement of Voxel Dimensions
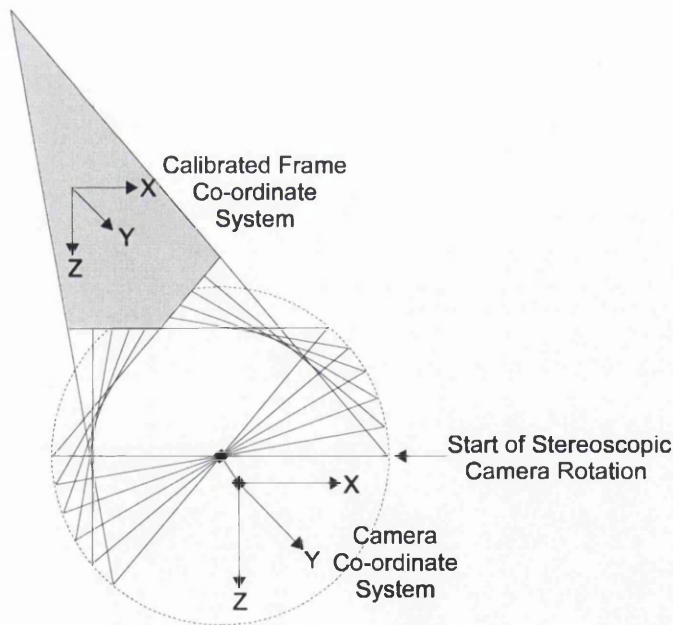
Figure 5-16 Actual Cartesian X-Z Plane Aligning the Camera and Object Co-ordinate Systems

The following examines the variation in X and Z axis voxel dimensions due to the rotation of the X-Z reference plane from the 'ideal' location (Figure 5-15) to the start of rotation base line (Figure 5-16).

Consider a voxel within the stereoscopic volume (Figure 5-17). The cylindrical dimension of the voxel in the X-axis is given by X_{vox_c}. However, when the cartesian information is referenced to the start base line a rotation of θ_x takes place. This results in a new voxel dimension of X_{vox} which is different in magnitude to X_{vox_c}.
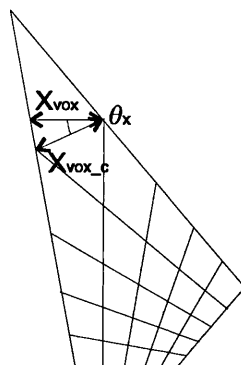
Figure 5-17 Apparent Change in Voxel Size in the X-axis Due to the Orientation of the X-Z Cartesian Reference Plane

From Figure 5-18 the Z-axis cylindrical dimension of the voxel is given by Z_{vox_c}. However, when the cartesian Z-axis information is referenced to the start base line a rotation of θ_z takes place. This results in a new dimension for the voxel of Z_{vox} which is different to the original magnitude.
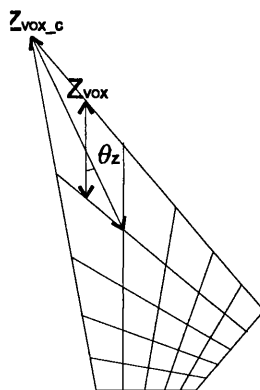
Figure 5-18 Apparent Change in Voxel Size in the Z-axis Due to the Orientation of the X-Z Cartesian Reference Plane

To establish if the cartesian dimensions X_{vox} and Z_{vox} are representative of volume elements in object space the effect of the rotation angle θ_x, which equals θ_z, on the magnitudes of the voxel in the X-Z plane must be evaluated. Results from this investigation, which are presented in Section 5.6.6, verify that resolved cartesian dimensions are representative of true voxel dimensions in object space.

The following sections describe the work which evaluates the algorithms (Section 4-10) in determining the available resolution for the stereoscopic arrangements considered in this work. Specifically, this is divided into the following :

- the general experimental procedure to determine voxel dimensions in object space, in mm / pixel;
- application of the theoretical procedure to the determination of equivalent voxel dimensions in object space, in mm / pixel;
- an example of both an experimental and theoretical evaluation of voxel dimensions for one experimental arrangement;
- an experiment to determine the applicability of resolving voxel dimensions in a cartesian format, as described previously in this section;
- the theoretical and experimental results to evaluate this section of the work.

5.6.3 The Experimental Determination of Voxel Dimensions

To evaluate the algorithms for the determination of voxel dimensions it is necessary to compare theoretical and known voxel sizes. To obtain voxel dimensions from object space an experimental procedure is defined which allows image values to be observed for known translations in object space. The objective of the work is to obtain voxel dimensions in selected parts of object space in mm / pixel which can be compared to equivalent theoretical values.

The Experimental Determination of Voxel Dimensions in the X- and Y-axes of Object Space :

To determine the size of voxels in object space a relationship is established between image space pixel values and known object space dimensions. To obtain image space measurements from the X and Y-axes of object space a square grid is used with targets positioned at equal increments between 0mm and 200mm in each axis (Figure 5-19). Another target is *fixed* in the FOV to allow relative pixel measurements to be made between this and each grid mark considered in each axis. Using a selected camera arrangement relative pixel measurements are made between grid increments and the fixed target at different camera-to-object distances. For each increment a pixel value is recorded. Thus, for known distances in the X- and Y-axes of object space equivalent x and y pixel information is obtained allowing voxel dimensions to be established in mm / pixel. The X and Y voxel dimensions can be determined from either left or right image space.

The grid used in this analysis is printed from an Hewlett Packard Laserjet 4 printer [129]. The resolution of the Laserjet is 600 dots per inch which is equivalent to 1 dot every 0.04mm. For this experimental work the accuracy of the grid information is one order of magnitude greater than that expected from this investigation. Indeed, the error due to translation of the grid along an optical rail is considered more significant than any error in the dimensions of the grid.

A photograph of the X-Y grid assembly used in this work is illustrated in Figure 5-20
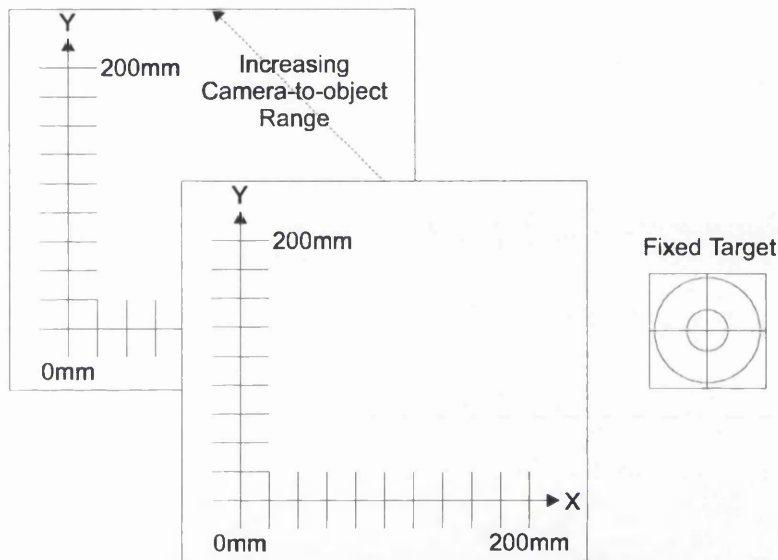
Figure 5-19 Experimental Grid for Voxel Measurements in the X- and Y-axes of Object Space
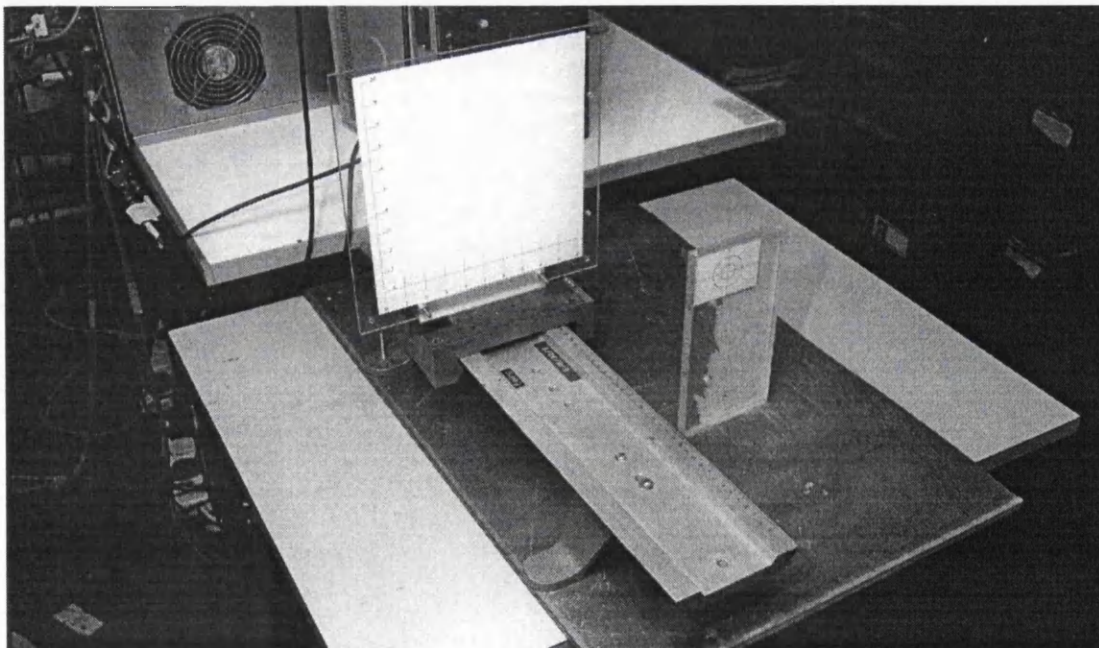
Figure 5-20 A Photograph of the X-Y Grid Assembly

Consider image space values, x_n and x_{n+1}, relating to adjacent increments of the target grid in the X-axis of object space (Figure 5-21), where X_{inc} is the distance between grid increments.
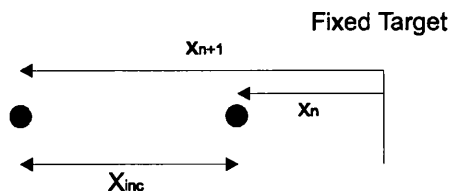
Figure 5-21 Calculation of Voxel Dimensions in the X-axis

To determine the size each pixel represents in the X-axis of object space a ratio of image to object space distances is evaluated. Thus, the available resolution in the X-axis is :

$$X_{vox(exp)} = \frac{X_{inc}}{(x_{n+1} - x_n)} = \frac{mm}{pixel} \qquad\qquad \text{Equation 5-3}$$

Where,

X_{inc} is the distance between adjacent increments in object space.

Using a similar approach to measurements from the Y-axis grid the object space resolution is :

$$Y_{vox(exp)} = \frac{Y_{inc}}{(y_{n+1} - y_n)} = \frac{mm}{pixel} \qquad\qquad \text{Equation 5-4}$$

Where,

Y_{inc} is the distance between adjacent increments in object space.

The Experimental Determination of Voxel Dimensions in the Z-axis of Object Space :

For image measurements from the Z-axis of object space a target is translated in increments between 0mm and 400mm (Figure 5-22) along an optical rail. Using a fixed reference target x pixel measurements are recorded from left and right image space at each range interval, thus, allowing the calculation of voxel dimensions in the Z-axis between adjacent target positions.
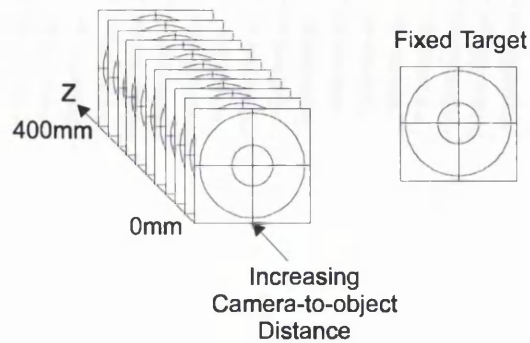
Figure 5-22 Experimental Arrangement for Voxel Measurements in the Z-axis

A photograph of the experimental arrangement used to obtain voxel dimensions in the Z-axis of object space is given in Figure 5-23.
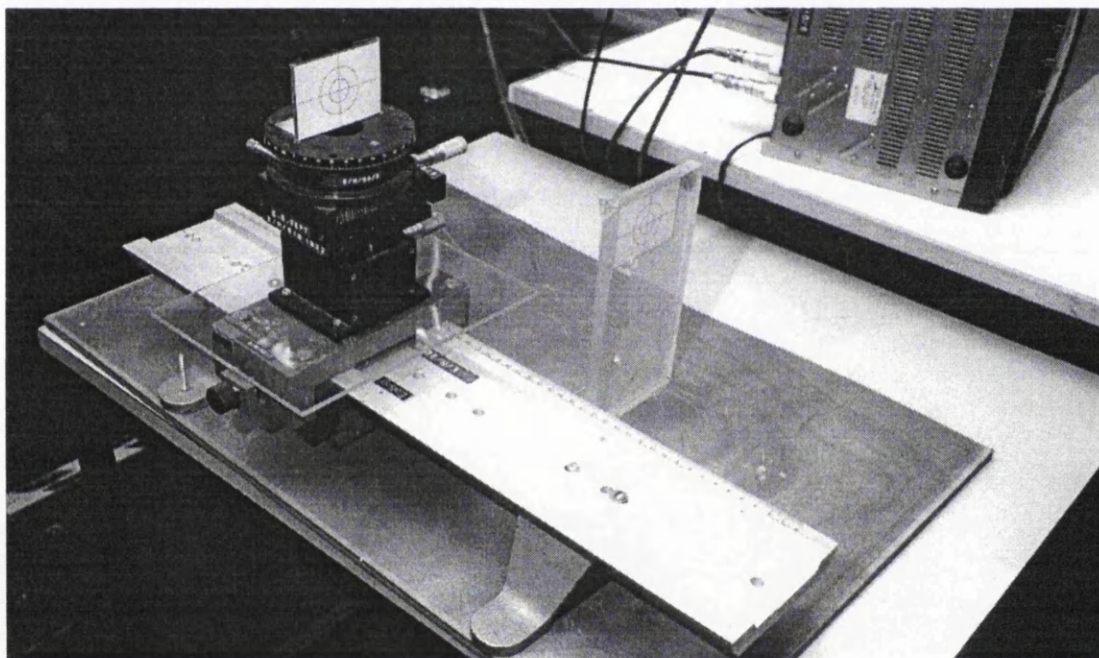
Figure 5-23 A Photograph of the Assembly Used to Determine Voxel Dimensions in the Z-axis

To determine the voxel size in the Z-axis of object space a quantity for disparity is resolved at each increment considered. Therefore, the difference in disparity at two known successive object space increments is used to determine the Z-axis resolution :

$$Z_{vox(exp)} = \frac{Z_{inc}}{\left|\left(x_{Ln} - x_{Rn}\right) - \left(x_{Ln+1} - x_{Rn+1}\right)\right|} = \frac{mm}{pixel} \qquad \text{Equation 5-5}$$

Where,

Z_{inc} is the distance between adjacent increments in object space.

For any stereoscopic arrangement the procedures described allow the resolution in selected parts of object space to be determined. The next section outlines the procedure for the theoretical determination of voxel dimensions equivalent to the experimentally observed values.

5.6.4 The Theoretical Determination of Voxel Dimensions

To determine the validity of the algorithms presented in Section 4.10 it is necessary to compare calculated resolution values with the equivalent experimental values obtained using the procedure described in Section 5.6.3. The procedure to obtain the theoretical resolution in each axis of object space is now described.

Theoretical Determination of Voxel Dimensions in the X-axis :

The procedure for the theoretical determination of the voxel resolution in the X-axis of object space is as follows :

- the left and right x image space pixel locations of the 20mm mark (Figure 5-19) obtained from the experimental procedure, described in Section 5.6.3, are used to calculate the theoretical X and Z co-ordinates of the mark location from Equation 4-20 and 4-22, respectively;

- a theoretical translation of -20mm in the X-axis is applied to calculate the theoretical pixel value x_a (Figure 5-24) using Equation 4-45 or Equation 4-46 dependent on whether left or right image space values, respectively, are considered. This calculated pixel value is the theoretical equivalent of the experimental value obtained from the 0mm grid mark;
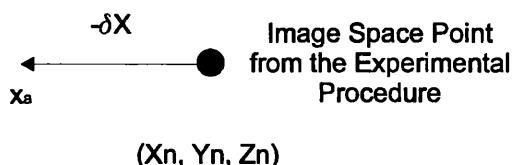
Figure 5-24 Determination of the Theoretical X-axis Resolution

- Once the pixel value, x_a, is calculated for the applied translation of -20mm the theoretical resolution is evaluated from the following expression :

$$X_{vox(cal)} = \frac{20}{|x - x_a|} = \frac{mm}{pixel}$$

Where,

x   ≡   the experimental x pixel value (from left or right image space) obtained from an X grid increment.

x_a ≡   the calculated x pixel value (pertaining to left or right image space) for a theoretical translation of -20mm from the original grid increment.

The procedure is repeated until the theoretical resolution, in mm / pixel, is obtained for all the grid increments considered in the experimental analysis. The theoretical resolutions obtained can be compared directly with those from the experimental procedure as, in both cases, the same increments in the X-axis of object space are considered.

Theoretical Determination of Voxel Dimensions in the Y-axis :

The procedure for the theoretical determination of the voxel resolution in the Y-axis of object space is as follows :

- the y pixel location of the 20mm grid mark, obtained from the experimental work, is used to calculate the theoretical Y co-ordinate of the mark location from Equation 4-21;

- a theoretical translation of -20mm in the Y-axis is applied to calculate the theoretical pixel value y_a (Figure 5-25) using Equation 4-55. This calculated pixel value is the theoretical equivalent of the experimental value obtained from the 0mm grid mark;
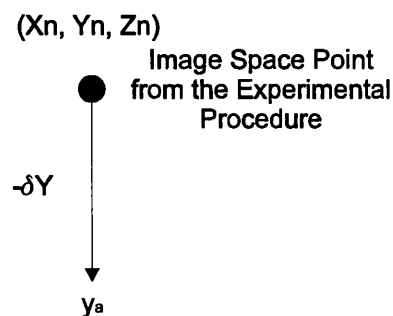
Figure 5-25 Determination of the Theoretical Y-axis Resolution

- Once the pixel value, y_a, is calculated for the applied translation of -20mm the theoretical resolution is evaluated from the following expression :

$$Y_{vox(cal)} = \frac{20}{|y - y_a|} = \frac{mm}{pixel}$$

Where,

y ≡ the experimental y pixel value obtained from a Y grid increment.

y_a ≡ the calculated y pixel value for a theoretical translation of -20mm from the original grid increment.

The procedure is repeated until the theoretical resolution, in mm / pixel, is obtained for all the grid increments considered in the experimental analysis. The theoretical resolutions obtained can be compared directly with those from the experimental procedure as, in both cases, the same increments in the Y-axis of object space are considered.

Theoretical Determination of Voxel Dimensions in the Z-axis :

The procedure for the determination of the Z-axis voxel resolution in object space is as follows :

- the left and right x pixel locations of the 0mm target position (Figure 5-22) obtained from the experimental procedure, described in Section 5.6.3, are used to calculate the theoretical X and Z co-ordinates of the target location from Equation 4-20 and 4-22 respectively;

- a theoretical translation of 40mm in the Z-axis is applied (Figure 5-26) to calculate the theoretical pixel disparity value $(x_L-x_R)_a$ from Equation 4-49 and Equation 4-50. This calculated disparity value is the theoretical equivalent of the experimental value obtained from the 40mm target position;

$(x_L-x_R)_a$

$+\delta Z$

Image Space Point
from the Experimental
Procedure

(Xn, Yn, Zn)
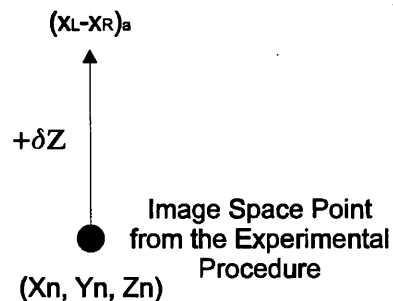
Figure 5-26 Determination of the Theoretical Z-axis Resolution

- Once the theoretical disparity value $(x_L\text{-}x_R)_a$ is calculated for the applied translation of 40mm the theoretical resolution is evaluated from the following expression :

$$Z_{vox(cal)} = \frac{40}{\left|\left(x_L - x_R\right) - \left(x_L - x_R\right)_a\right|} = \frac{mm}{pixel}$$

Where,

$(x_L\text{-}x_R)$ ≡   the experimental disparity value obtained from a Z target increment.

$(x_L\text{-}x_R)_a$ ≡   the calculated disparity value for a theoretical translation of +40mm from the original grid increment.

The procedure is repeated until the theoretical resolution, in mm / pixel, is obtained for all the increments considered in the experimental analysis. The theoretical resolutions obtained can be compared directly with those from the experimental procedure as, in both cases, the same increments in the Z-axis of object space are considered.

5.6.5 Determining Voxel Dimensions : An Example

This section presents experimentally and theoretically determined voxel dimensions for one stereoscopic arrangement considered in this work. The accuracy of each calculated voxel dimension is to 0.1mm. The minimum resolvable object space increment is expected to be 0.5mm, thus, the calculation accuracy is, at worst, five times better than object space resolution.

The following abbreviations are used in presentation of the results :

X_{inc} ≡   the translation increment in the X-axis of object space, in mm;

Y_{inc} ≡   the translation increment in the Y-axis of object space, in mm;

Z_{inc} ≡   the translation increment in the Z-axis of object space, in mm;

x_L ≡   observed x pixel value from left image space, in pixels;

x_R ≡   observed x pixel value from right image space, in pixels;

y ≡   observed y pixel value, in pixels;

$XL_{vox(exp)}$ ≡   X-axis resolution determined from experimental observations in left image space, in mm / pixel;

$XR_{vox(exp)}$ ≡   X-axis resolution determined from experimental observations in right image space, in mm / pixel;

$X_{vox(exp)} \equiv$ the average X-axis resolution determined from experimental observations, in mm / pixel;

$Y_{vox(exp)} \equiv$ the Y-axis resolution determined from experimental observations, in mm / pixel;

$Z_{vox(exp)} \equiv$ the Z-axis resolution determined from experimental observations, in mm / pixel;

$XL_{vox(cal)} \equiv$ the theoretical X-axis resolution from left image space, in mm / pixel;

$XR_{vox(cal)} \equiv$ the theoretical X-axis resolution from right image space, in mm / pixel;

$X_{vox(cal)} \equiv$ the average theoretical X-axis resolution, in mm / pixel;

$Y_{vox(cal)} \equiv$ the theoretical Y-axis resolution, in mm / pixel;

$Z_{vox(cal)} \equiv$ the theoretical Z-axis resolution, in mm / pixel.

For this work a stereoscopic camera arrangement is considered with the following settings :

Base width (mm)	500
Convergence Angle (degrees)	80
Focal Length (mm)	25
Camera Scan Rate (kHz)	100
Platform Rotation Speed (rpm)	0.67
Camera-to-object range (mm)	1100-1600

Determination of Voxel Dimensions in the X-axis of Object Space :

For this experimental arrangement, at a camera-to-object distance of 1100mm, consider the observed pixel data in the x-axis of image space (Table 5-9). For the incremental distance from 0mm to 20mm on the X-axis grid (Figure 5-19) the observed left pixel distance changes from 520 to 497 pixels. This gives a voxel resolution in the X-axis of :

$$XL_{vox(exp)} = \left(\frac{20}{|520 - 497|} \right) = 0.9 \text{ mm / pixel}$$

For the first incremental distance, from 0mm to 20mm, on the X-axis grid the observed right pixel value changes from 625 to 601 pixels (Table 5-9), giving an X-axis voxel resolution of :

$$XR_{vox(exp)} = \left(\frac{20}{|625 - 601|} \right) = 0.8 \text{ mm / pixel}$$

Therefore, to determine the mean voxel size in the X-axis of object space, as observed from the left and right images, the values of $XL_{vox(exp)}$ and $XR_{vox(exp)}$ are averaged to give $X_{vox(exp)}$ equal to 0.9 mm / pixel for the grid increment 0mm to 20mm. This procedure is repeated for every increment in the X-axis grid, i.e., from 20mm to 40mm, from 40mm to 60mm, etc.

To obtain the equivalent theoretical voxel size in the X-axis, initially, the X and Z co-ordinate values in object space are calculated using the image space values obtained experimentally from the 20mm mark on the X grid. The X co-ordinate value (Equation 4.20) is :

$$X = \frac{500\sin 80\sin\left(k_x\left(\dfrac{-601-497}{2}\right)\right)}{2\cos\left(80+\left(k_x\left(\dfrac{497-601}{2}\right)\right)\right)} = -449.9mm$$

Where k_x is the pixel-to-angle conversion factor (Equation 3.7) and for the experimental arrangement considered here equals 0.04.

The Z co-ordinate value, obtained from Equation 4.22, is :

$$Z = \frac{500\sin 80\cos\left(k_x\left(\dfrac{-601-497}{2}\right)\right)}{2\cos\left(80+\left(k_x\left(\dfrac{497-601}{2}\right)\right)\right)} = 1080.8mm$$

From Equation 4.42 the modified left pixel value which relates to a theoretically applied translation of -20mm, i.e., coincident with the 0mm grid mark, is :

$$\{x_L\}_{-\delta x} = \frac{1}{k_x}\cdot\left(\left(\left(\cos^{-1}\left(\frac{500\sin 80\sin\left(\tan^{-1}\left(\dfrac{|1080.8|}{|-449.9-20|}\right)-90\right)}{2.(-449.9-20)}\right)-80\right)+\left(90-\tan^{-1}\left(\dfrac{|1080.8|}{|-449.9-20|}\right)\right)\right)\right) = 520.8\,pixels$$

Therefore, for a theoretical translation of -20mm the new pixel location is determined as 520.8, which corresponds to the pixel location recorded experimentally of 520.

The theoretical resolution is now determined using the experimental pixel location at 20mm and the pixel value calculated for 0mm. Therefore, for the theoretical translation of - 20mm the size of the X-axis voxels is :

$$XL_{vox(cal)} = \frac{20}{520.8 - 497} = 0.8mm / pixel$$

Using the same method Equation 4.42 is used to find the modified right pixel value which relates to a theoretically applied translation of -20mm :

$$\{x_R\}_{-\delta x} = \frac{1}{k_x} \cdot \left(\left(-\cos^{-1}\left(\frac{500\sin 80 \sin\left(\tan^{-1}\left(\frac{|1080.8|}{|-449.9-20|}\right) - 90\right)}{2.(-449.9-20)} \right) - 80 \right) + \left(90 - \tan^{-1}\left(\frac{|1080.8|}{|-449.9-20|}\right)\right) \right) = 620.8 pixels$$

Therefore, for a theoretical translation of -20mm the new pixel location is determined as 620.8 which corresponds to the experimental pixel location of 625.

The theoretical resolution is now determined using the experimental pixel location at 20mm and the pixel value calculated for 0mm. Therefore, for the theoretical translation of - 20mm the size of the X-axis voxels are :

$$XR_{vox(cal)} = \frac{20}{620.8 - 601} = 1.0mm / pixel$$

To determine the mean voxel size in the X-axis, as calculated from the left and right images, the values of $XL_{vox(cal)}$ and $XR_{vox(cal)}$ are averaged to give $X_{vox(exp)}$ equal to 0.9 mm / pixel for the grid increment 0mm to 20mm. This procedure is repeated for each incremental step in the X-axis grid, i.e., from 20mm to 40mm, from 40mm to 60mm, etc.

Table 5-9 presents the results for the experimental and calculated resolution values for all considered increments on the X-axis grid, at a camera-to-object range of 1100mm. Table 5-10 presents the results pertaining to the experimental and calculated resolution values for all considered increments on the X-axis grid, at a camera-to-object range of 1500mm.

X_{inc}	X_L	X_R	$XL_{vox(exp)}$	$XL_{vox(cal)}$	$XR_{vox(exp)}$	$XR_{vox(cal)}$	$X_{vox(exp)}$	$X_{vox(cal)}$
mm	pixels	pixels	mm/pixel	mm/pixel	mm/pixel	mm/pixel	mm/pixel	mm/pixel
0	520	625	*	*	*	*	*	*
20	497	601	0.9	0.8	0.8	1.0	0.9	0.9
40	472	578	0.8	0.8	0.9	1.0	0.8	0.9
60	449	555	0.9	0.8	0.9	1.0	0.9	0.9
80	427	533	0.9	0.8	0.9	1.0	0.9	0.9
100	402	511	0.8	0.8	0.9	1.0	0.9	0.9
120	377	486	0.8	0.8	0.8	0.9	0.8	0.9
140	354	462	0.9	0.8	0.8	0.9	0.9	0.9
160	331	440	0.9	0.8	0.9	0.9	0.9	0.9
180	308	417	0.9	0.8	0.9	0.9	0.9	0.9
200	283	393	0.8	0.8	0.8	0.9	0.8	0.9
mean (mm/pixel)			0.9	0.8	0.9	1.0	0.9	0.9

Table 5-9 Experimental and Calculated Voxel Dimensions in the X-axis of Object Space for a Camera-to-object Range of 1100mm

The '-' indicates no measurement could be made as the grid mark was not in the stereoscopic field of view and '*' indicates no voxel resolution value could be determined as two adjacent grid increments are required.

X_{inc}	X_L	X_R	$XL_{vox(exp)}$	$XL_{vox(cal)}$	$XR_{vox(exp)}$	$XR_{vox(cal)}$	$X_{vox(exp)}$	$X_{vox(cal)}$
mm	pixels	pixels	mm/pixel	mm/pixel	mm/pixel	mm/pixel	mm/pixel	mm/pixel
0	262	223	*	*	*	*	*	*
20	245	204	1.2	1.1	1.1	1.2	1.1	1.1
40	227	186	1.1	1.1	1.1	1.2	1.1	1.1
60	209	169	1.1	1.1	1.2	1.1	1.1	1.1
80	190	153	1.1	1.1	1.3	1.1	1.2	1.1
100	173	136	1.2	1.1	1.2	1.1	1.2	1.1
120	155	117	1.1	1.1	1.1	1.1	1.1	1.1
140	138	98	1.2	1.1	1.1	1.1	1.1	1.1
160	120	81	1.1	1.1	1.2	1.1	1.2	1.1
180	102	63	1.1	1.1	1.1	1.1	1.1	1.1
200	83	-	1.1	-	-	-	-	-
mean (mm/pixel)			1.1	1.1	1.1	1.1	1.1	1.1

Table 5-10 Experimental and Calculated Voxel Dimensions in the X-axis of Object Space for a Camera-to-object Range of 1500mm

Determination of Voxel Dimensions in the Y-axis of Object Space :

For this experimental arrangement consider the observed pixel data in the y-axis of image space (Table 5-11), for a camera-to-object range of 1100mm. For the incremental distance from 0mm to 20mm on the Y-axis grid (Figure 5-19) the observed pixel distance changes from 637 to 605 pixels. This gives a voxel resolution in the Y-axis of :

$$Y_{vox(exp)} = \left(\frac{20}{|637 - 605|} \right) = 0.6 \text{ mm} / \text{pixel}$$

This procedure is repeated for each incremental step in the Y-axis grid, i.e., from 20mm to 40mm, from 40mm to 60mm, etc.

To obtain the equivalent theoretical resolution values, initially, the object space Y co-ordinate which relates to the image space value at the 20mm mark is calculated. Using the values of x_L and x_R from the 0mm X grid mark the Y co-ordinate (Equation 4.21) is :

$$Y = \frac{500(512 - 605)0.013}{50} \cdot \frac{\cos\left(-k_x \left(\frac{520 - 625}{2} \right) \right)}{\cos\left(80 + \left(k_x \left(\frac{520 - 625}{2} \right) \right) \right)} = -57.5$$

The Y co-ordinate value and the translation value of -20mm is substituted into Equation 4-55 to determine the theoretical pixel value coincident with the 0mm mark on the Y-axis grid. This is calculated as follows :

$$y - \delta y = 512 - \left(\frac{(-57.5 - 20)50\cos\left(80 + \left(k_x \left(\frac{520 - 625}{2} \right) \right) \right)}{500.0.013\cos\left(-k_x \left(\frac{520 - 625}{2} \right) \right)} \right) = 637.7$$

Therefore, for a theoretical translation of -20mm the new pixel location is determined as 637.7 which is equivalent to the experimental pixel location of 637.

The theoretical resolution is now determined using the experimental pixel location at 20mm and the pixel value calculated for 0mm. Therefore, for the theoretical translation of - 20mm the size of the Y-axis voxels are :

$$Y_{vox(cal)} = \frac{20}{637.7 - 605} = 0.6 \text{ mm} / \text{pixel}$$

This procedure is repeated for each incremental step in the Y-axis grid, i.e., from 20mm to 40mm, from 40mm to 60mm, etc.

Table 5-11 presents the results for the experimental and calculated resolution values for all considered increments on the Y-axis grid, at a camera-to-object range of 1100mm. Table 5-12 presents the results pertaining to the experimental and calculated resolution values for all considered increments on the Y-axis grid, at a camera-to-object range of 1500mm.

Y_{inc} mm	y pixels	$Y_{vox(exp)}$ mm/pixel	$Y_{vox(cal)}$ mm/pixel
0	637	*	*
20	605	0.6	0.6
40	573	0.6	0.6
60	543	0.7	0.6
80	511	0.6	0.6
100	480	0.7	0.6
120	448	0.6	0.6
140	417	0.7	0.6
160	386	0.7	0.6
180	355	0.7	0.6
200	324	0.7	0.6
mean value (mm/pixel)		0.7	0.6

Table 5-11 Experimental and Calculated Voxel Dimensions in the Y-axis of Object Space for a Camera-to-object Range of 1100mm

Y_{inc} mm	y pixels	$Y_{vox(exp)}$ mm/pixel	$Y_{vox(cal)}$ mm/pixel
0	613	*	*
20	589	0.8	0.8
40	566	0.9	0.8
60	542	0.8	0.8
80	518	0.8	0.8
100	495	0.9	0.8
120	471	0.8	0.8
140	447	0.8	0.8
160	425	0.9	0.8
180	401	0.8	0.8
200	377	0.8	0.8
mean value (mm/pixel)		0.8	0.8

Table 5-12 Experimental and Calculated Voxel Dimensions in the Y-axis of Object Space for a Camera-to-object Range of 1500mm

Determination of Voxel Dimensions in the Z-axis of Object Space :

Consider the observed pixel data in the x-axis of image space (Table 5-13). For the incremental distance from 40mm to 80mm on the Z-axis target (Figure 5-22) the disparity value changes from -55 to -37 pixels. This gives a voxel resolution in the Z-axis of :

$$Z_{vox(exp)} = \left(\frac{40}{|-55+37|} \right) = 2.2 \text{ mm} / \text{pixel}$$

To determine the equivalent theoretical Z-axis resolution the X and Z co-ordinates for the image space values of the 40mm target position are calculated. The X co-ordinate (Equation 4.20) is :

$$X = \frac{500 \sin 80 \sin \left(k_x \left(\frac{-200-145}{2} \right) \right)}{2 \cos \left(80 + \left(k_x \left(\frac{145-200}{2} \right) \right) \right)} = -157.7mm$$

The Z co-ordinate value, obtained from Equation 4.22, is as follows :

$$Z = \frac{500 \sin 80 \cos \left(k_x \left(\frac{-200-145}{2} \right) \right)}{2 \cos \left(80 + \left(k_x \left(\frac{145-200}{2} \right) \right) \right)} = 1265.4mm$$

Equation 4.49 is used to find the modified left pixel value which relates to a theoretically applied translation of +40mm, i.e., the point coincident with the 80mm target position :

$$\{x_L\}_{\delta z} = \frac{1}{k_x} \left(\left(\cos^{-1} \left(\frac{500 \sin 80 \cos \left(\tan^{-1} \left(\frac{|1265.4+40|}{|157.7|} \right) - 90 \right)}{2(1265.4+40)} \right) - 80 \right) + \left(90 - \tan^{-1} \left(\frac{|1265.4+40|}{|157.7|} \right) \right) \right)$$

The expression above yields a modified left pixel value of 148.1. Equation 4.50 is then used to find the modified right pixel value which relates to a theoretically applied translation of +40mm :

$$\{x_R\}_{\delta z} = \frac{1}{k_x}\left(\left(-\left(\cos^{-1}\left(\frac{500\sin80\cos\left(\tan^{-1}\left(\frac{|1265.4+40|}{|157.7|}\right)-90\right)}{2(1265.4+40)}\right)-80\right)\right)+\left(90-\tan^{-1}\left(\frac{|1265.4+40|}{|157.7|}\right)\right)\right)$$

The expression above yields a modified left pixel value of 186.6. Therefore, for a theoretical translation of the Z-axis target to the 80mm position the theoretical disparity value is -38.5 which is equivalent to the value obtained experimentally of -37.

The theoretical resolution is determined from the experimental disparity value at 40mm and the disparity calculated at 80mm. Thus, for the translation of 40mm the size of the Z-axis voxels is :

$$Z_{vox(cal)} = \frac{40}{-38.5+55} = 2.4mm\,/\,pixel$$

This procedure is repeated for each incremental step in the Z-axis, i.e., at 80mm to 120mm, at 120mm to 160mm, etc. Table 5-13 presents the results for the experimental and calculated resolution values for the considered increments in the Z-axis, at camera-to-object ranges between 1200 - 1600mm.

Z_{inc} mm	X_L pixels	X_R pixels	$(X_L\text{-}X_R)$ pixels	$Z_{vox(exp)}$ mm/pixel	$Z_{vox(cal)}$ mm/pixel
0	138	211	-73	-	-
40	145	200	-55	2.2	2.4
80	152	189	-37	2.2	2.4
120	159	177	-18	2.1	2.7
160	166	169	-3	2.7	2.9
200	171	160	11	2.9	3.1
240	177	152	25	2.9	3.2
280	181	144	37	3.3	3.4
320	186	137	49	3.3	3.6
360	191	130	61	3.3	3.8
400	196	124	72	3.6	4.0
mean value (mm/pixel)				2.9	3.2

Table 5-13 Experimental and Calculated Voxel Dimensions in the Z-axis of Object Space

An example of the procedure used to determine theoretical and experimental voxel dimensions has been given. To determine the suitability of the algorithms for the identification of true voxel sizes in object space the effect of rotating the X-Z cartesian reference plane is now investigated, as discussed in Section 5.6.2. This is achieved by maintaining a constant camera scan start plane and rotating the experimental arrangements (Figure 5-20 and Figure 5-23) in the X-Z plane at varying angular increments with respect to the start of scan.

5.6.6 The Effect of Object Rotation on the Cartesian Representation of Voxel Dimensions

The dimensions of voxels in the X-Z plane can be approximated using a cartesian reference plane, as described in Section 5.6.2. However, as the X-Z reference plane is aligned with the start of camera rotation (Figure 5-15) and not with the voxel structure itself (Figure 5-16) the actual X-Z cartesian voxel measurements will differ from their true size in object space. Therefore, to determine if the algorithms developed in Section 4.10 can be used to calculate voxel dimensions the effect of rotating the X-Z reference plane is now examined. This is achieved by placing the experimental apparatus (refer to Figure 5-20 and Figure 5-23) used to obtain X, Y and Z voxel measurements in object space at varying angles with respect to the start of the camera rotation base line. At each angular position the X, Y and Z voxel dimensions are determined both experimentally and theoretically.

The results presented are the mean resolution values in each axis, i.e., the object space resolution is determined, as explained in Sections 5.6.3, 5.6.4 and 5.6.5, and a mean value is calculated from all the voxel dimensions obtained in each axis to allow comparison of these values for each X-Z rotation considered. Rotations of 0°, 20° and 40° are considered sufficient to evaluate the suitability of the cartesian algorithms in determining voxel dimensions.

Experimental Hypothesis :

"To evaluate the affect of object rotation in the X-Z plane on theoretical and experimental voxel dimensions measured in 3-D object space."

For this experiment a stereoscopic arrangement is considered with the following settings :

Base width (mm)	500
Convergence Angle (degrees)	80
Focal Length (mm)	25
Camera Scan Rate (kHz)	200
Platform Rotation Speed (rpm)	0.67
Camera-to-object range (mm)	1200-1600

To allow the X-Y grid and the Z target to be rotated through defined increments in object space a rotary table was used (Figure 5-27). For the object rotations considered this device is deemed sufficiently accurate for any errors in the rotation setting to be ignored.
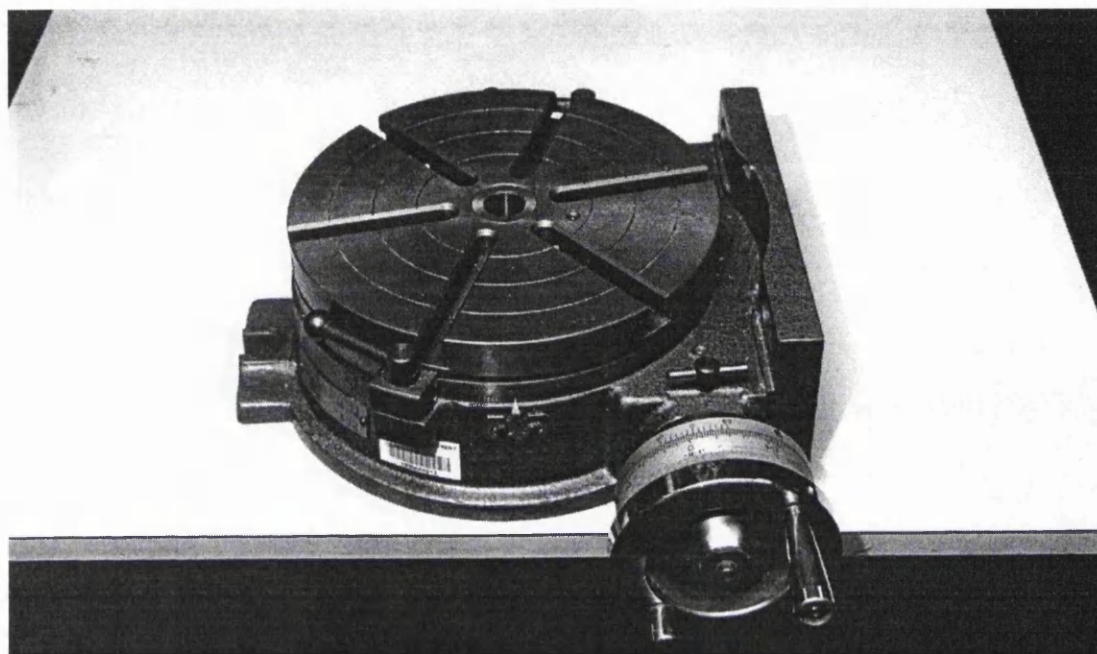
Figure 5-27 Rotary Table with Worm Drive

For voxel measurements in the X-Y grid a camera-to-object distance of 1200mm was considered and for measurements in the Z-axis of object space camera-to-object distances of between 1200mm and 1600mm were used.

Table 5-14 contains the results from this experiment. The voxel dimensions in the Y-axis remained constant as expected due to rotating the object in only the X-Z plane. In both the X-axis and Z-axis of object space the maximum difference between experimental and theoretical mean voxel dimensions is 0.2mm.

Rotation (°)	$X_{vox(exp)}$ mm/pixel	$X_{vox(cal)}$ mm/pixel	$Y_{vox(exp)}$ mm/pixel	$Y_{vox(cal)}$ mm/pixel	$Z_{vox(exp)}$ mm/pixel	$Z_{vox(cal)}$ mm/pixel
0	0.4	0.4	0.6	0.6	1.4	1.6
20	0.5	0.4	0.6	0.6	1.4	1.3
40	0.6	0.4	0.6	0.6	1.6	1.4

Table 5-14 The Effects of X-Z Plane Rotation on X, Y and Z Voxel Dimensions

As described in Section 5.6.2 the cartesian measurement of voxel dimensions is expected to change due to rotation of the X-Z reference plane from the ideal position (where the X-Z axis intersects adjacent voxel boundaries) to the start of rotation base line. However, from the experiment conducted it is demonstrated that a worst case rotation of the X-Z plane results in a maximum change of 0.2mm in X and Z object space voxel dimensions.

For the 0° rotation the mean voxel dimension in the X-axis is 0.4mm / pixel, thus, the maximum change of 0.2mm would have the greatest significance in this case. This gives a maximum possible error of 0.5 pixels when determining the resolution in object space. As the available resolution in image space is 1 pixel the change in voxel dimensions is considered sufficiently small to allow use of the derived algorithms in determining the system resolution.

Experimental Conclusion :

"From this work the use of cartesian measurements is validated for the evaluation of voxel characteristics within the stereoscopic volume."

The following section compares theoretical and experimental voxel dimensions for variations in selected stereoscopic parameters to provide a further test for the algorithms developed in Section 4.10.

5.6.7 Validation of the Algorithms in Determining Voxel Dimensions

The factors which govern image production, and hence the available resolution in object space, for the stereoscopic camera arrangement are as follows :

- camera base width;
- camera-to-base convergence angle;
- camera-to-object range;
- focal length of the camera lens;
- camera scan rate;
- camera rotation speed.

To evaluate the resolution algorithms theoretical values are compared to experimental values for a variation in camera scan rate, rotation speed and camera-to-object distance.

The base width, convergence angle and focal length of the camera arrangement are system geometric parameters whereas the scan rate and rotation speed directly determine the production of images from object space. Thus, it is considered that if the algorithms are corroborated for one geometric arrangement and variations in scan rate, rotation speed and camera-to-object range they may be applied to any stereoscopic arrangement of rotating line-scan cameras.

Experimental Hypothesis :

"To determine voxel dimensions in object space in all three co-ordinate axes and thereby validate the algorithms."

Experimental Conditions :

Base width (mm)	500
Convergence Angle (degrees)	80
Focal Length (mm)	25
Camera Scan Rate (kHz)	100 - 300
Platform Rotation Speed (rpm)	0.67 - 2.00
Camera-to-object range (mm)	1200-1600

For this work the scan rate is varied in 5 incremental steps between 100kHz and 300kHz whilst maintaining a rotation speed of 0.67 rpm. A variation in rotation speed in 5 incremental steps between 0.67rpm and 2rpm is then considered whilst maintaining a camera scan rate of 200kHz. For these parameter variations the experimental and theoretical voxel dimensions are obtained using the methodology described in Section 5.6.3 and Section 5.6.4, respectively.

Table 5-15, Table 5-16 and Table 5-17 present results for observed and calculated X, Y and Z-axis mean resolution values for a variation in camera scan rate from 100kHz to 300kHz.

D_{CO} (mm)	1100		1500	
F_{SR} (kHz)	$X_{vox(exp)}$	$X_{vox(cal)}$	$X_{vox(exp)}$	$X_{vox(cal)}$
100	0.9	0.9	1.1	1.1
150	0.6	0.6	0.8	0.8
200	0.4	0.4	0.6	0.6
250	0.4	0.3	0.5	0.5
300	0.3	0.3	0.4	0.4

Table 5-15 Calculated and Observed X-axis Voxel Dimensions, in mm / pixel, for a Variation in Camera Scan Rate

D_{CO} (mm)	1100		1500	
F_{SR} (kHz)	$Y_{vox(exp)}$	$Y_{vox(cal)}$	$Y_{vox(exp)}$	$Y_{vox(cal)}$
100	0.6	0.6	0.9	0.8
150	0.6	0.6	0.9	0.8
200	0.6	0.6	0.9	0.8
250	0.6	0.6	0.9	0.8
300	0.6	0.6	0.9	0.8

Table 5-16 Calculated and Observed Y-axis Voxel Dimensions, in mm / pixel for a Variation in

Camera Scan Rate

Camera-to-object Distance = 1200mm - 1600mm		
F_{SR} (kHz)	$Z_{vox(exp)}$	$Z_{vox(cal)}$
100	2.9	3.2
150	2.0	2.1
200	1.4	1.6
250	1.2	1.3
300	1.0	1.1

Table 5-17 Calculated and Observed Z-axis Voxel Dimensions, in mm / pixel, for a Variation in

Camera Scan Rate

Table 5-18, Table 5-19 and Table 5-20 present results showing the observed and calculated

mean resolution values for a variation in camera rotation speed from 0.67 to 2.00 rpm.

D_{CO} (mm)	1100mm		1500mm	
S_R(rpm)	$X_{vox(exp)}$	$X_{vox(cal)}$	$X_{vox(exp)}$	$X_{vox(cal)}$
0.67	0.4	0.4	0.6	0.6
1.00	0.7	0.7	0.9	0.9
1.34	0.9	1.0	1.2	1.2
1.67	1.1	1.1	1.5	1.7
2.00	1.3	1.6	1.7	1.9

Table 5-18 Calculated and Observed X-axis Voxel Dimensions, in mm / pixel, for a Variation in

Rotation Speed

D_{CO} (mm)	1100mm		1500mm	
S_R(rpm)	$Y_{vox(exp)}$	$Y_{vox(cal)}$	$Y_{vox(exp)}$	$Y_{vox(cal)}$
0.67	0.6	0.6	0.9	0.8
1.00	0.6	0.6	0.9	0.8
1.34	0.6	0.6	0.9	0.8
1.67	0.6	0.6	0.9	0.8
2.00	0.6	0.6	0.9	0.8

Table 5-19 Calculated and Observed Y-axis Voxel Dimensions, in mm / pixel, for a Variation in

Rotation Speed

Camera-to-object Distance = 1200mm - 1600mm		
S_R(rpm)	$Z_{vox(exp)}$	$Z_{vox(cal)}$
0.67	1.4	1.6
1.00	2.2	2.4
1.34	3.0	3.2
1.67	3.7	4.0
2.00	4.4	4.8

Table 5-20 Calculated and Observed Z-axis Voxel Dimensions, in mm / pixel, for a Variation in

Rotation Speed

As observed from the results in Table 5-15, Table 5-16, Table 5-17, Table 5-18, Table 5-19 and Table 5-20 the experimental and calculated voxel dimensions for variation of the range, camera scan rate and rotation speed validate the theoretical analysis undertaken. Therefore, the theoretical algorithms for determination of 3-D voxel dimensions in object space are verified for use with the stereoscopic system.

Experimental Conclusion :

"The theoretical algorithms for determination of 3-D voxel dimensions and, therefore, the available resolution in object space, are verified for use with the rotating line-scan system."

5.7 The Co-ordinate Measurement Capability of the Rotating Stereoscopic System

This section evaluates the applicability of the mathematical model to the stereoscopic system for the extraction of 3-D co-ordinates from object space. This work will examine :

- the selection of calibration control targets from the calibration frame;
- variation of the stereoscopic image start point in the camera rotation;
- the accuracy and precision of 3-D co-ordinate measurements;
- the affect of changing the camera / object system alignment;
- resolving 3-D vectors from object space.

Once the optimum control target configuration for use in the calibration procedure is identified the affect of varying the start of image capture in the camera rotation is addressed. Subsequently, the accuracy and precision of the 3-D co-ordinate measurements is established. Following this, the mathematical model is tested for variations in camera / object system alignment to provide further evidence to validate the use of the 3-D transformation. Finally, the capability of the camera system to determine 3-D vectors from object space is evaluated.

5.7.1 Experimental Approach to the Co-ordinate Measurement Analysis

For each pair of perspective images obtained from the camera arrangements considered the general approach to the experimentation consists of the following phases (Figure 5-28) :

- calibration of the stereoscopic camera system using control targets selected from the calibration frame in object space;
- calculation of the 3-D co-ordinates using different targets selected from the calibration frame;
- identification of the 3-D co-ordinate measurement errors.
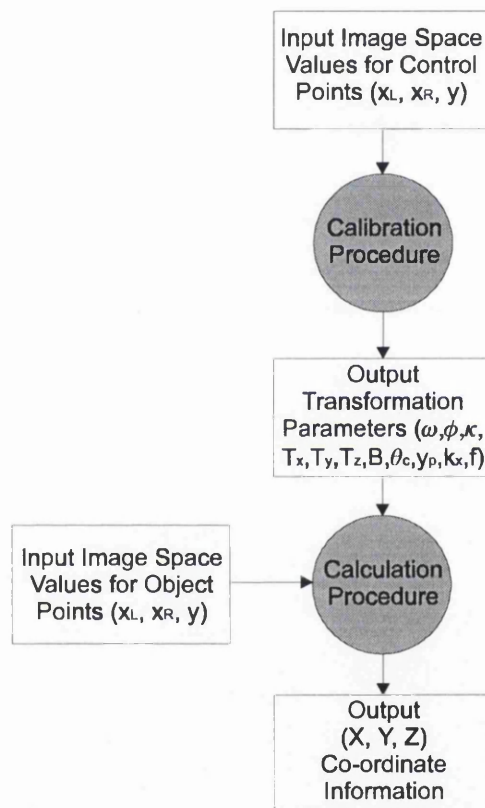
Figure 5-28 Resolving 3-D Co-ordinate Measurements Using the Stereoscopic System

The Calibration Procedure :

The camera system is calibrated by applying the 3-D conformal transformation derived specifically for the line-scan set-up. For each pair of perspective images obtained control points are selected. The observed x and y image data is saved to a file and passed to the calibration procedure which returns the transformation parameters necessary to mathematically align the camera and calibration frame. The derivation of this mathematical model is in Appendix D and is based on the general procedure outlined by Wolf [96] (refer to Section 2.3.4 and Section 4.8).

The Calculation Procedure :

The calculation procedure applies the calculated transformation parameters to image space co-ordinates of different object points selected from the calibration frame. The error in the resolved 3-D point co-ordinates are then calculated for each experimental set-up.

Both the 3-D conformal transformation calibration and calculation procedures are implemented in the 'C' software language in the program 'cam_xyz.c' [130].

Evaluating 3-D Measurement Errors :

For each experimental set-up, unless stated otherwise, three consecutive passes of the calibration frame are made to provide three sets of resolved 3-D co-ordinates relating to the same arrangement. Thus, the co-ordinate errors for each target are the mean of three runs. This procedure is adopted to provide experimental data which gives a reliable evaluation of the measurement capability associated with the rotating stereoscopic camera system.

5.7.2 Sample Images Obtained from the Rotating Stereoscopic Line-scan System

Before discussing the results from the stereoscopic investigation sample images obtained from the line-scan system are presented. These contain information of the calibration frame in object space from which targets are selected for use in the calibration and calculation procedures. The general experimental arrangement from which the images are taken is :

Camera-to-object range (mm)	1500
Base width (mm)	500
Convergence Angle (degrees)	80
Platform Rotation Speed (rpm)	2.0

Figure 5-29, Figure 5-30 and Figure 5-31 show left and right perspective images with a camera-lens focal length of 25mm, 50mm and 75mm, respectively, whilst maintaining a camera scan rate of 200kHz. In each view the target points are identified clearly, thus, demonstrating the suitability of the calibrated frame for use with the line-scan system.
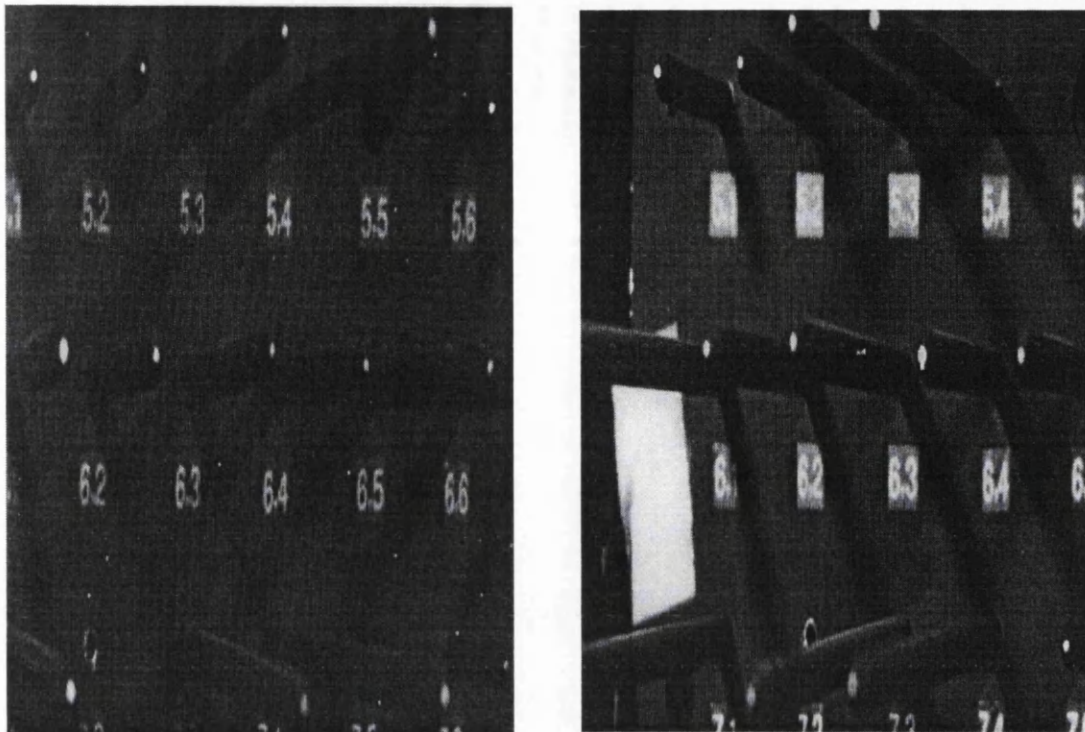
Figure 5-29 Left and Right Perspective Images with a Camera-lens Focal Length of 75mm
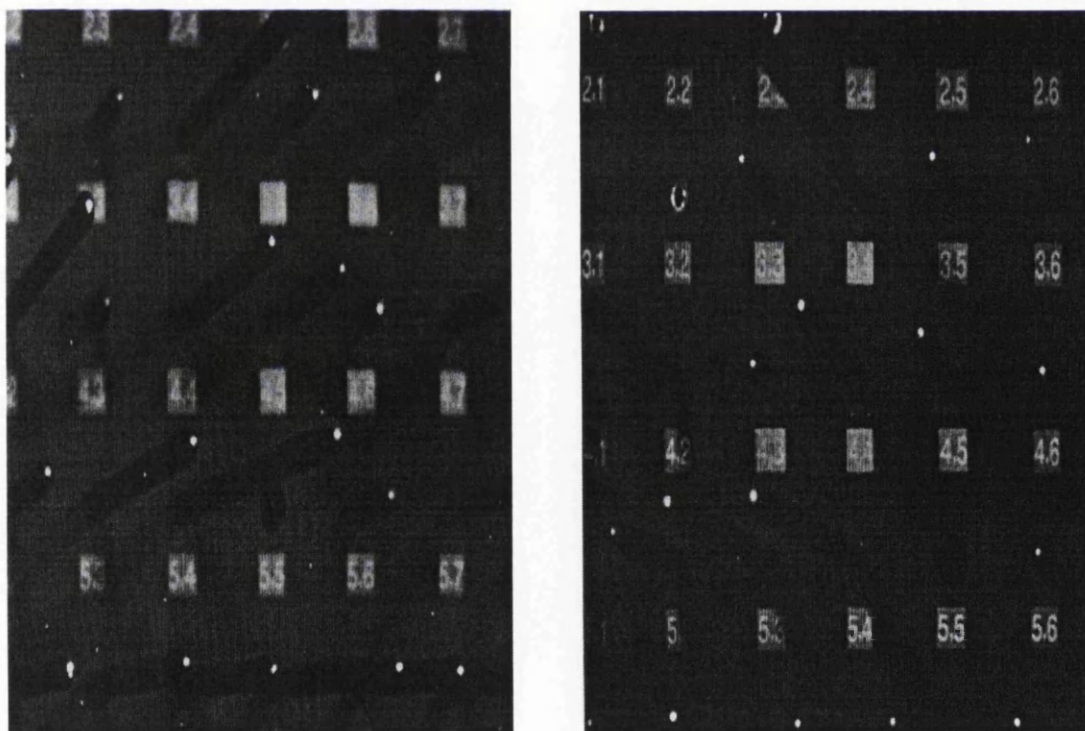
Figure 5-30 Left and Right Perspective Images with a Camera-lens Focal Length of 50mm
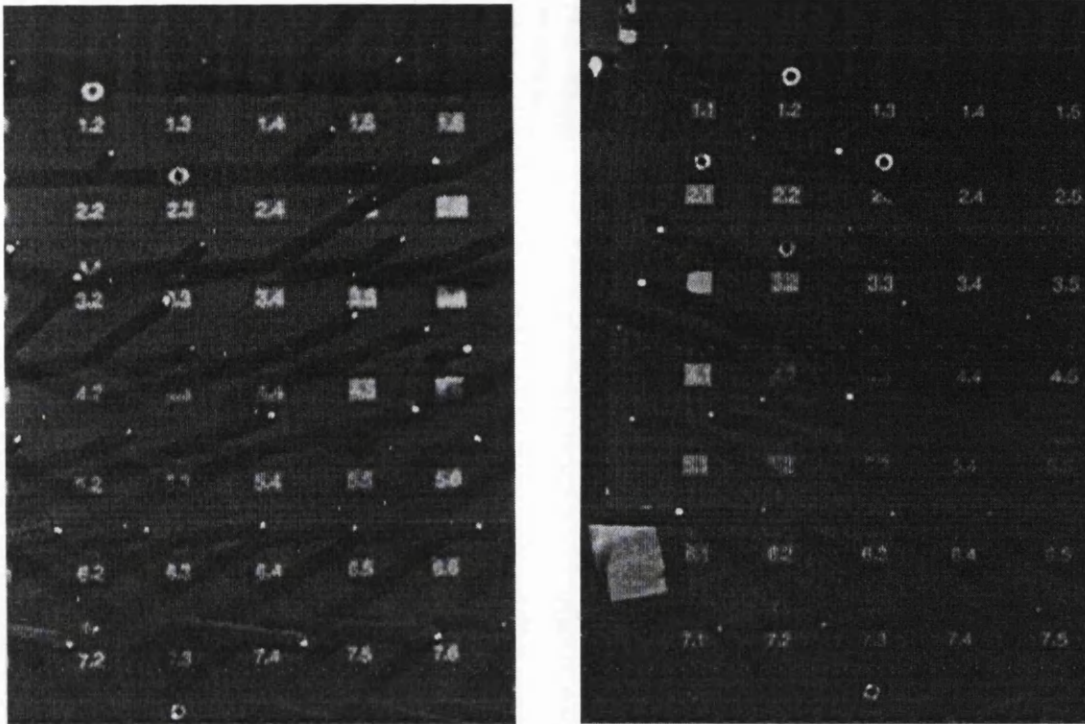
Figure 5-31 Left and Right Perspective Images with a Camera Lens Focal Length of 25mm

Figure 5-32 contains perspective views of the calibrated volume with a camera-lens focal length of 25mm, however, in this case the camera scan rate is 100kHz. Similar images would be obtained by maintaining a camera scan rate of 200kHz and doubling the rotation speed to 4 rpm.
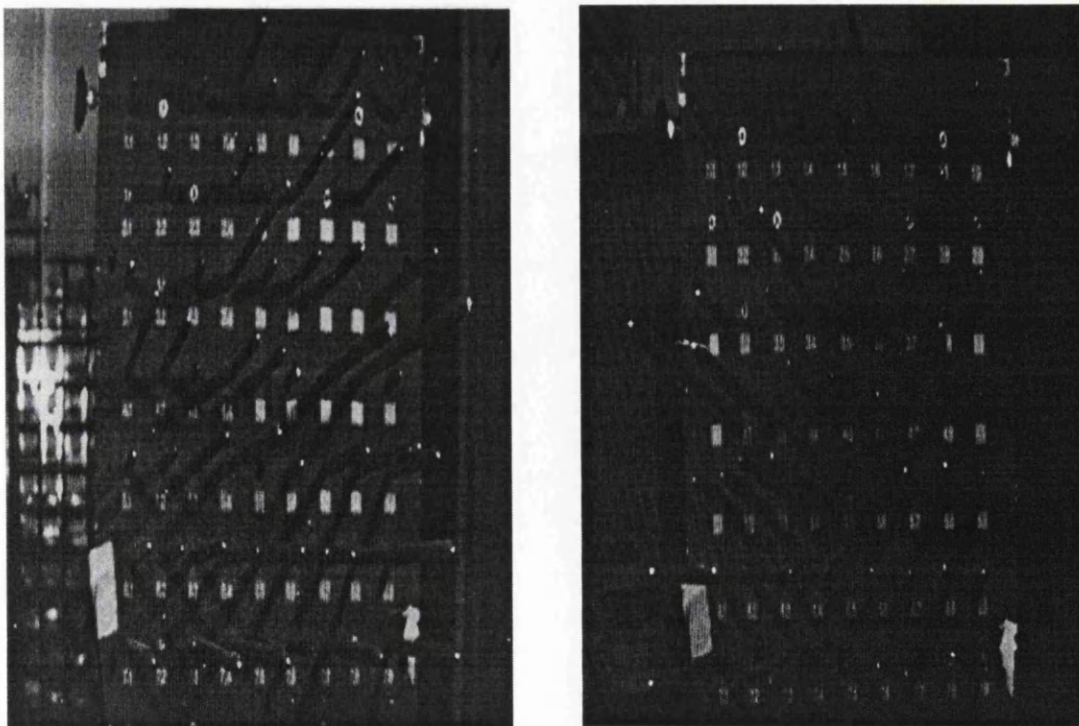
Figure 5-32 Left and Right Perspective Images with a Camera Scan Rate of 100kHz

Figure 5-33 shows left and right images obtained from the camera system with a scan rate of 300kHz and a focal length of 25mm.

Figure 5-33 Left and Right Perspective Images with a Camera Scan Rate of 300kHz

The experimental results from the stereoscopic line-scan investigation are now presented.

5.7.3 The Optimum Number of Control Targets Required for the Camera Calibration

To apply the 3-D conformal calibration procedure to the rotating line-scan system a minimum of 4 target locations are needed to provide a solution for the unknown camera transformation parameters. However, if more than the minimum number of control points are used an increase in the number of redundant equations allows an improved solution. The experimental work in this section determines the optimum number of control targets, selected from the calibration frame, required by the conformal transformation derived for the stereoscopic system.

The Selection of Control Targets :

General guidelines are adhered to when considering the selection of control targets from the calibration frame. As stated in the Manual of Photogrammetry [131], control targets are divided into two main categories :

- horizontal control targets;
- vertical control targets.

When selecting horizontal control targets the strongest configuration results from those around the perimeter of the region and when considering targets in the vertical axis they should be located throughout the region as well as around the perimeter.

From this discussion, the control targets should define the calibrated volume under consideration and only different targets within this should be used in the calculation procedure to resolve three-dimensional co-ordinates. Thus, for the experimental work with the line-scan system, the general procedure applied to the selection of control targets is as follows :

- select part of the calibrated volume for use in the co-ordinate analysis;
- select control targets which define the limits of the cartesian volume in the X, Y and Z-axes;
- select the targets to be passed to the calculation procedure from within the defined control volume.

Experimental Hypothesis :

"To determine the optimum number of control targets in object space for use in the calibration procedure"

Experimental Conditions :

Camera-to-object range (mm)	1500
Base width (mm)	500
Convergence Angle (degrees)	80
Focal Length (mm)	25
Camera Scan Rate (kHz)	200
Platform Rotation Speed (rpm)	0.67

Table 5-21 Experimental Parameter Settings for the Rotating Stereoscopic Line-scan System

Experimental Results :

As well as the control targets considered in this experimental work a further ten different targets are selected from the calibration frame to be used in the calculation procedure. To determine the optimum number of control targets for use with the 3-D conformal transformation the minimum number of four is considered initially. Following this the number of control targets is increased until the capability of the line-scan system to resolve the 3-D co-ordinates of the additional ten targets does not improve.

Each experiment is repeated three times to provide a mean value for the X, Y and Z co-ordinate measurement errors which result from the calculation procedure.

Four targets are selected from the calibration frame to act as the control points, a further ten targets in object space are selected for which the camera system resolves the 3-D co-ordinate information following the calibration procedure. Table 5-22 and Table 5-23 list the 3-D frame co-ordinates of the control targets and the additional targets used in the calculation procedure, respectively.

Frame Target	X (mm)	Y (mm)	Z (mm)
1.1	0.0	0.0	0.0
4.3	100.53	149.62	39.58
7.4	152.13	300.73	-331.11
9.4	151.14	400.25	-97.58

Table 5-22 3-D Frame Co-ordinates of the Control Targets

Frame Target	X (mm)	Y (mm)	Z (mm)
3.1	0.67	100.62	0.27
3.3	100.61	99.58	0.63
4.4	150.80	150.00	-141.38
5.2	51.03	200.29	-91.82
5.3	101.75	199.51	-211.50
5.4	151.62	201.99	-282.55
6.3	100.58	249.19	-198.69
6.4	150.18	250.18	-151.69
7.3	101.45	303.23	-297.79
8.4	150.04	351.62	-261.73

Table 5-23 3-D Frame Co-ordinates of the 'Calculation' Targets

For each of the three observations the X, Y and Z measurement errors in the calculated object space targets are presented in Table 5-24.

Target No.	X_1 (mm)	X_2 (mm)	X_3 (mm)	Y_1 (mm)	Y_2 (mm)	Y_3 (mm)	Z_1 (mm)	Z_2 (mm)	Z_3 (mm)
3.1	-1.5	-1.8	-1.6	-0.2	-0.6	-0.7	-0.8	1.6	3.0
3.3	0.2	0.4	0.1	-1.0	-1.0	-1.1	0.3	1.1	2.8
4.4	1.9	1.7	1.5	-4.1	-3.6	-3.2	4.9	2.8	3.8
5.2	-2.1	-2.1	-1.6	-2.0	-1.7	-1.4	-1.1	0.7	1.2
5.3	-2.2	-1.9	-1.4	-3.4	-3.0	-2.4	1.9	1.2	1.9
5.4	0.6	0.3	0.4	-4.3	-3.8	-3.2	3.6	1.6	2.8
6.3	-2.7	-2.4	-1.8	-2.3	-2.1	-1.8	1.3	1.1	1.6
6.4	0.7	0.8	0.8	-2.5	-2.7	-2.0	3.0	3.0	3.6
7.3	-3.4	-2.8	-2.1	-0.1	-0.3	-0.3	-1.4	-0.1	-0.6
8.4	0.0	0.1	0.1	1.5	1.1	0.7	0.3	0.6	-0.3

Table 5-24 3-D Co-ordinate Calculation Errors Using Four Control Targets in the Calibration

Where,

X_1, X_2 and X_3 are the errors in the resolved X co-ordinates for each experimental observation;

Y_1, Y_2 and Y_3 are the errors in the resolved Y co-ordinates for each experimental observation;

Z_1, Z_2 and Z_3 are the errors in the resolved Z co-ordinates for each experimental observation.

Table 5-25 shows the mean co-ordinate errors obtained from this calculation procedure, where X_{mean} is the average of X_1, X_2 and X_3 etc.

Target No.	X_{mean} (mm)	Y_{mean} (mm)	Z_{mean} (mm)
3.1	-1.6	-0.5	1.3
3.3	0.2	-1.0	1.4
4.4	1.7	-3.6	3.8
5.2	-1.9	-1.7	0.3
5.3	-1.8	-2.9	1.7
5.4	0.4	-3.8	2.7
6.3	-2.3	-2.1	1.3
6.4	0.8	-2.4	3.2
7.3	-2.8	-0.2	-0.7
8.4	0.1	1.1	0.2

Table 5-25 Mean Co-ordinate Calculation Errors for Three Observations Using Four Control Targets in the Calibration Procedure

The procedure, outlined previously, is now repeated using five, six and seven control targets in the camera calibration. Table 5-26 shows the mean co-ordinate errors from each calculation procedure using the same 10 targets considered previously.

Control N°	5			6			7		
Target No.	X_{mean} (mm)	Y_{mean} (mm)	Z_{mean} (mm)	X_{mean} (mm)	Y_{mean} (mm)	Z_{mean} (mm)	X_{mean} (mm)	Y_{mean} (mm)	Z_{mean} (mm)
3.1	-0.8	0.5	0.6	-0.5	0.5	0.6	0.0	0.5	0.8
3.3	-0.3	-0.6	1.1	-0.3	-0.6	1.1	0.0	-0.6	1.2
4.4	0.4	-1.1	0.6	0.3	-1.1	0.6	0.3	-0.5	1.5
5.2	-0.4	0.2	-2.2	0.1	0.3	-2.2	0.3	0.6	-1.6
5.3	-1.2	0.1	-1.3	-1.0	0.2	-1.3	-1.0	0.8	0.3
5.4	-0.9	-0.3	0.8	-0.8	-0.3	0.8	-1.2	0.6	2.3
6.3	-1.3	-0.2	-1.3	-1.1	-0.1	-1.3	-0.9	0.4	-0.1
6.4	0.1	-1.1	0.6	0.1	-1.1	0.6	0.2	-0.7	1.3
7.3	-1.2	0.6	-1.4	-0.8	0.7	-1.4	-0.8	1.4	0.8
8.4	-0.2	0.3	-0.9	0.0	0.3	-0.9	0.0	0.7	0.5

Table 5-26 Mean Co-ordinate Calculation Errors for Three Observations Using Five, Six and Seven Control Targets in the Calibration Procedure

For each control target configuration Table 5-25 and Table 5-26 list the mean errors between 3-D co-ordinates resolved by the camera system and the calibration frame data. To allow a comparison of the results calculated using each control configuration the rms values are calculated for the X, Y and Z measurement errors obtained from each experiment (Table 5-27).

Control Target N°	X rms error (mm)	Y rms error(mm)	Z rms error(mm)
4	1.6	2.3	2.0
5	0.8	0.6	1.3
6	0.6	0.6	1.2
7	0.6	0.7	1.2

Table 5-27 3-D Co-ordinate Calculation Errors using 4, 5, 6 and 7 Control Targets

The error in the calculated 3-D co-ordinates (Table 5-27) improves to an optimum level when using 6 control targets in the calibration procedure. Any further increase in the number of control targets does not lead to an improvement in the measurement errors. Thus, for the calibration procedure adopted in this research 6 control targets from the object frame are used to calculate the transformation parameters prior to the calculation of 3-D object space co-ordinates.

Experimental Conclusion :

"The optimum number of control targets for use with the line-scan system is 6. The use of additional targets does not lead to an improved solution of the calculated 3-D co-ordinates."

5.7.4 The Selection of the Control Targets

Now the optimum number of control targets is established different control configurations are assessed using the stereoscopic parameters presented in Table 5-21. This experimental work uses six control targets from different volumes of the calibration frame and evaluates their use in determining 3-D co-ordinates of the targets used in the calculation procedure.

The 6 control targets used in Section 5.7.3 covered a volume in object space of 150.95mm x 252.05mm x 298.42mm in the X, Y and Z axes respectively. This volume of object space represents the left hand side of the calibration frame as viewed from the rotation centre of the camera system. To provide a further test for the calibration procedure two different control volumes are now considered.

Experimental Hypothesis :

"To evaluate the use of 6 control targets selected from different volumes of the calibrated frame in the calibration procedure and the subsequent influence on the 3-D measurement capability"

Experimental Results :

Initially, 6 control targets are selected from the right hand side of the calibrated volume, as viewed from the centre of the stereoscopic rotation. The control volume is 151.54mm x 401.36mm x 416.63mm in the X, Y and Z axes respectively. The 3-D co-ordinate measurement errors obtained from the calculation procedure for three observations are shown in Table 5-28.

Target No.	X_{mean} (mm)	Y_{mean} (mm)	Z_{mean} (mm)
2.6	-0.1	0.1	0.4
2.8	0.7	-0.7	-2.2
3.7	-0.3	-0.2	1.3
5.6	0.2	1.1	1.0
5.9	0.3	-0.3	2.3
6.6	0.2	1.2	0.2
7.6	0.6	1.3	-2.1
7.7	-0.9	0.1	-2.5
7.9	-0.4	-1.3	-1.5
8.8	0.0	-0.3	2.0
rms error	0.5	0.8	1.7

Table 5-28 3-D Measurement Errors in Calculated Target Co-ordinates for Three Observations Using Six Control Targets in the Calibration Procedure

Another control volume was selected to cover the entire calibration frame. This volume covered dimensions in the X, Y and Z axes of 400.69mm x 401.29mm x 389.71mm, respectively. The co-ordinate measurement errors in the calculated frame targets for three observations are shown in Table 5-29.

Target No.	X_{mean} (mm)	Y_{mean} (mm)	Z_{mean} (mm)
15	0.8	-0.7	0.8
26	1.7	-1.4	-1.3
31	-0.5	0.9	1.7
45	-0.4	-0.4	-0.1
56	-0.8	0.6	-0.6
62	-0.2	0.7	-2.4
79	-0.4	-0.8	-1.0
82	-0.8	0.9	0.3
86	-0.1	-0.4	3.1
96	0.0	-0.7	1.1
rms error	0.7	0.8	1.5

Table 5-29 Measurement Errors in Calculated Frame Target Co-ordinates for Three Observations Using Six Control Targets in the Calibration Procedure

When using six targets in different control volumes the calculated rms measurement errors (presented in Table 5-27, Table 5-28 and Table 5-29) are of the same order of magnitude in each co-ordinate axis, i.e., ±0.5 to ±0.7mm in the X-axis of object space, ±0.6 to ±0.8mm in the Y-axis of object space and ±1.2 to ±1.7mm in the Z-axis of object space. Therefore, the results presented are considered to validate further the use of six control targets from the calibration frame in the calculation of 3-D object space co-ordinates.

Experimental Conclusion :

"_6 control points selected from different volumes of the calibration frame can be used in the 3-D conformal transformation to reconstruct 3-D co-ordinates of selected object targets_"

For the stereoscopic experiments conducted so far the start of image capture was maintained at a constant value for each set of observations to allow the extraction of consistent 3-D co-ordinate information. This was achieved by programming a constant timing delay into the image capture software. Now the effect of varying the start of image capture, by changing the timing delay, on the ability to resolve 3-D co-ordinates is investigated.

5.7.5 The Effect of Varying the Start of Image Capture on 3-D Measurements

This section will examine the effect of varying the start of image capture on the 3-D co-ordinates resolved by the camera system (Table 5-21).

Experimental Hypothesis :

"To evaluate the effect of changing the start of stereoscopic image capture on the capability to resolve three-dimensional co-ordinates from object space"

Experimental Results :

To determine the effect of varying the start of image capture 3 observations are made with a fixed image start point and 3 observations are made with variable start points in the camera rotation. The standard deviation of the absolute 3-D co-ordinate measurement errors, i.e. twice the rms value, are calculated to evaluate the difference between using a fixed and variable start of image capture.

Table 5-30 and Table 5-31 show the errors when using a fixed and variable image start point, respectively. From the standard deviation (σ) of the co-ordinate errors the start of image capture does not alter the capability of the system to resolve 3-D co-ordinates. This is because the X-Z reference plane of the mathematical model is coincident with the start of image capture irrespective of the stereoscopic camera position in the rotation.

Image Start (x pixels)	X_{rms} (mm)	Y_{rms} (mm)	Z_{rms} (mm)
570	0.6	0.7	1.4
570	0.6	0.5	1.4
570	0.5	0.5	1.9
σ (mm)	0.1	0.2	0.6

Table 5-30 Co-ordinate Measurement Errors For a Fixed Start of Image Capture

image Start (x pixels)	X_{rms} (mm)	Y_{rms} (mm)	Z_{rms} (mm)
566	0.6	0.6	1.4
574	0.7	0.7	1.8
761	0.6	0.7	1.4
σ (mm)	0.1	0.1	0.5

Table 5-31 Co-ordinate Measurement Errors for a Variable Start of Image Capture

Experimental Conclusion :

"Changing the stereoscopic image start point does not effect the capability of the rotating line-scan system to resolve three-dimensional co-ordinate information from object space"

5.7.6 Accuracy and Precision of 3-D Co-ordinate Measurements

The accuracy and precision of the resolved three-dimensional co-ordinate measurements is now investigated using an experimental set-up with the parameters given in Table 5-21.

The Manual of Photogrammetry defines accuracy as [98] : *"the degree of conformity with a standard, or the degree of perfection attained in a measurement"*

Precision is defined as [98] : *"a quality associated with the refinement of instruments and measurements, indicated by the degree of uniformity or identity of repeated measurements"*

This work evaluates the errors between calculated 3-D co-ordinates resolved by the camera system and the equivalent known calibration frame co-ordinates to obtain a measure of accuracy for the line-scan system. Specifically, this accuracy information is obtained from the worst case results after a series of 10 consecutive observations using the same experimental set-up. The precision of the resolved co-ordinates is then assessed by examining the repeatability, over 10 runs, of the 3-D co-ordinate measurements obtained.

Experimental Hypothesis :

"To examine the accuracy and precision of the calculated 3-D object space measurements when repeating the image capture for the same experimental set-up"

Experimental Results :

This hypothesis is investigated by taking 10 consecutive pairs of perspective images with the experimental arrangement considered. In each case the targets used in the calibration routine are identical and also the same frame targets are used for the calculation of the three-dimensional co-ordinates. For the ten frame targets under consideration the rms errors in the X, Y and Z co-ordinates resolved by the camera system for the ten experimental runs are presented in Table 5-32.

Observation N°	rms X error(mm)	rms Y error (mm)	rms Z error (mm)
1	0.7	0.7	1.8
2	0.7	0.9	2.1
3	0.6	0.5	1.4
4	0.3	0.5	2.0
5	0.7	0.6	1.5
6	0.5	0.5	1.5
7	0.5	0.5	1.9
8	0.4	0.8	1.5
9	0.6	0.6	1.4
10	0.6	0.5	1.5

Table 5-32 Calculated 3-D Co-ordinate Measurement Errors for a Series of Ten Observations

Accuracy of the Resolved 3-D Co-ordinates :

From Table 5-32, the worst case rms errors represent measurement inaccuracies in object space of ±0.7mm, ±0.9mm and ±2.1mm in the X, Y and Z-axes, respectively.

For this experimental set-up the voxel dimensions in object space are approximately 0.5mm / pixel in the X-axis, 0.7mm / pixel in the Y-axis and 1.4mm / pixel in the Z-axis. Therefore, as the error in the manual location of target positions is up to a magnitude of ±1 pixel in each axis of image space the expected measurement error, in mm of object space, is ±0.7mm in the X-axis, ±0.7mm in the Y-axis and ±1.4mm in the Z-axis.

Hence, the 3-D co-ordinate measurement errors presented in Table 5-32 are of the expected order of magnitude and, thus, validate the theoretical analysis undertaken.

Precision of the 3-D Co-ordinates :

The precision of the 3-D co-ordinates, over ten experimental runs, is now evaluated by taking the standard deviation of the co-ordinate measurement errors in each axis, thus, providing a measure of the spread of the calculated target co-ordinates.

In Table 5-32 the difference between calculated and known co-ordinates are expressed as rms errors. To evaluate the precision of these results they are considered in terms of the absolute error magnitudes. For example, for an rms error of ±0.5mm the magnitude of the absolute error is equal to twice this quantity, i.e., 1mm. The absolute error magnitudes are given in Table 5-33.

Observation N°	X error(mm)	Y error (mm)	Z error (mm)
1	1.4	1.4	3.6
2	1.4	1.8	4.2
3	1.2	1.0	2.8
4	0.6	1.0	4.0
5	1.4	1.2	3.0
6	1.0	1.0	3.0
7	1.0	1.0	3.8
8	0.8	1.6	3.0
9	1.2	1.2	2.8
10	1.2	1.0	3.0
σ(mm)	0.3	0.3	0.5

Table 5-33 Standard Deviation of the Absolute Errors in the Co-ordinate Measurement Capability : An Assessment of the Precision for Ten Repeated Experimental Observations

From Table 5-33 the standard deviation of the errors in the resolved X, Y and Z co-ordinates are 0.3mm, 0.3mm and 0.5mm respectively. Therefore, it can be stated :

- for repeated measurements in the X-axis of object space the resolved co-ordinates may contain errors of up to ±0.3mm;

- for repeated measurements in the Y-axis of object space the resolved co-ordinates may contain errors of up to ±0.3mm;

- for repeated measurements in the Z-axis of object space the resolved co-ordinates may contain errors of up to ±0.5mm.

The main objective of this work is to establish the characteristics of the rotating line-scan system and not to resolve 3-D co-ordinate measurements to the highest possible degree of accuracy. For the experimental set-up considered in this section the degree of accuracy and precision obtained is considered to validate this work for the following reasons :

- the co-ordinate measurement errors are governed by the resolution available in object space which is controlled by the image space resolution of 1 pixel in each axis;

- the error in the manual location of target positions is up to a magnitude of ±1 pixel in the x and y axes of image space.

Experimental Conclusion :

"For 10 independent observations using the same experimental arrangement the accuracy and precision of the calculated 3-D object space co-ordinates is considered to validate the capability of the rotating line-scan to obtain precise results to a defined degree of accuracy"

The following sections now test the 3-D conformal transformation by rotating the calibration frame in defined increments around the X, Y and Z axes of object space. This experimental work is conducted to evaluate the use of the calibration and calculation procedures for changes in the relative alignment of the camera and object systems.

5.7.7 Effect of Object Rotation about the X-axis

This section describes the experimental procedure necessary to quantify the effect of rotating the calibration frame with respect to the camera system (Table 5-21) in the X-axis of object space. This provides a further test to examine the suitability of the conformal transformation routine for use with the stereoscopic arrangement of rotating line-scan sensors.

Experimental Hypothesis :

"To verify that rotation of the calibration frame about the X-axis does not affect the integrity of the camera calibration procedure and, therefore, the calculation of 3-D co-ordinate data"

Experimental Results :

For this experimental work the calibration frame is rotated from a start position to 15 degrees around the X-axis in object space (Figure 5-34) in 5° increments.
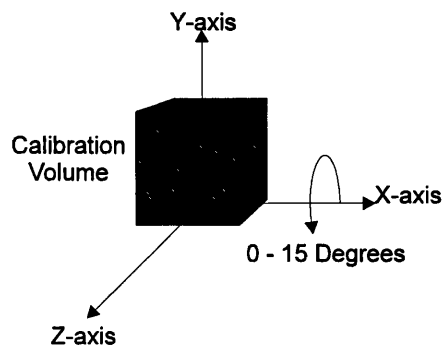
Figure 5-34 Calibration Frame Rotation around the X-axis

An initial observation is made at the start position, defined as 0 degrees, followed by additional observations at 5, 10 and 15 degrees. For each rotation around the X-axis three consecutive observations are made from which the mean measurement errors in the resolved X, Y and Z co-ordinates are calculated. The mean co-ordinate errors for the start position are presented in Table 5-34 and the mean 3-D co-ordinate measurement errors resulting from rotation angles of 5°, 10° and 15° are presented in Table 5-35.

Target No.	X_{mean} (mm)	Y_{mean} (mm)	Z_{mean} (mm)
3.3	-0.3	-0.6	1.1
4.4	0.3	-1.1	0.6
5.2	0.1	0.3	-2.2
5.3	-1.0	0.2	-1.3
5.4	-0.8	-0.3	0.8
6.3	-1.1	-0.1	-1.3
6.4	0.1	-1.1	0.6
7.3	-0.8	0.7	-1.4
8.4	0.0	0.3	-0.9

Table 5-34 3-D Co-ordinate Measurement Errors Over 3 Observations for 0° Rotation

Rotation(°)	5			10			15		
Target No.	X_{mean} (mm)	Y_{mean} (mm)	Z_{mean} (mm)	X_{mean} (mm)	Y_{mean} (mm)	Z_{mean} (mm)	X_{mean} (mm)	Y_{mean} (mm)	Z_{mean} (mm)
33	-0.8	0.3	-0.8	-0.8	-0.3	0.2	-0.8	-0.1	-1.0
44	0.2	-0.7	-0.8	0.2	0.4	-2.0	0.3	-1.2	0.5
52	0.1	0.8	-2.5	0.2	0.6	-1.1	-0.1	0.8	-2.4
53	-0.5	0.2	-1.2	-0.3	0.1	0.3	-0.4	-0.6	0.9
54	0.1	-0.5	0.7	0.4	-0.6	1.4	0.5	-1.0	0.9
63	-0.6	-0.4	-0.1	-0.2	0.0	-0.8	-0.6	0.0	0.6
64	-0.3	-0.9	0.4	-0.3	-0.3	-1.2	-0.3	-0.5	-1.5
73	-0.1	0.7	-1.6	0.3	1.3	-3.1	-0.3	0.9	-1.2
84	0.2	0.4	2.3	0.6	0.7	1.2	0.4	0.9	0.2

Table 5-35 3-D Measurement Errors for 5°, 10° and 15° Rotations About the X-axis

A summary of the rms measurement errors for rotation of the calibration frame about the X-axis of object space are presented in Table 5-36. From these results it is observed that changing the relative alignment of the camera and object systems does not alter significantly the ability of the 3-D transformation procedure to calculate three-dimensional co-ordinates from object space.

Rms Error	X-axis	Y-axis	Z-axis
Rotation (°)	mm	mm	mm
0	0.6	0.6	1.2
5	0.4	0.6	1.4
10	0.4	0.6	1.5
15	0.5	0.8	1.4

Table 5-36 3-D Co-ordinate Measurement Errors for Frame Rotation About the X-axis

Experimental Conclusion :

"Rotation of the calibration frame about the X-axis does not affect significantly the calculation of 3-D co-ordinate data"

5.7.8 Effect of Object Rotation about the Y-axis

The effect of rotating the calibration frame about the Y-axis of object space on the capability to resolve 3-D co-ordinates from object space is now determined using a stereoscopic arrangement with the experimental parameters presented in Table 5-21.

Experimental Hypothesis :

"To verify that rotation of the calibration frame about the Y-axis does not affect the integrity of the calibration procedure and, therefore, the calculation of 3-D co-ordinate data"

Experimental Results :

For this part of the experimental work the calibration frame is rotated from a start position to 15 degrees around the Y-axis in object space (Figure 5-35).
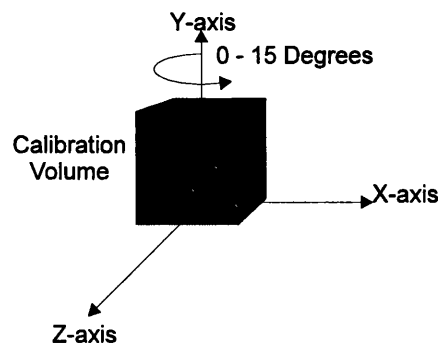
Figure 5-35 Calibration Frame Rotation about the Y-axis

An initial observation is made at the start position, defined as 0 degrees, followed by additional observations at 5, 10 and 15 degrees. For each rotation around the Y-axis three consecutive observations are made from which the mean measurement errors in the resolved X, Y and Z co-ordinates are calculated. The mean co-ordinate errors are presented in Table 5-37 for rotation angles of 5°, 10° and 15°, respectively.

Rotation(°)	5			10			15		
Point No.	X_{mean} (mm)	Y_{mean} (mm)	Z_{mean} (mm)	X_{mean} (mm)	Y_{mean} (mm)	Z_{mean} (mm)	X_{mean} (mm)	Y_{mean} (mm)	Z_{mean} (mm)
33	0.0	-1.3	-2.5	0.2	-0.6	-1.9	0.2	-1.4	0.6
44	0.9	-1.0	-0.1	0.7	-2.1	2.5	-0.3	-1.7	0.8
52	0.2	-1.9	0.7	0.4	-1.5	-1.0	0.4	-1.7	-1.0
53	-0.7	-0.4	1.1	-0.4	0.1	0.8	-0.1	-0.7	-0.3
54	-0.4	-1.7	3.1	0.2	-0.8	-0.2	0.8	-0.5	-2.6
63	-0.5	-0.7	3.4	0.3	-0.3	-0.3	0.4	0.0	-1.2
64	-0.5	-1.1	-0.5	-0.3	-1.1	-0.9	-0.4	-1.0	-0.3
73	-0.3	0.3	1.7	0.6	-0.5	-0.1	-0.1	0.4	0.2
84	0.1	-0.4	0.5	-0.1	0.1	3.1	-0.7	0.1	2.3

Table 5-37 3-D Co-ordinate Measurement Errors Over 3 Observations for 5°, 10° and 15° Rotations About the Y-axis

A summary of the rms measurement errors for rotation of the calibration frame about the Y-axis of object space are presented in Table 5-38. There is a deviation in the Y and Z-axes measurement errors in object space due to frame rotation about the Y-axis. However, it should be noted that these errors are of the same order of magnitude as those presented (Table 5-32) when testing the repeatability of measurements in Section 5.7.6. Therefore, it is concluded that changing the camera / object relationship by rotation of the calibration frame about the Y-axis of object space does not alter significantly the measurement capability of the stereoscopic system.

Rms Error	X-axis	Y-axis	Z-axis
Rotation (°)	mm	mm	mm
0	0.6	0.6	1.2
5	0.5	1.1	1.9
10	0.4	1.0	1.6
15	0.4	1.0	1.3

Table 5-38 Variation in 3-D Co-ordinate Data for Frame Rotation About the Y-axis

"Rotation of the calibration frame about the Y-axis does not affect significantly the calculation of 3-D co-ordinate data"

5.7.9 Effect of Object Rotation about the Z-axis

This section describes the experimental procedure necessary to quantify the effect of rotating the calibration frame around the Z-axis of object space. This is undertaken to investigate the suitability of the calibration routine for use with the stereoscopic arrangement of rotating line-scan sensors given in Table 5-21.

Experimental Hypothesis :

"To verify that rotation of the calibration frame about the Z-axis does not affect the integrity of the calibration procedure and, therefore, the calculation of 3-D co-ordinate data"

Experimental Results :

For this aspect of the experimental work the calibration frame was rotated from a start position to 15 degrees around the Z-axis in object space (Figure 5-36) in 5° increments.
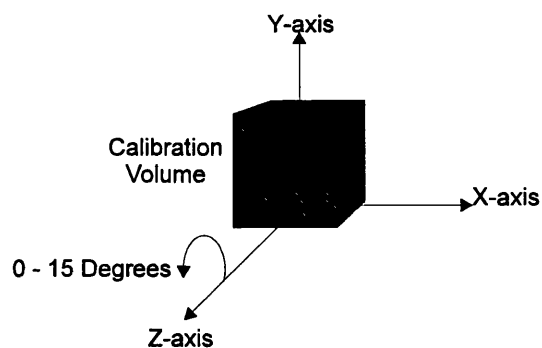
Figure 5-36 Calibration Frame Rotation about the Z-axis

An initial observation was made at the start position, defined as 0 degrees, followed by additional observations at 5, 10 and 15 degrees. For each rotation around the Z-axis three consecutive observations are made from which the mean measurement errors in the resolved X, Y and Z co-ordinates are calculated. The mean co-ordinate errors are presented in Table 5-39 for rotation angles of 5°, 10° and 15°.

Rotation(°)	5			10			15		
Point	X_{mean}	Y_{mean}	Z_{mean}	X_{mean}	Y_{mean}	Z_{mean}	X_{mean}	Y_{mean}	Z_{mean}
No.	(mm)	(mm)	(mm)	(mm)	(mm)	(mm)	(mm)	(mm)	(mm)
33	0.5	-0.3	0.6	0.0	-1.0	1.6	0.4	-0.5	-0.4
44	0.6	-1.4	0.4	-1.0	-1.0	1.3	0.0	-1.6	-0.5
52	-0.8	0.4	-1.8	-0.6	0.2	2.2	-1.1	0.6	-0.4
53	-0.6	-0.2	0.4	-0.5	0.0	0.5	0.5	-0.5	3.1
54	-0.1	-1.1	2.7	-0.5	-0.2	-0.2	0.5	-0.7	0.6
63	-0.8	0.1	0.2	-0.3	0.0	-1.0	0.3	-0.1	3.9
64	0.0	-0.6	1.8	-1.1	-1.1	2.2	-0.4	-0.8	-1.1
73	-1.0	1.2	1.8	-0.7	0.4	1.7	0.4	0.7	1.6
84	-0.3	1.2	3.0	-0.2	0.8	3.5	0.0	0.4	-1.4

Table 5-39 3-D Co-ordinate Measurement Errors Over 3 Observations for 5°, 10° and 15°

Rotations About the Z-axis

A summary of the rms measurement errors for rotation of the calibration frame about the Z-axis of object space are presented in Table 5-40. There is a deviation in the Y and Z-axes measurement errors due to frame rotation about the Z-axis which are of the same order of magnitude as those presented in the previous section. Therefore, it is concluded that rotation of the calibration frame about the Z-axis of object space does not alter significantly the measurement capability of the stereoscopic system.

Rms Error	X-axis	Y-axis	Z-axis
Rotation (°)	mm	mm	mm
0	0.5	0.6	1.2
5	0.6	0.9	1.7
10	0.6	0.7	1.8
15	0.5	0.8	1.9

Table 5-40 Variation in 3-D Co-ordinate Data for Frame Rotation About the Z-axis

Experimental Conclusion :

"Rotation of the calibration frame about the Z-axis does not affect significantly the calculation of 3-D co-ordinate data"

5.7.10 Resolving 3-D Vectors between Target Pairs in Object Space

In the previous sections it has been established the 3-D conformal transformation can be applied to a rotating line-scan system to resolve co-ordinate measurement information from the calibration frame. This section of the work will determine if, following the calibration procedure, the measurement system can be used to obtain 3-D co-ordinate data of similar accuracy / integrity from different physical volumes of object space.

Following an initial calibration procedure, if the object frame is then placed at different positions in the rotation but the camera / object relationship remains otherwise unchanged (Figure 5-37) 3-D vectors between target pairs may be determined using the transformation parameters from the initial calibration. This section investigates the capability of the rotating stereoscopic system (Table 5-21) to resolve 3-D vectors from volumes of object space, A and B, where the relationship between the camera and object systems is not directly calibrated.

Experimental Hypothesis :

"To determine whether 3-D vectors between target pairs can be extracted from the workspace using transformation parameters obtained from another volume of calibrated object space"
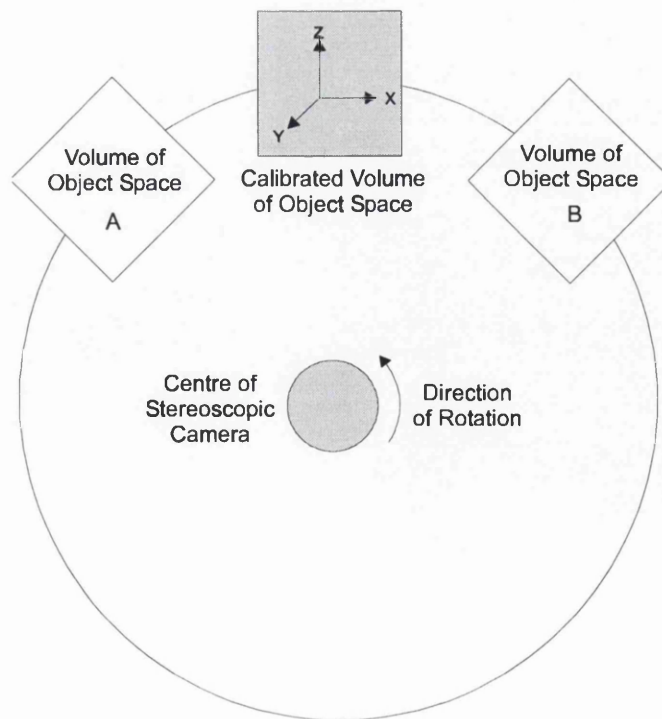
Figure 5-37 Object Volume Positions with Reference to the Centre of the Stereoscopic Rotation

Experimental Results :

In this work the frame is calibrated with respect to the camera system and the transformation parameters are used to determine 3-D vectors for target pairs selected from the calibration frame placed at different positions in the rotation. Specifically, the frame is placed to the left and right of the original position whilst approximately maintaining the original alignment with the camera system. This is achieved by placing the calibrated frame in different positions with the same camera-to-object range, shown as A and B in Figure 5-37.

The results in Table 5-41 show the 3-D vectors obtained from the original calibration frame data, the 3-D vectors calculated from the co-ordinates resolved in the original calibration volume and the 3-D vectors calculated from the left (A) and right (B) volumes of object space. The 3-D vector errors are calculated by referencing the results to the original calibration frame data and are presented in Table 5-42.

Target Pair	Original Frame Data	Calibrated Object Space	Object Space (A)	Object Space (B)
31 - 33	100.0	99.8	100.4	100.7
31 - 44	212.2	211.6	211.4	211.6
31 - 52	144.7	145.7	143.3	145.2
31 - 53	254.6	253.7	250.8	250.7
31 - 54	336.2	332.9	335.2	337.1
31 - 63	267.7	266.6	264.3	265.2
31 - 64	260.4	258.3	259.0	260.5
31 - 73	374.2	374.2	373.1	372.5
31 - 84	392.4	391.6	392.5	394.2
44 - 54	150.4	150.5	150.8	153.0
53 - 84	167.3	167.8	169.8	170.4
63 - 73	112.9	113.7	115.6	113.8
64 - 84	149.7	151.4	151.6	151.6
73 - 84	77.5	78.6	76.8	75.8

Table 5-41 3-D Vectors between Target Pairs from Original Frame Data and Object Space

Point Pair	Calibrated Object Space	Object Space (A)	Object Space (B)
31 - 33	-0.2	0.4	0.7
31 - 44	-0.6	-0.8	-0.6
31 - 52	1.0	-1.4	0.5
31 - 53	-0.9	-3.8	-3.9
31 - 54	-3.3	-1.0	0.9
31 - 63	-1.1	-3.4	-2.5
31 - 64	-2.1	-1.4	0.1
31 - 73	0.0	-1.1	-1.7
31 - 84	-0.8	0.1	1.8
44 - 54	0.1	0.4	-1.4
53 - 84	0.5	2.5	3.1
63 - 73	0.8	2.7	0.9
64 - 84	1.7	1.9	1.9
73 - 84	1.1	-0.7	-1.7
rms error	1.3	1.9	1.9

Table 5-42 3-D Vector Errors in Object Space

From Table 5-42, the rms errors in the 3-D vectors verify that valid 3-D vector measurement information can be extracted from indirectly calibrated object space using the three-dimensional conformal transformation.

Experimental Conclusion :

"3-D vectors between target pairs can be extracted from indirectly calibrated volumes of object space using transformation parameters from another physical volume of calibrated object space"

In this section the co-ordinate measurement capability of the rotating stereoscopic line-scan system has been examined. From this work the application of the 3-D conformal transformation has been verified for the extraction of co-ordinate information from defined volumes of object space. Now the applicability of the mathematical model has been validated it is examined for variations in the stereoscopic imaging parameters, therefore, allowing an assessment of the system characteristics.

5.8 Characteristics of the Rotating 3-D Line-scan System

In Section 5.6 the algorithms allowing calculation of voxel dimensions surrounding object space targets were validated and the use of the conformal transformation to extract 3-D co-ordinates from object space was verified in Section 5.7. This part of the work applies the resolution algorithms and the conformal transformation to examine the effects of variations in the stereoscopic parameters on the measurement capability of the line-scan system. The final objective of this work is to determine the measurement characteristics associated with the rotating 3-D line-scan system.

5.8.1 The Experimental Approach

In Section 5.7 the parameters of the stereoscopic arrangement were fixed whilst the applicability of the 3-D conformal transformation to the camera system was investigated. In the following experiments, the stereoscopic parameters are altered individually in defined steps. Using this approach the voxel dimensions and measurement capability will change in response to the parameter variations allowing the system characteristics to be identified. For each arrangement considered the approach to the experimental work is as described in Section 5.7.1.

Defined variations in the following parameters are investigated to evaluate the characteristics of the rotating stereoscopic line-scan system :

- camera-to-object range;
- camera base width and convergence angle;
- camera scan rate;
- camera rotation speed;
- focal length.

Unless otherwise stated, each experimental procedure described uses the control targets in Table 5-43 to calibrate the camera system and the frame targets identified from Table 5-44 in the calculation procedure to determine the 3-D co-ordinate measurement information.

Frame Target	X (mm)	Y (mm)	Z (mm)
1.1	0.0	0.0	0.0
1.4	151.11	0.774	-170.08
4.3	100.53	149.62	39.58
6.2	51.56	250.05	-162.60
7.4	152.13	300.73	-331.11
9.4	151.14	400.25	-97.58

Table 5-43 3-D Frame Co-ordinates of the Control Targets

Frame Target	X (mm)	Y (mm)	Z (mm)
3.1	0.67	100.62	0.27
3.3	100.61	99.58	0.63
4.4	150.80	150.00	-141.38
5.2	51.03	200.29	-91.82
5.3	101.75	199.51	-211.50
5.4	151.62	201.99	-282.55
6.3	100.58	249.19	-198.69
6.4	150.18	250.18	-151.69
7.3	101.45	303.23	-297.79
8.4	150.04	351.62	-261.73

Table 5-44 3-D Frame Co-ordinates of the Targets used in the Calculation Procedure

To allow a comparison of the results obtained from each part of this investigation it is decided to maintain a constant convergence plane (Figure 5-38) for each stereoscopic set-up considered. Apart from the variation in camera-to-object distance, the calibration frame is placed in the field of view so as to occupy a volume in object space around the convergence plane (Figure 5-39). This allows measurements to be obtained from equivalent sections of the stereoscopic volume and imposes a standard from which the characteristics associated with each parameter variation can be assessed.

To 'fix' a value for the convergence plane a stereoscopic camera configuration is selected with the following parameters :

Base Width (mm)	500
Convergence Angle (degrees)	80

From Equation 4-35, the range from the rotation centre to the convergence plane, Z_{con}, is calculated from the following expression :

$$Z_{con} = \frac{B \tan\theta c}{2}$$

Thus, for a base width of 500mm and a convergence angle of 80° the value for Z_{con} is 1418mm.
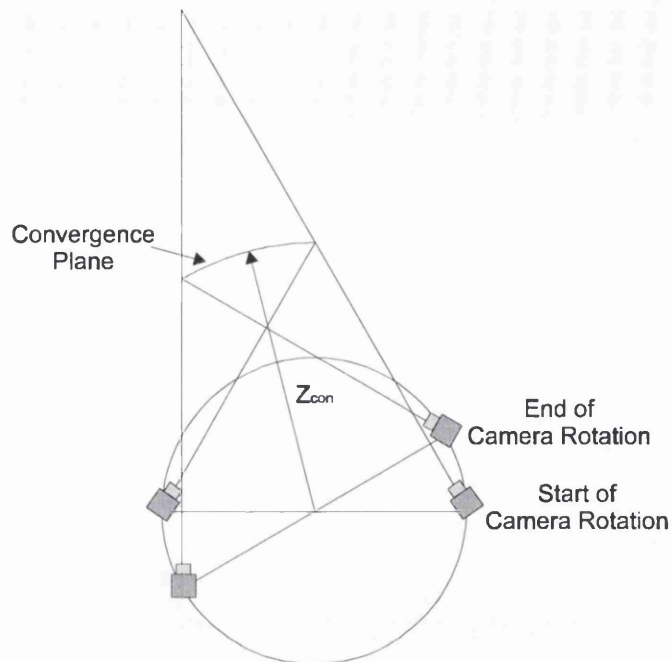
Figure 5-38 The Convergence Plane as Governed by Base Width and Convergence Angle
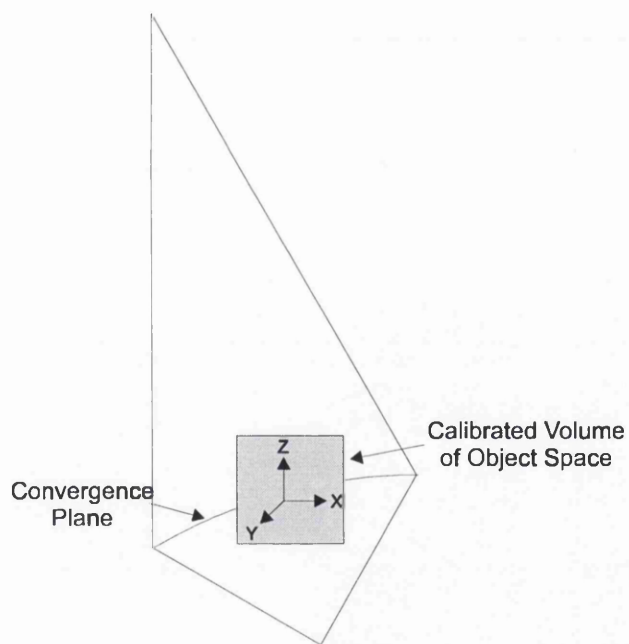
Figure 5-39 Calibrated Frame Position in the Stereoscopic Region

For each parameter variation the following attributes are identified :

- the extent of the stereoscopic volume in object space;

- the change in voxel dimensions in object space;

- the 3-D measurement capability.

For each experimental set-up, the extent of the stereoscopic volume in object space is calculated from the algorithms presented in Section 4.9 and the voxel dimensions are calculated using the resolution algorithms in Section 4.10.

To evaluate the change in voxel dimensions for variations in a given parameter it is decided to consider only one of the frame targets used in the calculation procedure, i.e., for one target the image co-ordinates are passed to the resolution algorithms to allow the minimum resolvable distance in each axis of object space to be calculated for each incremental parameter change. Thus, the 3-D measurement errors obtained may be compared with the equivalent resolution available in object space. Ideally, the voxel dimensions for all of the targets used in the calculation procedure should be identified, however, the use of one target is considered sufficient to demonstrate the approximate voxel structure for the variations in camera-to-object distance, camera rotation speed etc. In this work a target positioned near the centre of the Z-plane within the calibrated frame is used for which the surrounding voxel dimensions are calculated (target 6.4, Table 5-44).

Once the attributes of the stereoscopic volume are identified the measurement capability is assessed for each experimental arrangement. From this work the characteristics of the stereoscopic line-scan system will be identified.

5.8.2 Variation in Camera-to-object Range

This section will evaluate the characteristics associated with a change in camera-to-object range of between 1000mm and 2500mm, in 500mm increments.

Experimental Hypothesis :

"To investigate the three-dimensional characteristics associated with variations in the camera-to-object distance"

Experimental Conditions :

Base Width (mm)	500
Convergence Angle (degrees)	80
Focal Length (mm)	25
Camera Scan Rate (kHz)	200
Platform Rotation Speed (rpm)	0.67
Camera-to-object Distance (mm)	1000-2500

Experimental Results :

Table 5-45 contains the results obtained whilst varying the camera-to-object distance. The following abbreviations are used in the presentation of the results :

X_{vox} $\equiv$ X-axis voxel dimensions surrounding frame target 6.4, in mm / pixel;

Y_{vox} $\equiv$ Y-axis voxel dimensions surrounding frame target 6.4, in mm / pixel;

Z_{vox} $\equiv$ Z-axis voxel dimensions surrounding frame target 6.4, in mm / pixel;

X_{rms} $\equiv$ the rms X-axis co-ordinate measurement errors in the target positions calculated by the camera system, in mm;

Y_{rms} $\equiv$ the rms Y-axis co-ordinate measurement errors in the target positions calculated by the camera system, in mm;

Z_{rms} $\equiv$ the rms Z-axis co-ordinate measurement errors in the target positions calculated by the camera system, in mm.

D_{co} (mm)	X_{vox} (mm/pix)	X_{rms} (mm)	Y_{vox} (mm/pix)	Y_{rms} (mm)	Z_{vox} (mm/pix)	Z_{rms} (mm)
1000	0.3	0.7	0.5	0.7	0.6	1.2
1500	0.5	0.5	0.7	0.6	1.4	1.2
2000	0.7	1.0	1.0	1.3	2.6	3.4
2500	0.8	0.9	1.2	1.3	4.0	3.3

Table 5-45 Voxel Dimensions and Rms Co-ordinate Errors for a Variation in Camera-to-object Distance (D_{co})

Extent of the Stereoscopic Volume

Table 5-46 defines the extent of the stereoscopic volume in object space for the considered camera arrangement. For all camera-to-object distances, the stereoscopic volume remains unchanged as no camera parameters are varied in this experiment.

Z_{near} (mm)	702
Z_{far} (mm)	-
Z_{con} (mm)	1418
X_2 (mm)	509
Y_{zmin} (mm)	373
Y_{zmax} (mm)	-

Table 5-46 Stereoscopic Volume for a Variation in Camera-to-object Distance

Where,

- Z_{near}, Z_{far} and Z_{con} define the Z-plane (Figure 4-11) and are calculated from the equations in Section 4.9.3;
- X_2 defines the extent of the X-plane with reference to the start of the stereoscopic rotation (Figure 4-9), calculated from equation 4-25;
- Y_{zmin} and Y_{zmax} define the boundary in the Y-plane at the Z_{near} and Z_{far} limits (Figure 4-10), respectively, calculated from equation 4-33 and equation 4-34.

In Table 5-46 '-' indicates no Z_{far} and Y_{zmax} exists for the camera configuration as the ray geometry, for the experimental set-up considered, does not converge to a far limit in the Z-plane. This effect is demonstrated in Figure 5-40.
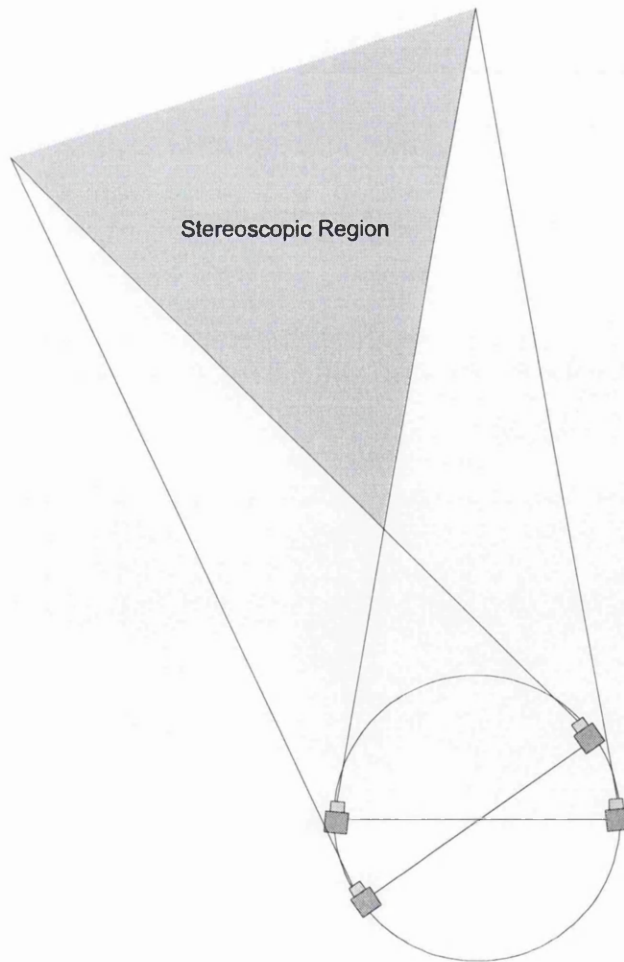
Figure 5-40 Stereoscopic Arrangement with an Undefined Far Limit in the Z-plane

Variation in Voxel Dimensions

For each variation in camera-to-object range Table 5-45 contains the calculated X, Y and Z voxel dimensions for target 6.4. The voxel dimensions are obtained using the algorithms defined in Section 4-10. For the target, a theoretical translation of ±5mm is applied in each axis and the resultant change in pixels allows dimensions, in mm / pixel, to be obtained.

Graph 5-1 shows the change in volume element dimensions for a variation in camera-to-object distance from 1000 to 2500mm. The following voxel characteristics are evident :

- the volume element dimensions in the X-axis of object space change from 0.3 to 0.8mm / pixel as the camera-to-object distance varies from 1000 to 2500mm;

- the volume element dimensions in the Y-axis of object space change from 0.5 to 1.2 mm / pixel as the camera-to-object distance varies from 1000 to 2500mm;

- the volume element dimensions in the Z-axis of object space change from 0.6 to 4.0mm / pixel as the camera-to-object distance varies from 1000 to 2500mm.
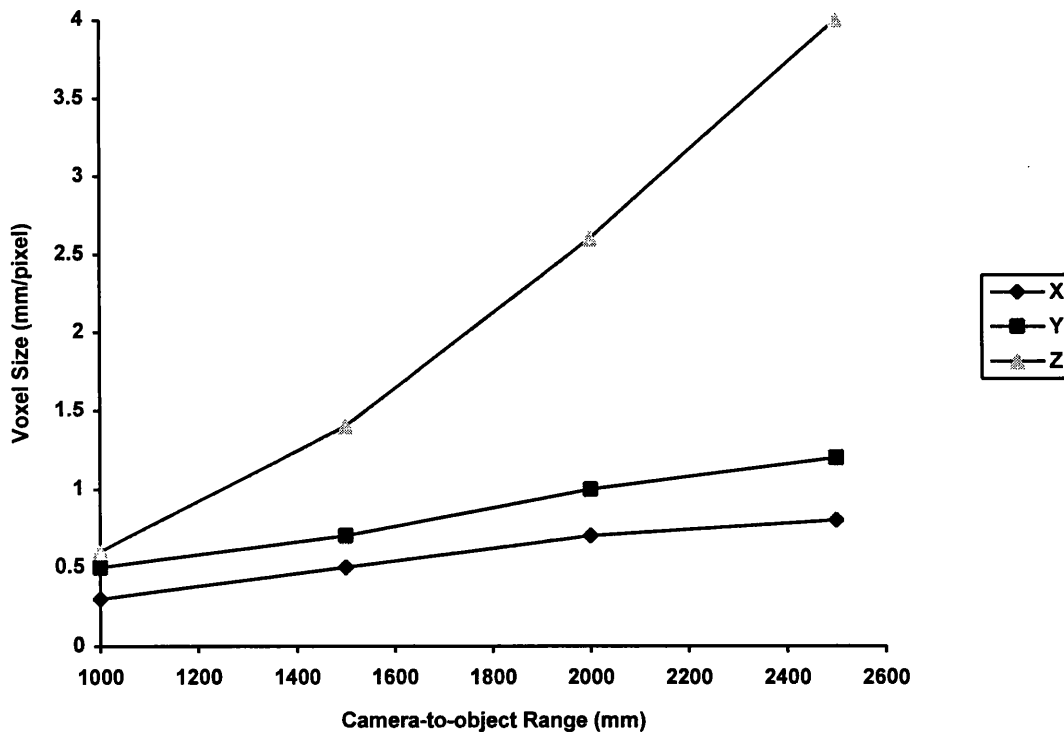
Graph 5-1 Voxel Size in 3-D Object Space for a Variation in Camera-to-object Distance

The change in voxel dimensions are as expected because each element 'stretches' in object space as the range to an object increases (this is demonstrated in Figure 5-15). Consider the voxel dimensions at a camera-to-object range of 1000mm and 2000mm. As the camera-to-object distance is doubled the voxel element dimensions in the X and Y axis of object space double. The voxel dimensions in the Z-axis quadruple with the same increase in range. Thus, the minimum resolvable distance in each axis of object space increases with range. Therefore, an increase in range results in a reduction in the capability of the line-scan system to resolve 3-D co-ordinate information.

The results from the co-ordinate measurement analysis are now discussed.

The Measurement Capability

From Table 5-45 the following measurement characteristics are stated :

- the rms co-ordinate measurement errors in the X-axis of object space vary between ±0.5mm and ±1.0mm as the camera-to-object distance changes from 1000 to 2500mm;

- the rms co-ordinate measurement errors in the Y-axis of object space vary between ±0.6mm and ±1.3mm as the camera-to-object distance changes from 1000 to 2500mm;

- the rms co-ordinate measurement errors in the Z-axis of object space vary between ±1.2mm and ±3.4mm as the camera-to-object distance changes from 1000 to 2500mm.

Assuming a possible measurement error of up to ±1.0 pixels in the x and y image axes (refer to Section 3.6.1) the magnitude of the errors in the resolved 3-D co-ordinates are as anticipated except for a camera-to-object distance of 1000mm.

Consider the errors in the 3-D co-ordinate measurements at a camera-to-object range of 2500mm. The approximate voxel dimensions in the X, Y and Z-axis are 0.8, 1.2 and 4mm / pixel, respectively. Therefore, the expected accuracy of the resolved X, Y and Z co-ordinates are ±0.8mm, ±1.2mm and ±4mm, respectively. Thus, from Table 5-45, the measurement errors are as expected.

Now consider the co-ordinate measurement errors at a range of 1000mm. The expected accuracy of the resolved X, Y and Z co-ordinates are ±0.3mm, ±0.5mm and ±0.6mm, respectively. The errors in the resolved co-ordinates are twice the expected magnitude. This is considered to be due to the distortion in the 25mm lens used in this experiment. As discussed in Section 5.5.2, the 25mm lens produces the worst case distortions which are apparent due to the range setting of 1000mm. As the range increases beyond this setting the effect of the lens distortions are minimised as the targets of interest appear closer to the image centre.

Experimental Conclusions :

The following summarises the results produced from a variation in camera-to-object distance :

- as the camera-to-object distance is doubled the size of the voxel elements in the X and Y axis of object space double. The voxel dimensions in the Z-axis quadruple with the same increase in range. Therefore, the available resolution in object space decreases as a function of increasing range;
- the stereoscopic camera system can resolve 3-D co-ordinates to the expected degree of accuracy except for small camera-to-object distances (< 1500mm) when lens distortion becomes apparent.

5.8.3 Variation in Convergence Angle and Base Width

From the co-ordinate measurement algorithms, presented in Section 4.7.1, it is observed that the stereoscopic base width setting may be considered as a scaling factor for object space measurements. Therefore, only a defined variation in convergence angle is considered in this part of the work. However, to maintain a constant convergence plane it is necessary to alter the base width parameter in accordance with the convergence angle selected. Specifically, this part of the experimentation evaluates the measurement characteristics associated with a change in the camera convergence angle of between 75° and 85°, in 2.5° increments. Further changes in convergence angle are not considered as this angle range defines the limits of the possible base width setting necessary to maintain a constant convergence plane.

Experimental Hypothesis :

"To investigate the three-dimensional characteristics associated with variation in the camera convergence angle"

Experimental Conditions :

Camera-to-object range (mm)	1500
Focal Length (mm)	25
Camera Scan Rate (kHz)	200
Platform Rotation Speed (rpm)	0.67
Convergence Angle (°)	75 - 85
Base Width (mm)	248 - 760

Experimental Results :

For each convergence angle setting used in the experimental work the base width is adjusted accordingly to maintain a convergence plane at a fixed distance from the centre of rotation. The combination of convergence angle / base width settings are presented in Table 5-47.

θ_c (°)	B (mm)
75.0	760
77.5	629
80.0	500
82.5	373
85.0	248

Table 5-47 Base Width Setting for Convergence Angle Variation

Table 5-48 contains the results obtained from the variation in the camera convergence angle.

θ_c (°)	X_{vox} (mm/pix)	X_{rms} (mm)	Y_{vox} (mm/pix)	Y_{rms} (mm)	Z_{vox} (mm/pix)	Z_{rms} (mm)
75.0	0.5	0.7	0.8	0.5	0.9	1.2
77.5	0.5	0.8	0.7	0.4	1.1	1.4
80.0	0.5	0.5	0.7	0.6	1.4	1.2
82.5	0.5	0.8	0.7	0.5	1.7	1.9
85.0	0.5	0.8	0.7	0.5	2.5	2.1

Table 5-48 Voxel Dimensions and Co-ordinate Errors for Variation in Convergence Angle (θ_c)

Extent of the Stereoscopic Region

Table 5-49 contains the information relating to the change in stereoscopic volume in object space for the variations in convergence angle. These relationships are illustrated in Graph 5-2.

θ_c	75.0°	77.5°	80.0°	82.5°	85.0°
Z_{near}(mm)	852	785	702	598	462
Z_{far} (mm)	4707	8918	-	-	-
Z_{con} (mm)	1418	1418	1418	1418	1418
X_2 (mm)	510	509	509	510	509
Y_{zmin} (mm)	462	421	373	373	243
Y_{zmax}(mm)	2551	4782	-	-	-

Table 5-49 Stereoscopic Volume for a Variation in Convergence Angle
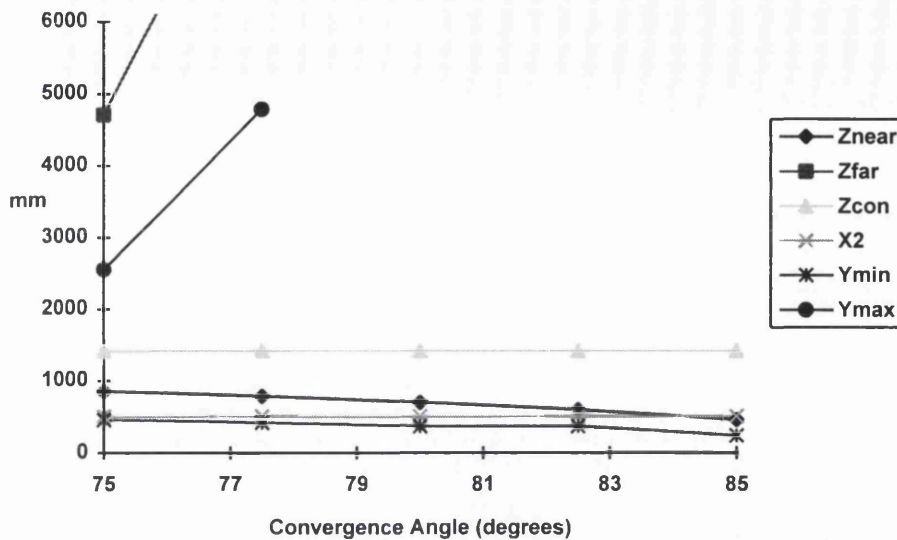
Graph 5-2 Stereoscopic Volume for a Variation in Convergence Angle

The following discusses the characteristics of the stereoscopic volume (Table 5-49) for the variation in the convergence angle / base width settings considered in this experiment.

For a given camera arrangement, from Figure 5-41, if *only* the convergence angle is increased the extent of the stereoscopic volume in the X and Z axes of object space would increase. Also, the distance of the stereoscopic volume from the rotation centre would increase, therefore, the magnitudes of Y_{zmin} and Y_{zmax} would increase.

If *only* the base width is decreased (Figure 5-42) this would have a similar effect to decreasing the convergence angle. However, for a change in base width the geometric shape of the X-Z stereoscopic plane remains identical, unlike the effects of changing convergence angle.

For the experiment considered, the convergence angle is increased whilst the base width is decreased to counteract the change in the position of the convergence plane. Therefore, from Figure 5-43, the magnitude of Z_{near}, and thus Y_{zmin}, decreases and the magnitude of Z_{far}, and thus Y_{zmax}, increases due to the stereoscopic volume being 'stretched' in the X-Z plane. It should be noted that the magnitude of X_2 remains approximately constant as it is controlled by the relationship between the convergence angle and base width (Equation 4-25). Also, as the co-ordinate measurements are taken from object space surrounding the convergence plane the voxel dimensions in the Y-axis remain approximately constant.
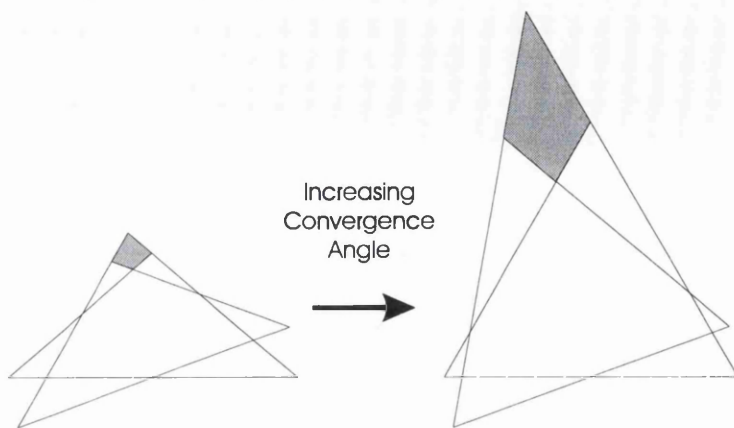
Figure 5-41 Increasing Convergence Angle whilst Maintaining a Constant Base Width
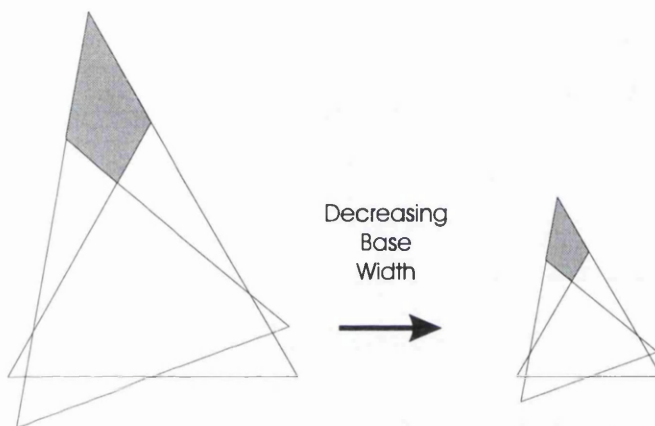
Figure 5-42 Decreasing Base Width whilst Maintaining a Constant Convergence Angle
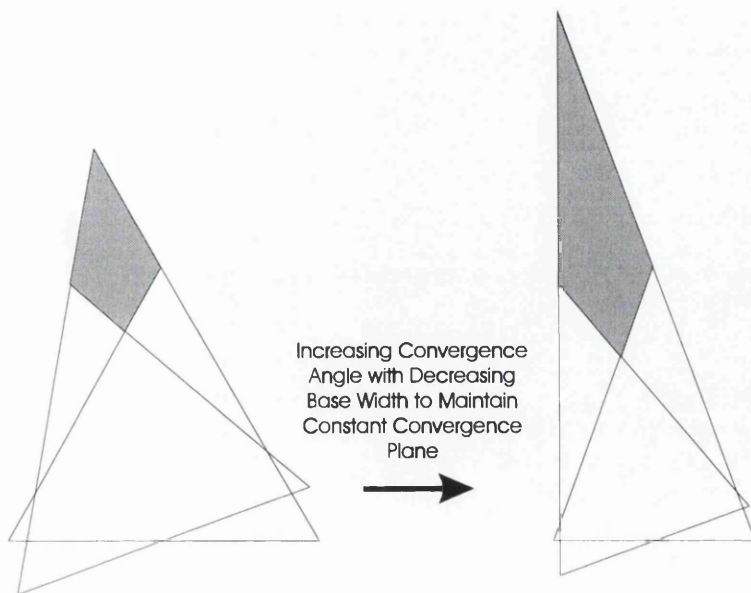
Figure 5-43 Increasing Convergence Angle with Decreasing Base Width to Maintain a Constant

Convergence Plane

Variation in Voxel Dimensions

Table 5-48 contains the calculated X, Y and Z voxel dimensions for target 6.4. Graph 5-3 shows the change in these volume element dimensions for a convergence angle variation between 75° and 85°. The following characteristics are evident :

- the volume element dimensions in the X-axis of object space remain constant at 0.5mm / pixel;

- the volume element dimensions in the Y-axis of object space remain approximately constant between 0.7 and 0.8 mm / pixel;

- the volume element dimensions in the Z-axis of object space increase from 0.9 to 2.5mm / pixel as the convergence angle increases from 75° to 85°.
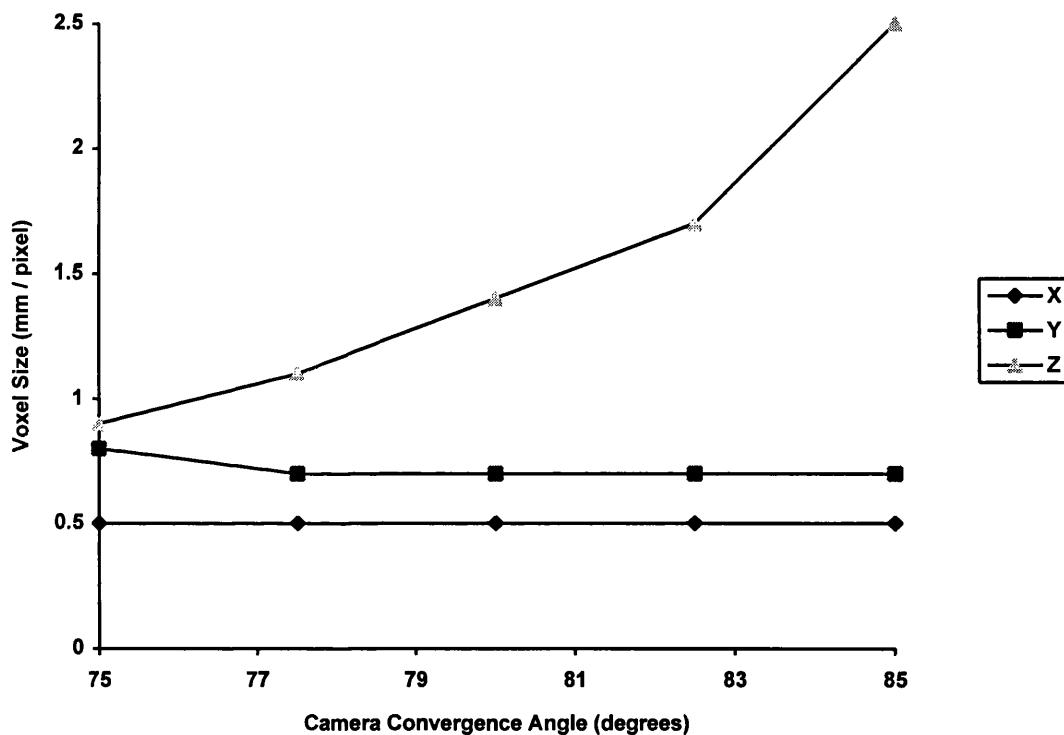
Graph 5-3 Voxel Size in 3-D Object Space for a Variation in Convergence Angle

The Measurement Capability

From Table 5-48 the following is stated :

- the rms measurement errors in the X-axis of object space vary between ±0.5mm and ±0.8mm as the convergence angle changes from 75° to 85°;

- the rms measurement errors in the Y-axis of object space vary between ±0.4mm and ±0.6mm as the convergence angle changes from 75° to 85°;

- the rms measurement errors in the Z-axis of object space vary between ±1.2mm and ±2.1mm as the convergence angle changes from 75° to 85°.

Assuming a possible measurement error of up to ±1.0 pixels in the x and y image axes the magnitude of the errors in the resolved 3-D co-ordinates are as anticipated.

Experimental Conclusions :

The following summarises the results produced from a variation of convergence angle / base width settings :

- voxel dimensions in the X and Y axes of object space remain approximately constant for a fixed convergence plane;

- for a fixed convergence plane the voxel dimensions in the Z axis of object space increase in size with increasing convergence angle;

- the stereoscopic system can resolve 3-D co-ordinates to the expected degree of accuracy for all convergence angle settings considered in this part of the work.

5.8.4 Variation in Scan Rate

This part of the work evaluates the characteristics of the stereoscopic system associated with a change in the camera scan rate of between 100kHz and 300kHz, in 50kHz increments.

Experimental Hypothesis :

"To investigate the three-dimensional characteristics associated with variation in the camera scan rate"

Experimental Conditions :

Camera-to-object range (mm)	1500
Base width (mm)	500
Convergence Angle (degrees)	80
Focal Length (mm)	25
Platform Rotation Speed (rpm)	0.67
Camera Scan Rate (kHz)	100 - 300

Experimental Results :

Table 5-50 contains the results obtained from variation of camera scan rate.

F_{SR} (kHz)	X_{vox} (mm/pix)	X_{rms} (mm)	Y_{vox} (mm/pix)	Y_{rms} (mm)	Z_{vox} (mm/pix)	Z_{rms} (mm)
100	1.0	0.6	0.7	1.0	2.7	1.4
150	0.7	0.6	0.7	1.0	1.8	1.7
200	0.5	0.5	0.7	0.6	1.4	1.2
250	0.4	0.6	0.7	0.9	1.1	1.6
300	0.3	0.6	0.7	0.9	0.9	1.4

Table 5-50 Voxel Dimensions and Co-ordinate Errors for a Variation in Camera Scan Rate (F_{SR})

Extent of the Stereoscopic Volume

For each variation in scan rate considered the extent of the stereoscopic volume is defined in Table 5-51 and is illustrated in Graph 5-4.

F_{SR}	100kHz	150kHz	200kHz	250kHz	300kHz
Z_{near}(mm)	477	604	702	779	841
Z_{far}(mm)	-	-	-	8942	4734
Z_{con}(mm)	1418	1418	1418	1418	1418
X_2(mm)	951	667	509	411	344
Y_{zmin}(mm)	241	317	373	417	451
Y_{zmax}(mm)	-	-	-	4783	2540

Table 5-51 The Stereoscopic Volume for a Variation in Scan Rate
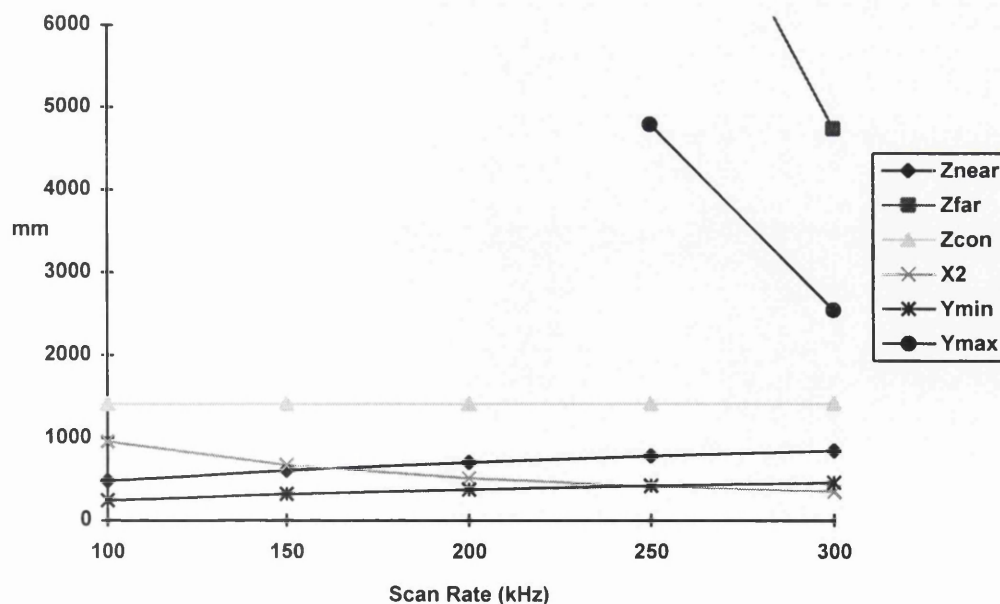
Graph 5-4 Extent of Stereoscopic Volume for a Variation in Scan Rate

As the scan rate increases the field of view in object space decreases due to a reduction in the time available to capture a complete image, as discussed in Section 3.2.3. The effect of varying the camera scan rate and, thus, the FOV in the movement axis, is illustrated in Figure 5-44. In (B) the field of view is reduced, when compared to the FOV in (A), due to an increased scan rate. Thus, for increasing scan rate, Z_{far}, Y_{zmax} and X_2 decrease in magnitude and the distance from the rotation centre to Z_{near} increases. As the camera geometry remains unchanged for a variation in scan rate the distance from the rotation centre to the convergence plane, Z_{con}, remains constant.

Convergence Plane   Convergence Plane

(A)   (B)
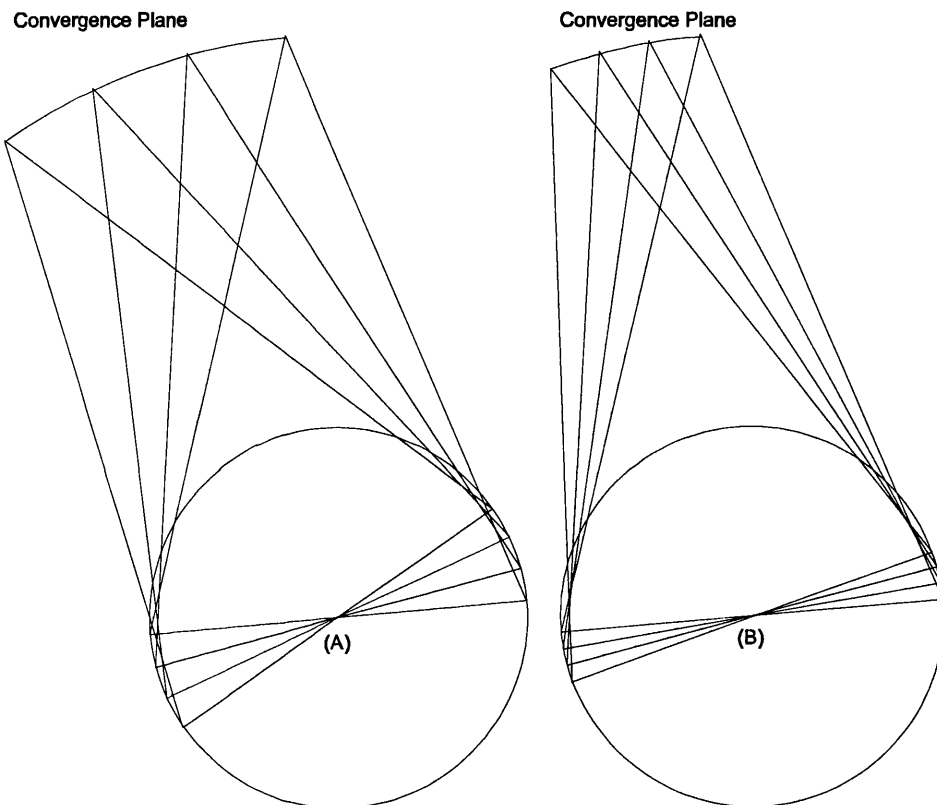
Figure 5-44 Decreasing FOV in Object Space with Increasing Camera Scan Rate

Variation in Voxel Dimensions

Table 5-50 contains the calculated X, Y and Z voxel dimensions for target 6.4. Graph 5-5 shows the change in these volume element dimensions for scan rate variation between 100kHz and 300khz. The following voxel characteristics are evident :

- X-axis voxel dimensions decrease from 1.0 to 0.3mm / pixel with increasing scan rate;

- Y-axis voxel dimensions remain constant at 0.7 mm / pixel;

- Z-axis voxel size decreases from 2.7 to 0.9mm / pixel with increasing scan rate.
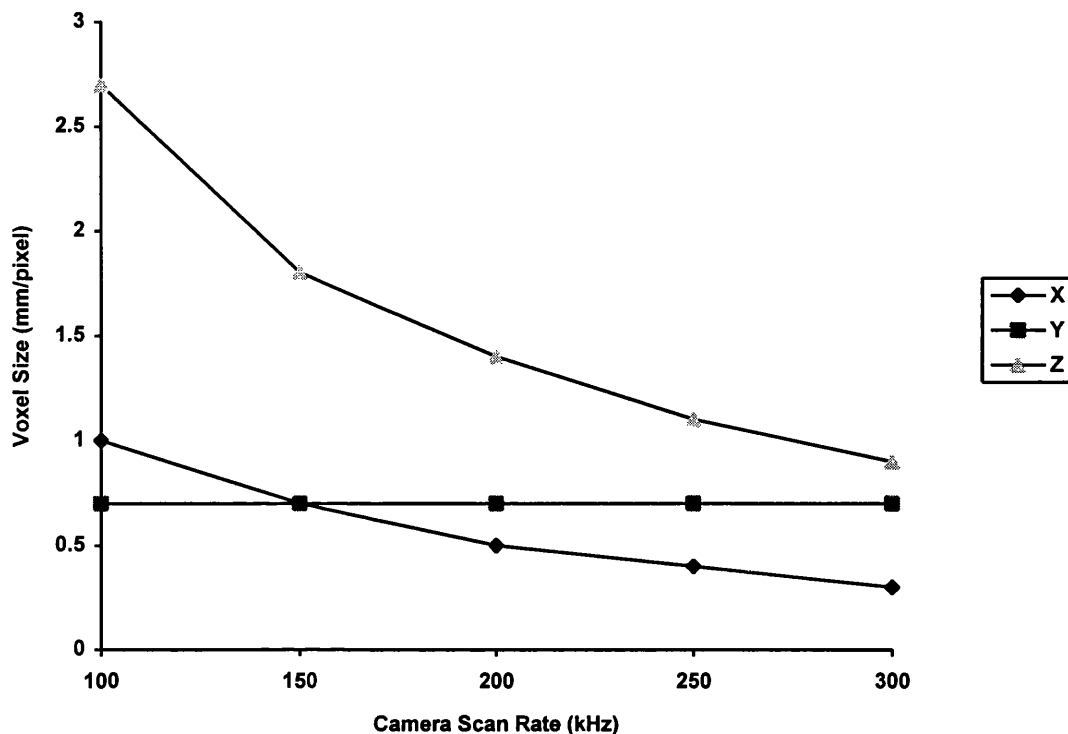
Graph 5-5 Voxel Size in 3-D Object Space for a Variation in Scan Rate

The Measurement Capability

From Table 5-50 the following is stated :

- the rms co-ordinate measurement errors in the X-axis of object space vary between ±0.5mm and ±0.6mm as the scan rate increases from 100 to 300kHz;

- the rms co-ordinate measurement errors in the Y-axis of object space vary between ±0.6mm and ±1.0mm as the scan rate increases from 100 to 300kHz;

- the rms co-ordinate measurement errors in the Z-axis of object space vary between ±1.2mm and ±1.7mm as the scan rate increases from 100 to 300kHz.

The errors are within the anticipated error of ±1 pixel except for scan rates of 250 and 300kHz. The additional errors at these settings are considered to be due to distortion in the 25mm lens. The same magnitude of error exists in the 1000mm range setting from the result in Table 5-45. From this, it is observed the voxel dimension in the X-axis is 0.3 mm / pixel which is the same order of magnitude as the X-axis voxel dimensions considered at scan rates of 250 and 300kHz. Thus, lens distortion causes the excessive errors in the resolved co-ordinates.

Experimental Conclusions :

The following summarises the results produced from a variation in camera scan rate :

- as the scan rate doubles in magnitude the voxel dimensions in the X and Z axes half in size and the Y-axis voxel dimensions remain unchanged. Therefore, the resolution available in the X-axis and Z-axis increases with a rise in scan rate;

- the stereoscopic camera system can resolve 3-D co-ordinates to the expected degree of accuracy except for large camera scan-rates (>200kHz) when lens distortion errors become apparent.

5.8.5 Variation in Rotation Speed

This part of the work evaluates the measurement characteristics associated with a change in rotation speed of between 0.67 and 2.0 rpm.

Experimental Hypothesis :

"To investigate the three-dimensional characteristics associated with variation in the camera rotation speed"

Experimental Conditions :

Camera-to-object range (mm)	1500
Base width (mm)	500
Convergence Angle (degrees)	80
Focal Length (mm)	25
Camera Scan Rate (kHz)	200
Rotation Speed (rpm)	0.67 - 2.00

Experimental Results :

Table 5-52 contains the results obtained from variation of camera rotation speed.

S_R (rpm)	X_{vox} (mm/pix)	X_{rms} mm	Y_{vox} (mm/pix)	Y_{rms} (mm)	Z_{vox} (mm/pix)	Z_{rms} (mm)
0.67	0.5	0.5	0.7	0.6	1.4	1.2
1.00	0.7	0.6	0.7	1.0	2.0	1.5
1.34	0.8	0.7	0.7	1.0	2.8	2.6
1.67	1.0	0.6	0.7	0.9	2.8	2.6
2.00	1.6	0.7	0.7	0.6	4.3	3.0

Table 5-52 Voxel Dimensions and Co-ordinate Errors for a Variation in Rotation Speed (S_R)

Extent of the Stereoscopic Volume

Table 5-53 defines the change in the stereoscopic volume for the variations considered in rotation speed. The change in stereoscopic volume is illustrated in Graph 5-6.

S_R	0.67rpm	1.00rpm	1.34rpm	1.67rpm	2.00rpm
Z_{near}(mm)	702	568	477	417	372
Z_{far}(mm)	-	-	-	-	-
Z_{con}(mm)	1418	1418	1418	1418	1418
X_2(mm)	509	739	951	1125	1262
Y_{zmin}(mm)	373	295	241	202	172
Y_{zmax}(mm)	-	-	-	-	-

Table 5-53 Stereoscopic Volume for a Variation in Rotation Speed

As discussed in Section 3.2.3, the rotation speed characteristics are of an inverse nature to those associated with scan rate, i.e., increasing scan rate causes a reduction in the field of view in object space whilst the FOV increases with rotation speed. The effect of varying rotation speed is illustrated in Figure 5-45. In (B) the field of view is reduced, in comparison to (A), due to decreasing rotation speed, resulting in a rise in magnitude of Z_{near} and Y_{zmin}. Consequently, Z_{far}, Y_{zmax} and X_2 decrease in magnitude with increasing rotation speed. As the camera geometry remains unchanged for a variation in rotation speed the distance from the rotation centre to the convergence plane, Z_{con}, remains constant.
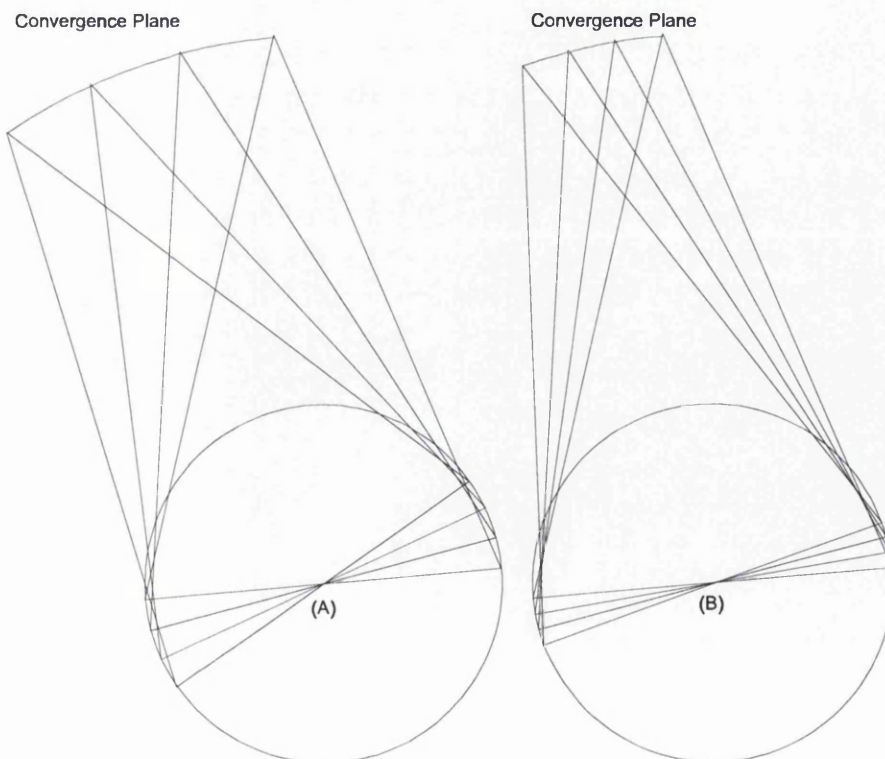
Figure 5-45 Decreasing FOV in Object Space with Decreasing Rotation Speed
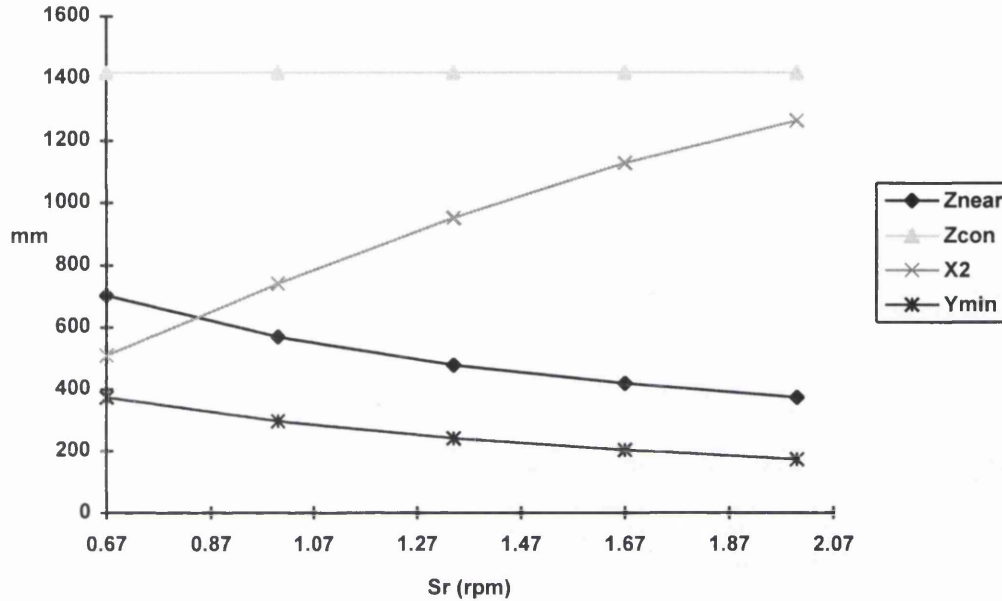
Graph 5-6 Extent of Stereoscopic Volume for a Variation in Rotation Speed

Variation in Voxel Dimensions

Table 5-52 contains the calculated X, Y and Z voxel dimensions for target 6.4. Graph 5-7 shows the change in these volume element dimensions for the rotation speed variation between 0.67rpm and 2.0rpm. The following voxel characteristics are evident :

- the volume element dimensions in the X-axis of object space increase from 0.5 to 1.6 mm / pixel with increasing rotation speed;

- the volume element dimensions in the Y-axis of object space remain constant at 0.7 mm / pixel;

- the volume element dimensions in the Z-axis of object space increase from 1.4 to 4.3mm / pixel with increasing rotation speed.
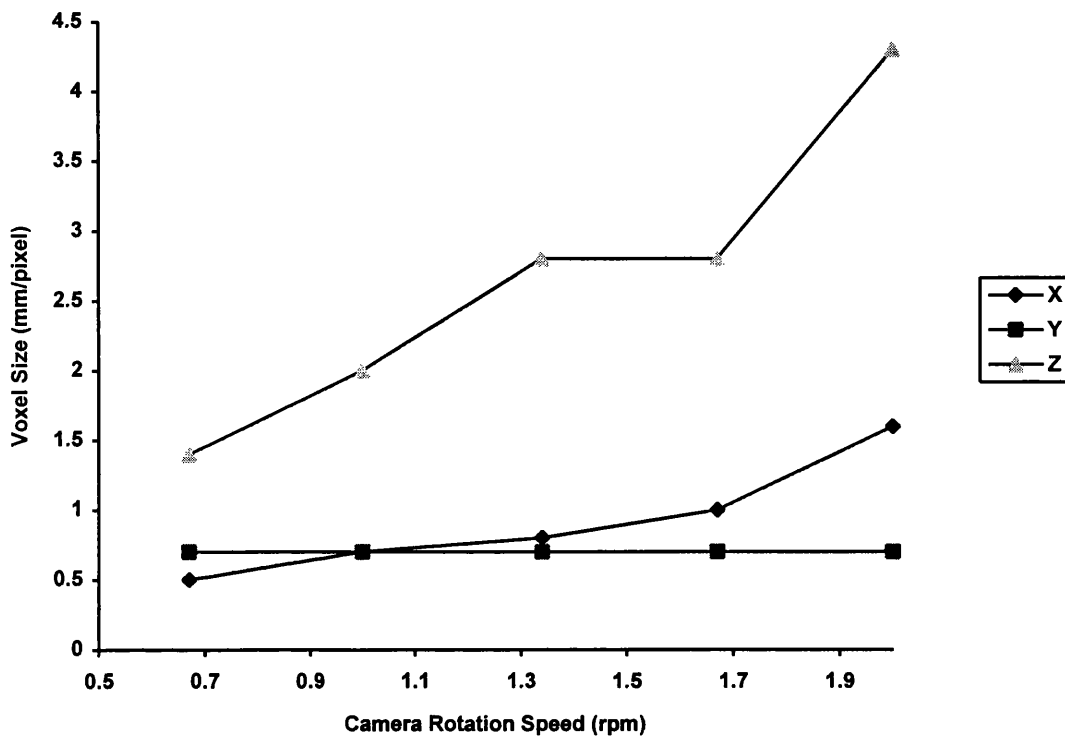
Graph 5-7 Voxel Size in 3-D Object Space for a Variation in Rotation Speed

The Measurement Capability

From Table 5-52 the following is stated :

- the rms measurement errors in the X-axis of object space vary between ±0.5mm and ±0.7mm as the rotation speed increases from 0.67 to 2.00 rpm;

- the rms measurement errors in the Y-axis of object space vary between ±0.6mm and ±1mm as the rotation speed increases from 0.67 to 2.00 rpm;

- the rms measurement errors in the Z-axis of object space vary between ±1.2mm and ±3.0mm as the rotation speed increases from 0.67 to 2.00 rpm.

Assuming a possible measurement error of up to ±1.0 pixels in the x and y image axes the magnitude of the errors in the resolved 3-D co-ordinates are to the anticipated level of accuracy.

Experimental Conclusions :

- as the rotation speed doubles in magnitude the voxel dimensions in the X and Z axes double in size and the Y-axis voxel dimensions remain unchanged. Thus,

the resolution available in the X-axis and Z-axis decreases with increasing rotation speed;

- the stereoscopic camera system can resolve 3-D co-ordinates to the expected degree of accuracy for all considered variations in rotation speed.

5.8.6 Variation in Focal Length

This part of the experimentation evaluates the stereoscopic measurement characteristics associated with camera-lens focal lengths of 25mm, 50mm and 75mm. For the focal length settings of 50mm and 75mm the field of view produced in the Y-axis could not provide the same target information from the calibration frame, as in the previous parameter variations. Therefore, for the experiments with the 50mm and 75mm focal lengths different targets were selected for use in the calibration and calculation procedures. For the 50mm lens the control and 'calculation' targets are shown in Table 5-54 and Table 5-55, respectively, and for the 75mm lens the control and 'calculation' targets are shown in Table 5-56 and Table 5-57, respectively.

Frame Point	X (mm)	Y (mm)	Z (mm)
4.1	2.13	150.39	-335.59
4.3	100.53	149.62	39.58
6.2	51.56	250.05	-162.60
7.4	152.13	300.73	-331.11
9.1	2.51	401.29	-297.83
9.4	151.14	400.25	-97.58

Table 5-54 3-D Frame Co-ordinates of the Control Targets used with the 50mm lens

Frame Point	X (mm)	Y (mm)	Z (mm)
4.2	51.04	150.93	-241.25
4.4	150.80	150.00	-141.38
5.2	51.03	200.29	-91.82
5.4	151.62	202.00	-282.55
6.1	1.075	251.59	-269.93
6.3	100.58	249.19	-198.69
6.4	150.18	250.18	-151.69
7.1	2.65	302.16	-298.38
8.2	51.85	354.63	-297.80
8.4	150.04	351.62	-261.73

Table 5-55 3-D Frame Co-ordinates of the 'Calculation' Targets used with the 50mm Lens

Frame Point	X (mm)	Y (mm)	Z (mm)
5.1	1.15	200.29	-49.72
5.4	151.62	202.00	-282.55
6.3	100.58	249.19	-198.69
7.1	2.65	302.16	-298.38
8.2	51.85	354.63	-297.80
8.4	150.04	351.62	-261.73

Table 5-56 3-D Frame Co-ordinates of the Control Targets used with the 75mm Lens

Frame Point	X (mm)	Y (mm)	Z (mm)
5.2	51.03	200.29	-91.82
5.3	101.75	199.51	-211.50
6.1	1.08	251.59	-269.93
6.2	51.56	250.05	-162.60
6.4	150.18	250.18	-151.69
7.4	152.13	300.73	-331.11

Table 5-57 3-D Frame Co-ordinates of the 'Calculation' Targets used with the 75mm Lens

Experimental Conditions :

Camera-to-object range (mm)	1500
Base width (mm)	500
Convergence Angle (degrees)	80
Camera Scan Rate (kHz)	200
Platform Rotation Speed (rpm)	0.67
Focal Length (mm)	25 - 75

Experimental Results :

Table 5-58 contains the results obtained from a variation in the camera lens focal length.

f (mm)	X_{vox} (mm/pix)	X_{rms} (mm)	Y_{vox} (mm/pix)	Y_{rms} (mm)	Z_{vox} (mm/pix)	Z_{rms} (mm)
25	0.5	0.5	0.7	0.6	1.4	1.2
50	0.5	0.6	0.3	0.4	1.4	1.6
75	0.5	0.5	0.2	0.4	1.4	2.0

Table 5-58 Voxel Dimensions and Co-ordinate Errors for a Variation in Focal Length (f)

Extent of the Stereoscopic Volume

From Table 5-59 Y_{zmin} is the only parameter of the stereoscopic volume that changes with focal length (Graph 5-8). Y_{zmax} would change with the focal length, however, for the camera arrangement considered the ray geometry does not converge to produce a Z_{far} point.

f	25mm	50mm	75mm
Z_{near}(mm)	702	702	702
Z_{far} (mm)	-	-	-
Z_{con} (mm)	1418	1418	1418
X_2 (mm)	509	509	509
Y_{zmin} (mm)	373	187	124
Y_{zmax}(mm)	-	-	-

Table 5-59 Extent of Stereoscopic Region for a Variation in Focal Length
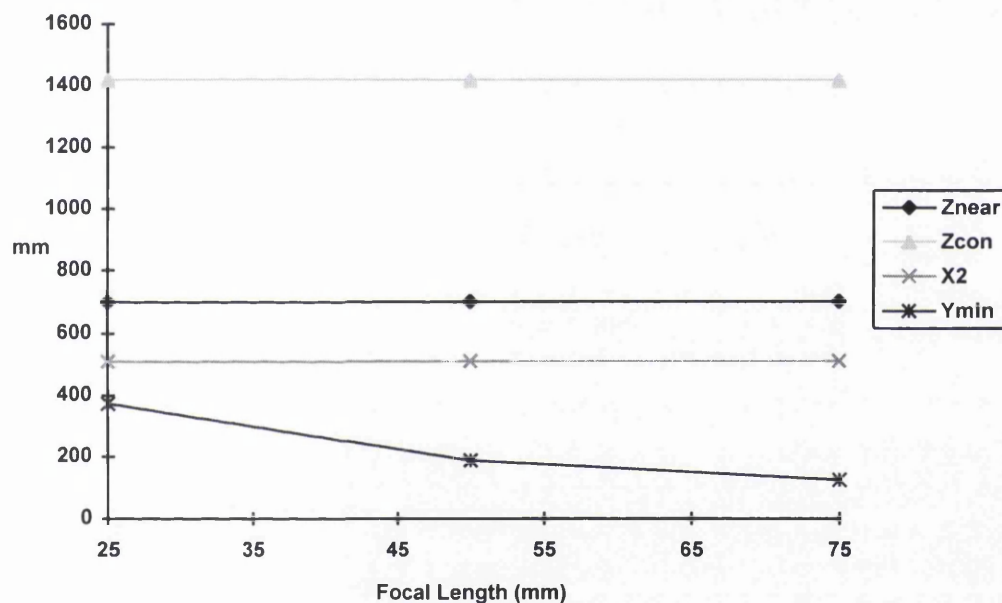
Graph 5-8 Stereoscopic Volume for a Variation in Focal Length

Variation in Voxel Dimensions

Table 5-54 contains the calculated X, Y and Z voxel dimensions for target 6.4. Graph 5-9 shows the change in volume element dimensions for a focal length variation between 25mm and 75mm. The following voxel characteristics are evident :

- X-axis voxel dimensions in object space remain constant at 0.5mm / pixel;

- Y-axis voxel dimensions in object space decrease from 0.7 to 0.2 mm / pixel;

- Z-axis voxel dimensions in object space remain constant at 1.4mm / pixel.

From Graph 5-9 it is observed that the voxel dimensions in the Y-axis of object space half in size as the camera-lens focal length is doubled.
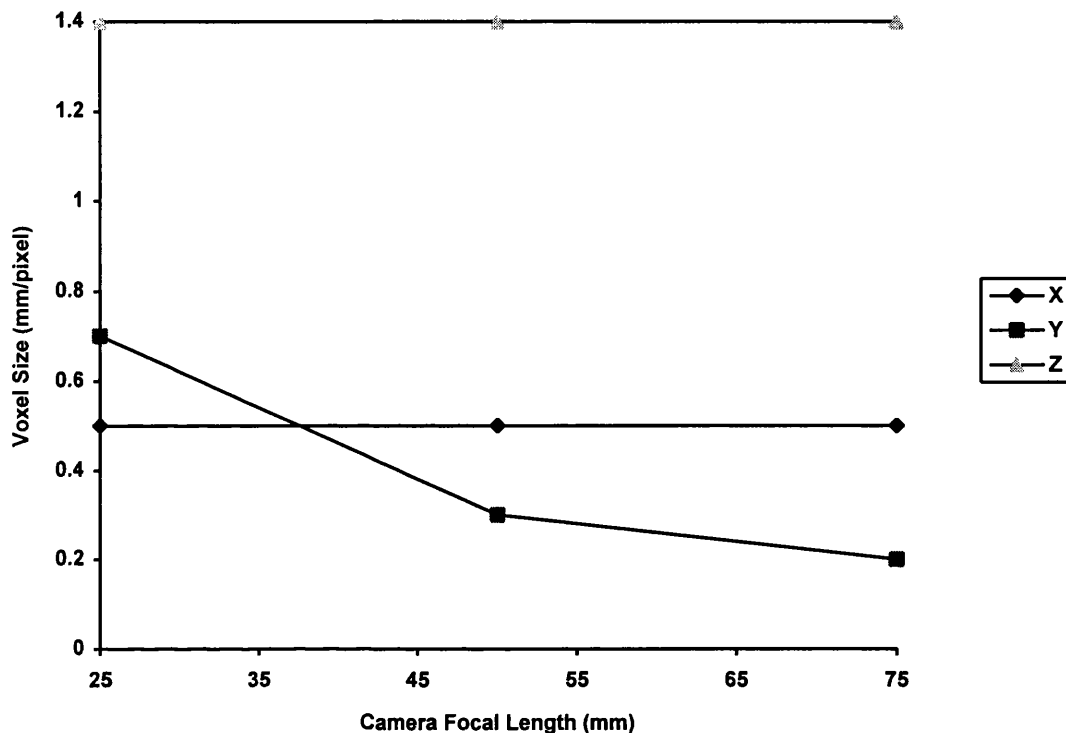
Graph 5-9 Voxel Size in 3-D Object Space for a Variation in Focal Length

The Measurement Capability

From Table 5-58 the following is stated :

- with a focal length setting of 25mm the rms errors in the resolved co-ordinates are ±0.5mm in the X-axis, ±0.6mm in the Y-axis and ±1.2mm in the Z-axis;

- with a focal length setting of 50mm the rms errors in the resolved co-ordinates are ±0.6mm in the X-axis, ±0.4mm in the Y-axis and ±1.6mm in the Z-axis;

- with a focal length setting of 75mm the rms errors in the resolved co-ordinates are ±0.5mm in the X-axis, ±0.3mm in the Y-axis and ±2.0mm in the Z-axis.

Assuming a possible measurement error of up to ±1.0 pixels in the x and y image axes the magnitude of the errors in the resolved co-ordinates are as anticipated for focal lengths of 25mm and 50mm. However, at a focal length of 75mm, the measurement error in the Y and Z co-ordinates are greater than expected. This error is not considered to be due to distortion as

the 75mm lens is expected to introduce the least amount of lens deformation and, at a camera-to-object distance of 1500mm, is considered to be insignificant (refer to Section 5.5.2).

For the 75mm lens, the voxel dimension in the Y-axis is 0.2 mm / pixel (Table 5-58). Thus, the number of y image pixels covering a target on the calibrated frame is, approximately, four times the number when using the 25mm lens. Therefore, due to the manual method of target location it is considered that the error when using the 75mm lens is to an acceptable level of accuracy.

Experimental Conclusions :

The following summarises the results produced from a variation in camera-lens focal length :

- as the focal length is doubled the voxel dimensions in the Y-axis of object space half in size, thus, the available resolution increases with focal length;
- the stereoscopic camera system can resolve 3-D co-ordinates to the expected degree of accuracy for all considered variations in focal length.

5.9 Summary

This chapter has detailed the research undertaken with a stereoscopic arrangement of rotating line-scan sensors. This work has been divided into the following areas of investigation :

- preliminary tests and experiments;
- determination of voxel size in object space;
- co-ordinate measurement capability;
- rotating stereoscopic line-scan characteristics.

The next chapter will present the conclusions from the research presented in this thesis.

6. SUMMARY, CONCLUSIONS AND FUTURE WORK

6.1 Introduction

This chapter completes this research by :

- summarising the results of the research presented in this thesis;
- presenting conclusions from the work undertaken with the rotating stereoscopic line-scan system;
- suggesting possible directions of future work.

6.2 Summary

A comprehensive discussion of results has already been presented throughout the main text of this thesis where appropriate.

The research described in this thesis was undertaken to investigate the use of rotating line-scan sensors in stereoscopic arrangements which are capable of extracting three-dimensional co-ordinate information from volumes of object workspace surrounding the camera system.

Initial work involved an appraisal of the line-scan device in a two-dimensional configuration. A 2-D system was constructed and experiments were undertaken to determine the suitability of the rotating sensor to the development of a stereoscopic camera arrangement. The results from this work verified that two-dimensional co-ordinate information could be obtained from a defined object space. Subsequently, a stereoscopic line-scan system was constructed for which a mathematical model was derived. Application of the algorithms enabled the 3-D location of targets in object space to be determined after a calibration procedure. Subsequently, an investigation into the measurement capability of the stereo-camera was undertaken to assess the suitability of the model.

Experimental work was conducted to quantify errors inherent in the rotating stereo-system and to isolate, if possible, the source of these errors. Further experiments were undertaken to determine the accuracy which could be achieved with such a system using the algorithms that were developed. The results indicate that three-dimensional position of targets in object space can be determined, at best, to an accuracy of ±0.5mm in the X-axis, ±0.6mm in the Y-axis and ±1.2mm in the Z-axis at a camera-to-object range of 1.5m.

6.3 Two-dimensional Line-scan System Results

An investigation into the two-dimensional operating characteristics of the line-scan device was completed in the preliminary stages of the research. This provided information on the fundamental points which allow image production from a rotating line-scan camera system. As a result of this analysis certain design considerations relating to the development of a stereoscopic arrangement of rotating line-scan sensors were identified. These included :

Repeatability :
- the assessment of the repeatability of image data in the x and y axes of image space due to the manual method of point location adopted in this research;

Image Space to Object Space Relationship :
- the establishment of a relationship between the angle of camera rotation and the pixel representation in the x-axis of image space;

Camera Calibration :
- the necessity to implement a camera calibration procedure in the final stereoscopic system design;

Calibrated Object Volume :
- the requirement for a 'unique' calibrated frame which provided enough targets for all of the considered stereoscopic arrangements.

A summary of the work undertaken with the rotating stereoscopic arrangement of line-scan sensors is now presented.

6.4 Results Obtained from the Stereoscopic Line-scan System

The primary aim of this research was to characterise rotating stereoscopic line-scan systems. The method selected to identify the attributes associated with the rotating line-scan system was to investigate the measurement capability of such an arrangement. This work was completed in the following phases :

- *Preliminary tests and experiments :*

  Before testing the co-ordinate measurement algorithms preliminary experimental work was undertaken to evaluate the possible errors inherent in each axis of the line-scan arrangement. Following this the DLT algorithm was applied to image space information obtained from the rotating line-scan system to determine if it could resolve 3-D co-ordinate information from object space.

- *Determination of voxel dimensions in object space :*

  The measurement capability of the stereoscopic system is determined directly by the resolution available in object space, therefore, to assess the applicability of the derived mathematical model a method of calculating 3-D voxel dimensions in object space was determined. This work validated the use of the algorithms, derived in Section 4.10, to extract voxel information from targets of interest in object space.

- *The co-ordinate measurement capability :*

  A mathematical model was derived specifically for use with the rotating line-scan system. This involved the use of absolute orientation methodology to develop a 3-D conformal transformation. Implementing this allowed calibration of the experimental arrangement which aligned mathematically the camera and object systems allowing the extraction of three-dimensional co-ordinate information from object space. This part of the work validated the mathematical model, derived in Section 4.0, for use with the rotating line-scan system.

- *Characteristics of the rotating stereoscopic line-scan system :*

  This part of the work verified the measurement capability of the rotating line-scan system for a variation in the parameters which govern image production. These parameters included :

> camera-to-object distance;

> stereo-camera base width;

> camera-to-base width convergence angle;

> camera scan rate;

> camera rotation speed;

> camera-lens focal length.

6.5 Conclusions

The aim of this research was to establish if a rotating stereoscopic arrangement of line-scan sensors could be used to determine the three-dimensional co-ordinates of targets of interest in object space. The final objective of the work was to determine the measurement characteristics associated with a variation in the stereoscopic parameters.

The following sections detail the work which demonstrates that these objectives have been achieved.

6.5.1 Preliminary Tests and Experiments

From the preliminary experimental work the following was determined :

- the error in the x-axis of image space due to inconsistencies in scan rate and rotation speed could be ignored for this work;

- lens distortion is apparent in the 25mm lens used in this research, however, by reducing the diameter of the lens aperture to a minimum and limiting the selected points as close to the image centre as possible the distortions are reduced to a minimum;

- the direct linear transformation cannot be applied to the stereoscopic arrangement of line-scan sensors.

6.5.2 Determination of Voxel Dimensions in Object Space

From the investigation of the voxel structure the following was determined :

- cylindrical voxel dimensions in object space can be calculated from an imposed cartesian co-ordinate system;

- typically, a 1 pixel increment in the x-axis of image space represents 0.5mm in the X-axis of object space, at a camera-to-object distance of 1500mm;

- typically, a 1 pixel increment in the y-axis of image space represents 0.7mm in the Y-axis of object space, at a camera-to-object distance of 1500mm;

- typically, a 1 pixel increment in the x-axis of image space represents 1.4mm in the Z-axis of object space, at a camera-to-object distance of 1500mm.

6.5.3 Co-ordinate Measurement Capability

From the investigation into the use of the 3-D conformal transformation, derived specifically for the stereoscopic line-scan system, the following results were obtained :

- the optimum number of control targets for use with the 3-D conformal transformation calibration is 6;

- control targets can be selected from any part of the calibration frame provided the targets used in the calculation procedure are selected from within the original calibration volume;

- changing the start of stereoscopic image capture does not alter the capability of the rotating line-scan system to resolve 3-D co-ordinates from object space;

- rotation of the calibration frame about the X-axis does not affect significantly the measurement capability of the camera system;

- rotation of the calibrated frame about the Y-axis does not affect significantly the measurement capability of the camera system;

- rotation of the calibrated frame about the Z-axis does not affect significantly the measurement capability of the camera system;

- using calibrated transformation parameters 3-D vectors can be extracted from other volumes of object space.

6.5.4 Rotating Stereoscopic Line-scan Characteristics

From the assessment of the rotating stereoscopic line-scan characteristics the following results were obtained :

Variation in Camera-to-Object Distance :

- as the camera-to-object distance is doubled the size of the voxel elements in the X and Y axis of object space double. The voxel dimensions in the Z-axis quadruple with the same increase in range. Therefore, the available resolution in object space decreases as a function of increasing range;

- the stereoscopic camera system can resolve 3-D co-ordinates to the expected degree of accuracy except for small camera-to-object distances (< 1500mm) when lens distortion becomes apparent.

Variation in Stereoscopic Camera Convergence Angle / Base Width :

- voxel dimensions in the X and Y axes of object space remain approximately constant for a fixed convergence plane;

- for a fixed convergence plane the voxel dimensions in the Z axis of object space increase in size with increasing convergence angle;

- the stereoscopic system can resolve 3-D co-ordinates to the expected degree of accuracy for all convergence angle settings considered in this part of the work.

Variation in Camera Scan Rate :

- as the scan rate doubles in magnitude the voxel dimensions in the X and Z axes half in size and the Y-axis voxel dimensions remain unchanged. Therefore, the resolution available in the X-axis and Z-axis increases with a rise in scan rate;

- the stereoscopic camera system can resolve 3-D co-ordinates to the expected degree of accuracy except for large camera scan-rates (>200kHz) when lens distortion becomes apparent.

Variation in Camera Rotation Speed :

- as the rotation speed doubles in magnitude the voxel dimensions in the X and Z axes double in size and the Y-axis voxel dimensions remain unchanged. Thus, the resolution available in the X-axis and Z-axis decreases with increasing rotation speed;

- the stereoscopic camera system can resolve 3-D co-ordinates to the expected degree of accuracy for all considered variations in rotation speed.

Variation in Camera Lens Focal Length :

- as the focal length is doubled the voxel dimensions in the Y-axis of object space half in size, thus, the available resolution increases with focal length;

- the stereoscopic camera system can resolve 3-D co-ordinates to the expected degree of accuracy for all considered variations in focal length.

6.5.5 Applications

From this work the capability to resolve three-dimensional co-ordinate information from object space has been identified. This would seem to provide solutions to specific problems in machine vision which would benefit from the capability to extract co-ordinate information from an 'all-round' view of the workspace surrounding the rotating camera platform. Previous work [45, 46, 47, 48, 49, 50, 51] in this area has involved predominantly the use of the conventional television camera for the production of similar images. However, to obtain a 'panoramic' field of view additional components have often been used in conjunction with the camera. These components have included a conic mirror, a fisheye lens and a vertical slit to facilitate the extraction of information from, for example, a 360° field of view.

The advantages of using a rotating line-scan system as opposed to other conventional television type systems include :

- no additional components are required to provide an 'all-round' field of view;

- the field of view of an image can be varied from any arc up to 360°. If the camera rotates 360° in the x-axis the images produced will contain information from the object space completely surrounding the line-scan arrangement;

- if the field of view is less than 360°, the area of object space under consideration can be selected by altering the start of image capture;

- the images produced by a rotating line-scan system may display information at a given resolution from a selected part of the surrounding object space.

Applications to which a rotating stereoscopic line-scan system may be suited are :

- security applications where continual surveillance of a 360° workspace is required;

- battlefield robotics where, for example, a 360° stereoscopic targeting system is required;

- image sequence analysis where the use of 'all-round' vision would allow different entry / exit positions in a scene to be monitored 'simultaneously';

- the construction of a three-dimensional model of a selected workspace surrounding the camera system in, for example, hazardous environments.

The applications would benefit from a rotating imaging system as the use of line-scan sensor technology has multiple advantages over standard television cameras. These include a higher possible resolution in each axis of the camera arrangement and an almost instantaneous image pan time due to the high scan rates / rotation speeds at which they may be driven.

6.6 Future Work

This section will outline possible directions for future work and is divided into the following areas:

- improving accuracy;

- associated areas of investigation.

6.6.1 Improving Accuracy

As stated in Section 2.5 it is not the purpose of this work to demonstrate the highest possible accuracy of the 3-D co-ordinate information extracted by the camera system. This research has developed a general mathematical model which has been validated experimentally in the extraction of co-ordinate information from object space and, from this, the system characteristics have been identified. It is considered that the generic algorithms in this thesis may be applied to

any rotating stereoscopic line-scan system in order to suit a specific application in machine vision.

To improve the accuracy of the resolved co-ordinate information there are several approaches that can be adopted. They include :

- developing more complex photogrammetric algorithms to include relative and interior orientation methodologies (as discussed in Chapter 2.0);
- the use of sub-pixel techniques.

6.6.2 Associated Areas of Investigation

The stereoscopic camera system developed here creates relative motion by camera rotation. This does not have to be the case. To produce two-dimensional images in the conventional sense it is only required that relative motion is inherent in the application. This can be achieved by rotation of the object with respect to a single static line-scan camera (Figure 6-1) or, indeed, a stereoscopic arrangement of static sensors.
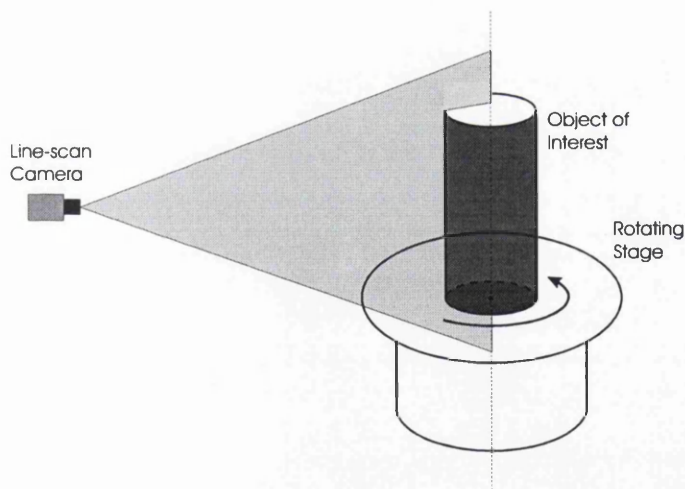
Figure 6-1 Object Rotation with respect to a Static Line-scan Camera

This process of image generation would allow the object of interest to be 'unfolded' as it rotates and would be suited to applications where inspection of objects is required.

References

References

1. B. Adaway, "Fruitful inspection", <u>Image Processing</u>, Vol. 1, Part 2, p. 18, 1989.

2. P.Seitz, M. T. Gale, H. Meier, J. M. Raynor, "Locometer : On-line inspection of locomotive wheel to rail movements using high precision CCD metrology", <u>SPIE In-process Optical Measurements and Industrial Methods</u>, Vol. 1266, pp. 39 - 45, 1990.

3. Y. Nomura, H. Naruse, A. Ide, M. Saga, "Visual inspection system for manhole facilities", <u>IEEE Int. Workshop Intelligent Robots & Systems</u>, Vol. 1, pp. 449 - 453, 1990.

4. D. Hutber, "Active stereo vision and its application to industrial inspection", <u>IEE Colloquium on Active and Passive Techniques for 3-D Vision</u>, pp. 1 - 4, Feb. 1991.

5. A. D. Marshall, D. R. Roberts, "Automatically planning the inspection of three-dimensional objects using stereo computer vision", <u>SPIE Three-Dimensional and Unconventional Imaging for Industrial Inspection and Metrology</u>, pp. 94 - 105, Oct. 1995.

6. S. B. Marapane, M. M. Trivedi, "Extracting depth by binocular stereo in a robot vision system", <u>SPIE Applications of Digital Image Processing XI</u>, Vol. 974, pp. 97 - 102, 1988.

7. H. T. Roman, B. A. Pellegrino, "Pipe crawling inspection robots : An overview", <u>IEEE Transactions on Energy Conversion</u>, Vol. 8, No. 3, pp. 576 - 583, Sept. 1993.

8. H. Ishida, T. Taketsugu, T. Ishimatsu, F. Kasagami, K. Kugai, "Two arc welding robots coordinated with 3-D vision sensor", <u>20th International Conference on Industrial Electronics, Control and Instrumentation</u>, Vol. 2, pp. 830 - 834, Sept. 1994.

References

9.   A. Ohya, E. Shoji, S. Yuta, "3-D range sensor using fiber grating for recognition of autonomous mobile robot's passage space", <u>Proceedings of the IEEE / RSJ / GI International Conference on Intelligent Robots and Systems</u>, Vol. 3, pp. 1759 - 1763, Sept. 1994.

10.   Y. F. Li, M. H. Lee, M. A. Rodrigues, J. J. Rowland, "Supervisory robotic control under vision guidance", <u>Proceedings of the IEEE / RSJ / GI International Conference on Intelligent Robots and Systems</u>, Vol. 3, pp. 2030 - 2035, Sept. 1994.

11.   R. Cipolla, N. J. Hollinghurst, "Human-robot interface by pointing with uncalibrated stereo vision", <u>Image and Vision Computing 14</u>, Elsevier Science B. V., pp. 171 - 178, 1996.

12.   M. Brady, A. Brint, W. Dickson, P. Foulkes, A. McIvor, G. Scott, "Vision and the Oxford AGV" <u>Presented at Image Processing : Blenheim Online Publications</u>, Middx, UK, pp. 267 - 286, 1988.

13.   M. A. Turk, D. G. Morgenthaler, K. D. Gremban, M. Marra, "VITS - A vision system for autonomous land vehicle navigation", <u>IEEE Transactions on Pattern Analysis and Machine Intelligence</u>, Vol. 10, No. 3, May 1988.

14.   Q. -T. Luong, J. Weber, D. Koller, J. Malik, "An integrated stereo-based approach to automatic vehicle guidance", <u>Proc. Fifth International Conference on Computer Vision</u>, pp. 52 - 57, June 1995.

15.   R. L. Horst, M. Negin, "Machine vision system for precision dimensional measurements and on-line SPC" <u>Conf. Record of the IEEE Ind. Appl. Soc. Ann. Meeting</u>, Vol. 2, pp. 1712 - 1716, 1989.

16.   M. C. Leu, R. M. Pherwani, "Vision system for three-dimensional position measurement based on stereo disparity", <u>Optics & Laser Technology</u>, Vol. 21, No. 5, pp. 319 - 324, 1989.

References

17. R. A. Bachnak, M. Celenk, "A stereo system for 3-D measurements in robot workspaces", <u>IEEE Int. Symp. on Intell. Control</u>, pp. 293 - 298, 1989.

18. F. Angrilli, G. Bianchini, G. Fanti, M. Mozzi, "On line measurements to control the forming process of glass vials", <u>SPIE Videometrics</u>, Vol. 1820, pp. 145 - 157, 1992.

19   N. Wittels, J. R. McClellan, K. Cushing, W. Howard III, A. Palmer, "How to select cameras for machine vision", <u>SPIE Optics, Illumination and Image Sensing for Machine Vision III</u>, Vol. 1005, 1988.

20. R-J. Ahlers, J. Lu, "Stereoscopic Vision - An Application Oriented Overview", <u>SPIE Optics, Illumination, and Image Sensing for Machine Vision IV</u>, Vol. 1194, pp. 298 - 308, 1989.

21   P. Cielo, "On-line optical sensors for industrial material inspection", <u>In-Process Optical Measurements and Industrial Methods</u>, Vol. 1266, pp. 22 - 38, 1990.

22. C. W. Moon, E. S. McVey, "Precision measurement techniques using computer vision", <u>Conference Record of the IEEE Industry Applications Society Annual Meeting</u>, Vol. 2, pp. 1521 - 1526, 1990.

23. L. Duvieubourg, J-G. Postaire, "Stereo vision with scan line cameras for intrusion detection", <u>ICARCV Second Int. Conf. on Automation, Robotics and Computer Vision</u>, Vol. 1, part CV9.3, pp. CV-9.3.1 - CV-9.3.5, 1992.

24. J. Lewis, R. Gill, A. S. White, "Active optical sensing for the control of flexible robots", <u>Advances in Manufacturing Technology VII</u>, ISBN 1 85790 00 7, pp. 351 - 355, University of Bath, September 1993.

25. M. Miethig, J.C. Renn, B.C. Doody, P. T. Jenkins, R. G. Ambrose, "A miniature variable scan camera for machine vision", <u>SPIE Cameras, Scanners and Image Acquisition Systems</u>, Vol. 1901, pp. 202 - 209, 1993.

References

26. D. J. Litwiller, M. Miethig, B. C. Doody, P. T. Jenkins, "High speed high resolution color line scan camera for machine vision", <u>SPIE Cameras, Scanners, and Image Acquisition Systems</u>, Vol. 1901, pp. 182 - 190, 1993.

27. A. R. Rao, " Future directions in industrial machine vision : a case study of semiconductor manufacturing applications", <u>Image and Vision Computing 14</u>, Elsevier Science B. V., pp. 3 - 19, 1996.

28. M. Robinson, S. C. Sood, "Real-time depth measurement in a stereoscopic television display", <u>SPIE Annual Technical Symposium</u>, Vol. 367, pp. 34 - 40, 1982.

29. M. Robinson, "Remote control vehicle guidance using stereoscopic displays", <u>Proceedings U.S. Human Factors Soc.</u>, Vol. 28, 1984.

30. A. M. Ariyaeeinia, "An active co-ordinate imaging system for robot vision", <u>Trent Polytechnic</u>, PhD Thesis, 1985.

31. P. J. Shuttleworth, "Visual feedback for robot manipulator control", <u>Trent Polytechnic</u>, PhD Thesis, 1989.

32. S. X. Godber, "The development of novel stereoscopic imaging sensors" <u>Nottingham Polytechnic</u>, PhD Thesis, 1991.

33. J. P. O. Evans, "Development of a 3-D x-ray system", <u>The Nottingham Trent University</u>, PhD Thesis, 1993.

34. S. X. Godber, M. Robinson, J. P. O. Evans, "The line-scan sensor : an alternative sensor modality for the extraction of 3-D co-ordinate information", <u>Optical Engineering - The Journal of SPIE</u>, 1995.

35. J. P. O. Evans, M. Robinson, S. X. Godber, "A new stereoscopic x-ray imaging technique using a single x-ray source : theoretical analysis", <u>Non-Destructive Testing & Evaluation International</u>, January 1996.

36. C. Smorenburg, A. L. G. van Valkenburg, "Automatic inspection of railway overhead wires", SPIE Industrial Inspection, Vol. 1010, pp. 107 - 117, 1988.

37. B. Neldam, "Vision based inspection and quality control for use in industrial laundries", SPIE Industrial Inspection, Vol. 1010, pp. 118 - 121, 1988.

38. F. Truchetet, H. Jender, L. F. C. Lew-Yan-Voon, "Inspection of continuously moving metallic tubes by artificial vision : modelisation and results", 20th International Conference on Industrial Electronics, Control and Instrumentation, Vol. 2, pp. 749 - 754, 1994.

39. J. D. Burjoski, "Novel hardware architecture for real-time, continuous line scan processing", SPIE Vol. 2347, pp. 340 - 351, 1994.

40. Z. Jian, L. Bo, W. Liying, S. Liankui, G. Hai, "Optical integrated testing instrument for pipe interior parameter measurement and inspection", SPIE Three-dimensional and Unconventional Imaging for Industrial Inspection and Metrology, Vol. 2599, pp. 400 - 405, Oct. 1995.

41. Y-S. Li, T. Y. Young, C-C, Huang, "Noncontact measurement using line-scan cameras : Analysis of positioning error", IEEE Transactions on Industrial Electronics, Vol. 36, No. 4, pp. 545 - 551, Nov. 1989.

42. J-L. Bruyelle, J-G. Postaire, "Direct range measurement by linear stereovision for real-time obstacle detection in road traffic", Robotics and Autonomous Systems 11, pp. 261 - 268, 1993.

43. E. C. Di Mauro, K. R. Wadhams, P. E. Wellstead, "On- and off-line measurement of paper shrinkage", Control '94, Conference Publication No. 389, pp. 1229 - 1234, March 1994.

References

44.   D. F. Garcia, M. Garcia, J. L. Diaz, J. R. Arias, J. Garcia, "Real-time flatness sensor based on a linear vision multiprocessor system", <u>20th International Conference on Industrial Electronics, Control and Instrumentation</u>, Vol. 2, pp. 873 - 878, Sept. 1994.

45.   Y. Yagi, S. Kawato, "Panorama scene analysis with conic projection", <u>IEEE Workshop on Intelligent Robots and Systems</u>, Vol. 1, pp. 181 - 187, July 1990.

46.   Y. Yagi, Y. Lin, M. Yachida, "Detection of unknown moving objects by reciprocation of observed information between mobile robot", <u>Proceedings of the IEEE / RSJ / GI International Conference on Intelligent Robots and Systems</u>, Vol. 2, pp. 996 - 1003, Sept. 1994.

47.   S. J. Oh, E. L. Hall, "Guidance of a mobile robot using an omnidirectional vision navigation system", <u>Proc. SPIE Mobile Robots II</u>, Vol. 852, pp. 288 - 300, 1987.

48.   T. Morita, Y. Yasukawa, Y. Inamoto, T. Uchiyama, S. Kawakami, "Measurement in three dimensions by motion stereo and spherical mapping", <u>Proc. CVPR</u>, pp. 422 -428, 1989.

49.   S. Zimmerman, D. Kuban, "A video pan / tilt / magnify / rotate system with no moving parts", <u>Proc. IEEE / AIAA 11th Digital Avionics Systems</u>, pp. 523 - 531, Oct. 1992.

50.   H. Ishiguro, M. Yamamoto, S. Tsuji, "Acquiring omnidirectional range information", <u>Systems and Computers in Japan</u>, Vol. 23, No. 4, pp. 47 - 56, 1992.

51.   S. Li, M. Chiba, S. Tsuji, "Estimating camera motion precisely from omni-directional images", <u>Proceedings of the IEEE / RSJ / GI International Conference on Intelligent Robots and Systems</u>, Vol. 2, pp. 1126 - 1132, Sept. 1994.

52.   Z. Hong, N. Ahuja, "Target tracking and cumulative depth map generation from binocular image sequences", <u>Intelligent Autonomous Systems 3</u>, pp. 24 - 32, Feb. 1993.

53.   M. Tanaka, N. Maru, F. Miyazaki, "3-D tracking of a moving object by an active stereo vision system", <u>20th International Conference on Industrial Electronics, Control and Instrumentation</u>, Vol. 2, pp. 816 - 820, Sept. 1994.

54.   J. A. Freer, B. J. Beggs, H. L. Fernandez-Canque, F. Chevrier, A. Goryashko, "Moving object surveillance and analysis for camera based security systems", <u>IEE 29th International Carnahan Conference on Security Technology</u>, pp. 67 - 71, Oct. 1995.

55.   T. Takano, K. Ushita, N. Aoyama, S. Ikeda, I. Nishimura, "Intruder detection system by image processing", <u>IEE 28th International Carnahan Conference on Security Technology</u>, pp. 31 - 33, Oct. 1994.

56.   A. Mecocci, F. Bartolini, V. Cappellini, "Image sequence analysis for counting in real time people getting in and out of a bus", <u>Signal Process (Netherlands)</u>, Vol. 35, Part 2, pp. 105 - 116, 1994.

57.   A. Jones, "Some theoretical aspects of the design of stereoscopic television systems", <u>C.E.G.B. Research Division</u>, March, 1980.

58.   R. Spottiswoode, N. L. Spottiswoode, C. Smith, "Basic principles of the three-dimensional film", <u>Journal of the SMPTE</u>, pp. 249 - 286, Oct. 1952.

59.   N. A. Valyus, "Stereoscopy", <u>The Focal Press</u>, 1966.

60.   A. T. Forman, "Depth measurement in three-dimensional television images", <u>Trent Polytechnic</u>, Project Report 1983.

61.   M. Perini, "Single camera 3-D system", <u>Trent Polytechnic</u>, 1984.

62.   M. Robinson, "Three-dimensional vision for bomb disposal", <u>8th International Conference on Special Equipment for the Police</u>, INTERPOL HQ, Paris, Nov. 1983.

References

63. M. Robinson, S. C. Sood, "Calibration and depth resolution of a stereoscopic video display", <u>SPIE</u>, Vol. 402, pp. 162 - 165, 1983.

64. M. Robinson, A. M. Ariyaeeinia, "An active co-ordinate imaging system for robot vision", SPIE Applications of Artificial Intelligence, Vol. 657, pp. 141 - 151, 1986.

65. M. Robinson, "3-D Television for teleoperator, measurement, and robot vision applications", <u>Proc. of International Workshop on Nuclear Robotic Technologies</u>, Vol. 3, paper 18, 1987.

66. M. Robinson, P. Shuttleworth, "Visual feedback for robotic manipulator control", <u>Proc. 8th International Conference on Robot Vision and Sensory Control</u>, pp. 65 - 70, May 1989.

67. P. Shuttleworth, M. Robinson, "Vision guided robot control", <u>International Conference on Intelligent Autonomous Systems 2</u>, pp. 459 - 464, Dec. 1989.

68. B. K. P. Horn, <u>Robot Vision</u>, MIT Press, London, 1986.

69. G. L. LaPrade, <u>The Manual of Photogrammetry</u>, Fourth Edition, American Society of Photogrammetry, pp. 519 - 544, 1980.

70. T. Okoshi, <u>Three-dimensional Imaging Techniques</u>, Academic Press, pp. 49 - 59, 1976.

71. T. C. Pong, M. A. Kenner, J. Otis, "Stereo / motion cues in pre-attentive vision processing : some experiments with random dot stereographic image sequences", <u>IEEE Proc. of the Workshop on visual motion</u>, pp. 314 - 320, March 1989.

72. H. Davson, <u>Davson's Physiology of the eye</u>, 5th Edition, Macmillan Press London, pp. 449 - 485, 1990.

73. L. Tychsen, <u>Adler's Physiology of the eye</u>, 9th Edition, Mosby - Year Book Inc., pp. 773 - 853, 1992.

74.   J. E. W. Mayhew, J. P. Frisby, "3D Model Recognition from Stereoscopic Cues", MIT Press, 1991.

75.   E. R. Davies, Machine Vision, Academic Press, London, 1990.

76.   R. M. Haralick, L. G. Shapiro, "Glossary of computer vision terms", Pattern Recognition, Vol. 24, No. 1, pp. 69 - 93, 1991.

77.   S. B. Kang, J. A. Webb, C. L. Zitnick, T. Kanade, " A multibaseline stereo system with active illumination and real-time image acquisition", Proc. 5th International Conference on Computer Vision, pp. 88 - 93, U.S.A., June 1995.

78.   M. S. Mousavi, R. J. Schalkoff, "A neural network approach for stereo vision", SOUTHEASTCON '90,Vol. 3, pp. 808 - 812, U.S.A, April 1990.

79.   H. Haggren, "Photogrammetric Machine Vision", Optics and Lasers in Engineering, 10, pp. 265 - 286, 1989.

80.   C. C. Slama, C. Theurer, S. W. Henrikson, Manual of Photogrammetry, 4th Edition, American Society of Photogrammetry, 1980.

81.   S. F. El-Hakim, "Real-time image metrology with CCD cameras", Photogrammetric Engineering and Remote Sensing, Vol. 52, No. 11, pp. 1757 - 1766, Nov. 1986.

82.   C. S. Fraser, "State of the art in industrial photogrammetry", 16th International Congress of International Society for Photogrammetry and Remote Sensing, Vol. 27, Part B5, Commission V, pp. 166 - 181, Kyoto, 1988.

83.   H. Ruther, N. Parkyn, "Near real-time photogrammetry on a personal computer", Photogrammetric Record, 13(75), pp. 415 - 422, April 1990.

84. P. C. Gustafson, "The application of real-time and near real-time photogrammetry in industry : a test of accuracy", <u>16th International Congress of International Society for Photogrammetry and Remote Sensing</u>, Vol. 27, Commission V, pp. V-198 - V-205, Kyoto, 1988.

85. G. T. Marzan, H. M. Karara, "A computer program for direct linear transformation solution of the collinearity condition and some applications of it", <u>Proceedings of the Symposium on Close Range Photogrammetric Systems</u>, Champaign, Ill. 1975.

86. W. Faig, "Calibration of close-range photogrammetric systems : mathematical formulation", <u>Photogrammetric Engineering and Remote Sensing</u>, Vol. 41, No. 12, pp. 1479 - 1486, Dec. 1975.

87. R. Y. Tsai, "A versatile camera calibration technique for high-accuracy 3D machine vision metrology using off-the-shelf TV cameras and lenses", <u>IEEE Journal of Robotics and Automation</u>, Vol. RA-3, No. 4, pp. 323 - 344, Aug. 1987.

88. M. A. Sid-ahmed, M. T. Boraie, "Dual camera calibration for 3-D Machine Vision Metrology", <u>IEEE Transactions on Instrumentation and Measurement</u>, Vol. 39, No. 3, pp. 512 - 516, June 1990.

89. X-.W. Tu, B. Dubussson, "CCD camera model and its physical characteristics consideration in calibration task for robotics", <u>IEEE International Workshop on Robot and Human Communication</u>, pp. 75 - 77, 1992.

90. C-. C. Wang, "An accurate calibration method of effective focal length for machine vision applications", <u>Computers ind. Engng</u>, Vol. 26, No. 1, pp. 73 - 91, 1994.

91. G. Paar, W. Polzleitner, M. Ulm, "Automatic extrinsic calibration using a flat target", <u>27th ISATA</u>, pp. 245 - 252, Aachen, Germany, 1994.

92. G. P. Stein, "Accurate internal camera calibration using rotation, with analysis of sources of error", Proceedings. Fifth International Conference on Computer Vision, pp. 230 - 236, Cambridge, Massachusetts, June 1995.

93. M. Roberts, A. J. Naftel, "A genetic algorithm approach to camera calibration in 3D machine vision", IEE Colloquium on Genetic Algorithms in Image Processing and Vision, pp. 12/1 - 12/5, London, Oct. 1994.

94. P. Grattoni, G. Pettiti, F. Pollastri, "Geometric camera calibration : a comparison of methods", IEEE, 7803-0078/91/0600-1775$01.00, pp. 1775 - 1779, 1991.

95. K. W. Wong, Manual of Photogrammetry, 4th Edition, American Society of Photogrammetry, pp. 37 - 101, 1980.

96. P. R. Wolf, Elements of photogrammetry, 2nd Edition, McGraw-Hill International Editions, 1983.

97. Cosmicar CCTV Lenses, Cosmicar, 1994.

98. "Definitions of terms and symbols used in photogrammetry", Manual of Photogrammetry, 4th Edition, American Society of Photogrammetry, 1980.

99. M. Li, D. Betsis, "Hand-eye Calibration", Proceedings. Fifth International Conference on Computer Vision, pp. 40 - 45, Cambridge, Massachusetts, June 1995.

100. J. G. Baker, Manual of Photogrammetry, 4th Edition, American Society of Photogrammetry, pp. 117 - 129,1980.

101. S. K. Ghosh, Analytical Photogrammetry, 2nd Edition, Pergamon Press, Oxford, U.K, ISBN 0-08-036103-X, pp. 115 - 121, 1988.

102. D. C. Brown, "Decentering Distortion of lenses", Photogrammetric Engineering, Vol. 32, No. 3, May 1966, pp. 444 - 462.

103.   W. H. Press, W. T. Vetterling, S. A. Teukolsky, B. P. Flannery, <u>Numerical Recipes in C : The Art of Scientific Computing</u>, 2nd Edition, Cambridge University Press, pp. 59 - 70, 1992.

104.   K. A. Stroud, <u>Engineering Mathematics</u>, Third Edition, MacMillan Education Ltd, pp. 448 - 450, 1987.

105.   J. Stern, "CCD Imaging", <u>Photomethods</u>, May 1986.

106.   G. F. Amelio, "Charge-coupled devices", <u>CCD Solid State Imaging Technology</u>, Loral-Fairchild CCD Databook, pp. 280 - 288, 1994 / 1995.

107.   D. King, "Charge-coupled device image sensors in industry", <u>Australian Electronics Engineering</u>, Vol. 22, Part 5, May 1989.

108.   L. Thorpe, E. Tamura, T. Iwasaki, "New advances in CCD Imaging", <u>SMPTE Journal</u>, pp. 378 - 387, May 1988.

109.   F. H. Bower, "CCD Fundamentals", <u>CCD Solid State Imaging Technology</u>, Fairchild-Weston Databook, pp. 219 - 222, 1987.

110.   S-W. Shih, Y-P. Hung, W-S. Lin, "Accuracy assessment on camera calibration method not considering lens distortion", <u>IEEE Comp. Soc. on Computer Vision and Pattern Recognition</u>, pp. 755 - 757, June 1992.

111.   H. B. Loving, <u>Manual of Photogrammetry</u>, 4th Edition, American Society of Photogrammetry, pp. 579 - 581,1980.

112.   M. H. Freeman, <u>Optics - 10th Edition</u>, Butterworths, London, 1990.

113.   <u>CAM / CCD1000 Series Line Scan Cameras</u>, Loral Fairchild CCD Databook, pp. 182 - 186, 1994 / 1995.

114.   DIS3000 Operating Manual, Digital Imaging Systems, 1987

115.   M. Waite, S. Prata, C : Step-by-Step - 1st Edition, The Waite Group, 1989.

116.   Digiplan Electronic Motion Control, IF1 & IF2 RS232 Interface User Information,
        Parker Digiplan Ltd, Dorset, England.

117.   Tandy 4000 LX, Installation and Operation Manual, Cat. No. 25-5100,
        Tandy Corporation, 1988.

118.   D. R. Askeland, The Science and Engineering of Materials, Third S.I. Edition,
        Chapman & Hall, London, 1996.

119.   A. S. Morris, Measurement and calibration for quality assurance, Prentice Hall
        International (UK) Ltd, London, 1991.

120.   J. Stewart, Calculus, 2nd Edition, ISBN 0-534-13212-X, Brooks / Cole Publishing
        Company, 1991.

121.   Protter and Protter, Calculus with analytic geometry, 4th Edition, ISBN 0-86720-093-6,
        Jones and Bartlett Publishers, 1988.

122.   H. A. Kruegle, "Lenses for CCTV systems", CCTV Magazine, March / April 1991.

123.   K. G. Harding, "Light source models for machine vision", SPIE Optics, Illumination, and
        Image Sensing for Machine Vision IV, Vol. 1194, pp. 112 - 121, 1989.

124.   User's Manual, 488-PC2 IEEE 488 Bus Interface Card, ICS Electronics Corporation,
        Publication Number 123077, Rev 0, August 1993.

125.   System Users Guide, Co-ordinate Measurement Machine, Order No : AA-5279B-TC,
        Digital Equipment Corporation.

126.   Command Code List, <u>LK Inspection Software</u>, LK Tool Company Ltd, East Midlands
        Airport.

127.   Technical Data, <u>Quick Assembly Two and Three Channel Optical Encoders</u>, Hewlett
        Packard, Farnell Components Data Service, Leeds.

128.   K. B. Atkinson, <u>Developments in Close Range Photogrammetry</u>, 1st Edition, Applied
        Science Publishers Ltd, London, 1980.

129.   <u>HP LaserJet 4 and 4M Printers User's Manual</u>, 1st Edition, Hewlett Packard, Part No.
        C2001 - 90950, Germany, October 1992.

130.   R. S. Petty, "3-D Vision Group : Rotating Stereoscopic Line-scan System : software
        listing", <u>The Nottingham Trent University</u>, Dryden Street Library, Software Section, April
        1997.

131.   J. E. Combs, <u>Manual of Photogrammetry</u>, 4th Edition, American Society of
        Photogrammetry, p. 397,1980.

Appendix A

Derivation of the *Parallax* Relationship for a Convergent Stereoscopic Camera System

Derivation of the Parallax Relationship for a Convergent Stereoscopic Camera System

The following analysis is an adaptation of earlier work by Spottiswoode and Spottiswoode[58], and can be derived with the aid of the diagram shown in Figure A-1.

$$\tan(\beta - \sigma) = \left(\frac{r}{f}\right)$$

$$\left(\frac{r}{f}\right) = \left(\frac{\tan\beta - \tan\sigma}{1 + \tan\beta\,\tan\sigma}\right) \quad \text{and} \quad \left(\frac{L}{f}\right) = \left(\frac{\tan\alpha + \tan\sigma}{1 - \tan\alpha\,\tan\sigma}\right)$$

$$\tan\alpha = \frac{1}{z}\left(q - \frac{B}{2}\right) \quad \text{and} \quad \tan\beta = \frac{1}{z}\left(q + \frac{B}{2}\right)$$

The disparity 'p' of an object point is given by :

$$p = (L - r)$$

Therefore :

$$\frac{p}{f} = \frac{L - r}{f} = \left(\frac{\tan\alpha + \tan\sigma}{1 - \tan\alpha\,\tan\sigma}\right) - \left(\frac{\tan\beta - \tan\sigma}{1 + \tan\beta t\,\tan\sigma}\right)$$

$$\frac{p}{f} = \frac{\tan\alpha + 2\tan\alpha\,\tan\beta\,\tan\sigma + 2\tan\sigma + \tan\beta\,\tan^2\sigma - \tan\beta - \tan\alpha\,\tan^2\sigma}{1 + \tan\sigma(\tan\beta - \tan\alpha) - \tan\alpha\,\tan\beta\,\tan^2\sigma}$$

$$\frac{p}{f} = \frac{2\tan\sigma + (\tan\alpha - \tan\beta)(1 - \tan^2\sigma) + 2\tan\alpha\,\tan\beta\,\tan\sigma}{1 + \tan\sigma(\tan\beta - \tan\alpha) - \tan\alpha\,\tan\beta\,\tan^2\sigma}$$

As :

$$\tan\beta - \tan\alpha = \frac{B}{z} \quad \text{and} \quad \tan\alpha\,\tan\beta = \frac{1}{z^2}\left(q^2 - \frac{B^2}{4}\right)$$

The following can be stated :

$$\frac{p}{f} = \frac{2\tan\sigma - \dfrac{B}{z}(1 - \tan^2\sigma) + 2\tan\sigma\left(\left(\dfrac{q^2}{z^2}\right) - \left(\dfrac{B^2}{4z^2}\right)\right)}{1 + \dfrac{B}{z}\tan\sigma - \left(\left(\dfrac{q^2}{z^2}\right) - \left(\dfrac{B^2}{4z^2}\right)\right)\tan^2\sigma}$$

A-2

In a system designed for viewing by a human observer : tanσ, (B / z) and (q / z) are all <<1. Thus neglecting terms which are a product of two or more such terms gives the following, which is the disparity of a point in image space at a range 'z' from the stereoscopic camera base line :

$$p = 2f \tan\sigma - \frac{Bf}{z}$$
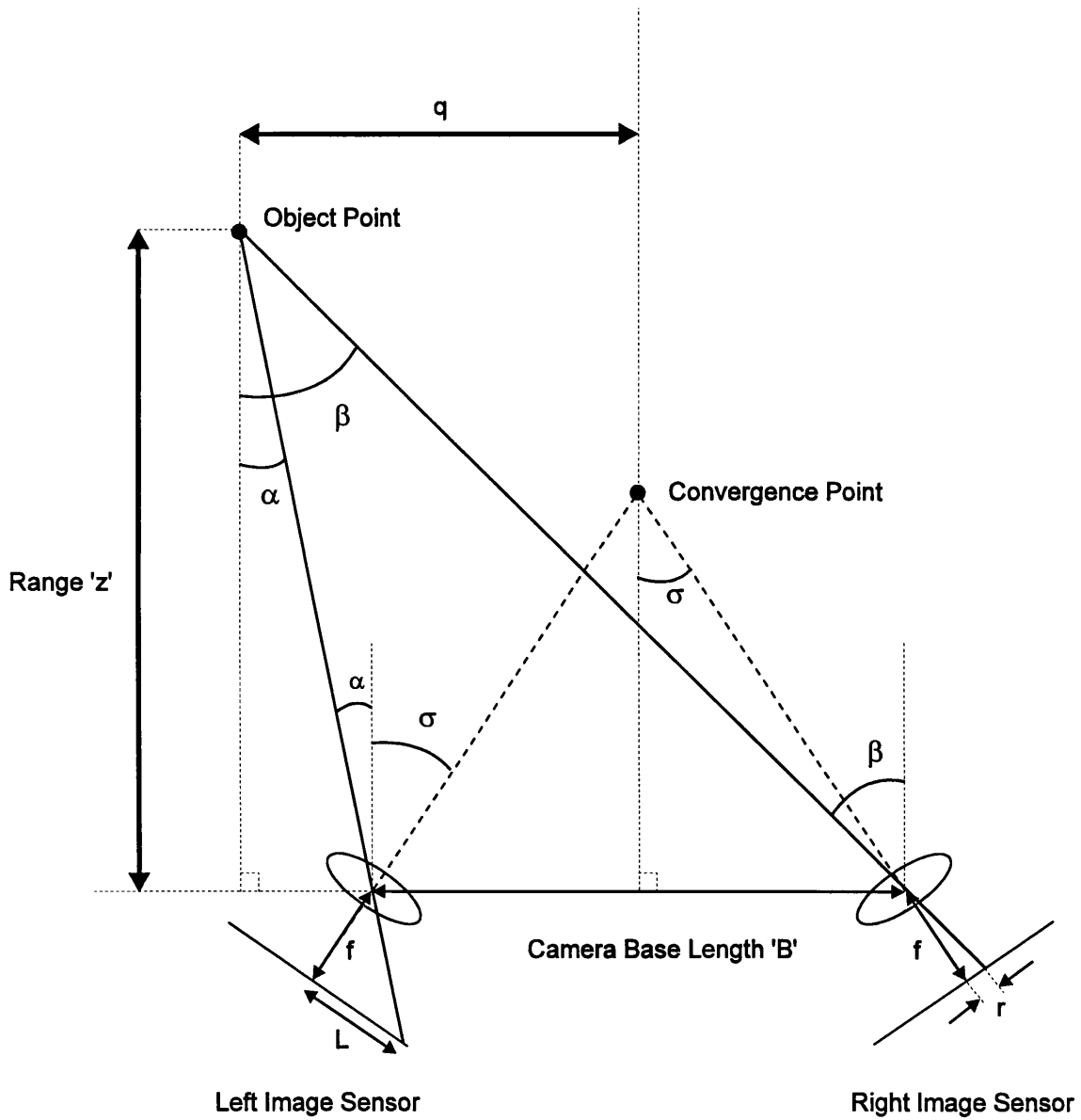
Figure A-1 The Geometric Arrangement of a Convergent Stereoscopic Camera System

Appendix B

Experimental Results from the Rotating Two-dimensional Line-scan System

Centre-of-Rotation Results

B.1.   X-axis Algorithm Verification : Variation in Camera-to-Object Distance

f = 25mm; X=610mm; F_{SR} = 80 kHz; S_R = 1.67.

D_{CO} (mm)	x Observed	x Calculated	Image Space Error (pixels)	Object Space Error (mm)
500	398	395.6	2.4	2.7
600	357	355.1	1.9	2.5
700	321	320.7	0.3	4.5
800	293	291.5	1.5	2.8
900	267	266.5	0.5	1.0
1000	246	245.1	1.0	2.1
1100	229	226.5	2.5	6.1
1200	211	210.4	0.6	1.6
1300	197	196.3	0.7	2.1
1400	185	183.8	1.2	3.7

B.2   X-axis Algorithm Verification : Variation In Rotation Speed

f = 25mm; X = 610mm; F_{SR} = 80 kHz; D_{CO} = 500m.

Rotation Speed (S_R)	x Observed	x Calculated	Image Space Error (pixels)	Object Space Error (mm)
1.67	399	395.6	3.4	3.8
2.50	266	263.8	2.2	3.7
3.33	200	197.8	2.2	4.9
4.17	160	158.3	1.7	4.7
5.00	133	131.9	1.1	3.7
5.83	114	113.0	1.0	3.9
6.67	100	98.9	1.1	4.5
7.50	89	87.9	1.1	5.0
8.33	80	79.1	0.9	5.0

B.3   X-axis Algorithm Verification : Variation In Camera Scan Rate

f = 25mm; Xos = 610mm; D_{CO} = 0.5m; S_R = 1.67.

Scan Rate (F_{SR})	x Observed	x Calculated	Image Space Error (pixels)	Object Space Error (mm)
30	150	148.4	1.6	4.8
40	200	197.8	2.2	4.9
50	250	247.3	2.7	4.8
60	299	296.7	2.3	3.4
70	348	346.1	1.8	2.3
80	398	395.6	2.4	2.7
90	447	445.1	1.9	1.9

B.4   Y-axis Algorithm Verification : Variation In Centre-of-Rotation To Object Distance

$f = 25mm$; $Y=200mm$; $F_{SR} = 80$ kHz; $S_R = 1.67$; $SL = 0.000013m$.

D_{CO} (mm)	y Observed	y Calculated	Image Space Error (pixels)	Object Space Error (mm)
500	767	769.2	2.2	0.6
600	640	641.1	1.1	0.3
700	550	549.4	0.6	0.2
800	480	480.8	0.8	0.3
900	426	427.4	1.4	0.7
1000	386	384.6	1.4	0.7
1100	349	349.7	0.7	0.4
1200	321	320.5	0.5	0.3
1300	297	295.8	1.2	0.8
1400	274	274.8	0.8	0.6

B.5   Y-axis Algorithm Verification : Variation In Rotation Speed

$f = 25mm$; $Y = 200mm$; $F_{SR} = 80$ kHz; $D_{CO} = 500mm$; $SL = 0.000013m$.

Rotation Speed (S_R)	y Observed	y Calculated	Image Space Error (pixels)	Object Space Error (mm)
1.67	768	769.2	1.2	0.3
2.50	768	769.2	1.2	0.3
3.33	768	769.2	1.2	0.3
4.17	769	769.2	0.2	0.1
5.00	768	769.2	1.2	0.3
5.83	769	769.2	0.2	0.1
6.67	768	769.2	1.2	0.3
7.50	768	769.2	1.2	0.3
8.33	768	769.2	1.2	0.3

B.6   Y-axis Algorithm Verification : Variation In Camera Scan Rate

$f = 25mm$; $Y = 200mm$; $D_{CO} = 500mm$; $S_R = 1.67$; $SL = 0.000013m$.

Scan Rate (F_{SR})	y Observed	y Calculated	Image Space Error (pixels)	Object Space Error (mm)
30	768	769.2	1.2	0.3
40	768	769.2	1.2	0.3
50	768	769.2	1.2	0.3
60	768	769.2	1.2	0.3
70	768	769.2	1.2	0.3
80	769	769.2	0.2	0.1
90	769	769.2	0.2	0.1

<u>Deviation Along The Centre-of-Rotation Results</u>

B.7   X-axis Algorithm Verification : Variable Camera Distance Along The Central Axis Of

Rotation

f = 25mm; X=600mm; F_{SR} = 80 kHz; S_R = 5/3; D_{RO} = 700mm.

d_r (mm)	x Observed	x Calculated	Image Space Error (pixels)	Object Space Error (mm)
50	324	320.7	3.3	4.8
100	323	320.7	2.3	3.1
150	324	320.7	3.3	4.1
200	323	320.7	2.3	2.6
250	322	320.7	1.3	1.3
300	323	320.7	2.3	2.1
350	323	320.7	2.3	1.8
400	323	320.7	2.3	1.5
450	324	320.7	3.3	1.8
500	322	320.7	1.3	0.6

B.8   X-axis Algorithm Verification : Variation In Centre-of-Rotation To Object Distance

Camera Distance From The Central Axis Of Rotation (d_r) = 250mm

f = 25mm; X=610mm; F_{SR} = 80 kHz; S_R = 5/3.

D_{RO} (mm)	x Observed	x Calculated	Image Space Error(pixels)	Object Space Error (mm)
600	359	355.1	3.9	5.2
700	324	320.7	3.3	5.2
800	295	291.5	3.5	6.3
900	269	266.5	2.5	5.0
1000	247	245.1	2.0	4.5
1100	226	226.5	0.5	1.2
1200	213	210.4	2.6	7.0
1300	197	196.3	0.7	2.0
1400	185	183.8	1.2	3.8
1500	173	172.8	1.2	4.0

B.9   X-axis Algorithm Verification : Variation In Rotational Displacement Speed

$d_r = 250$mm

$f = 25$mm; $X = 610$mm; $F_{SR} = 80$ kHz; $D_{RO} = 700$mm.

Rotation Speed(rpm)	x Observed	x Calculated	Image Space Error (pixels)	Object Space Error (mm)
5/3	323	320.7	2.3	3.6
15/6	217	213.8	3.2	7.5
20/6	162	160.4	1.6	5.0
25/6	130	128.3	1.7	6.6
5	109	106.9	2.1	9.9
35/6	93	91.6	1.4	7.7
20/3	82	80.2	1.8	11.3
45/6	73	71.3	1.7	12.0
25/3	66	64.1	1.9	14.9

B.10   X-axis Algorithm Verification : Variation In Camera Scan Rate

$d_r = 250$mm

$f = 25$mm; $X = 610$mm; $D_{RO} = 700$mm; $S_R = 5/3$.

Scan Rate (F_{SR})	x Observed	x Calculated	Image Space Error(pixels)	Object Space Error(mm)
30	122	120.3	1.7	7.1
40	163	160.4	2.6	8.1
50	203	200.5	2.6	6.5
60	243	240.5	2.5	5.2
70	282	280.6	1.4	2.5
80	323	320.7	2.3	3.6
90	363	360.8	2.2	3.1

B.11   Y-axis Algorithm Verification : Variable Camera Distance Along Central Axis Of Rotation

$f = 25$mm; $Y=200$mm; $F_{SR} = 80$ kHz; $S_R = 5/3$; $D_{RO} = 700$mm; $SL = 0.000013$m.

d_r (mm)	y Observed	y Calculated	Image Space Error(pixels)	Object Space Error(mm)
50	593	591.7	1.3	0.4
100	642	641.0	1.0	0.3
150	698	699.3	1.3	0.4
200	768	769.2	1.2	0.3
250	854	854.7	0.7	0.2
300	960	961.5	1.5	0.3

B.12   Y-axis Algorithm Verification : Variation In Centre-of-Rotation To Object Distance

$d_r = 250mm$

$f = 25mm$; $Y=200mm$; $F_{SR} = 80$ kHz; $S_R = 5/3$; $SL = 0.000013m$.

D_{RO} (mm)	y Observed	y Calculated	Image Space Error(pixels)	Object Space Error(mm)
700	856	854.7	1.3	0.5
800	698	699.3	1.3	0.5
900	591	591.7	0.7	0.3
1000	514	512.8	1.2	0.6
1100	453	452.5	0.5	0.3
1200	406	404.9	1.1	0.7
1300	367	366.3	1.3	0.9
1400	336	334.4	1.6	1.2

Deviation From The Centre-of-Rotation Results

B.13   X-axis Algorithm Verification : Variation In Camera Distance From The Central Axis Of Rotation

$f = 25mm$; $X=610mm$; $F_{SR} = 80$ kHz; $S_R = 5/3$; $D_{RO} = 700mm$.

d_s (mm)	θ_R (degrees)	x Observed	x Calculated	Image Space Error (pixels)	Object Space Error (mm)
50	42.06	332	328.6	3.4	3.1
100	43.08	338	336.6	1.4	2.0
150	44.12	348	344.7	3.3	4.7
200	45.21	356	353.2	2.8	3.9
250	46.35	362	362.1	0.1	0.1
300	47.57	375	371.7	3.3	4.3
350	48.90	384	382.0	2.0	2.6
400	50.37	394	393.6	0.5	0.6
450	52.06	407	406.7	0.3	0.4
500	54.04	422	422.2	0.2	0.2

B.14   X-axis Algorithm Verification : Variation In Centre-of-Rotation To Object Distance

Camera Distance From The Central Axis Of Rotation (d_s) = 250mm

$f = 25$mm; X=610mm; F_{SR} = 80 kHz; S_R = 5/3.

D_{RO} (mm)	θ_R (degrees)	x Observed	x Calculated	Image Space Error (pixels)	Object Space Error (mm)
600	53.08	411	414.7	3.7	4.2
700	46.35	364	362.1	1.9	2.6
800	41.12	324	321.3	2.7	4.2
900	36.94	289	288.6	0.4	0.7
1000	33.52	264	261.9	2.1	4.2
1100	30.66	240	239.6	0.4	0.9
1200	28.25	221	220.7	0.3	0.7
1300	26.18	206	204.6	1.4	3.7
1400	24.39	193	190.6	2.4	6.9
1500	22.83	181	178.4	2.7	8.4

B.15   X-axis Algorithm Verification : Variation In Rotational Displacement Speed

d_s = 250mm

θ_R = 46.35°

$f = 25$mm; X = 610mm; F_{SR} = 80 kHz; D_{RO} = 700mm.

Rotation Speed(rpm)	x Observed	x Calculated	Image Space Error(pixels)	Object Space Error(mm)
5/3	365	362.1	2.9	3.9
15/6	244	241.4	2.6	5.2
20/6	183	181.1	1.9	5.1
25/6	147	144.8	2.2	7.4
5	122	120.7	1.3	5.2
35/6	105	103.5	1.5	7.0
20/3	92	90.5	1.5	8.1
45/6	82	80.5	1.5	9.1
25/3	74	72.4	1.6	10.7

B.16 X-axis Algorithm Verification : Variation In Camera Scan Rate

d_s = 250mm; θ_R = 46.35°, f = 25mm; X = 610mm; D_{RO} = 700mm; S_R = 5/3.

Scan Rate (F$_{SR}$)	x Observed	x Calculated	Image Space Error (pixels)	Object Space Error (mm)
30	137	135.8	1.2	4.3
40	182	181.1	0.9	2.4
50	228	226.3	1.7	3.7
60	275	271.6	1.4	2.5
70	319	316.9	2.1	3.2
80	364	362.1	1.9	2.6
90	410	407.4	2.6	3.1

B.17 Y-axis Algorithm Verification : Variation In Camera Distance From The Central Axis Of Rotation

f = 25mm; Y=200mm; F_{SR} = 80 kHz; S_R = 5/3; D_{RO} = 700mm; SL = 0.000013m.

d$_s$ (mm)	y Observed	y Calculated	Image Space Error (pixels)	Object Space Error (mm)
50	558	557.4	0.6	0.2
100	558	557.4	0.6	0.2
150	564	565.6	1.6	0.6
200	573	574.1	1.1	0.4
250	591	591.7	0.7	0.2
300	609	610.5	1.5	0.5
350	631	630.5	0.5	0.2
400	676	674.8	1.2	0.4
450	713	712.4	0.7	0.2
500	786	784.9	1.1	0.3

B.18 Y-axis Algorithm Verification : Variation In Centre-of-Rotation To Object Distance

d_s = 250mm, f = 25mm; Y=200mm; F_{SR} = 80 kHz; S_R = 5/3; SL = 0.000013m.

D$_{RO}$ (mm)	Ypd Observed	Ypd Calculated	Image Space Error (pixels)	Object Space Error (mm)
600	700	699.3	0.7	0.2
700	593	591.7	1.3	0.4
800	507	506.1	0.9	0.4
900	448	447.2	0.8	0.4
1000	395	396.5	1.5	0.8
1100	335	334.4	0.6	0.3
1200	328	328.7	0.7	0.4
1300	302	300.5	1.5	1.0
1400	278	278.7	0.7	0.5
1500	261	259.9	1.1	0.9

Appendix C

Symbols used in the 'Analysis of a Rotating Stereoscopic Line-scan System'

Symbols used in the Stereoscopic Line-scan Analysis

B $\equiv$ camera-to-camera base width, in mm;

θ_c $\equiv$ camera-to-base width convergence angle, in degrees;

F_{SR} $\equiv$ camera scan rate, in hz;

S_R $\equiv$ rotational displacement speed of the rotating platform, in rpm;

f $\equiv$ camera-lens focal length, in mm;

Z_n $\equiv$ 'line-of-sight' distance from the centre of the rotational stage to a point, 'n', of interest in cylindrical object space, in mm;

Y_n $\equiv$ Y co-ordinate of a point 'n' in cylindrical object space, in mm;

Θ_n $\equiv$ rotation angle from a fixed reference point (the start point of camera scan) to a point, 'n', of interest in cylindrical object space, in degrees;

X $\equiv$ X co-ordinate of a point 'n' in cartesian object space, in mm;

Y $\equiv$ Y co-ordinate of a point 'n' in cartesian object space, in mm;

Z $\equiv$ Z co-ordinate of a point 'n' in cartesian object space, in mm;

θ_{Ln} $\equiv$ rotation angle necessary to view a point of interest 'n' for the left camera, with respect to the image start point, in degrees;

θ_{Rn} $\equiv$ rotation angle necessary to view a point of interest 'n' for the right camera, with respect to the image start point, in degrees;

x_{Ln} $\equiv$ x-axis pixel distance to the point of interest 'n' obtained from left image space, with respect to the start of image capture;

x_{Rn} $\equiv$ x-axis pixel distance to the point of interest 'n' obtained from right image space, with respect to the start of image capture;

k_x $\equiv$ the x-pixel distance-to-rotation angle conversion factor.

D_{co} $\equiv$ camera-to-object distance at the instant of image capture, in mm;

y_n $\equiv$ Y co-ordinate of a point 'n' derived from image space, in pixels,

SL $\equiv$ sensing *element length*, in mm;

f $\equiv$ camera lens focal length, in mm;

y_p $\equiv$ the pixel through which the optical axis of the lens pierces the sensor.

Symbols used in the Stereoscopic Line-scan Analysis

Z_{near} ≡   'line-of-sight' distance from the centre of the rotational stage to the near point of the stereoscopic region, in cylindrical object space, in mm;

Z_{far} ≡   'line-of-sight' distance from the centre of the rotational stage to the far point of the stereoscopic region, in cylindrical object space, in mm;

Z_{con} ≡   'line-of-sight' distance from the centre of the rotational stage to the convergence circumference, in cylindrical object space, in mm.

XL_{vox} ≡   theoretical resolution surrounding a point 'n' in the X-axis of cartesian object space as inferred from left image space values, in mm / pixel.

XR_{vox} ≡   theoretical resolution surrounding a point 'n' in the X-axis of cartesian object space as inferred from right image space values, in mm / pixel.

Z_{vox} ≡   theoretical resolution surrounding a point 'n' in the Z-axis of cartesian object space as inferred from right image space values, in mm / pixel.

Y_{vox} ≡   theoretical resolution surrounding a point 'n' in the Y-axis of cartesian object space as inferred from Y image space values, in mm / pixel.

Appendix D

Derivation of the '3-D Conformal Transformation' for use with the Rotating Stereoscopic Line-scan System

3-D Conformal Transformation Derivation for the Rotating Stereoscopic Line-scan System

This appendix will detail the derivation of the 3-D conformal transformation model for the rotating stereoscopic line-scan system. The general algorithms, developed by Wolf, are used in conjunction with the mathematical model derived for the line-scan system (refer to Chapter 4.0) to obtain a 3-D transformation model specifically for use in this research.

For each frame point used in the calibration procedure a set of equations result which relate the X, Y and Z point co-ordinates with the unknown initial parameters. For a frame point, P, the following equations can be inferred using the mathematical procedure given by Wolf :-

$$X_p = \left(m_{11}X + m_{21}Y + m_{31}Z \right) + T_x$$
$$Y_p = \left(m_{12}X + m_{22}Y + m_{32}Z \right) + T_y$$
$$Z_p = \left(m_{13}X + m_{23}Y + m_{33}Z \right) + T_z$$

Where X, Y and Z represent the Cartesian co-ordinate algorithms relating camera image space quantities to object space point locations. These algorithms were presented previously in Section 4.7, however, they are repeated again here as follows :-

$$X := \frac{B \cdot \sin(\theta c) \cdot \sin\left[kx \left(\frac{-x_{Rn} - x_{Ln}}{2} \right) \right]}{2 \cdot \cos\left[\theta c + \left[kx \left(\frac{x_{Ln} - x_{Rn}}{2} \right) \right] \right]}$$

$$Y := \frac{B \cdot \left(yp - y_n \right) \cdot r}{2} \cdot \frac{\cos\left(-kx \cdot \frac{x_{Ln} - x_{Rn}}{2} \right)}{\cos\left[\theta c + \left(kx \cdot \frac{x_{Ln} - x_{Rn}}{2} \right) \right]}$$

$$Z := \frac{B \cdot \sin(\theta c) \cdot \cos\left[kx \left(\frac{-x_{Rn} - x_{Ln}}{2} \right) \right]}{2 \cdot \cos\left[\theta c + \left[kx \left(\frac{x_{Ln} - x_{Rn}}{2} \right) \right] \right]}$$

To solve each set of equations they are linearised using Taylor's theorem. Using Taylor's theorem the linearised form of the first three equations is as follows :-

$$X_p := \left(X_p\right)_0 + \left(\frac{\delta X_p}{\delta \omega}\right)_0 \cdot \delta\omega + \left(\frac{\delta X_p}{\delta \phi}\right)_0 \cdot \delta\phi + \left(\frac{\delta X_p}{\delta \kappa}\right)_0 \cdot \delta\kappa + \left(\frac{\delta X_p}{\delta T_x}\right)_0 \cdot \delta T_x + \left(\frac{\delta X_p}{\delta T_y}\right)_0 \cdot \delta T_y + \left(\frac{\delta X_p}{\delta T_z}\right)_0 \cdot \delta T$$

$$+ \left(\frac{\delta X_p}{\delta B}\right)_0 \cdot \delta B + \left(\frac{\delta X_p}{\delta \theta c}\right)_0 \cdot \delta\theta c + \left(\frac{\delta X_p}{\delta kx}\right)_0 \cdot \delta kx + \left(\frac{\delta X_p}{\delta yp}\right)_0 \cdot \delta yp + \left(\frac{\delta X_p}{\delta r}\right)_0 \cdot \delta r$$

$$Y_p := \left(Y_p\right)_0 + \left(\frac{\delta Y_p}{\delta \omega}\right)_0 \cdot \delta\omega + \left(\frac{\delta Y_p}{\delta \phi}\right)_0 \cdot \delta\phi + \left(\frac{\delta Y_p}{\delta \kappa}\right)_0 \cdot \delta\kappa + \left(\frac{\delta Y_p}{\delta T_x}\right)_0 \cdot \delta T_x + \left(\frac{\delta Y_p}{\delta T_y}\right)_0 \cdot \delta T_y + \left(\frac{\delta Y_p}{\delta T_z}\right)_0 \cdot \delta T$$

$$+ \left(\frac{\delta Y_p}{\delta B}\right)_0 \cdot \delta B + \left(\frac{\delta Y_p}{\delta \theta c}\right)_0 \cdot \delta\theta c + \left(\frac{\delta Y_p}{\delta kx}\right)_0 \cdot \delta kx + \left(\frac{\delta Y_p}{\delta yp}\right)_0 \cdot \delta yp + \left(\frac{\delta Y_p}{\delta r}\right)_0 \cdot \delta r$$

$$Z_p := \left(Z_p\right)_0 + \left(\frac{\delta Z_p}{\delta \omega}\right)_0 \cdot \delta\omega + \left(\frac{\delta Z_p}{\delta \phi}\right)_0 \cdot \delta\phi + \left(\frac{\delta Z_p}{\delta \kappa}\right)_0 \cdot \delta\kappa + \left(\frac{\delta Z_p}{\delta T_x}\right)_0 \cdot \delta T_x + \left(\frac{\delta Z_p}{\delta T_y}\right)_0 \cdot \delta T_y + \left(\frac{\delta Z_p}{\delta T_z}\right)_0 \cdot \delta T$$

$$+ \left(\frac{\delta Z_p}{\delta B}\right)_0 \cdot \delta B + \left(\frac{\delta Z_p}{\delta \theta c}\right)_0 \cdot \delta\theta c + \left(\frac{\delta Z_p}{\delta kx}\right)_0 \cdot \delta kx + \left(\frac{\delta Z_p}{\delta yp}\right)_0 \cdot \delta yp + \left(\frac{\delta Z_p}{\delta r}\right)_0 \cdot \delta r$$

The first six partial derivatives for each of X, Y and Z are those given by Wolf. The following five derivatives are those which allow the general mathematical procedure to be applied to the line-scan system and are given as follows, for the X, Y and Z-axes, respectively :-

For the X-axis :

$$\left(\frac{\delta X_p}{\delta B}\right)_0 \cdot \delta B := \frac{1}{2} \cdot \sin(\theta c) \cdot \frac{\sin\left[kx\left(\frac{-1}{2} \cdot x_{Rn} - \frac{1}{2} \cdot x_{Ln}\right)\right]}{\cos\left[\theta c + kx\left(\frac{1}{2} \cdot x_{Ln} - \frac{1}{2} \cdot x_{Rn}\right)\right]}$$

$$\left(\frac{\delta X_p}{\delta\theta c}\right)_0 \cdot \delta\theta c := \frac{1}{2}\cdot B\cdot\cos(\theta c)\cdot\frac{\sin\left[kx\cdot\left(\frac{-1}{2}\cdot x_{Rn} - \frac{1}{2}\cdot x_{Ln}\right)\right]}{\cos\left[\theta c + kx\cdot\left(\frac{1}{2}\cdot x_{Ln} - \frac{1}{2}\cdot x_{Rn}\right)\right]} + \blacksquare$$

$$\frac{1}{2}\cdot B\cdot\sin(\theta c)\cdot\frac{\sin\left[kx\cdot\left(\frac{-1}{2}\cdot x_{Rn} - \frac{1}{2}\cdot x_{Ln}\right)\right]}{\cos\left[\theta c + kx\cdot\left(\frac{1}{2}\cdot x_{Ln} - \frac{1}{2}\cdot x_{Rn}\right)\right]^2}\cdot\sin\left[\theta c + kx\cdot\left(\frac{1}{2}\cdot x_{Ln} - \frac{1}{2}\cdot x_{Rn}\right)\right]$$

$$\left(\frac{\delta X_p}{\delta kx}\right)_0 \cdot \delta kx := \frac{1}{2}\cdot B\cdot\sin(\theta c)\cdot\cos\left[kx\cdot\left(\frac{-1}{2}\cdot x_{Rn} - \frac{1}{2}\cdot x_{Ln}\right)\right]\cdot\frac{\left(\frac{-1}{2}\cdot x_{Rn} - \frac{1}{2}\cdot x_{Ln}\right)}{\cos\left[\theta c + kx\cdot\left(\frac{1}{2}\cdot x_{Ln} - \frac{1}{2}\cdot x_{Rn}\right)\right]} + \blacksquare$$

$$\frac{1}{2}\cdot B\cdot\sin(\theta c)\cdot\frac{\sin\left[kx\cdot\left(\frac{-1}{2}\cdot x_{Rn} - \frac{1}{2}\cdot x_{Ln}\right)\right]}{\cos\left[\theta c + kx\cdot\left(\frac{1}{2}\cdot x_{Ln} - \frac{1}{2}\cdot x_{Rn}\right)\right]^2}\cdot\sin\left[\theta c + kx\cdot\left(\frac{1}{2}\cdot x_{Ln} - \frac{1}{2}\cdot x_{Rn}\right)\right]\cdot\left(\frac{1}{2}\cdot x_{Ln} - \frac{1}{2}\cdot x_{Rn}\right)$$

$$\left(\frac{\delta X_p}{\delta y_p}\right)_0 \delta y_p = 0$$

$$\left(\frac{\delta X_p}{\delta r}\right)_0 \delta r = 0$$

For the y-axis :-

$$\left(\frac{\delta Y_p}{\delta B}\right)_0 \cdot \delta B := \frac{1}{2}\cdot(yp - y_n)\cdot r\cdot\frac{\cos\left[kx\cdot\left(\frac{1}{2}\cdot x_{Ln} - \frac{1}{2}\cdot x_{Rn}\right)\right]}{\cos\left[\theta c + kx\cdot\left(\frac{1}{2}\cdot x_{Ln} - \frac{1}{2}\cdot x_{Rn}\right)\right]}$$

$$\left(\frac{\delta Y_p}{\delta\theta c}\right)_0 \cdot \delta\theta c := \frac{1}{2}\cdot B\cdot(yp - y_n)\cdot r\cdot\frac{\cos\left[kx\left(\frac{1}{2}\cdot x_{Ln} - \frac{1}{2}\cdot x_{Rn}\right)\right]}{\cos\left[\theta c + kx\left(\frac{1}{2}\cdot x_{Ln} - \frac{1}{2}\cdot x_{Rn}\right)\right]^2}\cdot\sin\left[\theta c + kx\left(\frac{1}{2}\cdot x_{Ln} - \frac{1}{2}\cdot x_{Rn}\right)\right]$$

$$\left(\frac{\delta Y_p}{\delta kx}\right)_0 \cdot \delta kx := \frac{-1}{2}\cdot B\cdot(yp - y_n)\cdot r\cdot\sin\left[kx\left(\frac{1}{2}\cdot x_{Ln} - \frac{1}{2}\cdot x_{Rn}\right)\right]\cdot\frac{\left(\frac{1}{2}\cdot x_{Ln} - \frac{1}{2}\cdot x_{Rn}\right)}{\cos\left[\theta c + kx\left(\frac{1}{2}\cdot x_{Ln} - \frac{1}{2}\cdot x_{Rn}\right)\right]} + \blacksquare$$

$$\frac{1}{2}\cdot B\cdot(yp - y_n)\cdot r\cdot\frac{\cos\left[kx\left(\frac{1}{2}\cdot x_{Ln} - \frac{1}{2}\cdot x_{Rn}\right)\right]}{\cos\left[\theta c + kx\left(\frac{1}{2}\cdot x_{Ln} - \frac{1}{2}\cdot x_{Rn}\right)\right]^2}\cdot\sin\left[\theta c + kx\left(\frac{1}{2}\cdot x_{Ln} - \frac{1}{2}\cdot x_{Rn}\right)\right]\cdot\left(\frac{1}{2}\cdot x_{Ln} - \frac{1}{2}\cdot x_{Rn}\right)$$

$$\left(\frac{\delta Y_p}{\delta yp}\right)_0 \cdot \delta yp := \frac{1}{2}\cdot B\cdot r\cdot\frac{\cos\left[kx\left(\frac{1}{2}\cdot x_{Ln} - \frac{1}{2}\cdot x_{Rn}\right)\right]}{\cos\left[\theta c + kx\left(\frac{1}{2}\cdot x_{Ln} - \frac{1}{2}\cdot x_{Rn}\right)\right]}$$

$$\left(\frac{\delta Y_p}{\delta r}\right)_0 \cdot \delta r := \frac{1}{2}\cdot B\cdot(yp - y_n)\cdot\frac{\cos\left[kx\left(\frac{1}{2}\cdot x_{Ln} - \frac{1}{2}\cdot x_{Rn}\right)\right]}{\cos\left[\theta c + kx\left(\frac{1}{2}\cdot x_{Ln} - \frac{1}{2}\cdot x_{Rn}\right)\right]}$$

For the Z-axis :-

$$\left(\frac{\delta Z_p}{\delta B}\right)_0 \cdot \delta B := \frac{1}{2}\cdot\sin(\theta c)\cdot\frac{\cos\left[kx\left(\frac{-1}{2}\cdot x_{Rn} - \frac{1}{2}\cdot x_{Ln}\right)\right]}{\cos\left[\theta c + kx\left(\frac{1}{2}\cdot x_{Ln} - \frac{1}{2}\cdot x_{Rn}\right)\right]}$$

$$\left(\frac{\delta Z_p}{\delta\theta c}\right)_0 \cdot \delta\theta c := \frac{1}{2}\cdot B\cdot\cos(\theta c)\cdot \frac{\cos\left[kx\cdot\left(\frac{-1}{2}\cdot x_{Rn} - \frac{1}{2}\cdot x_{Ln}\right)\right]}{\cos\left[\theta c + kx\cdot\left(\frac{1}{2}\cdot x_{Ln} - \frac{1}{2}\cdot x_{Rn}\right)\right]} + \blacksquare$$

$$\frac{1}{2}\cdot B\cdot\sin(\theta c)\cdot \frac{\cos\left[kx\cdot\left(\frac{-1}{2}\cdot x_{Rn} - \frac{1}{2}\cdot x_{Ln}\right)\right]}{\cos\left[\theta c + kx\cdot\left(\frac{1}{2}\cdot x_{Ln} - \frac{1}{2}\cdot x_{Rn}\right)\right]^2}\cdot\sin\left[\theta c + kx\cdot\left(\frac{1}{2}\cdot x_{Ln} - \frac{1}{2}\cdot x_{Rn}\right)\right]$$

$$\left(\frac{\delta Z_p}{\delta kx}\right)_0 \cdot \delta kx := \frac{-1}{2}\cdot B\cdot\sin(\theta c)\cdot\sin\left[kx\cdot\left(\frac{-1}{2}\cdot x_{Rn} - \frac{1}{2}\cdot x_{Ln}\right)\right]\cdot \frac{\left(\frac{-1}{2}\cdot x_{Rn} - \frac{1}{2}\cdot x_{Ln}\right)}{\cos\left[\theta c + kx\cdot\left(\frac{1}{2}\cdot x_{Ln} - \frac{1}{2}\cdot x_{Rn}\right)\right]} + \blacksquare$$

$$\frac{1}{2}\cdot B\cdot\sin(\theta c)\cdot \frac{\cos\left[kx\cdot\left(\frac{-1}{2}\cdot x_{Rn} - \frac{1}{2}\cdot x_{Ln}\right)\right]}{\cos\left[\theta c + kx\cdot\left(\frac{1}{2}\cdot x_{Ln} - \frac{1}{2}\cdot x_{Rn}\right)\right]^2}\cdot\sin\left[\theta c + kx\cdot\left(\frac{1}{2}\cdot x_{Ln} - \frac{1}{2}\cdot x_{Rn}\right)\right]\cdot\left(\frac{1}{2}\cdot x_{Ln} - \frac{1}{2}\cdot x_{Rn}\right)$$

$$\left(\frac{\delta X_p}{\delta y_p}\right)_0 \delta y_p = 0$$

$$\left(\frac{\delta X_p}{\delta r}\right)_0 \delta r = 0$$

Appendix E

Research Papers Pertaining to the Research Presented in this Thesis

3-D Imaging Group

Richard Petty

Primary Authorships :

Petty R S, Godber S X, Robinson M, Evans P, "Rotational displacement line-scan imaging", <u>SPIE/IS&T Electronic Imaging Newsletter</u>, Vol. 5, No. 1, March, 1995

Petty R S, Godber S X, Robinson M, Evans J P O, "3-D vision systems using rotating 1-D sensors", <u>IEE Colloquium on 'The Application of Machine Vision' Digest No: 1995/113</u>, pp. 6/1-6/6, London, May, 1995.

Petty R S, Godber S X, Evans J P O, Robinson M, "Three-dimensional line-scan imaging system for measurement", <u>SPIE 2599A Symp. East '95: Three-Dimensional Imaging and Laser-Based Systems for Metrology and Inspection</u>, Philadelphia, October, 1995.

Petty R S, Godber S X, Evans J P O, Robinson M, "A rotating 3-D line-scan imaging system for co-ordinate measurement", <u>ISPRS Conf. on Optical 3-D Measurement Techniques</u>, Vienna, October, 1995.

Secondary Authorships :

Godber S.X., Petty R., Robinson M., Evans P., " Stereoscopic line-scan systems using rotational movement", <u>4th European Workshop on Three-Dimensional Television</u>, pp. 111-117, Rome, Italy, October, 1993.

Godber S.X., Petty R., Robinson M., Evans P., "A panoramic line-scan imaging system for teleoperator control", <u>SPIE 2177 Symposium on Electronic Imaging Science and Technology: Stereoscopic Displays and Applications V</u>, pp. 247-257, California, U.S.A., February, 1994, ISBN 0-8194-1472-7.

Godber S.X., Petty R., Robinson M., Evans P., "Line-scan vision systems using rotational movement", <u>ISPRS Commission V Intercongress Symposium: Close Range Imaging Systems and Their Performance</u>, pp. 109-113, Melbourne, Australia, March, 1994, ISSN 0256-1840.

Godber S.X., Petty R.S., Robinson M., Evans P., "One-dimensional sensors for robotics control", <u>International Dedicated Conference on Robotics, Motion and Machine Vision</u>, pp. 345-352, Aachen, Germany, November, 1994, ISBN 0-947719-69-5.

Godber S X , Petty R S, Evans J P O, Robinson M, "3-D line-scan image acquisition from a rotating platform", <u>SPIE 2555 Symp. on Optical Science, Engineering & Instrumentation</u>, San Diego, July, 1995.

Godber S X, Petty R S, Evans J P O, Robinson M, "Novel stereoscopic line-scan image production", <u>IWS3DI'95 - Proc. Intl. Workshop on Stereoscopic and Three-Dimensional Imaging '95</u>, pp. 187-194, Greece, September, 1995.

Other Authorships :

Evans J P O, Robinson M, Godber S X, Petty R S, "The development of 3-D (stereoscopic) imaging systems for security applications", <u>29th IEEE Intl. Carnahan Conference on Security Technology</u>, Sanderstead, Surrey, UK, October, 1995.

Appendix E

Research Papers Pertaining to the Research Presented in this Thesis

3-D Imaging Group

Richard Petty

Primary Authorships :

Petty R S, Godber S X, Robinson M, Evans P, "Rotational displacement line-scan imaging", SPIE/IS&T Electronic Imaging Newsletter, Vol. 5, No. 1, March, 1995

Petty R S, Godber S X, Robinson M, Evans J P O, "3-D vision systems using rotating 1-D sensors", IEE Colloquium on 'The Application of Machine Vision' Digest No: 1995/113, pp. 6/1-6/6, London, May, 1995.

Petty R S, Godber S X, Evans J P O, Robinson M, "Three-dimensional line-scan imaging system for measurement", SPIE 2599A Symp. East '95: Three-Dimensional Imaging and Laser-Based Systems for Metrology and Inspection, Philadelphia, October, 1995.

Petty R S, Godber S X, Evans J P O, Robinson M, "A rotating 3-D line-scan imaging system for co-ordinate measurement", ISPRS Conf. on Optical 3-D Measurement Techniques, Vienna, October, 1995.

Secondary Authorships :

Godber S.X., Petty R., Robinson M., Evans P., " Stereoscopic line-scan systems using rotational movement", 4th European Workshop on Three-Dimensional Television, pp. 111-117, Rome, Italy, October, 1993.

Godber S.X., Petty R., Robinson M., Evans P., "A panoramic line-scan imaging system for teleoperator control", SPIE 2177 Symposium on Electronic Imaging Science and Technology: Stereoscopic Displays and Applications V, pp. 247-257, California, U.S.A., February, 1994, ISBN 0-8194-1472-7.

Godber S.X., Petty R., Robinson M., Evans P., "Line-scan vision systems using rotational movement", ISPRS Commission V Intercongress Symposium: Close Range Imaging Systems and Their Performance, pp. 109-113, Melbourne, Australia, March, 1994, ISSN 0256-1840.

Godber S.X., Petty R.S., Robinson M., Evans P., "One-dimensional sensors for robotics control", International Dedicated Conference on Robotics, Motion and Machine Vision, pp. 345-352, Aachen, Germany, November, 1994, ISBN 0-947719-69-5.

Godber S X , Petty R S, Evans J P O, Robinson M, "3-D line-scan image acquisition from a rotating platform", SPIE 2555 Symp. on Optical Science, Engineering & Instrumentation, San Diego, July, 1995.

Godber S X, Petty R S, Evans J P O, Robinson M, "Novel stereoscopic line-scan image production", IWS3DI'95 - Proc. Intl. Workshop on Stereoscopic and Three-Dimensional Imaging '95, pp. 187-194, Greece, September, 1995.

Other Authorships :

Evans J P O, Robinson M, Godber S X, Petty R S, "The development of 3-D (stereoscopic) imaging systems for security applications", <u>29th IEEE Intl. Carnahan Conference on Security Technology</u>, Sanderstead, Surrey, UK, October, 1995.